Neutron scattering and magnetization studies of the spin correlations on the kagomé lattice antiferromagnet $KFe_3(OH)_6(SO_4)_2$

by

Kittiwit Matan

B.A. Physics
The University of Chicago (2001)

Submitted to the Department of Physics
in partial fulfillment of the requirements for the degree of

Doctor of Philosophy

at the

MASSACHUSETTS INSTITUTE OF TECHNOLOGY
[February 2008]
October 2007

Author ....
Department of Physics
October 22, 2007

Certified by ....
Young S. Lee
Mark Hyman Jr. Career Development Professor and Associate Professor
Thesis Supervisor

Accepted by ....
Thomas J. Greytak
Professor, Associate Department Head for Education

Neutron scattering and magnetization studies of the spin correlations on the kagomé lattice antiferromagnet $KFe_3(OH)_6(SO_4)_2$

by

Kittiwit Matan

Submitted to the Department of Physics
on October 22, 2007, in partial fulfillment of the
requirements for the degree of
Doctor of Philosophy

Abstract

The collective behavior of interacting magnetic moments can be strongly influenced by the topology of the underlying lattice. In geometrically frustrated spin systems, interesting spin dynamics and chiral correlations may develop that are related to the spin arrangement on triangular plaquettes. We report studies of the spin-wave excitations and spin chirality on a two-dimensional geometrically frustrated lattice. Our new chemical synthesis methods allow us to produce large single crystal samples of $KFe_3(OH)_6(SO_4)_2$, an ideal kagomé lattice antiferromagnet. The spin-wave excitations have been measured using high-resolution inelastic neutron scattering. We directly observe a flat mode which corresponds to a lifted "zero energy mode," verifying a fundamental prediction for the kagomé lattice. A simple Heisenberg spin Hamiltonian provides an excellent fit to our spin-wave data. The antisymmetric Dzyloshinskii-Moriya interaction is the primary source of anisotropy and explains the low-temperature magnetization and spin structure.

In addition, combined thermodynamic and neutron scattering measurements reveal that the phase transition to the ordered ground-state is unusual. At low temperatures, application of a magnetic field induces a transition between states with different non-trivial spin-textures. The transition indicated by the sudden increase in the magnetization arises as the spins on alternating layers, which are previously oppositely canted due to the ferromagnetic interplane coupling, rotate 180° to align the canting moment along the $c-$axis. These observations are consistent with the ordering induced by the Dzyloshinskii-Moriya interaction. Elastic neutron scattering measurements in high field verify the 180° spin rotation at the transition.

The critical behavior in jarosite cannot be categorized by any known universality classes. We propose a scenario where both 2D XY and 2D Ising symmetries are present. The former represents a continuous planar rotational symmetry corresponding to the $SO(2)$ symmetry, while the latter is a discrete symmetry associated with the Z_2 symmetry. Depending on which measurements are performed, the critical behavior of the system can belong to either $SO(2)$ or Z_2 universality classes with two distinct critical temperatures; one is associated with the spontaneous breaking of the Z_2 symmetry, and the other corresponds to a topological order (BKT transition) due to vortex-antivortex binding. The former occurs at a slightly higher temperature than the latter. Neutron scattering measurements show a signature of the BKT transition, while specific heat measurements show a feature of the 2D Ising transition. Above T_N, the in-plane spin gap vanishes, and the system retains the $SO(2)$ symmetry when measured with neutron scattering. On the other hand, specific heat measurements show a feature of the 2D Ising transition, since the underlying symmetry of the spin Hamiltonian is the time-reversal or Z_2 symmetry.

Thesis Supervisor: Young S. Lee
Title: Mark Hyman Jr. Career Development Professor and Associate Professor

Acknowledgments

First and foremost, I thank Young for his guidance and support during my graduate career. His wisdom and insights into physics problems have guided me through my research. His prudent guidance helped me to reach my true potential, and often beyond what I thought I was capable of. He has always challenged me with difficult problems, which subsequently lead me to more accurate and deeper understanding of physics. I owe him great gratitude.

I thank my collaborators at the Department of Chemistry for providing me with wonderful samples. Without their samples, this work would not be possible. For that, I am grateful to Daniel Grohol, Bart M. Bartlett, Emily Nytko-Lutz, Matthew Shores, and Dan Nocera. I thank my collaborators at NIST Center for Neutron Research (NCNR), Jeff Lynn, Seung-Hun Lee, Ying Chen, Jae-Ho Chung, and Qing Huang; at HFIR, Oak Ridge National Laboratory, Steve Nagler and Mark Lumsden; at Berlin Neutron Scattering Center, Dr. Sikolenko; and at the Japanese Atomic Energy Agency, Shuichi Wakimoto and Kazu Kakurai. They have taught me a lot about how to use neutron scattering instruments, and I am grateful for their hospitality during my experiments at their laboratories. I thank the staff at NCNR, Bill Clow, Even Fitzgerald, and WangChun Chen, for their help during my neutron scattering experiments. I am grateful to Taner Yildirim and A. Brooks Harris for their theoretical insights. I deeply thank Pouyan Ghaemi for many fruitful discussions and great ideas.

I thank my friends and colleagues in Young's group for their friendship. Being the first student in Young's group made it especially hard for me to adjust to a life of a graduate student. Eric arrived in the following spring, and his friendship made my life in graduate school and my trips to many laboratories both in the US and UK enjoyable. I am also grateful to Ryan and Rich for their help with my research. I deeply thank Goran for sharing his unique view of the world with me. I have learned so many interesting things through our daily small-talk while we were sharing our office. I am grateful to Joel for his help with my experiments and for proof-reading

this thesis. I thank all UROPs in the group, Daniel and Yi-Wen. I also grateful to Andrea and Deepak for their support and for hosting our poker games. I also thank Boris for his friendship and support.

I sincerely thank Fang Chou for his guidance during my initial years at MIT. I was motivated by his love and enjoyment of doing science. I thank Dr. Cho for his help with my measurements during his visit. I am very grateful to all members of my thesis committee, Marc Kastner, Xiao-Gang Wen and Eric Hudson.

I thank all of my Thai friends for their heartwarming support and encouragement. It was always fun taking road trips or just hanging out with them. In particular, I thank P′Bo and P′Kob for their hospitality during my early years at MIT. I am grateful to Pop, who endures my lack of skill in tennis. I thank P′Yong, Ae+, Nok, Lek, Pun, Aw, Jeab, and N′Gift for their sincere friendship and support. I am grateful to Nok, N'Puye, P'Peng, Ae+ and Yeaw for proof-reading this thesis. I deeply thank N′Jane for her encouragement during my difficult time.

I thank my parents, brothers, and all of my relatives at home for their moral support. I apologize for having to miss out on most of their important events. I am also very grateful to Ajarn Pitiwong for introducing me to science. Most importantly, I would like to dedicate this work to my mom. Her childhood story has always inspired me to keep learning. This thesis is a tribute to her love of learning.

Contents

List of Figures

List of Tables

Chapter 1

Introduction

The physics of geometrically frustrated spin systems [1, 2] is unconventional due to the collective behavior of interacting electron spins that are influenced by the topology of the underlying lattice. The coupling between the lattice and the spin interactions makes it difficult or in some cases impossible for the systems to be in a unique lowest possible energy state. Some systems can have an ordered state at low temperature, but the ordering temperature is much lower than that predicted by traditional theories of condensed matter physics such as Mean-Field theory. Other systems do not order at any finite temperatures even though exchange interactions between the magnetic spins are large. This competition between the lattice frustration and the exchange interactions results in the presence of novel, unconventional spin structures and spin dynamics of ground states such as spin ice [3, 4, 5, 6], spin nematic [7], spin liquid [8, 9, 10], and spin glass [11, 12, 13, 14, 15]. More interestingly is a phenomenon called quantum spin liquid, whose property includes the sought-after "resonating valence bond" state [16], proposed by Anderson [17] in the attempt to explain high transition temperature (high-T_C) superconductivity (Ref. [18, 19] and references therein).

One fundamental question in condensed matter physics is about the ground state of an antiferromagnet in 2 dimensions. Fig. 1-1 shows two possible ground states in a square lattice with antiferromagnetic coupling. In the classical case, spins prefer to align anti-parallel to their nearest neighbors, creating a static "up-down" state.

However, this state is not an eigenstate of the spin Hamiltonian. This implies that, in the quantum case, there must be a state with even lower energy than the up-down state. It has been proposed that such a state is the quantum spin-liquid state, where two nearest-neighboring spins form a singlet pair. This pair can move around, and resonate among themselves, creating the so called resonating valence bond, which is believed to be a mechanism of high-T_C superconductivity [17]. It has also been proposed that the quantum spin-liquid state exists in geometrically frustrated spin systems, such as triangular and kagomé lattices. Better understanding and observation of this quantum spin-liquid state in a real system would contribute tremendously to the advance of the condensed matter physics, and would lead to better understanding of high-T_C superconductivity.

A geometrically frustrated magnet is unusual in that they may have disordered ground-states in which an enormous number of spin configurations share the same energy [1, 20]. It is believed that the ground state of a $S = 1/2$ geometric-frustrated lattice antiferromagnet is not ordered, and it is an ideal system to search for the quantum spin liquid state [21, 22, 23, 24]. In addition, the study of cooperative systems between electronic and magnetic components will advance the development of a new class of materials, such as spintronic systems.

The simplest example of geometrical frustration is the case of a single triangular plaquette with a nearest-neighbor Ising-type antiferromagnetic interaction between a pair of spins located at each corner of the triangle as shown in Fig. 1-2. For antiferromagnetism, the lowest possible energy state is when all spins align anti-parallel to each other. However, in the triangular plaquette, this spin arrangement cannot be achieved since one of the three spins cannot align itself anti-parallel to its two neighbors simultaneously as shown in Fig. 1-2. In general, the strong geometrical frustration appears in most compounds with triangle-based lattice and nearest-neighbor antiferromagnetic interaction. Examples of geometrically frustrated systems are face-centered-cubic (FCC), pyrochlore, triangular and kagomé lattices as shown in Fig.1-3. The name "kagomé" is originated from a Japanese word for one particular type of Japanese basket weave patterns. FCC can be thought of as a three-dimensional (3D)

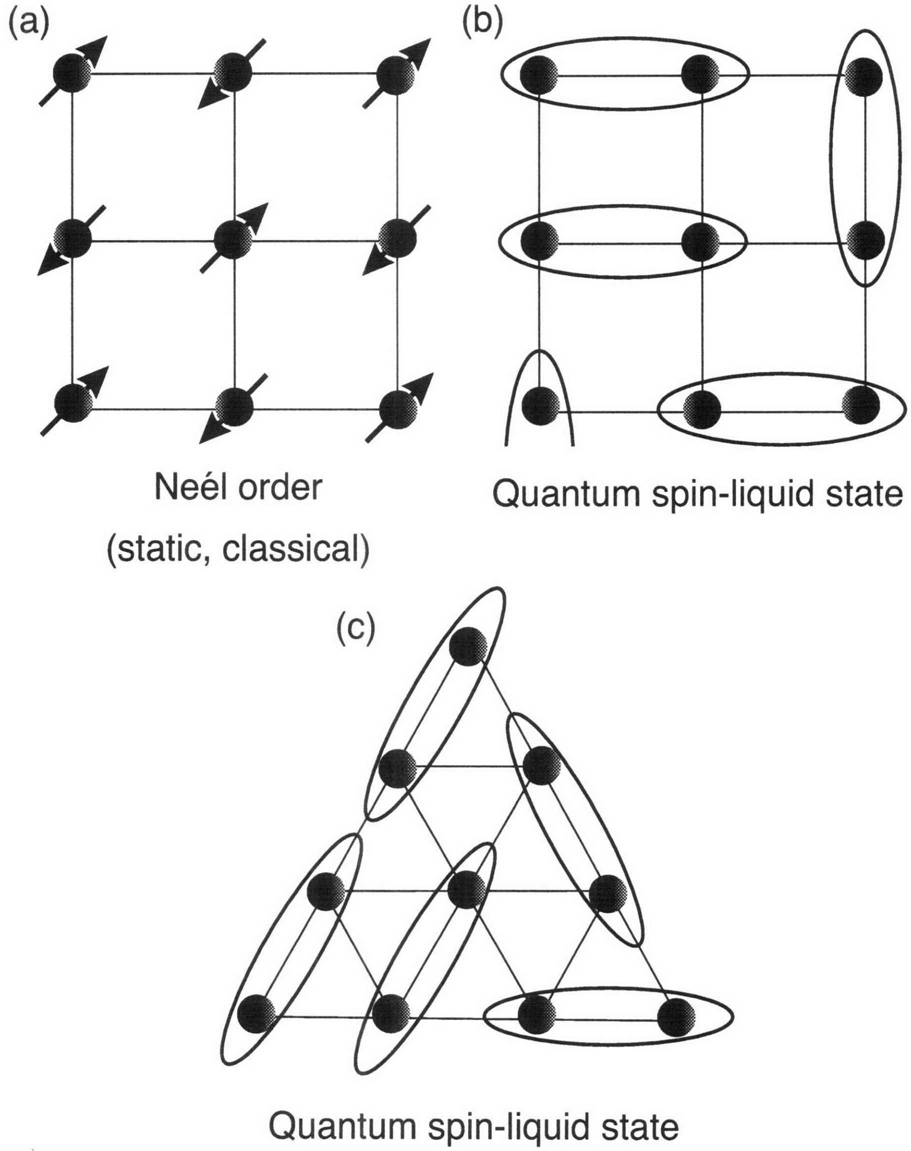

Figure 1-1: Possible ground states of an antiferromagnet in 2 dimensions. a) Neél order in a square lattice. b) Quantum spin-liquid state in a square lattice. c) Quantum spin-liquid state in a triangular lattice.

analogue of triangular lattice. The FCC lattice is formed by a set of edge-sharing tetrahedra, while the triangular lattice is formed by a set of edge-sharing triangles. Similarly, pyrochlore is a 3D analogue of a kagomé lattice. While pyrochlore is comprised of corner-sharing tetrahedra, the kagomé lattice is a network of corner-sharing triangles.

The frustration shown in Fig. 1-2 is relaxed when the symmetry of the systems changes from Ising-type to planar (XY) and isotropic (Heisenberg) spins. A ground state of the XY or Heisenberg spins on the frustrated triangle-based lattices is the so-called 120° state, where angles between any two spins on the triangle are 120°. In this ground state, the vector sum of all spins on the corners of the triangle or tetrahedron is zero, i.e., $\sum \mathbf{S}_i = 0$. The distinction between corner-sharing and edge-sharing lattices also becomes crucial for XY and Heisenberg spins. For simplicity, we will only consider the 2D lattices, triangular and kagomé. For the edge-sharing triangular lattice, once the 120° arrangement of the spins on one triangle is chosen, the direction of all other spins on the lattice can be uniquely determined. On the other hand, this is not the case for the corner-sharing kagomé lattice; there is no unique ground state when the 120° arrangement is chosen for a single triangular plaquette. As shown in Fig. 1-4, once the arrangement of the spins on the top triangle is chosen to satisfy the 120° arrangement, the bottom two spins can have two different spin arrangements, both of which satisfy the 120° requirement. This is due to the lower degree of connectivity in the kagomé lattice. While there are six nearest neighbors for the triangular lattice, there are only four nearest neighbors for the kagomé lattice. Therefore, the kagomé lattice is considered more frustrated than the triangular lattice.

The spin orientation on a triangle can also be characterized by vector chirality, which is defined by a normal vector $\mathbf{K}_v$ to each triangle:

$$\mathbf{K}_v = \frac{2}{3\sqrt{3}}(\mathbf{S}_1 \times \mathbf{S}_2 + \mathbf{S}_2 \times \mathbf{S}_3 + \mathbf{S}_3 \times \mathbf{S}_1), \tag{1.1}$$

where $\mathbf{S}_1$, $\mathbf{S}_2$ and $\mathbf{S}_3$ are spins on the triangle as labeled in Fig. 1-5. The chirality is positive with amplitude +1 (negative with amplitude -1) if the spins on the triangle

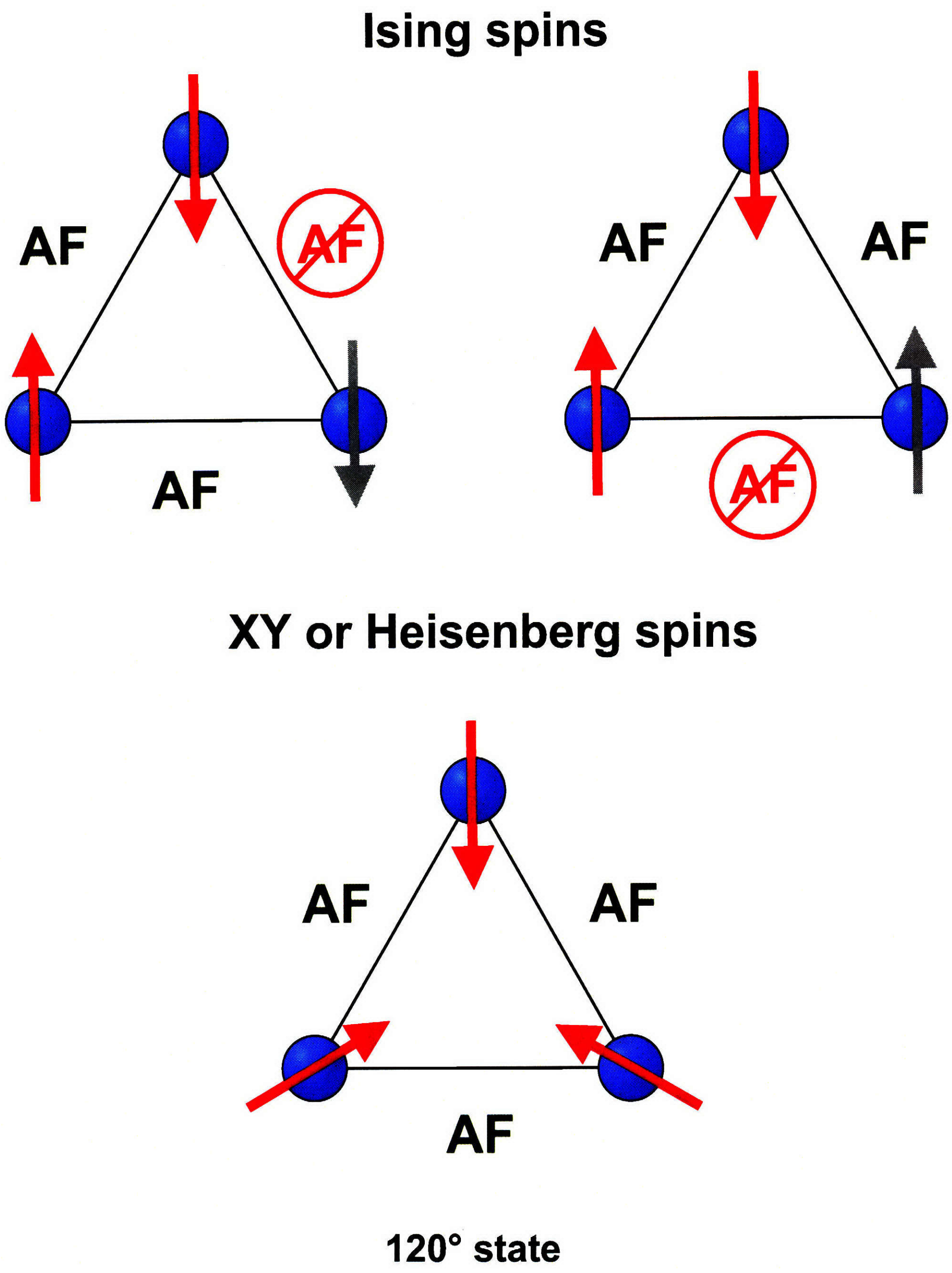

Figure 1-2: Spins on corners of a triangle with Ising-type antiferromagnetic interaction. The spin on the right corner cannot satisfy both antiferromagnetic bonds with its two neighboring spins simultaneously, and becomes “frustrated”. For XY and Heisenberg spins, a ground state is the 120° state. The bottom diagram shows one of infinitely degenerate states with 120° arrangement.

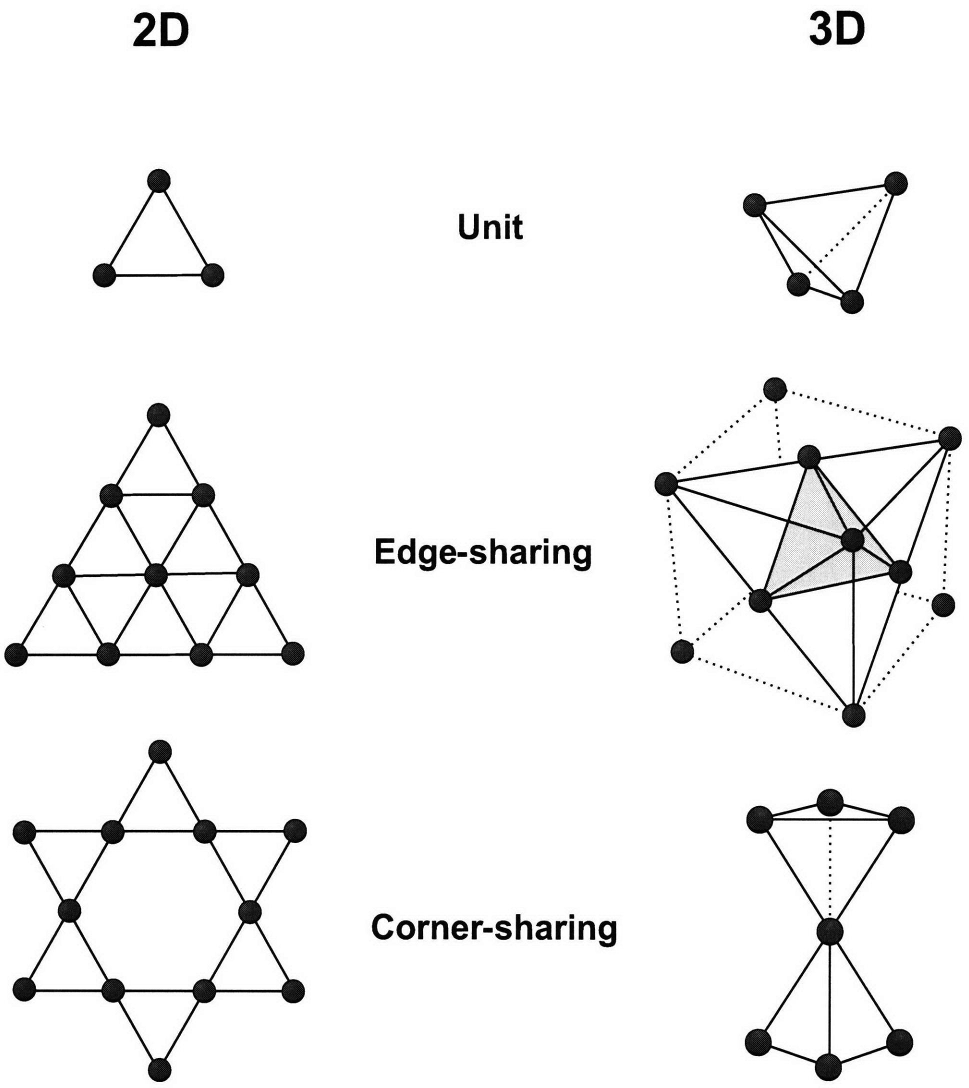

Figure 1-3: Examples of frustrated magnetic lattices. The left column shows 2D lattices, and the right column shows 3D lattices. The second and third rows correspond to lattices with edge-sharing and corner-sharing triangles or tetrahedra, respectively. The shaded areas indicate shared surfaces for the FCC lattice.

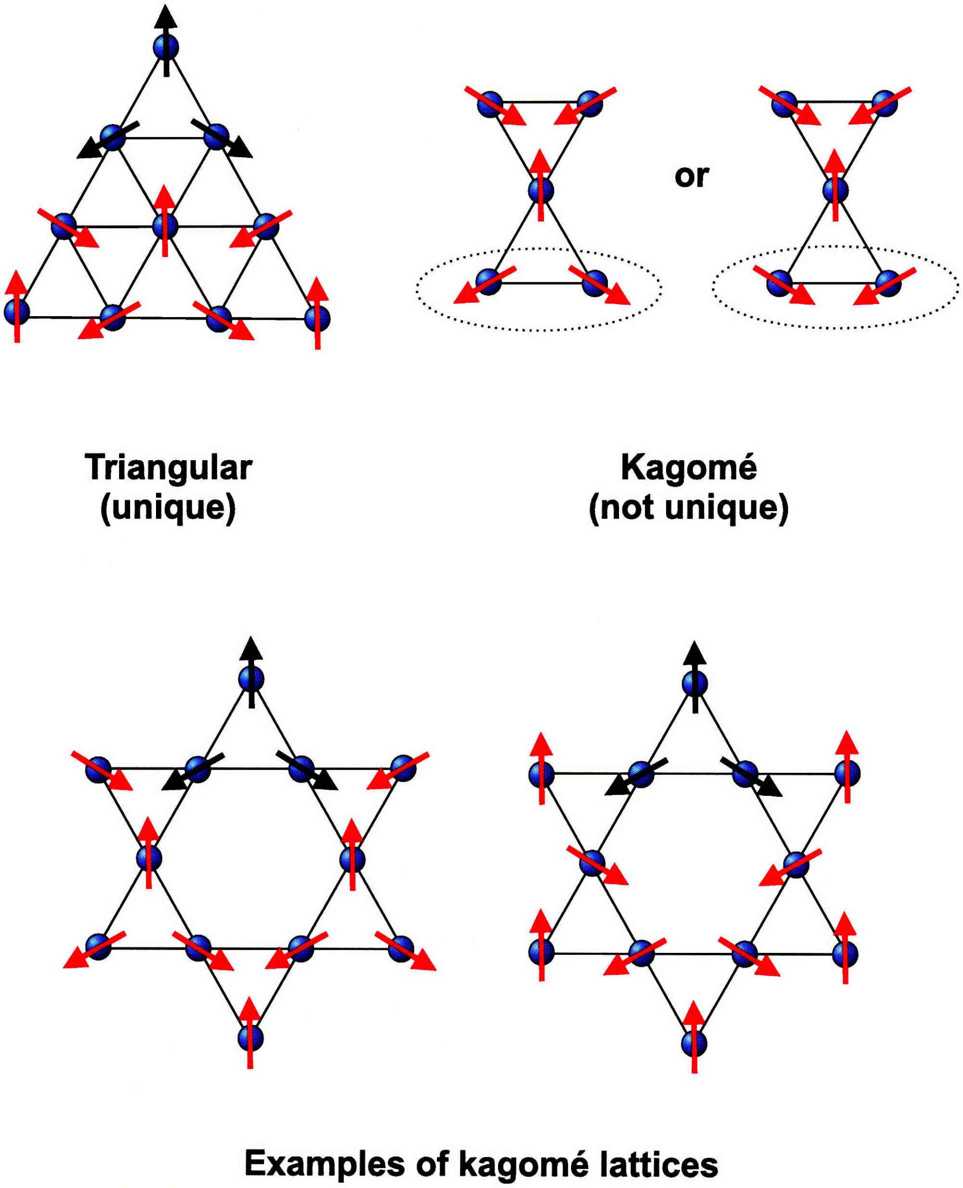

Figure 1-4: Antiferromagnetic ground state for triangular and kagomé lattices. Once the spin arrangement on the top triangle (shown in black) is chosen, the configuration of the spins on the whole lattice can be uniquely determine for the triangular lattice. On the other hand, for the kagomé lattice, there is no unique ground state.

rotate 120° clockwise (counterclockwise) as one traverses around the triangle clockwise. For the triangular lattice, the chirality on two adjacent triangles have opposite signs. However, in the kagomé lattice, the chirality on each triangle is independent of those on the adjacent ones, indicative of a higher degree of frustration. This type of chirality was first introduced by Villain in 1977 [25].

The other type of chirality observed in magnetic material is the scalar chirality, defined on each triangular plaquette as

$$\mathrm{K}_s = \mathbf{S}_1 \cdot (\mathbf{S}_2 \times \mathbf{S}_3)\,. \tag{1.2}$$

The presence of this type of chirality (in static or fluctuating forms) can have important consequences in strongly correlated electron systems, such as yielding an anomalous Hall effect in metallic materials [26, 27]. Fig. 1-5 shows spin configurations with zero and non-zero values of the net scalar chirality in the triangle-based lattices.

The kagomé lattice is one of the most highly frustrated two-dimensional lattices. For isotropic Heisenberg spins, the ground state of a kagomé antiferromagnet is infinitely degenerate due to frustration and low dimensionality (2D), but the system is believed to be ordered at $T = 0$ by the process of thermal and quantum fluctuations known as *ordering by disorder* [28, 29, 30, 31, 32, 33, 34]. For non-zero temperatures, the degeneracy can be lifted in the presence of next-nearest-neighbor interactions [35, 36], single-ion anisotropies [37, 38], or Dzyaloshinskii-Moriya (DM) interactions [39], allowing for the establishment of long-range order.

Two of the most common spin configurations on the kagomé lattice are "$q = 0$" and $\sqrt{3}\times\sqrt{3}$ structures. Fig. 1-6 shows $q = 0$ and $\sqrt{3}\times\sqrt{3}$ structures with positively uniform and staggered vector chirality, respectively. In the $q = 0$ structure with uniform positive chirality, the spins on each triangle form the 120° state, and point either toward (all-in) or away from (all-out) the center of the triangle. In the $\sqrt{3}\times\sqrt{3}$ structure, the signs of the vector chirality on adjacent triangles are opposite. The name $q = 0$ originates from the fact that the 2D magnetic unit cell is the same as the

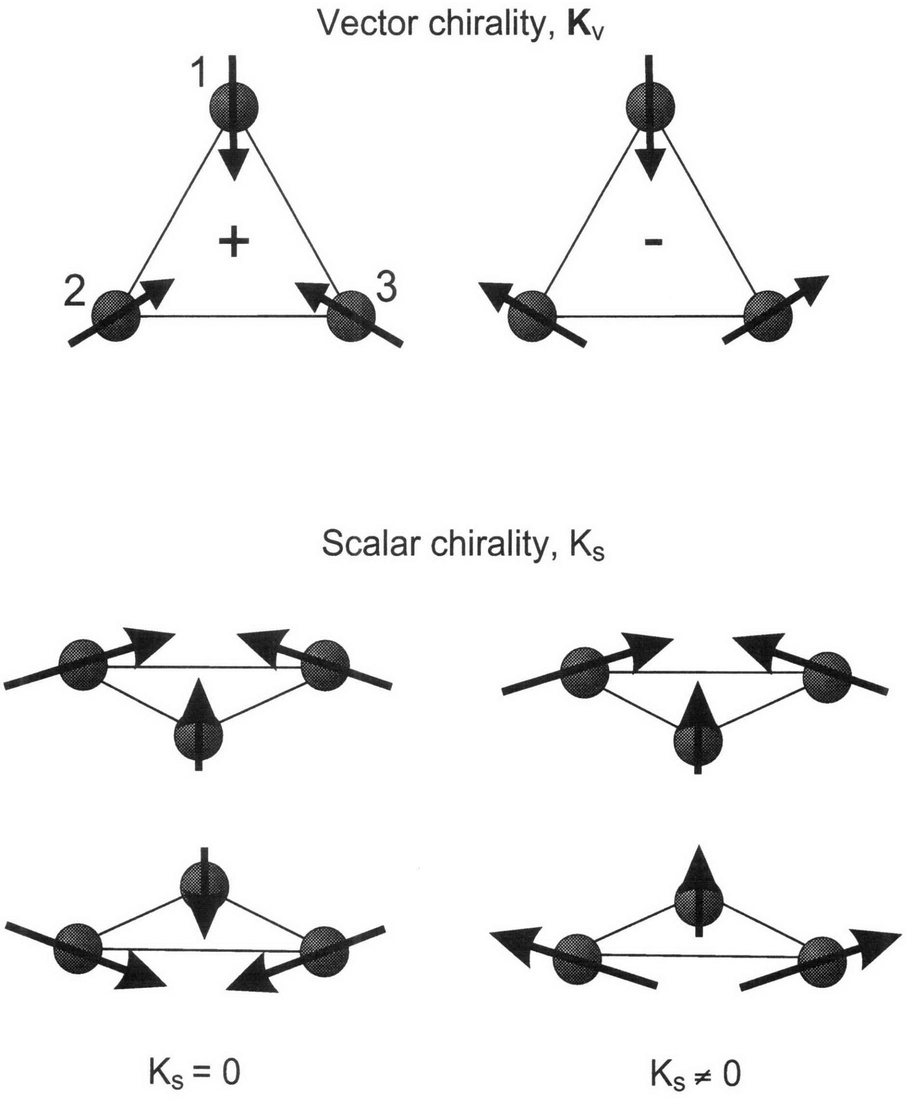

Figure 1-5: The diagram shows vector chirality and scalar chirality. The vector chirality is positive (negative) if the spins on the triangle rotate 120° clockwise (counterclockwise) as one transverse around the triangle clockwise. The net scaler chirality is non-zero if the spins cant out of the kagomé planes in opposite directions.

2D structural unit cell, and the name $\sqrt{3} \times \sqrt{3}$ indicates that the 2D magnetic unit cell is three times as large as the 2D structural unit cell as shown by the yellow shaded area in Fig. 1-6. Using Monte Carlo simulations, Reimers and Berlinsky show that the *ordering by disorder* in the classical Heisenberg kagomé lattice antiferromagnet resulting from thermal and quantum fluctuations favors the $\sqrt{3} \times \sqrt{3}$ structure over the $q = 0$ structure as $T \rightarrow 0$ [29, 31, 32]. This $\sqrt{3} \times \sqrt{3}$ ordered state at $T = 0$ was also confirmed by Sachdev using a systematic large-N analysis on the kagomé lattice [33].

One of the distinctive features of the frustrated kagomé lattice Heisenberg model is the presence of "zero energy modes," which result from the highly degenerate, but connected, ground state manifold [40, 41]. The only constraint for the ground state is that the spins on each triangle be oriented 120° relative to each other. Fig. 1-6 depicts the zero energy mode for the kagomé lattice Heisenberg model. The loops at the tips of the spins illustrate rotations of two of the spin sublattices about the axis defined by the direction of the third spin sublattice. In the case of $q = 0$ structure, these spins form a chain, and collectively rotate around the loop path with no change in energy since the 120° angles on each triangle are maintained. Furthermore, the spins on different parallel chains, which can be either along the a or b crystallographic direction, can be excited independently. Hence, this type of excitation costs no energy and is nondispersive [35, 40, 41, 38]. For the $\sqrt{3} \times \sqrt{3}$ structure, instead of forming a chain, these spins form a hexagon as shown in Fig. 1-6. Similarly, the spins on different hexagons can be excited independently, making the excitation nondispersive. It is interesting to note that the spin configurations with uniform positive and negative chirality are connected. For example, one can rotate all horizontal chains of spins without breaking the 120° state to go from one configuration with positive chirality to the other with negative chirality and vice versa. This is not the case for the $\sqrt{3}\times\sqrt{3}$ structure, which has the staggered chirality. Experimentally, this zero energy mode cannot be observed directly since it occurs at zero energy. However, in iron jarosite the ground state degeneracy is lifted, and this mode is raised to a finite energy due to the presence of anisotropic interactions. This makes it possible to detect this mode

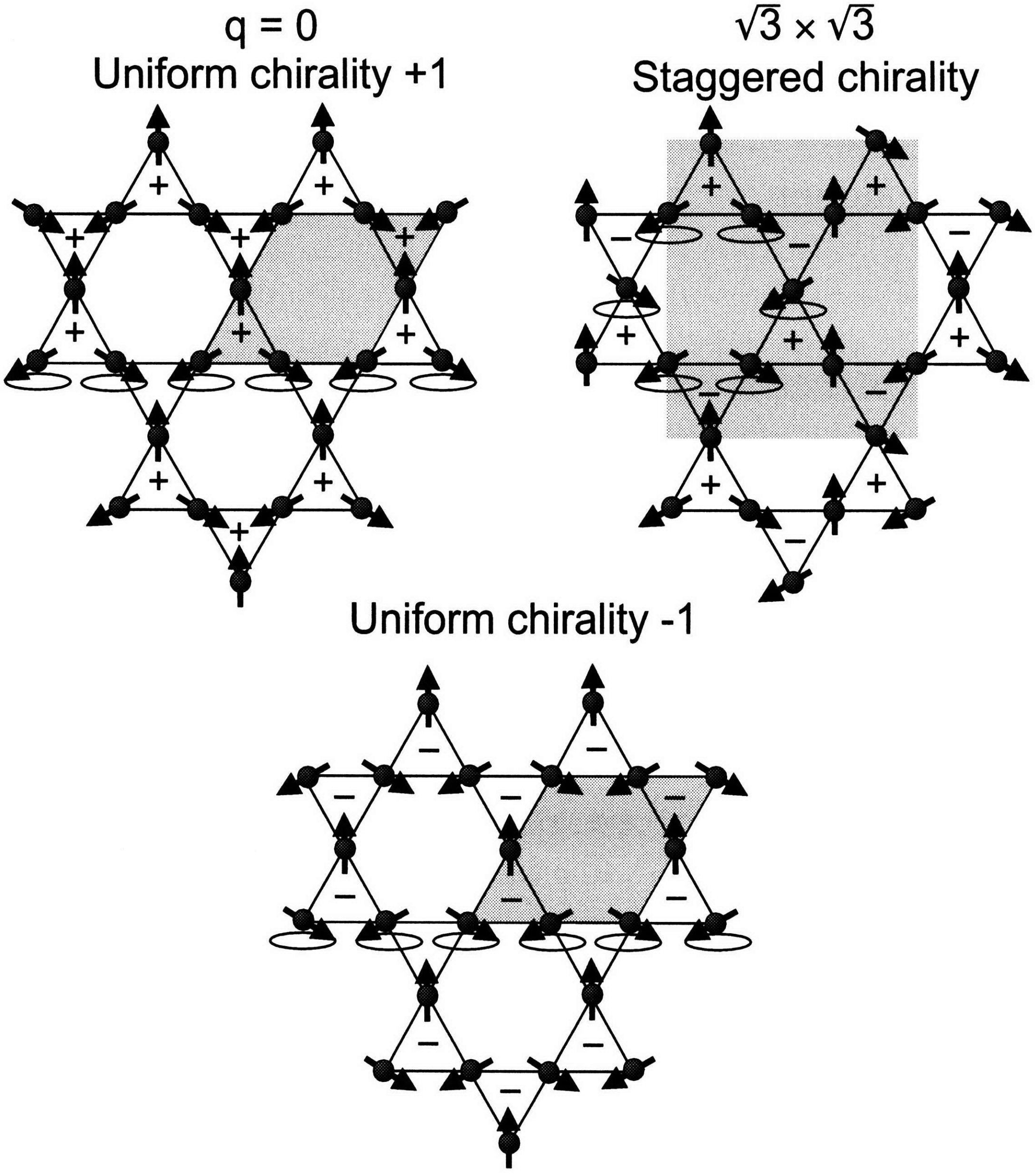

Figure 1-6: The kagomé lattice with spins arranged in two different configurations. The q=0 structure, which is the ground state configuration for iron jarosite. The spin arrangement has uniform, positive vector chirality, indicated by the + within each triangular plaquette. The magnetic unit cell, shown by the yellow shaded area, is the same as the chemical unit cell. An alternate spin arrangement with staggered vector chirality, known as the $\sqrt{3} \times \sqrt{3}$ structure, whose magnetic unit cell is three times as large as that of the q=0 structure. The loops at the tips of the spins illustrates the zero energy mode for both spin configurations.

directly using inelastic neutron scattering.

1.1 Realizations of the kagomé lattice antiferromagnet

Although long regarded as a prime model for studying geometrically frustrated spin systems, the kagomé lattice compounds have escaped precise magnetic characterization because compounds that form this lattice are difficult to make pure and in large single-crystal form. Several materials, such as kagomé-bilayer garnet compounds, $SrCr_9Ga_3O_{19}$ (SCGO) [42, 43, 44, 45, 46, 47, 48, 49, 50, 51] and $Ba_2Sn_2ZnCr_{7p}Ga_{10-7p}O_{22}$ (BSZCGO) [52, 53, 54, 55], kagomé-staircase compounds [56, 57, 58, 59, 60, 61, 62, 63, 64], and volborthite [65, 66, 67], are believed to be realizations of the kagomé lattice antiferromagnet, and have been studied experimentally. However, theses materials are often plagued by non-stoichiometry issues or have structural differences from the ideal kagomé network. For example, in SCGO and BSZCGO an additional triangular lattice intercalated between the kagomé planes complicates the magnetic properties of the kagomé network, and in volborthite the triangles forming the kagomé lattice are not equilateral, making the antiferromagnetic coupling between neighboring spins non-isotropic. Recently, the $S = 1/2$ kagomé lattice antiferromagnet $ZnCu_3(OH)_6Cl_2$ and lindgrenite (organic-inorganic hybrid compound) have been synthesized and studied experimentally [68, 69, 70, 71, 72, 73, 74], which should lead to a better understanding of the disordered state or possible quantum spin-liquid state in the geometrically frustrated magnets.

One realization of the kagomé lattice antiferromagnet is jarosite. This class of compounds is particularly ideal for a study of the kagomé lattice for the following reasons. First, it consists of single layers of undistorted kagomé planes, and these planes remain undistorted down to low temperatures ($T < 5$ K). Second, this jarosite can be synthesized with compositions that are stoichiometrically pure. This ensures that we are primarily studying the effects of geometrical frustration rather than the effects of disorder. Third, large single crystals can be made, which allow investigations of spin correlations of this kagomé compound that would not be possible with powder samples alone.

The jarosite family is one subgroup of a very large group of minerals called alunite, which consists of more than 40 isostructural compounds [75, 76, 77, 78]. The general formula of the alunite supergroup is $AM_3(\mathrm{OH}, \text{-}\mathrm{OH_2})_6(\mathrm{TO_4})_2$. The A site is occupied by a monovalent, divalent or trivalent cation, such as $\mathrm{Na^+}$, $\mathrm{K^+}$, $\mathrm{Rb^+}$, $\mathrm{Tl^+}$, $\mathrm{NH_4}^+$, $\mathrm{H_3O^+}$, $\mathrm{Ca^{2+}}$, $\mathrm{Ba^{2+}}$, $\mathrm{Pb^{2+}}$, $\mathrm{Hg^{2+}}$, $\mathrm{Bi^{3+}}$, and rare earths. The M site is occupied by an $\mathrm{Al^{3+}}$, $\mathrm{Cr^{3+}}$, $\mathrm{V^{3+}}$, or $\mathrm{Fe^{3+}}$ ion in an octahedral environment formed by six oxygens. The T site is occupied by a $\mathrm{S^{6+}}$, $\mathrm{P^{5+}}$, or $\mathrm{As^{5+}}$ in a tetrahedral environment formed by four oxygens. The oxygen octahedral and tetrahedral environments for the M and T sites are shown in Fig. 1-7 by purple octahedra and blue tetrahedra, respectively.

Jarosite was first discovered in 1852 by August Breithaupt, a German mineralogist, in the Barranco del Jaroso, Almera, Andalusia, Spain. The name jarosite originated from this region in southern Spain where the mineral was first found. It was also discovered on Mars in 2004 by *Opportunity*, one of two rovers sent to explore Mars by NASA. The discovery gives strong evidence that liquid water was once present on Mars [79, 80, 81].

The jarosite family has the general chemical formula of $AM_3(\mathrm{OH})_6(\mathrm{SO_4})_2$, and is comprised of non-magnetic monovalent or bivalent cations such as $\mathrm{Na^+}$, $\mathrm{K^+}$, $\mathrm{Rb^+}$, $\mathrm{NH^+}$, $\mathrm{Ag^+}$, $\mathrm{Tl^+}$, $\mathrm{H_3O^+}$, or $\frac{1}{2}\mathrm{Pb^{2+}}$, and magnetic ions such as $\mathrm{Fe^{3+}}$, $\mathrm{Cr^{3+}}$, or $\mathrm{V^{3+}}$ [37, 82, 83, 38, 84, 85, 86, 87, 88, 89, 90, 91, 92, 93, 94, 95]. The magnetic ions located inside tilted octahedral cages formed by six oxygen atoms sit at each corner of the corner-sharing triangles that form the perfect kagomé planes. The faces of the triangles are alternately capped by the sulfate group $\mathrm{SO_4^{2-}}$ with the A^+ ions sitting on the site opposite to the sulfate caps as shown in Fig. 1-7. The kagomé planes are well separated by these non-magnetic A^+ ions (e.g., $\mathrm{K^+}$ ions shown by the green spheres in Fig. 1-7 for $\mathrm{KFe_3(OH)_6(SO_4)_2}$) and the sulfate groups $\mathrm{SO_4^{2-}}$, which form tetrahedral environment shown by the blue tetrahedra in Fig. 1-7. The interlayer coupling is negligibly small, attesting to the two-dimensionality of the system. Unlike SCGO

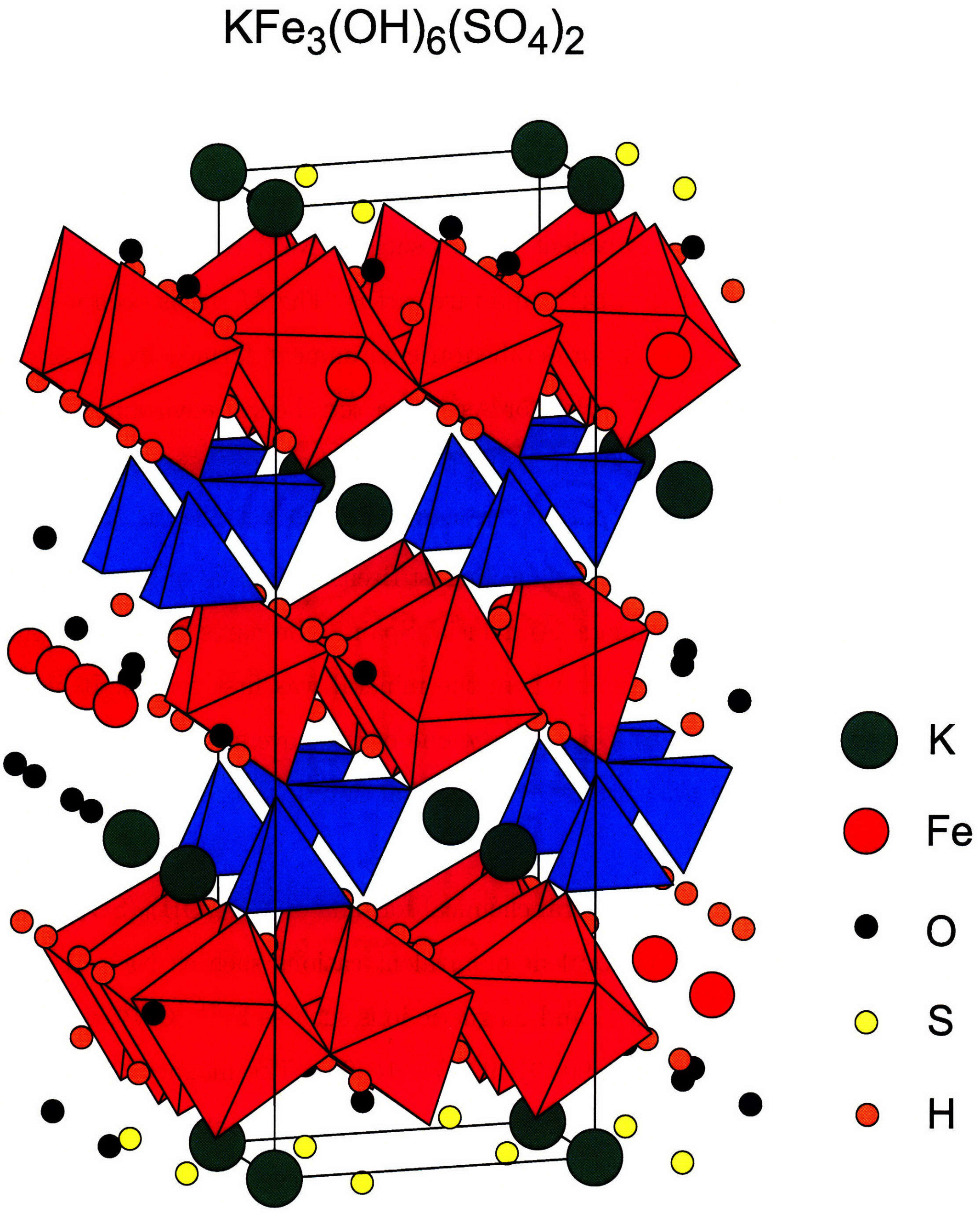

Figure 1-7: Crystal structure of $KFe_3(OH)_6(SO_4)_2$. One structural unit cell contains three kagomé layers of magnetic Fe^{3+} ions.

and vorborthite, jarosite has no magnetic ions between the kagomé planes, and the magnetic ions in jarosite form a perfect kagomé network (comprised of equilateral triangles), making it an ideal compound to study the effects of the geometric frustration. It is interesting to note that due to the difference of the $d-$orbital occupancy of the magnetic M^{3+} ions in the tetrahedral crystal field in different types of jarosites, the superexchange interactions of Fe^{3+} and Cr^{3+} spins in iron and cromium jarosites are antiferromagnetic, while the superexchange interaction between V^{3+} spins in vanadium jarosite is ferromagnetic [89].

We have studied extensively two types of iron jarosites, $KFe_3(OH)_6(SO_4)_2$ (K jarosite) and $AgFe_3(OH)_6(SO_4)_2$ (Ag jarosite). The magnetic properties of these two compounds are basically the same due to the basic magnetic unit, the $Fe_3^{III}(\mu-OH)_3$, which is structurally homologous in these two jarosites. The magnetic Fe^{3+} spins located inside tilted octahadral environments formed by six oxygen atoms form perfect kagomé planes. These planes stack up along the $c-$axis with a negligibly small ferromagnetic interplane coupling. Due to the presence of anisotropic interactions and the interplane coupling, the spins order three-dimensionally at low temperature. In 1968, the first attempt to study the magnetic structure of jarosite was done by Takano *et al.* using Mössbauer measurements [96, 97]. The obtained spin structure was qualitatively similar to the $q = 0$ structure [97]. However, neutron diffraction is needed to correctly refine the spin structure. That came in 1986 when Townsend *et al.* [98] performed power neutron diffraction on $KFe_3(OH)_6(SO_4)_2$ to investigate its magnetic structure. However, their proposed spin configuration is not quite correct. It was later corrected by Inami *et al.* [37] in 2000. They have shown that the spins order in a coplanar $q = 0$ structure below the Néel temperature $T_N = 65$ K. The 2D magnetic unit cell is identical to the 2D nuclear (structural) unit cell. However, the stacking-up of the kagomé planes causes the doubling of the magnetic unit cell along the c direction. It takes six kagomé planes to form a magnetic unit cell, instead of three planes that form a nuclear (structural) unit cell, as shown in Fig. 1-8.

The 3D long-rang order (LRO) has been observed in all except one jarosite called the hydronium jarosite $(H_3O)Fe_3(OH)_6(SO_4)_2$ [99, 100, 101, 102]. For some time, the occupancy of the magnetic sites in this compound was the highest in the jarosite family (about 97%). The absence of LRO in this kagomé lattice compound with nearly complete magnetic site occupancy led some scientists to believe that the true ground state of the perfect kagomé lattice is of a disordered, spin-glass type, and that the presence of LRO in other jarosites with incomplete coverage of magnetic sites is due to the site defects. In addition, site deficiency might result in the successive magnetic phase transition found in some jarosite samples [103]. The inability to produce stoichiometrically pure samples of other types of jarosite prevented study of the magnetic properties of the perfect kagomé network, leading to this misinterpretation [104, 105]. Using a new redox-based hydrothermal method, Grohol *et al.* were able to produce jarosite samples with a nearly complete occupancy of magnetic sites for all types of jarosite, and proved that the absence of LRO in the hydronium jarosite is due to structural and magnetic disorder that arises from proton transfer from the hydronium ion H_3O^+ located between the kagomé layers to the bridging hydroxide ions in the kagomé planes:

$$(H_3O)Fe_3(OH)_6(SO_4)_2 \rightarrow (H_3O)_{1-x}(H_2O)_xFe_3(OH)_{6-x}(H_2O)_x(SO_4)_2. \quad (1.3)$$

The above reaction shows the proton transfer from the interlayer hydronium ion to the bridging hydroxyls (from H_3O^+ to OH^-), where water molecules are formed. These water molecules can be detected using inferred spectroscopy [89].

In the past, jarosites were synthesized in the laboratory by precipitation from hydrolyzed acidic solutions of sulfate anions and monovalent or trivalent cations while heated between 100-200°C under hydrothermal conditions. The overall chemical reaction is represented by the following chemical equation:

$$3Fe_2(SO_4)_3+A_2SO_4+12H_2O \rightarrow 2AFe_3(OH)_6(SO_4)_2+6H_2SO_4. \quad (1.4)$$

However, under these conditions, the monovalent cation A^+ is prone to replacement

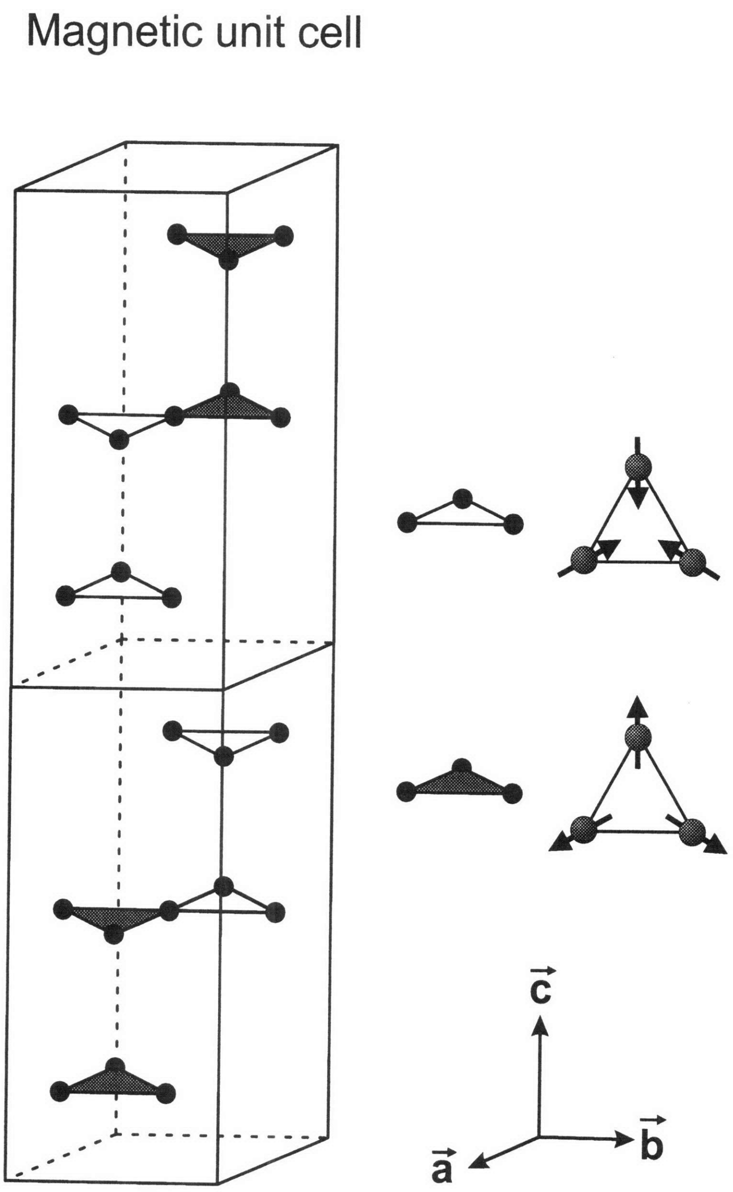

Figure 1-8: This diagram shows the stacking-up of the kagomé planes along the c direction. The magnetic unit cell is twice as large as the nuclear (structural) unit cell, caused by the doubling of the the magnetic unit cell along the c direction. The 2D magnetic unit cell is the same as the 2D nuclear unit cell. White triangles indicate all-in arrangement, and blue triangles indicate all-out arrangement.

by hydronium ions H_3O^+.

$$A\mathrm{Fe_3(OH)_6(SO_4)_3}+x\mathrm{H_3O^+} \rightarrow A_{1-x}\mathrm{(H_3O)Fe_3(OH)_6(SO_4)_3}+xA^+. \qquad (1.5)$$

The proton transfer to form water molecules also prevents the accrual of negative charge on the kagomé lattice sites, resulting in the Fe^+ site vacancies [89].

$$A\mathrm{Fe_3(OH)_6(SO_4)_3}+3x\mathrm{H^+} \rightarrow A\mathrm{Fe}_{3-x}\mathrm{(H_2O)}_{3x}\mathrm{(OH)}_{6-3x}\mathrm{(SO_4)_3}+x\mathrm{Fe^{3+}}. \qquad (1.6)$$

In addition with this method, only microcrystalline materials are obtained owing to the heightened acidity of the solution as well as the speed and intractability of the precipitation reaction [37, 38, 104, 106, 107]. Therefore, most previous studies reported samples with a 70-94% occupancy of magnetic sites. The only compound that has been synthesized with near 100% occupancy of the magnetic sites is $(H_3O)Fe_3(OH)_6(SO_4)_2$ with the magnetic site occupancy of about 97%. Consequently, the magnetic properties of these non-stochiometrical compounds appear non-universal and sample-dependent with ordering temperatures varying from 18 K to 65 K. To fully understand the physics of a geometrically frustrated magnet in the kagomé lattice antiferromagnets, it is very important to develop a synthesis method that yields stoichiometrically pure compounds with close to 100% occupancy of magnetic sites.

Alternatively, Sasaki and Konno have synthesized the jarosite-group compounds $AFe_3(OH)_6(SO_4)_2$ with $A^+ = Ag^+$, K^+ and NH_4^+ by supplying Fe^{3+} ions using three different methods: biological oxidation of Fe^{2+} ions by biological products, chemical oxidation of Fe^{2+} ions by slow addition of H_2O_2, and chemical oxidation by rapid addition of H_2O_2 [108]. The compositions of their final products highly depend on the methods of preparation and are independent of the jarosite species. The morphology of the crystals is determined by the production rate of Fe^{3+} ions, and monovalent species. Furthermore, compared with the standard hydrothermal method, all three methods yields lower levels of stoichiometric purity. Therefore, their synthesis methods fail to produce high quality crystals for a study of magnetism.

The challenges confronting the synthesis of pure jarosites have been overcome with the development of redox-based hydrothermal methods [93]. Our collaborators led by Dr. Daniel G. Nocera at the Department of Chemistry at MIT have designed a new synthesis route, in which Fe^{3+} ions are generated in a controlled environment, where the redox reaction is carefully monitored, prior to the precipitation of jarosite [89]. By controlling the rate in which Fe^{3+} is generated, we can tune the Fe^{3+} concentration to an optimal value so that the replacement by the hydronium ions is minimal or disappears. In addition, using this redox-based hydrothermal method, the group is able to synthesize a new class of stoichimetrically pure and single crystal samples[1] of V^{3+}-based jarosites $AV_3(OH)_6(SO_4)_2$, where A=Na^+, K^+, Rb^+, NH_4^+ and Ti^+. The synthesis and characterization of this class of material can be found in Ref. [91, 92, 109].

1.2 Synthesis and characterizations

The detailed synthesis procedure of iron jarosite can be found in the articles by Grohol *et al.* in Ref. [89, 90, 110, 111]. In this section, I will summarize their synthesis approach to obtain the stoichiometrically pure powder and single crystal samples we used in our magnetic and neutron scattering measurements. The $AFe_3(OH)_6(SO_4)_2$ with A =K^+ and Ag^+ were synthesized by oxidizing metallic iron under hydrothermal conditions in the acidic solutions of A^+ and SO_4^{2-} ions. There are two steps of oxidizing the metal material by protons and oxygen, respectively. First, protons that are present in the acidic solution oxidize the starting material Fe to produce Fe^{2+}. Since Fe^{2+} is stable in the acidic solution, it cannot be oxidized to produce Fe^{+3}, which one needs in precipitation process to produce jarosite, by protons. Instead, oxygen is needed in the production of Fe^{3+}. Grohol *et al.* found that the redox reactions prior to precipitation are significant to produce the stoichimetrically pure

---

[1] Single crystal samples reported in a literature are often natural-grown, and therefore susceptible to impurity. As far as we know, we are the only group who possesses synthetic, pure and large single crystal samples.

jarosite samples. The reaction in Eq. (1.4) is modified to:

$$\begin{aligned} \mathrm{Fe}+2\mathrm{H}^+ &\rightarrow \mathrm{Fe}^{2+}+\mathrm{H}_2, \\ 2\mathrm{Fe}^{2+}+\frac{1}{2}\mathrm{O}_2+2\mathrm{H}^+ &\rightarrow 2\mathrm{Fe}^{3+}+\mathrm{H}_2\mathrm{O}. \end{aligned} \tag{1.7}$$

The acidity of the solution is moderated and slowly decreases during these reactions because H^+ ions are turned into H_2 and water. We believe that the fact that Fe^{3+} ions are slowly generated from these reactions controls the precipitation process in Eq. 1.8, which yields highly stoichimetrically pure samples. These redox reactions are followed by precipitation of the Fe^{3+} ions to produce single crystal samples of iron jarosite.

$$3\mathrm{Fe}^{3+}+2A_2\mathrm{SO}_4+6\mathrm{H}_2\mathrm{O} \rightarrow A\mathbf{Fe_3(OH)_6(SO_4)_2}+3A^++6\mathrm{H}^+. \tag{1.8}$$

Therefore, the overall reaction is the following:

$$3\mathrm{Fe}+\frac{3}{4}\mathrm{O}_2+3\mathrm{H}^++2A_2\mathrm{SO}_4+\frac{9}{2}\mathrm{H}_2\mathrm{O} \rightarrow A\mathbf{Fe_3(OH)_6(SO_4)_2}+3A^++3\mathrm{H}_2. \tag{1.9}$$

Using the synthesis method, they were able to produce single crystal samples of iron jarosites $KFe_3(OH)_6(SO_4)_2$ with > 96% occupancy of magnetic Fe^{3+} ions. The A (K, Ag) site occupancy was 100(1)%, and the level of deuteration was 100(1)% for deuterated powder samples [112]. In addition, they were able to make large single crystal samples (up-to 10 mm in length and 48 mg in mass), which make it possible for us to study this compound using a high-resolution triple-axis neutron scattering technique.

The following recipes for the syntheses of $KFe_3(OH)_6(SO_4)_2$ and $AgFe_3(OH)_6(SO_4)_2$ are taken from Ref. [89] and [94, 113].

Synthesis of $\mathbf{KFe_3(OH)_6(SO_4)_2}$ from Ref. [89]

> The 4.88 g (28.0 mml) K_2SO_4 were dissolved in 50 mL of distilled water and transfered into the Teflon liner of a 125-mL pressure vessel. A 0.560 g piece (10 mmol) of 2-mm diameter, 99.99% iron (Aldrich) wire was added to this solution. The vessel was enclosed and placed into an oven at 202°C for the

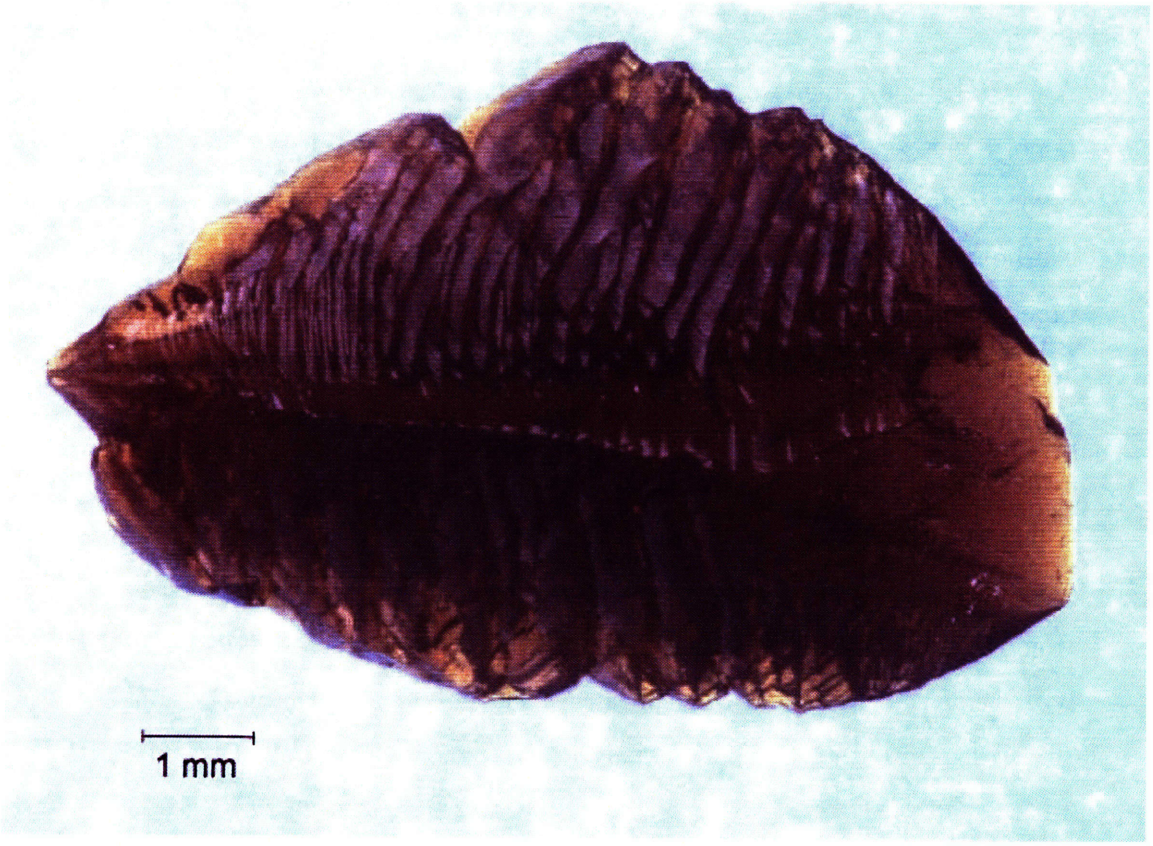

Figure 1-9: A single crystal of $KFe_3(OH)_6(SO_4)_2$, mass = 48 mg. Courtesy of D. Grohol.

K_2SO_4 reaction. After 4 days at these elevated temperatures, the oven was cooled at 0.3°C min^{-1} to room temperature. The yellow-orange product, which precipitated on the walls of the Teflon liner, was isolated by filtration, washed with distilled water and dried in air. Yield of $KFe_3(OH)_6(SO_4)_2$: 0.37 g (22% based on Fe). Analytically calculated for $H_6KFe_3S_2O_{14}$: H 1.21, K 7.81, Fe 33.46, S 12.81. Found: H 1.29, K 7.68, Fe 33.41, S 12.94.

Synthesis of $AgFe_3(OH)_6(SO_4)_2$ from Ref. [94]

A 125-mL teflon liner was charged with 0.563 g of 2.00 mm iron wire (10.1 mmol). In a separate beaker, the nitrate salt of the interlayer cation (1.711 g of silver nitrate (10.07 mmol)) was dissolved in 50 mL of deionized water. Into this solution, 2.2 mL of concentrated sulfuric acid (40 mmol) was added via Mohr pipet, and the resulting solution was allowed to stir for 15 min. The beaker solution was poured into the Teflon liner, which was then capped and placed into steel hydrothermal bomb under an atmosphere of oxygen using an Aldrich Atmosbag. The tightened bomb was heated at a rate of 5 °C/min to 210 °C, which was maintained for 72 hours. The oven was then cooled to room temperature at a rate of 0.1 °C/min. A yellow-orange crystalline powder was isolated from the walls and the bottom of the Teflon liner, and the product was washed with deionized water and dried in air. Yield of $AgFe_3(OH)_6(SO_4)_2$: 1.697 g (88.5% based on starting Fe). Analytically calculated for $H_6AgFe_3S_2O_{14}$: H 1.06, Ag 18.94, Fe 29.41, S 11.26. Found: H 1.12, K 18.82, Fe 29.50, S 11.35.

Chemical analysis of $KFe_3(OH)_6(SO_4)_2$ and $AgFe_3(OH)_6(SO_4)_2$ indicates that the Fe^{3+} occupancy is 100.0(3)% and the K^+ content is 99.5(5)%. In addition, the inferred spectroscopy shows no indication of water molecules in the samples. This results show that H_2O produced by the protonation of OH^- by H+, which causes the magnetic site vacancies, is absent.

1.2.1 Structural characterization

X-ray and neutron diffractions were used to characterize nuclear structures of iron jarosites [37, 87, 89, 94]. Table 1.1, 1.2, and 1.3 show the crystallographic data and

Table 1.1: Crystalographic data for $A\mathrm{Fe_3(OH)_6(SO_4)_2}$ with A^+=$\mathrm{Na^+}$, $\mathrm{K^+}$, and $\mathrm{Rb^+}$.

Empirical formula	$\mathrm{H_6NaFe_3S_2O_{14}}$	$\mathbf{H_6KFe_3S_2O_{14}}$	$\mathrm{H_6RbFe_3S_2O_{14}}$
Formula weight	484.71	500.81	561.90
Crystal system	rhombohedral	rhombohedral	rhombohedral
Space group	$R\bar{3}m$	$R\bar{3}m$	$R\bar{3}m$
a (Å)	7.342(3)	7.3044(7)	7.3131(7)
c (Å)	16.605(10)	17.185(2)	17.568(3)
α (degrees)	90	90	90
γ (degrees)	120	120	120
V (Å^3)	775.3 (7)	794.1(2)	813.7(2)
ρ_{calc}	3.114	3.141	3.440

Table 1.2: Crystallographic data for $A\mathrm{Fe_3(OH)_6(SO_4)_2}$ with A^+=$\frac{1}{2}\mathrm{Pb^{2+}}$ and $\mathrm{Ag^+}$.

Empirical formula	$\mathrm{H_6Pb_{0.5}Fe_3S_2O_{14}}$	$\mathbf{H_6AgFe_3S_2O_{14}}$
Formula weight	565.32	569.59
Crystal system	rhombohedral	rhombohedral
Space group	$R\bar{3}m$	$R\bar{3}m$
a (Å)	7.328(2)	7.3300(9)
c (Å)	16.795(6)	16.497(3)
α (degrees)	90	90
γ (degrees)	120	120
V (Å^3)	781.1(4)	767.62(19)
ρ_{calc} (g/cm^3)	3.606	3.696

Table 1.3: Atomic coordinates in the rhombohedral crystal system for $A\mathrm{Fe}_3(\mathrm{OH})_6(\mathrm{SO}_4)_2$ with $A = \mathrm{Na}^+$, K^+, and Rb^+ measured by X-ray diffraction.

$\mathrm{NaFe}_3(\mathrm{OH})_6(\mathrm{SO}_4)_2$	x	y	z
Na	0	0	0
S	0	0	0.3125(1)
Fe	0.3333	0.1667	0.1667
O(1)	0	0	0.4006(4)
O(2)	0.2200(7)	0.1100(3)	0.2829(2)
O(3)	0.1260(4)	0.2519(7)	0.1329(2)

$\mathbf{KFe}_3(\mathbf{OH})_6(\mathbf{SO}_4)_2$	x	y	z
K	0	0	0
S	0	0	0.3087(2)
Fe	0.3333	0.1667	0.1667
O(1)	0	0	0.3936(4)
O(2)	0.2203(7)	0.1102(3)	0.2795(2)
O(3)	0.1276(4)	0.2553(7)	0.1349(2)

$\mathrm{RbFe}_3(\mathrm{OH})_6(\mathrm{SO}_4)_2$	x	y	z
Rb	0	0	0
S	0	0	0.3061(2)
Fe	0.3333	0.1667	0.1667
O(1)	0	0	0.3888(5)
O(2)	0.2196(8)	0.1098(4)	0.2771(3)
O(3)	0.1280(5)	0.2560(9)	0.1370(3)

Table 1.4: Atomic coordinates in the hexagonal crystal system for $KFe_3(OH)_6(SO_4)_2$ measured by neutron diffraction.

Atoms	x	y	z
K	0	0	0
Fe	0.5	0.5	0.5
S	0	0	0.3092(7)
O(1)	0	0	0.3941(3)
O(2)	0.2227(2)	-0.2227	-0.0534(2)
H	0.1953(4)	-0.1953	0.1106(3)
O(3)	0.1287(2)	-0.1287	0.1349(2)

Table 1.5: Selected bond distances in Å for $A\mathrm{Fe}_3(\mathrm{OH})_6(\mathrm{SO}_4)_2$ with A =K and Ag.

	K Jarosite	Ag Jarosite
A-O(2)	2.971(4)	2.962
A-O(3)	2.826(4)	2.714
S-O(1)	1.460(7)	1.463(8)
S-O(2)	1.481(4)	1.477(5)
Fe-O(2)	2.066(4)	2.041(5)
Fe-O(3)	1.9865(16)	1.9881(19)
Fe $\cdots$ Fe	3.652	3.665

Table 1.6: Selected bond angles in degrees for $A\text{Fe}_3(\text{OH})_6(\text{SO}_4)_2$ with A =K and Ag.

	K Jarosite	Ag Jarosite
O(1)-S-O(2)	109.80(17)	109.5(2)
O(2)-S-O(2)	109.15(17)	109.4(2)
O(2)-Fe-O(2)	180	179.999(1)
O(2)-Fe-O(3)	91.77(13)	91.44(16)
O(2)-Fe-O(3)	88.23(13)	88.56(16)
O(3)-Fe-O(3)	180	179.999(1)
O(3)-Fe-O(3)	90.5(2)	92.0(3)
O(3)-Fe-O(3)	89.5(2)	88.0(3)
Fe-O(3)-Fe	133.6(2)	134.4(3)
Fe-O(2)-S	130.0(2)	130.3(3)
FeO_6 tilt	17.4	17.9

atomic coordinates for iron jarosites with A^+=Na^+, K^+, Rb^+, Pb^{2+} and Ag^+. The tables are taken from Ref. [89, 94]. Table 1.4 taken from Ref. [37] shows the atomic coordinates for $\text{KFe}_3(\text{OH})_6(\text{SO}_4)_2$ measured on one of their two powder samples by neutron diffraction. The jarosites crystallizes in the $R\bar{3}m$ space group in the hexagonal or rhombohedral structure axis with atomic coordinates listed in Table 1.3. The bond distances and bond angles for jarosites are measured in Ref. [89, 94] and shown in Table 1.5 and 1.6. The tilt angle of the octahedra enclosing the magnetic Fe^{3+} ions is 17.5(5)°. This angle is approximately the same for all jarosites with SO_4^{2-} caps. The tilt angle is smaller in jarosites with SeO_4^{2-} caps ($\approx 14.5°$) [94]. This tilt angle will become important when we calculate spin-wave excitations to extract spin Hamiltonian parameters.

1.2.2 Magnetic characterization

Magnetization and neutron scattering measurements were used to characterize magnetic properties and structures of iron jarosite. Magnetization measurements were performed on the jarosite samples to extract the magnetic ordering temperature and Curie-Weiss temperature. The ordering temperature is indicated by a peak in the d.c. susceptibility. The Curie-Weiss temperature is obtained from fitting high-temperature data ($T > 150$ K) to the Curie-Weiss law $\chi = C'/(T - \Theta'_{CW})$, where C' is a Curie-Weiss constant and Θ' is a Curie-Weiss temperature as shown in Fig. 1-10. Table 1.7 taken from Ref. [94] shows the magnetic characterization of the jarosite samples. The parameter $f = |\Theta'_{CW}|/T_N$ is an empirical parameter indicating the degree of frustration of the spin systems. Neutron scattering measurements performed on powder samples show that the in-plane magnetic structure of iron jarosite $KFe_3(OH)_6(SO_4)_2$ is the $q = 0$ structure. The spin orientation between the kagomé planes is influenced by an interplane ferromagnetic coupling, which leads to the spin structure shown in Fig. 1-8 [37, 87]. The magnitude of the ordered moments per Fe^{3+} ion obtained from the refinement is $3.80(6)\mu_B$, which is smaller than the value evaluated from the magnetization measurements shown in Table 1.7.

From the Curie-Weiss fit (Fig. 1-10), the effective moment μ_{eff} and the nearest-neighbor exchange coupling J can be calculated using the high-temperature series analysis of Harris *et al.* for the kagomé lattice [35]. As a result, the correction factors of 9/8 and 3/2 are introduced to the expressions of Θ_{CW} and C obtained from standard mean-field theory. The modified formulae for C' and Θ'_{CW} are the following:

$$C' = \frac{9}{8}C = \frac{9}{8}\frac{N\mu_{eff}^2}{3k_B} \tag{1.10}$$

$$|\Theta'_{CW}| = \frac{3}{2}|\Theta_{CW}| = \frac{3}{2}\frac{zJS(S+1)}{3k_B}, \tag{1.11}$$

where z is the number of nearest neighbors ($z = 4$), and S is the magnetic spin of the Fe^{3+} ions ($S = 5/2$). Therefore, the expressions for μ_{eff} and J are:

$$\mu_{eff} = 2.82\sqrt{\frac{8}{9}C'} \tag{1.12}$$

$$J = \frac{1}{2}\frac{|\Theta'_{CW}|}{S(S+1)}, \tag{1.13}$$

The calculated values for μ_{eff} and J are shown in Table 1.4. These values ought to be compared with the values in Table 3.1. An excellent agreement verifies the validity of the correction to the mean field coefficients introduced by Harris *et al.* for the geometrically frustrated kagomé lattice. Fig. 1-11 shows d.c magnetic susceptibility (M/H) as a function of temperature measured on a single crystal sample of $KFe_3(OH)_6(SO_4)_2$ when a magnetic field is parallel and perpendicular to the $c-$axis. The data can be divided into three regions. In the first region between 5 K and 65 K, the spins order into the $q = 0$ structure. In Chapter 3 and 4, the spin-reorientation transition, scalar chirality and spin-wave excitations in this region are discussed, respectively. In the second region between 65 K and 120 K, even though the long-range spin order disappears, the XY anisotropy due to the out-of-plane component of anisotropic exchange interactions still persists, and confine the spins to move within the kagomé plane. In Chapter 5, the vector chirality and spin fluctuations in this region are examined. In the third region above 120 K, the spins are in the frustrated paramagnetic state, and the magnetic susceptibility can be described by the modified Curie-Weiss law introduced by Harris *et al.* [35].

Table 1.7: Magnetic characterization for $AFe_3(OH)_6(SO_4)_2$ with $A = Na^+$, K^+, Rb^+, $\frac{1}{2}Pb^{2+}$ and Ag^+.

Compounds	T_N(K)	$\Theta'_{CW}(K)$	f	C' $(\frac{\mathrm{cm^3 \cdot K}}{\mathrm{mol\ Fe}})$	μ_{eff} (μ_B)	J (meV)
$NaFe_3(OH)_6(SO_4)_2$	61.7	-825	13.5	5.91	6.46	4.06
$KFe_3(OH)_6(SO_4)_2$	**65.4**	**-828**	**12.7**	**5.77**	**6.39**	**4.08**
$RbFe_3(OH)_6(SO_4)_2$	64.4	-829	12.9	5.82	6.41	4.08
$Pb_{0.5}Fe_3(OH)_6(SO_4)_2$	63.4	-813	12.8	6.03	6.53	4.00
$AgFe_3(OH)_6(SO_4)_2$	**59.7**	**-803**	**13.5**	**5.06**	**5.98**	**3.95**

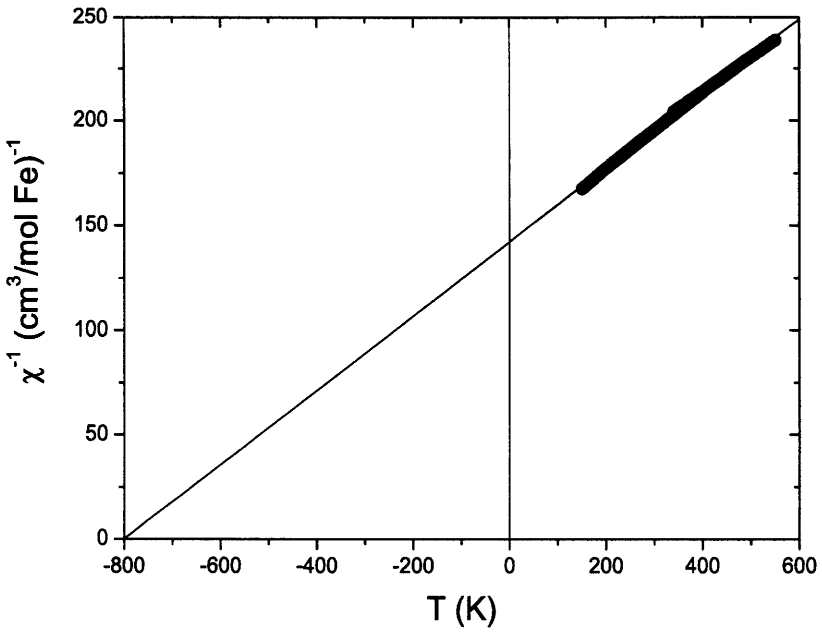

Figure 1-10: The Curie-Weiss fit to the magnetic susceptibility of a powder sample of $KFe_3(OH)_6(SO_4)_2$ at high temperature.

1.3 Spin Hamiltonian and anisotropic exchange interactions

Although the spins on the kagomé lattice are believed not to order at any finite temperatures due to frustration and low dimensionality, in jarosite, small anisotropic terms in the spin Hamiltonian are present resulting from either the Dzyaloshinskii-Moriya (DM) interaction or single-ion anisotropy, which cause the spins to order three-dimensionally as discussed above. The DM interaction is a perturbation on the Heisenberg spin Hamiltonian. This interaction is present if there is no inversion center between two magnetic sites [114, 115, 116]. To first approximation, the general form of the spin Hamiltonian including single-ion type anisotropy is given by:

$$\begin{aligned}\mathcal{H} &= \sum_{nn}\left[J\,\mathbf{S}_i\cdot\mathbf{S}_j + \mathbf{D}_{ij}\cdot\mathbf{S}_i\times\mathbf{S}_j\right] \\ &\quad + D\sum_i\left(S_i^{y'}\right)^2 - E\sum_i\left[\left(S_i^{z'}\right)^2 - \left(S_i^{x'}\right)^2\right],\end{aligned} \tag{1.14}$$

where Σ_{nn} indicates summation over pairs of nearest neighbors, J is the nearest-neighbor interaction, $\mathbf{D}_{ij} = (0, D_p, D_z)$ is the DM vector, and D and E are the single-ion anisotropy constants in a local frame defined in Ref. [38]. The direction of the DM vector oscillates from bond to bond as discussed in Ref. [117]. The single-ion anisotropy is expected to be very small as pointed out in Ref. [39] since it appears at second order in the spin-orbit coupling, whereas the DM interaction appears at first order. In Chapter 3 and 4, we will show that the DM term describes the ordered state and the spin-wave dispersion in jarosite better than the single-ion anisotropic term.

In jarosite, the DM interaction causes the spins to order at a non-zero temperature by lifting the infinite degenerate ground states, and determines the ground-state spin arrangement. The z component of the DM vector D_z confines the spins to be within the kagomé planes, and hence effectively acts like an easy-plane anisotropy. In addition, it is responsible for the $q = 0$ spin structure that has been observed in iron jarosite. The sign of D_z breaks the symmetry between positive and negative chirality. In fact, in iron jarosite, the uniform positive vector chirality, which we believe persists above the ordering temperature [110], indicates that the sign of D_z is negative as verified by the results from our spin-wave measurements [112]. The in-plane component of the DM vector D_p forces the spins to cant out of the kagomé planes, consistent with the observed umbrella spin configuration [110], which will be discussed in Chapter 3. It also breaks the rotational symmetry around the $c-$axis, which results in the Ising-type of ordering in the planes (all-in-all-out spin arrangement). The DM interaction has also been observed in the measurements of the magnetization and EPR spectra in spin frustrated perovskite cuprates [118, 119, 120, 121, 122, 123, 124, 125], the pyrochlore antiferromagnet [126, 127], and molecule-based magnets [128, 129, 130, 131, 132]. In jarosite, the DM interaction explains the spin structure in the ordered state ($T < T_N$), and spin dynamics for $T > T_N$. Furthermore, the DM interaction provides an excellent fit to our spin-wave data.

Aristov and Maleyev have described how to detect spin chirality induced by the DM interaction using the polarized neutron scattering in Ref. [133]. Polarized neu-

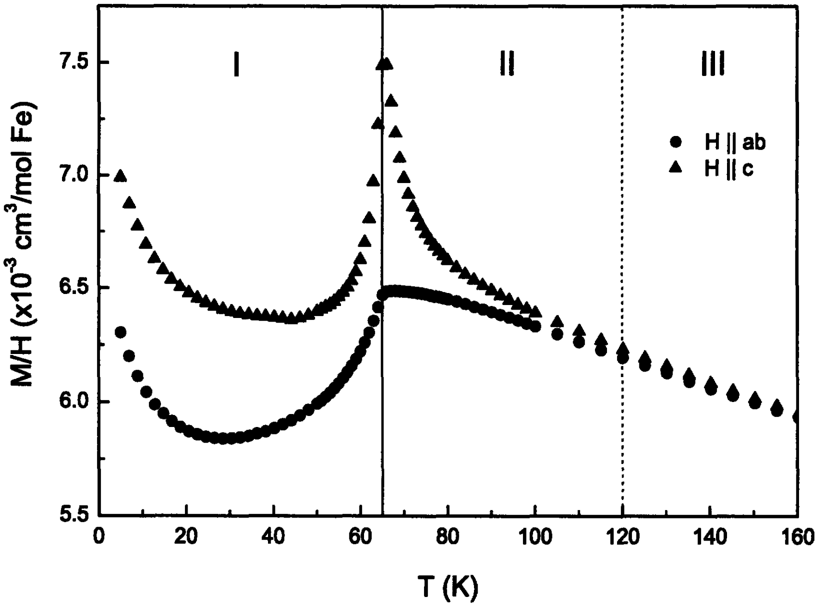

Figure 1-11: The magnetic susceptibility of a single-crystal sample of $KFe_3(OH)_6(SO_4)_2$.

tron scattering and spin chirality will be discussed in Chapter 2, and the results from polarized neutron scattering measurements will be presented in Chapter 3 and Chapter 5. The calculations of spin-wave spectrum have been done on the kagomé lattice antiferromagnet [35, 39, 134, 135, 117], and on the spin Hamiltonian with the DM interaction [136, 137, 117]. In particular, the spin-wave calculations on the kagomé lattice antiferromagnet by Yildirim and Harris [117] is directly related to our spin-wave measurements. Therefore, their results are reproduced in Chapter 4 and Appendix A.

1.4 Thesis Outline

In this thesis, we report the results of magnetization and neutron scattering measurements on two jarosite compounds $KFe_3(OH)_6(SO_4)_2$ and $AgFe_3(OH)_6(SO_4)_2$. The studies of this group of ideal kagomé lattice antiferromagnets allow us to investigate the effects of the geometric frustration and collective behavior (static and dynamic) of interacting spins.

In Chapter 2, we describe features of the neutron scattering technique. Elastic, inelastic, and polarized neutron scattering from nuclei and magnetic moments are reviewed. The instrumental set-up of the triple-axis spectrometer is presented, and the instrumental resolution function is discussed.

Chapter 3 deals with the spin re-orientation transition in the ordered state ($T < T_N$). The DM interaction is discussed in detail. The field-induced transition between states with different non-trivial spin textures is reported. The results of the magnetization and elastic neutron scattering measurements in high fields are presented. The effects of the DM interaction on the spin structure in the ordered state are discussed.

In Chapter 4, the results of the the spin-wave measurements at low temperature using inelastic neutron scattering are presented. We directly observe a lifted "zero energy mode," verifying a fundamental prediction for the kagomé lattice. Two spin models with the DM interaction and the single-ion anisotropy are used to fit the results. We conclude that the DM interaction is the primary source of the small anisotropy.

Chapter 5 contains studies of the spin chirality and short-range spin correlations on jarosite for $T > T_N$. The results obtained from inelastic and quasi-elastic neutron scattering are presented. The critical behavior of a two-dimensional geometrically frustrated lattice is discussed.

Chapter 2

Neutron Scattering

Advances in condensed matter physics depend tremendously on experimental techniques used to probe physical properties and structures of matters. Ever since its discovery, neutron scattering has played a significant role in probing varied excitations and (magnetic or nuclear) structures in matters. Neutrons were discovered in 1932 by Chadwick after series of experiments showing that these uncharged particles were able to penetrate through nuclei of an atom. Not long after that in 1936 did physicists find diffraction pattern when they scattered neutrons off crystals [138]. This new and powerful technique leads to several new discoveries in physics, especially in a field of condensed matter physics [138, 139]. In fact, this technique has so much impact on the development of science that its creators B. N. Brockhouse (McMaster University) and C. G. Shull (MIT) were awarded Nobel Prize in 1994 for their works in the fields of elastic and inelastic neutron scattering. The technique has led physicists to better understanding of magnetic systems. Specifically, neutron scattering has played a key role in the study of magnetism in high transition-temperature (high-T_C) superconductors [18, 19].

Due to the absence of charge and small absorption cross-section, neutrons do not interact electronically with electrons and nuclei, and can penetrate through matters to allow for studies of bulk properties. On the other hand, they scatter off nuclei via the short-range strong-force interaction. The elastic scattering of neutrons from nuclei shows us where and which kind atoms are, while the inelastic analog tells us about "what atoms do". The equally important property of neutrons is the fact that they also carry a magnetic moment $\hat{\mu}_n = \gamma \mu_N \hat{\sigma}$, where $\gamma = -1.913$ is the nuclear gyromagnetic ratio, $\mu_N = \frac{e}{2m_N} = 3.152 \times 10^{-5}$ meV T^{-1} is the nuclear magneton, and $\hat{\sigma}$ is the spin operator. Therefore, neutrons can scatter off magnetic moments arising from the spins of both electrons and nuclei, and from orbital angular momentum of electrons via the dipole-dipole interaction. The magnetic field that is generated by electrons in crystals gives a natural unit for the range (strength) of the dipole-dipole interaction, which is equal to $\gamma r_0 = \frac{\gamma e^2}{m_e c^2} = -0.54 \times 10^{-12}$ cm, where r_0 is the classical electron radius. Therefore, the magnetic scattering cross-section is comparable to the nuclear scattering cross-section. This fact distinguishes neutron scattering from X-ray or any other light scattering methods, and makes neutron scattering the unique scattering technique that is capable of probing magnetism in matter.

Neutrons from a reactor source are produced in the nuclear fission using ^{235}U as a fuel (see Ref. [140] for more information on neutron sources around the world). To obtain the desired energy of neutrons to use for scattering measurements, these neutrons are cooled down in a moderator, which consists of heavy water (D_2O). The *thermal* neutrons that come out from the moderator have a Maxwellian distribution of energies with characteristic temperature (energy) of about 350 K (30 meV), which gives the typical energy range of 5-100 meV. To obtain lower energy neutrons, a cryogenic moderator typically consisting of liquid H_2 or CH_4, whose temperature is kept at about 20 K, is used. The typical energy range of *cold* neutrons is 0.1-10 meV. In our measurements, we have used both *thermal* and *cold* neutrons generated by the reactor sources to study magnetic structure and excitations in the kagomé lattice antiferromagnet. The other type of the neutron sources is a spallation source, which generates pulses of 10^{14} neutrons with a frequency of 10-50 Hz [140].

2.1 Neutron scattering cross section

In the scattering process, the incident neutrons with an initial momentum $\mathbf{k}$ and initial energy E are scattered by a target, and the scattered neutrons leave the target with a final momentum $\mathbf{k}'$ and final energy E'. In the neutron scattering experiment, the partial different cross-section is measured [141]:

$$\frac{d^2\sigma}{d\Omega\, dE'} = \text{number of neutrons of incident energy } E \text{ scattered into an element of solid angle d}\Omega \text{ with energies between } E' \text{ and } E'\text{+d}E' \text{ normalized by the incident flux of neutrons.} \tag{2.1}$$

The partial cross-section can be calculated using Fermi's Golden rule. In addition, based on the assumption that the scattered neutron wave function can be described by a plane wave, one can use the first Born approximation. This assumption is valid if the incident neutron state is not perturbed significantly, and if the probability of the multiple scattering of the neutron is small. The latter can be thought of the consequence of the former. If the interaction governing the scattering process is weak, then it is unlikely for the multiple scattering to occur.

The scattering process changes the state of the target from λ to λ', and the spin polarization of the neutrons from σ to σ'. Therefore, the general form of the partial cross-section is given by [141]:

$$\left(\frac{d^2\sigma}{d\Omega\, dE'}\right)_{\lambda'}^{\lambda} = \frac{\mathbf{k}'}{\mathbf{k}} \sum_{\lambda\lambda'\sigma\sigma'} p_\lambda p_\sigma \left|\left\langle \mathbf{k}'\sigma'\lambda' \middle| \hat{V} \middle| \mathbf{k}\sigma\lambda \right\rangle\right|^2 \delta(\hbar\omega + E_\lambda - E_{\lambda'}) \tag{2.2}$$

where p_λ and p_σ are the probability distributions of the initial target state and the incident neutron polarization, respectively. These two parameters are important since one needs to average over all ranges of the accessible initial states. $\hat{V}$ is an operator for the scattering potential between the neutrons and target.

Nuclear scattering

The scattering of neutrons from nuclei is governed by the strong-force interaction. Although, there is no complete theory explaining the nature of this interaction, experimentally, it has been shown that a range of this interaction is of the order of

0.15×10^{-12} cm compared to the neutron wavelength of the order of 10^{-12} cm. Since the range of interaction is about 10 times smaller than the neutron wavelength, the scattering cross-section of neutrons by nuclei is isotropic, and can be characterized by only one parameter called the scattering length b, which can be a complex number. The imaginary part of the scattering length represents the absorption cross-section (the capture of neutrons by the nuclei). For the *thermal* and *cold* neutrons used in the scattering measurements, this absorption cross-section is negligibly small.

The scattering potential $\hat{V}$, which is isotropic, is given by a delta function centered at the positions of the nuclei.

$$\hat{V}(\mathbf{r}) = \frac{2\pi\hbar^2}{m} \sum_l b_l \delta(\mathbf{r} - \mathbf{R}_l) \tag{2.3}$$

where $\mathbf{R}_l$ is the positions of the nuclei on a lattice. Using Eq. 2.2 and 2.3, one can calculate the partial cross-section for the nuclear scattering for a monatomic target, which has the following form:

$$\frac{d^2\sigma}{d\Omega\, dE'} = \left(\frac{d^2\sigma}{d\Omega\, dE'}\right)_{\text{coh}} + \left(\frac{d^2\sigma}{d\Omega\, dE'}\right)_{\text{incoh}}, \tag{2.4}$$

where

$$\left(\frac{d^2\sigma}{d\Omega\, dE'}\right)_{\text{coh}} = N \frac{\mathbf{k}'}{\mathbf{k}} \frac{\sigma_c}{4\pi} S\left(\mathbf{Q}, \omega\right) \tag{2.5}$$

and

$$\left(\frac{d^2\sigma}{d\Omega\, dE'}\right)_{\text{incoh}} = N \frac{\mathbf{k}'}{\mathbf{k}} \frac{\sigma_i}{4\pi} S_i\left(\mathbf{Q}, \omega\right) \tag{2.6}$$

where $S(\mathbf{Q}, \omega)$ is the dynamic structure factor, and σ_c and σ_i are the the coherent and incoherent scattering cross-sections, respectively. In real systems, the scattering length b varies from nucleus to another due to the variations of isotope and nuclear spin orientation with respect to the neutron. Therefore, in a crystal, the scattering potential varies from one lattice point to the next. σ_c gives the average of the scattering cross-section arising from the coherently interference effects, which is proportional to the mean square of the scattering length $|\bar{b}|^2$. On the other hand, σ_i gives the incoherent part of the scattering cross-section, which is proportional to the mean-square deviation of the scattering length $\delta_{ll'}\overline{\left|b-\bar{b}\right|^2} = \delta_{ll'}\left(\overline{|b|^2} - \left|\bar{b}\right|^2\right)$. $\delta_{ll'}$ indicates that the incoherent scattering arises from the self correlations due to the same particle. The dynamic nuclear structure factor is given by:

$$S\left(\mathbf{Q},\omega\right) = \frac{1}{2\pi\hbar N}\int_{-\infty}^{\infty} dt\; e^{-i\omega t}\int d\mathbf{r}\; d\mathbf{r}'\; e^{i\mathbf{Q}\cdot\mathbf{r}}\left\langle \hat{\rho}(\mathbf{r}'-\mathbf{r},0)\hat{\rho}(\mathbf{r}',t)\right\rangle, \qquad (2.7)$$

where $\hat{\rho}(\mathbf{r}',t)$ is the microscopic particle density operator with the particle at position $\mathbf{r}$ and at time t. Essentially, the dynamic nuclear structure factor is the time and spatial Fourier transform of the time-dependent pair correlation function $\langle\hat{\rho}(\mathbf{r}'-\mathbf{r},0)\hat{\rho}(\mathbf{r}',t)\rangle$. Since $S_i(\mathbf{Q},\omega)$ is a measure of the correlations of the same particle at different time ($\mathbf{r}$=0), $S(\mathbf{Q},\omega)$ also contains $S_i(\mathbf{Q},\omega)$. The coherent part can be divided into two parts, inelastic and elastic scattering. The inelastic scattering is due to the dynamic correlations of the particles at two different positions at different time, and the elastic scattering is due to the static correlations of the particles at two different positions in the limit where $t \rightarrow \infty$.

Magnetic scattering

We will consider a general expression for the partial differential cross-section for scattering unpolarized neutrons by an electron. The magnetic spin of the neutron will feel the force generated by the moving electron via the dipole-dipole interaction, which is given by:

$$\begin{aligned}\hat{V}(\mathbf{r}) &= -\gamma\mu_N\hat{\sigma}\cdot\mathbf{H} \qquad (2.8)\\ &= \gamma\mu_N\left\{2\mu_B\hat{\sigma}\cdot\nabla\times\left(\frac{\hat{\mathbf{s}}\times\mathbf{r}}{|\mathbf{r}|^3}\right) - \frac{e}{2m_e c}\left(\hat{\mathbf{p}}_c\cdot\frac{\hat{\sigma}\times\mathbf{r}}{|\mathbf{r}|^3} + \frac{\hat{\sigma}\times\mathbf{r}}{|\mathbf{r}|^3}\cdot\hat{\mathbf{p}}_c\right)\right\},\end{aligned}$$

where $\mathbf{r}$ is the distance from the electron, and $\mathbf{p}_c$ is the momentum of the electron. The first term represents the dipole-dipole interaction between the neutron spin and the electron spin (spin contribution) while the second term is due to the interaction between the neutron spin and the orbital motion of the electron (orbital contribution).

The latter vanishes if the orbital angular momentum is quenched ($L = 0$) due to the presence of a crystal field splitting.

Using Eq. 2.2 and 2.8, one can calculate the partial cross-section for the magnetic scattering of unpolarized neutrons by localized spins, which is given by the following expression [141, 142]:

$$\frac{d^2\sigma}{d\Omega\, dE'} = N_M \frac{\mathbf{k}'}{\mathbf{k}} (\gamma r_0)^2 \left[\frac{g}{2} f(\mathbf{Q}) e^{-W}\right]^2 \sum_{\alpha,\beta} \left(\delta_{\alpha\beta} - \hat{Q}_\alpha \hat{Q}_\beta\right) S^{\alpha\beta}(\mathbf{Q}, \omega), \tag{2.9}$$

where α and β are vector components x, y, or z, and N_M is a number of magnetic unit cells in the crystal. $f(\mathbf{Q}) = \int \rho_s(\mathbf{r})\, e^{i\mathbf{q}\cdot\mathbf{r}}\, d\mathbf{r}$ is the magnetic form factor with $F(0) \equiv 1$, where $\rho_s(\mathbf{r})$ is the normalized density function of unpaired electrons on an atom. The Debye-Waller factor e^{-W} arises from the small fluctuations of the magnetic ions given small-displacement, harmonic oscillators about the mean positions defined by the lattice points, and is temperature-dependent. The geometrical factor is due to the dipole-dipole interaction of the neutron spin with the electron spin and/or orbital angular momentum. The magnetic scattering cross-section only arises from the components of the neutron spin that is perpendicular to the momentum transfer $\mathbf{Q}$.

$S^{\alpha\beta}(\mathbf{Q}, \omega)$ is the dynamic magnetic structure factor. It is the space and time Fourier transform of the spin-pair correlation function $\langle S^\alpha(0,0) S^\beta(\mathbf{r},t)\rangle$, which is given by:

$$S^{\alpha\beta}(\mathbf{Q}, \omega) = \frac{1}{2\pi\hbar} \sum_{\mathbf{r}} \int_{-\infty}^{\infty} dt\; e^{i(\mathbf{Q}\cdot\mathbf{r} - \omega t)} \langle S^\alpha(0,0) S^\beta(\mathbf{r},t)\rangle, \tag{2.10}$$

Similar to the nuclear scattering, the magnetic scattering has two contributions, incoherent and coherent. The incoherent contribution is due to the spin-pair correlation between the same spin at different times, and is the Fourier transform of $\langle S^\alpha(0,0) S^\beta(\mathbf{0},t)\rangle$. The coherent contribution can be divided into two parts, elastic and inelastic scattering. The elastic scattering or Bragg scattering is given by the static correlation function of spins at two different positions in the $t \to \infty$ limit. It is the Fourier transform of $\langle S^\alpha(0,0) S^\beta(\mathbf{r},0)\rangle$. The inelastic scattering is a measure of the dynamic correlation function of spins at two different positions, which can be related to the magnetic susceptibility. It is the Fourier transform of $\langle S^{\alpha}(0,0)S^{\beta}(\mathbf{r},t)\rangle - \langle S^{\alpha}(0,0)S^{\beta}(\mathbf{r},0)\rangle$.

2.1.1 Elastic or Bragg scattering

The coherent, elastic scattering arises from the time average of the density function $\rho(\mathbf{r})$ and/or spin operator $\mathbf{S}(\mathbf{r})$. For the elastic nuclear scattering, the partial cross-section from a Bravais lattice is given by [140]:

$$\left.\frac{d\sigma}{d\Omega}\right|_{\text{nuclear}} = N\frac{(2\pi)^3}{\nu_0}\sum_{\mathbf{G}}\delta\left(\mathbf{Q}-\mathbf{G}\right)\left|F_N(\mathbf{Q})\right|^2, \tag{2.11}$$

where $F_N(\mathbf{Q})$ is the static nuclear structure factor:

$$F_N(\mathbf{Q}) = \sum_j \bar{b}_j\, e^{i\mathbf{Q}\cdot\mathbf{d}_j}\, e^{-W_j}, \tag{2.12}$$

where $\mathbf{d}_j$ is the atomic positions in a unit cell, ν_0 is the volume of the unit cell, N is the number of unit cells in a crystal, and $\mathbf{G}$ is the reciprocal lattice vector. $\bar{b}_j$ and e^{-W_j} are the nuclear scattering length and the Debye-Waller factor of the atom at position j, respectively.

For $KFe_3(OH)_6(SO_4)_2$, the neutron refinement of the nuclear structure gives the atomic coordinates shown in Table 1.5. The space group of the crystal structure is $R\bar{3}m$ in hexagonal or rhombohedral axes. In the hexagonal axis, the Bragg reflection condition is satisfied if $-h+k+l=3n$, where h, k, and l are the Miller indices and n is an integer [143]. One advantage of neutron scattering over x-ray scattering is that it can locate a position of deuterium in the crystal. Due to the large incoherent cross-section for hydrogen, most samples used in neutron studies are deuterated. For deuterium, the incoherent part of the scattering is relatively small. Therefore, the atomic coordinate of hydrogen (deuterium) can be determined using neutron scattering as shown in Table 1.5, but cannot be determined using x-ray scattering as the atomic coordinate of hydrogen is absent in Table 1.3.

For the coherent elastic magnetic scattering, the partial cross-section from a magnetically ordered crystal with a single type of magnetic ion is given by [140, 142]:

$$\left.\frac{d\sigma}{d\Omega}\right|_{\text{magnetic}} = N_M \frac{(2\pi)^2}{\nu_M} \sum_{\mathbf{G}} \delta(\mathbf{Q} - \mathbf{G}_M) |\mathbf{F}_M(\mathbf{Q})|^2, \tag{2.13}$$

where N_M is the number of magnetic unit cells in a crystal, ν_M is the magnetic unit cell volume, and G_M is the the reciprocal lattice vector of the magnetic unit cell. $\mathbf{F}_M(\mathbf{Q})$ is the static magnetic structure factor, which is given by:

$$|\mathbf{F}_M(\mathbf{Q})|^2 = (\gamma r_0)^2 \left[\frac{g}{2} f(\mathbf{Q})\ e^{-W}\right]^2 \sum_{\alpha,\beta} \left(\delta_{\alpha\beta} - \hat{Q}_\alpha \hat{Q}_\beta\right) F_\alpha^*(\mathbf{Q}) F_\beta(\mathbf{Q}), \tag{2.14}$$

where

$$F_\alpha(\mathbf{Q}) = \sum_{\mathbf{d}} S^\alpha(\mathbf{d})\ e^{i\mathbf{Q}\cdot\mathbf{d}}, \tag{2.15}$$

where $\mathbf{d}_j$ is the positions of the magnetic ion in a unit cell.

For $KFe_3(OH)_6(SO_4)_2$, the magnetic structure as shown in Fig. 1-8 has been determined using powder neutron diffraction by Inami *et al.* [37]. The magnetic Bragg positions in the reciprocal space are shown in Fig. 2-1. The figure shows the magnetic Bragg peaks in the (HKL) positions where the slices are taken along the L direction and (H, K) plane. The stacking arrangement of the kagomé planes causes the doubling-up of the magnetic unit cell along the c direction as discussed in Chapter 1 and shown in Fig. 1-8. This results in the positions of the magnetic Bragg peaks at half-integer L. The 2D magnetic scattering rod is a result of in-plane short-range correlations above the ordering temperature.

2.1.2 Inelastic scattering

The coherent inelastic scattering corresponds to the density fluctuations in time and space, which can be translated to a function of momentum and energy using the Fourier transform. The inelastic contribution can be calculated by subtracting out the coherent elastic contribution from the total dynamic structure factor. Since we will

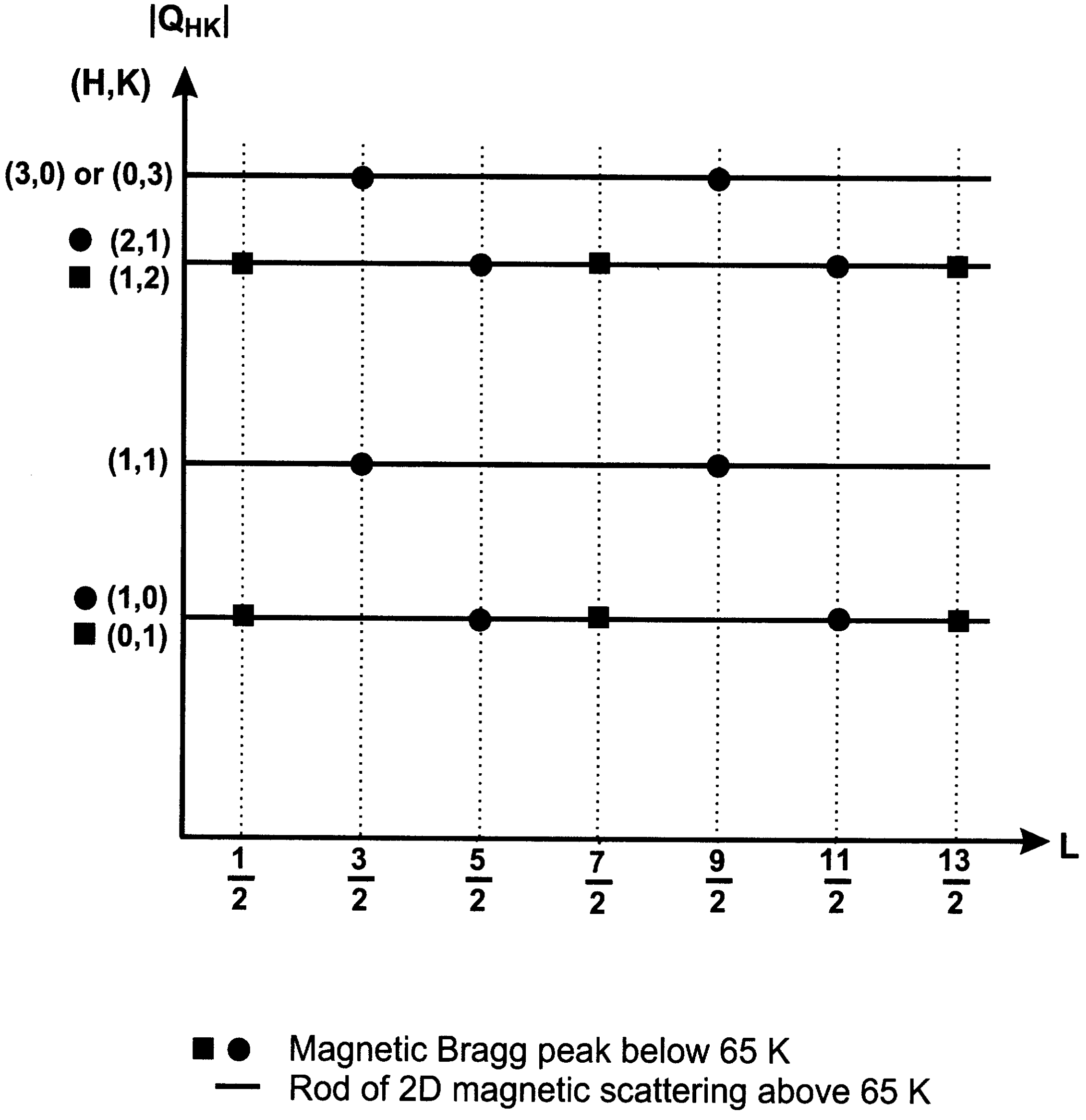

Figure 2-1: A reciprocal space map of the magnetic Bragg peaks and 2D magnetic scattering rods in $KFe_3(OH)_6(SO_4)_2$.

only consider the inelastic scattering of the magnetic system, specifically spin-wave excitations and quasi-elastic scattering in $\mathrm{KFe_3(OH)_6(SO_4)_2}$, only inelastic magnetic scattering is discussed here. For the discussion of the inelastic nuclear scattering, the reader should turn to the excellent books on neutron scattering by Lovesey [144, 141], Squires [145], and Shirane *et al.* [140]. From Eq. 2.9, the cross-section for the inelastic magnetic scattering can be written as [142]:

$$\begin{aligned} \frac{d^2\sigma}{d\Omega\, dE'} &= N_M \frac{\mathbf{k}'}{\mathbf{k}} (\gamma r_0)^2 \left[\frac{g}{2} f(\mathbf{Q}) e^{-W}\right]^2 \sum_{\alpha,\beta} \left(\delta_{\alpha\beta} - \hat{Q}_\alpha \hat{Q}_\beta\right) \\ &\quad \times \left[S^{\alpha\beta}(\mathbf{Q},\omega) - S^{\alpha\beta}_{\text{elastic}}(\mathbf{Q},\omega)\right], \end{aligned} \tag{2.16}$$

where $S^{\alpha\beta}_{\text{elastic}}(\mathbf{Q},\omega)$ is the elastic contribution to the scattering cross-section as discussed in the previous section. The inelastic part of the dynamic structure factor can be related to the energy dissipative part of the dynamical susceptibility via the fluctuation-dissipation theorem [142]:

$$S^{\alpha\alpha}(\mathbf{Q},\omega) - S^{\alpha\alpha}_{\text{elastic}}(\mathbf{Q},\omega) = \frac{1}{\pi}(n(\omega)+1)\chi''^{\alpha\alpha}(\mathbf{Q},\omega) \tag{2.17}$$

where $n(\omega) = (e^{\hbar\omega/k_B T} - 1)^{-1}$ is the Bose thermal factor, and $\chi''(\mathbf{Q},\omega)$ is the imaginary part of the generalized susceptibility. Another important relation is the Kramers-Kronig relation that connects the real and imaginary parts of the generalized susceptibility, χ' and χ'', respectively [140].

$$\chi'(\mathbf{Q},\omega) = \frac{1}{\pi}\int_{-\infty}^{\infty} d\omega' \, \frac{\chi''(\mathbf{Q},\omega)}{\omega - \omega'}. \tag{2.18}$$

For $\omega = 0$ and the $\mathbf{Q} \to 0$ limit, one obtains the static bulk susceptibility $\chi'(0,0)$, which can be measured using a magnetometer, such as a Superconducting Quantum Interference Device (SQUID).

The scattering function from spin-waves in an antiferromagnet for small wave vectors q can be given by [140]:

$$S_{\mathrm{sw}}(\mathbf{Q},\omega) = S\sum_{\mathbf{G}_M,\mathbf{q}} \frac{\omega_0}{\omega_{\mathbf{q}}} \; [(n(\omega_{\mathbf{q}})+1)\delta(\mathbf{Q}-\mathbf{q}-\mathbf{G}_M)\delta(\omega-\omega_{\mathbf{q}}) \\ +n(\omega_{\mathbf{q}})\delta(\mathbf{Q}-\mathbf{q}-\mathbf{G}_M)\delta(\omega-\omega_{\mathbf{q}})], \tag{2.19}$$

where ω_0 is a constant, and $\mathbf{G}_M$ is the antiferromagnetic superlattice vectors. The first term in the parenthesis corresponds to the creation of a magnon, and the second term corresponds to the destruction of a magnon. From Eq. 2.19, we learn that the scattering function is inversely proportional to the spin-wave energies $\omega_{\mathbf{q}}$ for small q. This result will become relevant when we analyze the data obtained from the spin-wave measurements on jarosite ($KFe_3(OH)_6(SO_4)_2$) in Chapter 4.

In addition, we also study the short-range correlations above the ordering temperature. The scattering function as a function of $\mathbf{q}$ in this disordered state can be described by a Lorentzian:

$$S(\mathbf{q}) \propto \frac{1}{1+\xi^2 q^2}, \tag{2.20}$$

The Fourier transform of Eq. 2.20 gives the spatial correlation function in the form of an exponential decay:

$$\langle S^\alpha(0) S^\alpha(\mathbf{r})\rangle \propto e^{-r/\xi}, \tag{2.21}$$

where ξ is the correlation length. The studies of the short-range correlations and critical scattering above the ordering temperature in jarosite are discussed in Chapter 5.

2.1.3 Polarized Neutron scattering

So far, we have not taken full advantage of the neutron scattering technique. Spin states of both incident and scattered neutron beams are ignored, which results in loss of some useful information. By specifying the spin states of the incident and scattered beams, one can distinguish magnetic scattering from nuclear scattering [146]. Furthermore, the cross section of the polarized neutrons is sensitive to spin chirality [147, 148, 149]. Therefore, the polarized neutron scattering technique is ideal to study chirality in frustrated magnets.

Using polarized neutron scattering, Plakhty *et al.* measured the chiral susceptibility above the ordering temperature, and were able to determine the chiral critical exponents, β_c, γ_c, and ν_c of the average chirality (chiral order parameter), the chiral susceptibility, and the chiral correlation length in the triangular lattice antiferromagnet CsMnBr$_3$ [150]. They measured the difference, $\Delta I(\omega, Q) = I^{\uparrow}(\omega, Q) - I^{\downarrow}(\omega, Q)$, where $I^{\uparrow}(\omega, Q)$ and $I^{\downarrow}(\omega, Q)$ are the intensities for incident neutron polarization parallel and antiparallel to the scattering vector, respectively. Fig. 3 in Ref. [150] shows the chiral order parameter (ΔI) of the triangular antiferromagnet CsMnBr$_3$ fit to a power law with exponents 0.42 and 0.44. ΔI is non-zero if the populations of positive and negative chirality domains are not equal.

Polarization analysis of the neutron scattering on a triple-axis instrument was first discussed in a 1969 paper by Moon, Riste and Koehler [146]. In polarization analysis, one needs to consider how the scattering process depends on the polarization of the neutron beam. Firstly, one has to calculate the cross-section for the scattering process where the incident neutron beam is polarized. Secondly, one has to calculate the polarization of the scattered neutrons due to the properties of the target. It is possible for the scattered beam to become polarized even though the incident beam is unpolarized. The generic formula for the cross-section from the polarized neutrons is given by [141]

$$\frac{d^2\sigma}{d\Omega\, d\omega} = \frac{k'}{k} \sum_{\lambda',\lambda} p_\lambda \operatorname{Tr}\left[\hat{\rho} \left\langle \lambda | \hat{V}^{\dagger}(\mathbf{Q}) | \lambda' \right\rangle \left\langle \lambda' | \hat{V}(\mathbf{Q}) | \lambda \right\rangle \right] \delta(\hbar\omega + E_\lambda - E_{\lambda'}), \tag{2.22}$$

and the cross-section for the polarization of the scattered beam is given by

$$\mathbf{P}_f \left(\frac{d^2\sigma}{d\Omega\, d\omega}\right) = \frac{k'}{k} \sum_{\lambda',\lambda} p_\lambda \operatorname{Tr}\left[\hat{\rho} \left\langle \lambda | \hat{V}^{\dagger}(\mathbf{Q}) | \lambda' \right\rangle \hat{\sigma} \left\langle \lambda' | \hat{V}(\mathbf{Q}) | \lambda \right\rangle \right] \delta(\hbar\omega + E_\lambda - E_{\lambda'}), \tag{2.23}$$

where $\hat{\rho}$ is the density matrix of the beam, $\hat{\rho} = \frac{1}{2}(1 + \mathbf{P} \cdot \hat{\sigma})$, and $\hat{\sigma}$ is the Pauli matrix.

For purely magnetic, spin-only scattering, $\hat{\mathbf{V}}(\mathbf{Q})$ is given by

$$\hat{V}(\mathbf{Q}) = \hat{\sigma} \cdot r_0 \sum_i \exp(i\mathbf{Q} \cdot \mathbf{R}_i) \left[\hat{\mathbf{Q}} \times (\hat{\mathbf{S}}_i \times \hat{\mathbf{Q}})\right]. \tag{2.24}$$

The traces in Eq. 2.22 and 2.23 are calculated in Ref. [141]. For purely magnetic, spin-only scattering, the cross-section for the polarized beam in Eq. 2.22 can be re-written as [141, 151]

$$\frac{d^2\sigma}{d\Omega\, d\omega} \propto \left\langle \mathbf{M}_{\perp Q} \cdot \mathbf{M}^{\dagger}_{\perp Q} \right\rangle - i \left\langle \mathbf{M}_{\perp Q} \times \mathbf{M}^{\dagger}_{\perp Q} \right\rangle \cdot \mathbf{P}_i, \tag{2.25}$$

where $\mathbf{P}_i$ is the polarization of the incident neutrons and $\mathbf{M}_{\perp Q}$ is the component of the spin $\mathbf{S}$ perpendicular to the wave vector $\mathbf{Q}$. In the dipole approximation,

$$\mathbf{M}_{\perp Q} = r_0 \sum_{\mathbf{l,d}} \exp(i\mathbf{Q} \cdot \mathbf{R}_{ld}) \frac{1}{2} g_d F_d(\mathbf{q}) \left[\hat{\mathbf{Q}} \times \left(\hat{\mathbf{S}}_{ld} \times \hat{\mathbf{Q}}\right)\right]. \tag{2.26}$$

Similarly, the polarization of the scattered beam in Eq. 2.23 can be re-written as

$$\begin{aligned} \mathbf{P}_f \left(\frac{d^2\sigma}{d\Omega\, d\omega}\right) \quad \propto \quad & \left\langle (\mathbf{P}_i \cdot \mathbf{M}_{\perp Q}) \mathbf{M}^{\dagger}_{\perp Q} \right\rangle + \left\langle \left(\mathbf{P}_i \cdot \mathbf{M}^{\dagger}_{\perp Q}\right) \mathbf{M}_{\perp Q} \right\rangle \\ & \left\langle \mathbf{M}_{\perp Q} \cdot \mathbf{M}^{\dagger}_{\perp Q} \right\rangle \mathbf{P}_i + i \left\langle \mathbf{M}_{\perp Q} \times \mathbf{M}^{\dagger}_{\perp Q} \right\rangle, \end{aligned} \tag{2.27}$$

where $\mathbf{P}_f$ is the polarization of the scattered beam. In chirality experiments, one is only interested in the chiral term $\left\langle \mathbf{M}_{\perp Q} \times \mathbf{M}^{\dagger}_{\perp Q} \right\rangle$ in Eq. 2.25 and 2.27. To measure this term, one needs to get rid of the other terms in the expressions. As suggested by the above equations, there are three methods to measure the chiral term.

1. Use polarized incident beam, but don't analyze the polarization of the scattered beam.

2. Use unpolarized incident beam, but analyze the polarization of the scattered beam.

3. Use polarized incident beam, and analyze the polarization of the scattered beam.

First, one can get rid of the first term in Eq. 2.25 by measuring the difference, $\Delta I(\omega, Q) = I^{\uparrow}(\omega, Q) - I^{\downarrow}(\omega, Q)$, where $I^{\uparrow}(\omega, Q)$ and $I^{\downarrow}(\omega, Q)$ are the intensities for incident neutron polarization parallel and antiparallel to the scattering vector, respectively. By changing the polarization of the incident beam, the second term in Eq. 2.25 will change sign while the sign of the first term remains the same. Hence, taking the difference between these two intensities will get rid of the first term. Plakhty *et al.* used on this method to measure spin chirality in the triangular lattice antiferromagnet $CsMnBr_3$ [150, 152, 147, 153, 148, 149]. $\Delta I(\omega, Q)$ is given by

$$\Delta I = (\mathbf{K}_v \cdot \mathbf{Q})\,(\mathbf{P}_i \cdot \mathbf{Q})\,, \tag{2.28}$$

where $\mathbf{K}_v$ is the vector chirality defined in Eq. 1.1.

The second and third method are inconvenient and less efficient. Both methods rely on the fact that the scattered neutrons off a system with a chiral order are polarized, independent of the polarization of the incident neutrons. In the second method, the incident beam is unpolarized; hence $\mathbf{P}_i = 0$. Therefore, the first three terms in Eq. 2.27 are zero. In the third method, the polarization of the incident and scattered beam are chosen such that the contributions of the first three terms vanish. Such measurements are made possible by using spherical polarimetry or Cryogenic Polarization Analysis Device (CRYOPAD) to measure the transverse components of the polarization [154, 155, 156].

However, in jarosite, the ordered state is the $q = 0$ state with uniform chirality, whose polarized neutron cross section of the chiral term vanishes everywhere, in contrast to a triangular system and kagomé system with staggered chirality. However, we can utilize polarized neutron scattering technique to study polarization of spin-waves (Chapter 4), and polarization of spin fluctuations above T_N (Chapter 5). For the latter, polarized neutron scattering will be able to tell us whether or not the fluctuations are confined within the kagomé plane. For linearly polarized neutron scattering analysis, where the spin direction of the incident neutrons is parallel to that of the scattered neutrons, the spin-only scattering process can be explained by the following equations [140],

$$\begin{aligned} U^{++} &= -pS_{\perp z}, \\ U^{--} &= +pS_{\perp z}, \\ U_{+-} &= -p(S_{\perp x} + iS_{\perp y}), \\ U_{+-} &= -p(S_{\perp x} - iS_{\perp y}, \end{aligned} \tag{2.29}$$

where p is the magnetic amplitude. x is along **Q**, z is perpendicular to the scattering plane, and y is in the scattering plane, and perpendicular to both x and z. The positive and negative signs indicate the polarization of incident and scattered neutrons. If **P** and **Q** are parallel along x, all magnetic scattering are in the spin-flip channel. On the other hand, if **P** is along y (z), perpendicular to **Q**, then the magnetic scattering in the spin-flip channel is due to the spin component perpendicular to both **Q** and **P** or in the z (y) direction, and the magnetic scattering in the non-spin-flip channel is due to the spin component parallel to **P** in the y (z) direction. Therefore, using linearly polarized neutron scattering analysis, one can distinguish between in-plane and out-of-plane spin excitations and spin fluctuations, which will be further discussed in Chapter 4 and Chapter 5, respectively.

In the next section, we will examine an instrument that makes all of the aforementioned neutron scattering measurements possible.

2.2 Triple-axis spectrometer

One of the most important instruments in neutron scattering is a triple-axis spectrometer [140], which was invented by Brockhouse in 1961. All of the neutron scattering measurements presented in this thesis were performed on the following triple-axis spectrometers: HB1 at High Flux Isotope Reactor at the Oak Ridge National Laboratory (ORNL) Oak Ridge, TN, SPINS, BT7 and BT9 at the NIST Center for Neutron Scattering (NCNR), Gaithersburg, MD, E1 at the Berlin Neutron Scattering Center (BENSC), Hahn-Meitner-Institut in Berlin, Germany, and TAS-1 at the

Japanese Atomic Energy Agency (JAEA) in Tokai, Japan.

The triple-axis spectrometer allows for the measurements of the scattering functions $S(\mathbf{Q},\omega)$ by systematically varying the momentum transfer $\mathbf{Q} = \mathbf{k} - \mathbf{k}'$ and energy transfer $\omega = E - E'$, where E ($\mathbf{k}$) and E' ($\mathbf{k}'$) are the initial and final energies (momenta) of neutrons. Fig. 2-2 show a schematic diagram of the standard triple-axis neutron spectrometer. The three axes in a triple-axis spectrometer are the monochromator axis, the sample axis, and the analyzer axis as shown in the diagram. The initial energy E and momentum $\mathbf{k}$ of neutrons are selected from the "white" beam coming out the reactor by the nuclear Bragg condition of a monochromator crystal. After being filtered to get rid of undesired high energy neutrons at higher harmonics of the selected neutron wavelength, neutrons are collimated, counted by a monitor, and scattered off a sample. The scattered neutrons will be analyzed by an analyzer crystal using nuclear Bragg diffraction to select the final neutron energy E' and momentum $\mathbf{k}'$, and collected by a detector. The rotation of the sample axis, which defines an angle θ, and the rotation of the scattering arm connecting the sample and the analyzer, which defines an angle 2θ, determine the scattering vector $\mathbf{Q}$, and the directions of $\mathbf{k}$ and $\mathbf{k}'$ in the scattering plane as shown in Fig. 2-2.

To obtain high incident intensity at the sample, the monochromator crystal must satisfy the following criteria [140]. First, a mosaic crystal should be used to accommodate the beam divergence. Second, the crystal should have a small unit-cell, and a large scattering length. Third, the material should have a low absorption cross-section, a large Debye temperature, and a small incoherent scattering cross-section. In our neutron scattering measurements, a pyrolytic graphite (PG) was used as a monochromator crystal. A PG crystal has a hexagonal, layered structure with good alignment of the $(00L)$ planes ($\sim 0.5°$), but with random alignment of all other (hkl) planes. This randomness reduces multiple Bragg and incoherent scattering, which is crucial to keep the background low. In addition, to further increase incident intensity, a vertically focusing PG monochromator is employed at SPINS and BT7.

However, the Bragg diffracted neutrons from the monochromator crystal can still contain higher order harmonics of neutrons with wavelengths λ/n, where λ is the

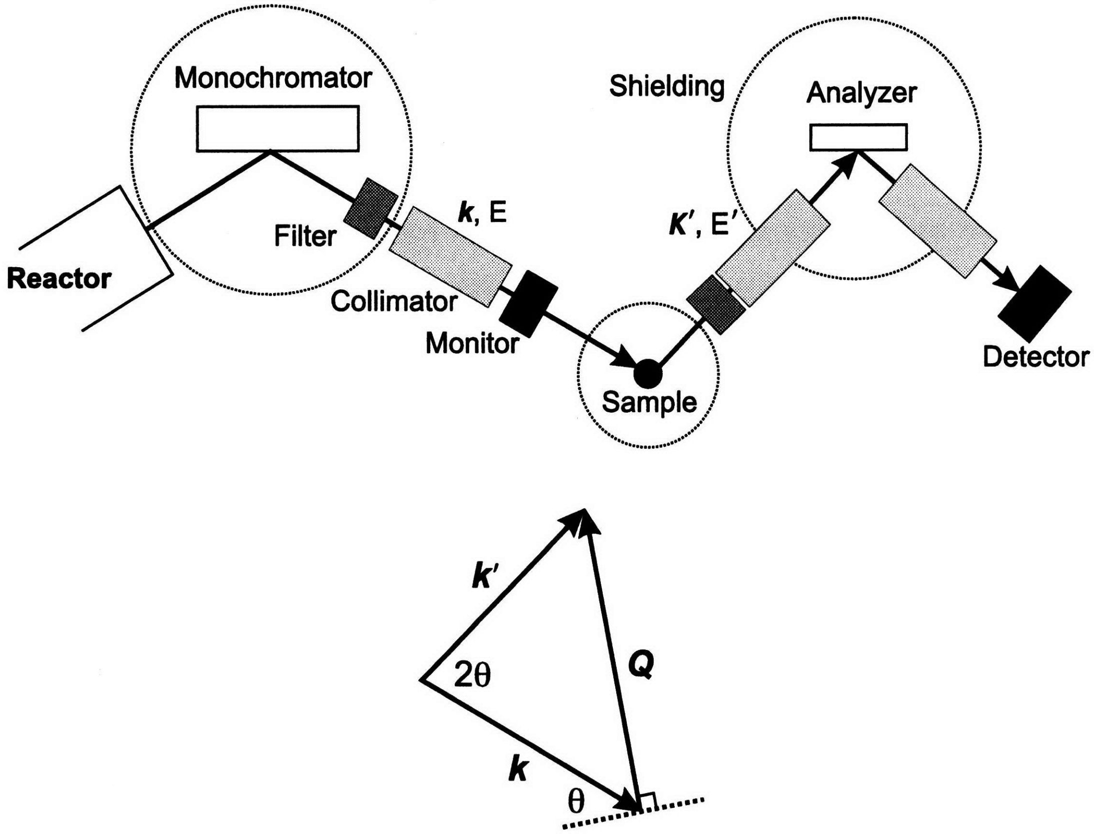

Figure 2-2: A schematic diagram of the triple-axis spectrometer and scattering triangle.

selected wavelength of the neutrons and n is an integer. Therefore, a filer is used to eliminate these high energy neutrons. Ideally, a large transmission at λ with a negligibly small transmission at $\lambda/2$, $\lambda/3$, and etc. is preferable. In our measurements on thermal beamlines, a PG filter was used. For the PG filter, this condition is satisfied for energies of 13.7 meV, 14.7 meV, 30.5 meV and 41 meV (see Ref. [140] for the transmission of a PG filter as a function of energy). For inelastic scattering measurement on the 'cold' instrument SPINS, where the final energy energy of neutrons is fixed at 3 meV and 5 meV, a BeO and Be filters cooled to liquid nitrogen temperature are placed after the sample to filter out neutrons with energies higher than 3.7 meV and 5 meV, respectively

Another important component of the triple-axis spectrometer is a collimator. A role of the collimator is to constraint the angular divergence of the neutron beam, and to reduce the background caused by incoherent scattering. The collimator consists of parallel thin blades made of steel and coated with cadmium, which is a good neutron absorber. Most collimators have a typical horizontal angular beam divergence between 0.1° and 1.5°. The values of the beam divergences of all collimator on the triple-axis spectrometer are used to calculate the resolution function, which will be discussed in the next section. The good collimated beam in the horizontal direction is necessary to achieve good momentum and energy resolution. However, the beam divergence in the vertical direction does not affect the resolution in the scattering plane; therefore, it is intentionally kept at a large value for higher neutron flux. When a small crystal is measured with broad collimation, the beam divergence can become narrow. If this effective collimation due to the crystal size is smaller than that of the collimators, it should be included in the resolution function calculation. In our neutron scattering measurements of the $KFe_3(OH)_6(SO_4)_2$ crystals, the collimation is reduced by about a factor of two due to small samples.

For a polarized neutron scattering experiment, the polarization of the incident neutrons is achieved by reflecting neutrons off a Heussler crystal or transmitting them through polarized ^{3}He gas. Polarized^{3}He gas is used to polarize incident neutron and analyze the polarization of the scattered neutron at BT7. On the other hand, Heussler crystals replace PG monochromators, and are used to polarize the incident beam as well as to analyze the polarization of the scattered beam at TAS-1. A guide field is installed along the whole neutron path to prevent the de-polarization of the beam. In the longitudinal measurements where only the projection of the scattered beam along the direction of the incident beam polarization is measured, the flipper is used to change the polarization of the scattered beam. In addition, it is also possible to measure transverse component of the polarization, where the polarization of the incident and scattered beams are decoupled. In the transverse measurements, CRYOPAD is used to selected the transverse components of the scattered beam. The readers are encouraged to look at Ref. [154, 156] and references therein for more detailed descriptions of CRYOPAD and its functionality.

2.3 Resolution function

One important feature that differentiates neutron scattering from x-ray scattering is the fact that a neutron beam has finite angular divergences. The advantage of this is that one can work with a much larger number of neutrons, and is able to probe bulk properties of the sample, instead of probing a 'local' (small-region) property when one works with a much narrower x-ray beam. However, the disadvantage of having the finite beam divergence is that the energy and momentum of neutrons are not well-defined and are instead distributed within a small range about the average values $(\omega_0, \mathbf{Q}_0)$. This distribution of energy and momentum has to be considered when one wants to compare a measured signal with the scattering function derived in the previous sections. Therefore, one has to describe the measured signal as a convolution of a instrumental resolution function and the scattering function, whose relation is given by [140]:

$$I(\omega_0, \mathbf{Q}_0) = \int d\omega \, d\mathbf{Q} \, \frac{1}{V_i} R(\omega - \omega_0, \mathbf{Q} - \mathbf{Q}_0) S(\mathbf{Q}, \omega), \tag{2.30}$$

where

$$V_i = \int d\mathbf{k} \, P_i(\mathbf{k} - \bar{\mathbf{k}}). \tag{2.31}$$

$P_i(\mathbf{k} - \bar{\mathbf{k}})$ is the probability distribution of the incident neutron with wave vectors $\mathbf{k}$ and with a mean value of $\bar{\mathbf{k}}$.

The resolution function $R(\omega - \omega_0, \mathbf{Q} - \mathbf{Q}_0)$ is peaked at $(\omega_0, \mathbf{Q}_0)$ and decreases as ω and $\mathbf{Q}$ deviate from these mean values. The shape and size of the resolution function depend on the parameters of the instrumental configurations, such as the monochromator and analyzer crystal mosaics, horizontal and vertical collimations, neutron energies, and neutron momenta ($\mathbf{k}$ and $\mathbf{k}'$). If one assumes that the mosaic distributions of both monochromator and analyzer, and the transmission functions of the collimations are gaussian, then the resolution function can be expressed as a four-dimensional gaussian distribution function. This distribution was first derived by Cooper and Nathans in 1967 [157, 158, 159, 160], and refined by Chesser and Axe in 1973 [161]. The four-dimensional gaussian distribution for the resolution ellipsoid is given by:

$$R(\omega - \omega_0, \mathbf{Q} - \mathbf{Q}_0) = R_0 \exp\left(-\frac{1}{2}\Delta\mathbf{Q}M\Delta\mathbf{Q}\right), \tag{2.32}$$

where

$$\Delta\mathbf{Q} = \left(\frac{m_n}{\hbar Q_0}(\omega - \omega_0), Q_{||} - Q_0, Q_{bot}, Q_z\right), \tag{2.33}$$

and M is a 4×4 matrix. R_0 and M are functions of the instrumental parameters, $\bar{\mathbf{k}}$, $\bar{\mathbf{k}}'$ and 2θ. The reader should turn to the excellent book by Shirane *et al.* [140] for detailed discussions on this topic.

For simplicity, one can assume that the beam divergence is small, and that the resolution function in the vertical direction is uncoupled from the other three coordinates. Therefore, the 4×4 matrix M can be separated into a 3×3 matrix for ω, $\Delta Q_{||}$, and $\Delta Q_{\perp}$, and a 1×1 matrix for ΔQ_z. The relevant resolution ellipsoid can be represented in a three dimensional phase space, and has a shape of a flattened cigar. In general, a computer program is used to calculate this resolution ellipsoid. One of such programs is developed by members of Broholm Group from John Hopkins University. The program written in IDL called *LINKA*[1] shows cross-sections and projections of the three-dimensional ellipsoid on all three axes, ω, $\Delta Q_{||}$, and $\Delta Q_{\perp}$. In addition, the ω- and Q-widths are readily calculated.

One can take advantage of the resolution ellipsoid in the inelastic and quasi-elastic scattering measurements. In the inelastic measurements of spin-waves, if one orients the major (long) axis of the resolution ellipsoid along the parallel dispersion surface of the spin-waves, then a narrow peak with high intensity will be measured. In other words, the resolution width is governed by the orientation of the resolution ellipsoid with respect to the dispersion surface. This will become apparent in our spin-wave measurements on the $\mathrm{KFe_3(OH)_6(SO_4)_2}$ crystals, whose results will be present in Chapter 4. In the quasi-elastic measurements of the 2D scattering from a single kagomé plane, whose Fourier transform is a scattering rod along the L direction, we oriented the scattering rod along the vertical direction by mounting the sample in

---

[1] courtesy of Goran Gasparovic

the $(HK0)$ zone. In this instrumental configuration, the broad vertical resolution ellipsoid integrates over a wide range of $\mathbf{Q}$-space along the scattering rod. These results will be presented in Chapter 5. One can also measure the energy integrated intensity $S(\mathbf{q}) = \int d\omega\ S(\mathbf{q}, \omega)$ by working on a two-axis mode (withholding energy analysis). This technique called the "quasi-elastic approximation" was first carried out by Birgeneau *et al.* [162, 163, 164] in 1970s.

Chapter 3

Scalar chirality and spin re-orientation transition

In this chapter, we report high-field magnetization measurements and a spin re-orientation transition as a function of magnetic field. As discussed in Chapter 1, the presence of the interlayer coupling and the spin anisotropy resulting from the DM interaction causes the spins in the kagomé planes to order three-dimensionally at a non-zero temperature by lifting the huge ground-state degeneracy, thus determining the ground-state spin configuration. The ground state of iron jarosite is shown in Fig. 1-6 and 1-8. Elhajal *et al.* show that the DM interaction can give rise to LRO in the kagomé lattice, and induce spins to cant out of the kagomé planes to form an "umbrella" structure of ferromagnetically aligned moments within the layers [39, 165, 166] giving each layer a net ferromagnetic moment. The presence of the canted moment in the kagomé lattice with anisotropic exchange interactions has been discussed by Nishiyama *et al.* [38] for the single-ion type anisotropy and by Elhajal *et al.* [39] and Yildirim *et al.* [117] for the DM interaction. However, in the absence of an applied field, the ferromagnetic interplane coupling causes the canted moments to align antiferromagnetically along the *c*-axis. It is interesting to note that if the interplane coupling is antiferromagnetic, then the canted moments will align ferromagnetically along the *c*-axis, which will give a non-zero value of the net canted moment at zero field.

The field-induced spin-canting transition corresponds to a non-trivial change in the spin-texture of the iron jarosite samples. In particular, the transition yields a net, non-zero value for the *scalar chirality* [26, 27, 167, 168, 169, 170, 171], defined on each triangular plaquette as

$$K_S = \mathbf{S}_1 \cdot (\mathbf{S}_2 \times \mathbf{S}_3). \tag{3.1}$$

K_S is positive (negative) if the canted moment is along the positive (negative) c direction. As previously mentioned, the presence of this type of chirality (in static or fluctuating forms) can have important consequences in strongly correlated electron systems, such as yielding an anomalous Hall effect in metallic materials [26, 27, 172]. For $H < H_C$ the net scalar chirality for our jarosite sample is zero because the contributions from neighboring planes are equal and opposite. However, for $H > H_C$ the spins on the alternating kagomé planes rotate 180° (as depicted in Fig. 3-14), and the net scalar chirality becomes non-zero. There are few materials with non-zero scalar chirality in the ordered state, especially on a two-dimensional lattice. In iron jarosite, we have discovered a phase transition in which a net scalar chirality can be switched on by a magnetic field.

Before looking at the results of magnetization and neutron scattering measurements, we will start off this chapter by briefly reviewing the DM interaction in Section 3.1. In Section 3.2, magnetization and specific heat measurements on deuterated and non-deuterated samples of two jarosites $KFe_3(OH)_6(SO_4)_2$ and $AgFe_3(OH)_6(SO_4)_2$ are presented. Then, calculations of the spin Hamiltonian parameters and canting angle are carried out. Section 3.3 contains the results from two sets of neutron scattering experiments; one is inelastic scattering, and the other is elastic scattering in a high field. The latter shows spin re-arrangement at the critical field due to the 180° spin rotation. Section 3.4 concludes this chapter by the discussion of the spin re-orientation transition and phase diagram of jarosite in Section 3.4., followed by a summary in Section 3.5.

3.1 Dzyaloshinskii-Moriya Interaction

The DM interaction was first discussed in an attempt to explain weak ferromagnetism in antiferromagnetic crystals, such as $\alpha{-}Fe_2O_3$ [173], and the carbonates of manganese (Mn) and cobalt (Co). Numerous mechanisms have been proposed including an impurity effect and antiferromagnetic-domain effect. However, they all failed to completely explain the phenomenon. In 1958, Dzyaloshinskii proposed a phenomenological theory explaining this weak ferromagnetism [114]. His formulation and argument are purely based on the symmetry of a crystal. He argued that when there is no inversion symmetry between two magnetic ions in the crystal, there is a term governing the spin interaction that favors antiferromagnetic spin arrangement with canted spins. These canted spins lead to weak ferromagnetism in the antiferromagnetic crystals. This term can be expressed by:

$$\mathbf{D} \cdot (\mathbf{S}_1 \times \mathbf{S}_2). \tag{3.2}$$

In 1960, Moriya extended this phenomenological theory of Dzyaloshinskii, and developed a microscopic theory of this antisymmetric interaction [115, 116] with the use of the superexchange formulation proposed by Anderson [174] about one year earlier. Moriya showed that the DM interaction is linearly proportional to the spin-orbit coupling, and follows the following rules [116]:

> Suppose that two magnetic ions are located at A and B, and C is a midpoint bisecting AB.
>
> 1. If a center of inversion is located at C, then $\mathbf{D} = 0$.
> 2. If there exists a mirror plane perpendicular to AB passing through C, then $\mathbf{D}$ is parallel to the mirror plane or perpendicular to AB
> 3. If there exists a mirror plane passing through both A and B, then $\mathbf{D}$ is perpendicular to the mirror plane.
> 4. If a two-fold rotation axis is perpendicular to AB, and passes through C, then $\mathbf{D}$ is perpendicular to the two-fold axis.

5. If there exists an $n-$fold axis ($n > 2$) along AB, then **D** is parallel to AB.

These rules can be applied to the kagomé lattice. The reader should turn to the papers by Elhajal *et al.* for detailed discussion of the DM interaction on the kagomé and pyrochlore lattices [39, 126, 127, 175]. Since there is no center of inversion for the kagomé lattice, the first rule is not applicable. Therefore, the DM interaction is not forbidden by the symmetry of the lattice. In addition, in a perfect kagomé lattice, the kagomé plane is a mirror plane passing through both magnetic sites. Therefore, by the third rule, the DM vector **D** is perpendicular to the kagomé plane.

However, in jarosite, the symmetry of the perfect kagomé lattice is lowered due to the tilting of the octahedral cage around the magnetic Fe^{3+} ion. The axial axis of the octahedron is not perpendicular to a kagomé plane as shown in Fig. 1-7. Hence, the kagomé plane is no longer a mirror plane when all atoms in the crystal are considered. The oxygen atoms forming the octahedron are responsible for the crystal field felt by the magnetic ion inside, and involved in the superexchange mechanism between the magnetic ions, which gives rise to the DM interaction. Therefore, the modification of the DM vector is necessary. For jarosite, the mirror plane is perpendicular to the bond between two magnetic ions, which goes through the mid-point as shown in Fig. 3-1; hence, the second rule is applicable. Therefore, **D** lies within this mirror plane, or perpendicular to the bond. The DM vector has not only an out-of-plane component D_z, but also an in-plane component D_y, and lies within the mirror plane shown in Fig. 3-1 [117, 176].

From the symmetry considerations, the direction of the DM vector only depends on the tilting of the oxygen octahedron. From Fig. 1-7, if the octahedra on the middle layer tilt outward, then the octahedra that lie right on top or below will tilt inward. Therefore, the direction of the out-of-plane component changes from out-of the page (outward) to in-to the page (inward) when one moves up or down a layer, while the in-plane component always points toward the center of the triangle as shown in Fig. 3-1, which summarizes the results of these purely symmetry considerations.

Unfortunately, these symmetry considerations do not determine a precise direction or value of the DM vector, which depend on microscopic details, and can only be calculated by a microscopic theory. However, once the DM vector is calculated for one bond, all other DM vectors can be determined using symmetries of the crystals. It is also important to point out that even though the direction of the out-of-plane component of the DM vector alternates from bond to bond, its sign in the local axis defined by the symmetry of the crystal structure is uniform. This gives rise to the $q = 0$ arrangement at low temperature. In addition, we believe that the uniform out-of-plane component is responsible for uniform chirality of spin fluctuations above T_N, which will be discussed in Chapter 5. The microscopic calculations of the DM interaction on the kagomé lattice have been carried out by Elhajal *et al.* [39] by applying Moriya's formulation [115].

Using the superexchange formulation [174], one can calculate the isotropic exchange interaction J_{ij} in Eq. 1.14. J_{ij} is proportional to t_{ij}^2/U, where t_{ij} is the intersite hopping and U is the on-site Coulomb repulsion. On the other hand, the DM vector D_{ij} is proportional to $\lambda t_{ij}^2/\Delta U$, where λ is the spin-orbit coupling and Δ is the crystal field splitting. Therefore, the DM vector appears in first order in the spin-orbit coupling. In contrast, the single-ion anisotropy is second order in λ, and will be ignored. Using Moriya's formulation [115], Elhajal *etal.* were able to derive the microscopic description of the DM vector in terms of the transfer integrals [39], which I will not reproduce here. Instead, I will discuss how the DM interaction gives rise to the 2D spin structure and "umbrella" structure in the ordered state.

In Fig. 3-1, the outward and inward tilts of the octahedra correspond to the DM vector pointing in opposite directions. For the outward tilted octahedra, the out-of-plane component points upward, while for the inward tilted octahedra, it points downward. On the other hand, the in-plane component always points toward the center of the triangles, regardless of the orientation of the octahedra [117, 176]. The microscopic calculations determine the direction of the DM vector in the mirror plane with respect to the tilting axis of the octahedron. As we shall see later in this chapter and Chapter 4, the magnetization measurements of the canting angle and neutron

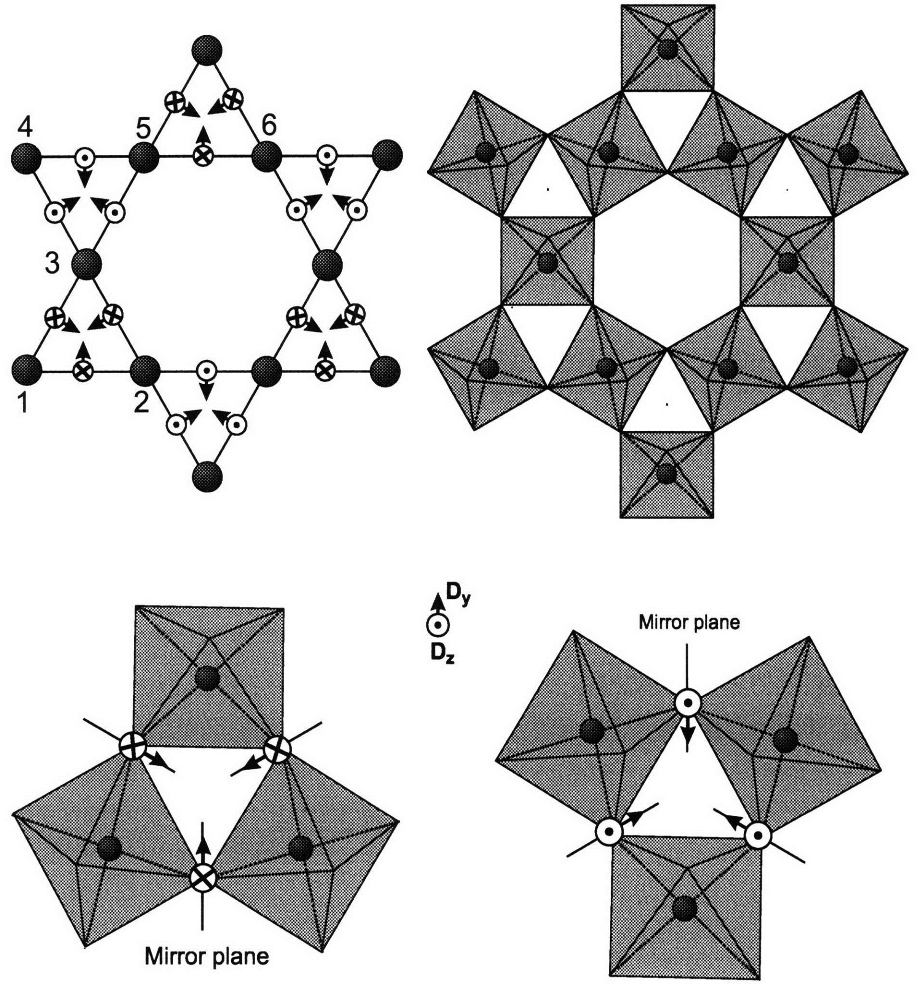

Figure 3-1: This diagram shows the DM vectors on the kagomé lattice. The z component D_z has the same sign, but the in-plane component D_y changes from bond to bond. The tilting of the octahedra is shown in the lower diagram. The DM vector lies within the mirror plane bisecting the bond connecting two magnetic sites. Without loss of generality, one can assume that the outward (inward) tilting of the octahedra corresponds to the DM vector pointing away from (toward) the center of the triangle.

scattering measurements of spin-waves cannot uniquely determine the direction of the in-plane component of the DM vector.

As discussed in Chapter 1, the DM interaction causes the spins on the kagomé lattice to order at a non-zero temperature by lifting the infinite degenerate ground states, and determine the ground-state spin arrangement. The z component of the DM vector D_z confines the spins to be within the kagomé planes, and hence effectively acts like an easy-plane anisotropy. In addition, it is responsible for the $q = 0$ spin structure that has been observed in iron jarosite. The sign of D_z breaks the symmetry between positive and negative chirality. In jarosite D_z is less than zero, which leads to the $q = 0$ structure with positive chirality. (Note that the definition of the DM vector used in this thesis is given in Ref. [117], where the sign of the DM vector is opposite to that used in Ref. [39]. Besides the change of sign, the discussions given here are consistent with Ref. [39]) The in-plane component of the DM vector D_y forces the spins to be canted out of the kagomé planes, consistent with the observed umbrella spin configuration. D_y also breaks the rotational symmetry around the $c-$axis, which results in the Ising-type of ordering in the planes (all-in-all-out spin arrangement).

Fig. 3-2 shows the in-plane component of the DM vector and the spin canting on two adjacent kagomé planes. If the out-of-plane components of the DM vectors on a triangle point downward, and the spins have the all-in (all-out) arrangement, then the canted moment is along the $-z$ or $(+z)$ direction or into (out-of) the page. On the other hand, if the out-of-plane components point upward, and the spins have the all-in (all-out) arrangement, then the the canted moment is along the $+z$ $(-z)$ direction or out-of (into) the page. Fig. 3-2 shows the canted moment on two adjacent kagomé planes in the ground state at zero field assuming the ferromagnetic interplane coupling. When the field larger than the critical field $(H > H_C)$ is applied along the direction perpendicular to the kagomé plane ($+z$ direction), the spins on the second plane rotate 180° causing the canted moment to flip as shown in Fig. 3-17. This leads to weak ferromagnetism observed in jarosite. The 180° spin rotation results from the competition between the ferromagnetic interplane coupling and the Zeeman energy. Within the kagomé plane, the DM vectors on the adjacent bonds point into

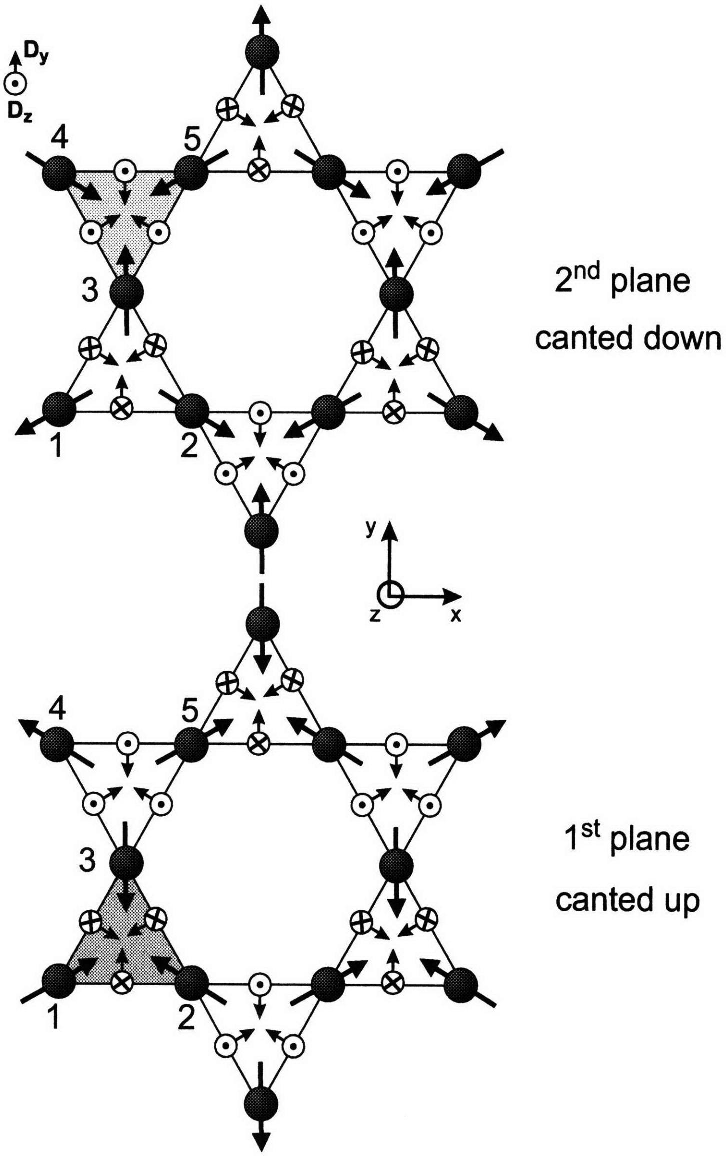

Figure 3-2: This diagram shows the DM vectors and the spin canting on two adjacent kagomé planes in the ground state assuming a ferromagnetic interplane coupling. 'Canted down' indicates that the canted moment points into the page, and 'canted up' indicates that the canted moment points out of the page. Note that the second plane is shifted with respect to the first plane so that the two shaded triangles lie on top of each other.

opposite directions as shown in Fig. 3-2. The following section discusses the field-induced spin re-orientation transition in two jarosite compounds, $KFe_3(OH)_6(SO_4)_2$ and $AgFe_3(OH)_6(SO_4)_2$ by means of magnetization and neutron scattering measurements.

3.2 Magnetization and specific heat measurements

$\mathbf{KFe_3(OH)_6(SO_4)_2}$

To study the spin-canting transition in high field, we first measured the magnetization of a single crystal sample (mass of 13.5 mg) of $KFe_3(OH)_6(SO_4)_2$ using a commercial Superconducting Quantum Interference Device (SQUID) magnetometer by Quantum Design. Measurements were taken with the applied field oriented along the *c*-axis ($H \parallel c$) and within the *ab* plane ($H \parallel ab$) as shown in Fig. 3-3a. At low fields ($H < 5$ T) with the field along *c*, a sharp peak appears near 65 K, indicative of the transition to the 3D magnetically ordered state. This result is consistent with previous measurements on powder samples prepared under similar synthesis conditions [89]. When the field is aligned along the *ab*-direction, the sharp peak is absent and is replaced by a broad cusp.

Fig. 3-3b shows the specific heat C of powder samples of $KFe_3(OH)_6(SO_4)_2$ measured using a commercial Physical Properties Measurement System (PPMS) by Quantum Design. At zero field, a peak in the specific heat is found at the magnetic transition temperature of 65 K. The entropy associated with the 3D magnetic transition (integrating C/T over the temperature range from 2 K to 100 K) represents $\sim 50\%$ of the $R \ln 6$ (where R is the molar gas constant) total entropy expected for the spin $5/2$ system. This suggests that short-range correlations have already formed at much higher temperatures. Measurements of the specific heat at a 13.7-Tesla field shows two transitions, one at about 64 K and the other at 48.5 K as shown in Fig. 3-4. The former corresponds to the transition to the ordered state, which is shifted slightly to lower temperature at high field. In addition, the peak becomes broader

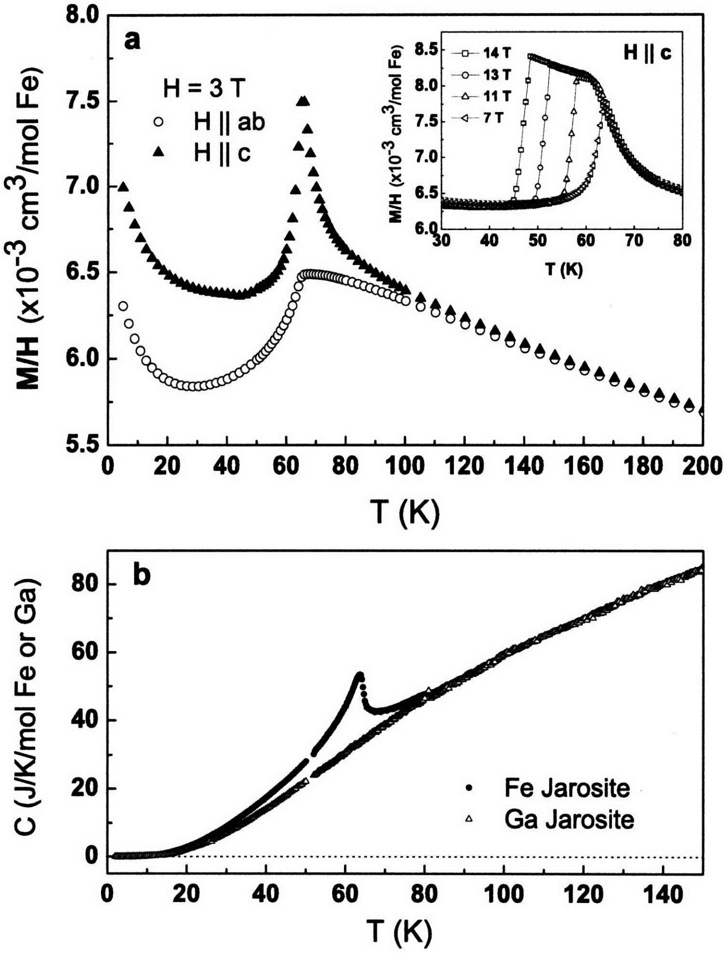

Figure 3-3: Magnetization and specific heat measurements of $KFe_3(OH)_6(SO_4)_2$. (a) M/H versus temperature with the applied field in two orientations, $H \parallel c$ and $H \parallel ab$ measured on a single crystal sample using a SQUID magnetometer. The inset shows M/H for $H \parallel c$ for fields up to 14 Tesla measured using an AC coil set. The upturn in the magnetization at low temperatures (below 20 K) can be described by Curie behavior in which the density of free spins corresponds to $\sim 0.3\%$ of the total number of spins. (b) Specific heat of powder samples of $KFe_3(OH)_6(SO_4)_2$ (closed symbols) and the non-magnetic isostructural compound $KGa_3(OH)_6(SO_4)_2$ (open symbols). The $KGa_3(OH)_6(SO_4)_2$ data are scaled to match the Fe-jarosite data at high temperatures and are used to estimate the phonon contribution.

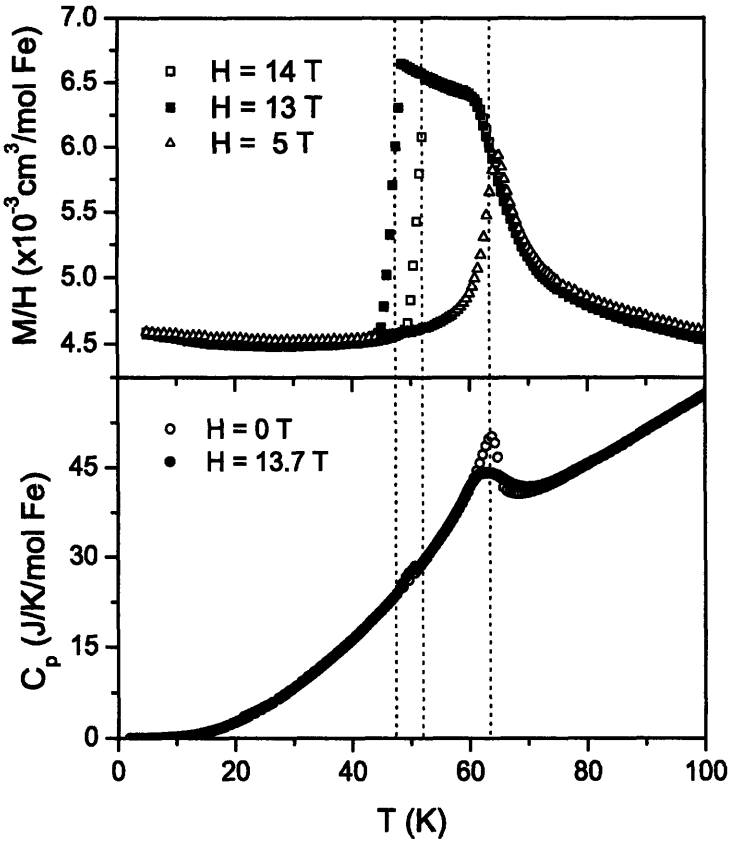

Figure 3-4: Magnetization and specific heat measurements of $KFe_3(OH)_6(SO_4)_2$. The top panel shows M/H versus temperature with the applied field H = 14, 13 and 5 T along $H \parallel c$ measured on a single crystal sample using a PPMS magnetometer. (bottom) Specific heat of powder samples of $KFe_3(OH)_6(SO_4)_2$ measured at $H = 0$ T (open symbols) and $H = 13.7$ T (closed symbols). The dotted lines indicated two magnetic transitions at 64 K and 48.5 K.

in the presence of the magnetic field. The latter occurs at the same temperature where the sharp drop in the magnetization was observed, corresponding to the spin re-orientation transition from the anti-aligned canting state to aligned canting state.

At high temperatures ($T > 150$ K), the susceptibility is isotropic and follows a Curie-Weiss law $\chi = C/(T - \theta_{CW})$, consistent with previous results on powder samples [89]. Fits to this law between 150 K and 550 K yield values $\theta_{CW} = -800(30)$ K, and $C = 5.6(2)$ cm^3 K/mol Fe (Fig. 1-10). Because the data are taken for $T < |\theta_{CW}|$, we extract the effective moment μ_{eff} and the nearest neighbor exchange coupling J using the high-temperature series analysis of Harris *et.al.* for the kagomé lattice [35].

Our results indicate that $J = 45(2)$ K $= 3.9(2)$ meV and $\mu_{\text{eff}} = 6.3(2)\ \mu_B$ (close to the spin-only value of 5.92 μ_B for Fe^{3+} with $S = 5/2$). We note that a small next-nearest neighbor interaction ($J_2 > 0$) would serve to reduce the calculated value of J by an amount of order J_2.

The peak in M/H for $H \parallel c$ at $T = 65$ K indicates the presence of weak ferromagnetism along the c-direction. Our measurements on single crystals allow us to explore this model of canted moments. The inset of Fig. 3-3(a) shows M/H as a function of temperature measured in high fields ($H \geq 7$ T). At these high fields, the peak broadens and the downturn in the magnetization shifts to lower temperatures. Such behavior has been observed in the square-lattice antiferromagnet La_2CuO_4 [177] for which the DM interaction does indeed result in weak ferromagnetism [178].

Critical Field, H_c, and canted moment, ΔM

To investigate this spin canting further, we made magnetization measurements as a function of magnetic field along the c direction as shown in Fig. 3-5(a). The results show an abrupt change in the magnetization at a critical field, H_C, which we define as the field at which dM/dH is a maximum. We interpret this abrupt increase as a change from canted moments being oppositely directed between planes to canted moments aligned in the same direction. This change is caused by a 180° rotation of all spins on the alternating layers that were previously oppositely canted, as shown in the inset of Fig. 3-5(b). The critical field as a function of temperature is also shown in Fig. 3-5(b). For comparison, Fig. 3-5(c) shows the integrated intensity of the (1 1 $\frac{3}{2}$) magnetic Bragg peak measured with neutron diffraction. We found that H_C scales quite closely with the staggered moment $M^\dagger$ (which is proportional to the square-root of the Bragg intensity). The mean-field result for La_2CuO_4 gives $H_C \propto M^\dagger/\chi^\dagger$, where $\chi^\dagger$ is the 2D staggered susceptibility [178]. In our case, the staggered susceptibility for the kagomé lattice is expected a have weaker temperature-dependence than the square lattice due to the geometrical frustration [41].

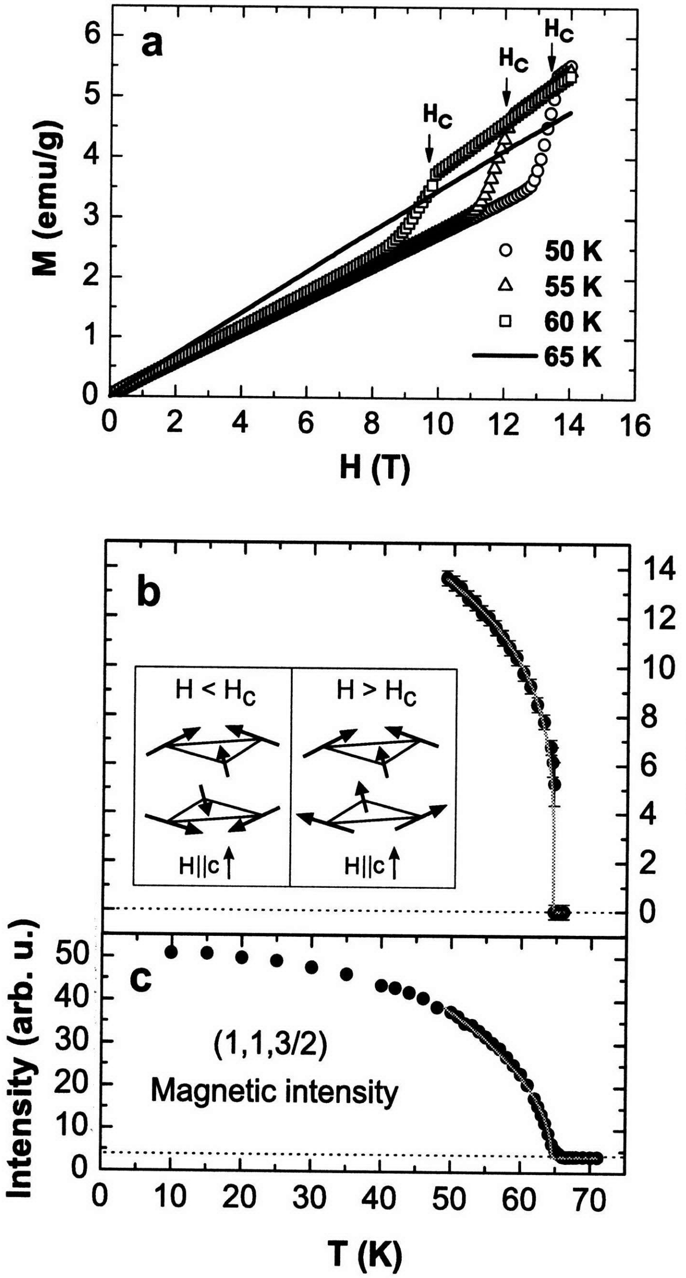

Figure 3-5: Measurements of the field-induced transition to a state with non-zero scalar chirality. (a) Magnetization versus applied field for several temperatures with $H \parallel c$. The H_C values indicate the fields where dM/dH is maximum. (b) H_C versus temperature. The inset depicts the change in the spin configuration below and above H_C. (c) Integrated intensity of the (1,1,1.5) magnetic Bragg peak measured with neutron diffraction on a single crystal in zero field. This quantity is proportional to $(M^{\dagger})^2$, the square of the staggered moment. The lines in panels (b) and (c) correspond to power-law forms for H_C and $M^{\dagger}$ with a fixed exponent $\beta = 0.25$ and $T_N = 64.5$ K for $T > 50$ K.

Canting Angle, η, and interplane coupling, J_c

Below $T = 49$ K, the critical field becomes larger than 14 T, the maximum field of our magnetometer. Hence, it is not possible to extract the low-temperature values of H_C and the canted moment. However, an estimate for the canted moment can be made by considering the jump in the magnetization in the vicinity of H_C. For the data taken at $T = 50$ K, we obtain a canting angle for the ordered moment of $0.65(6)^\circ$ with respect to the kagomé plane for $H \simeq H_C$ (this angle will increase upon cooling, as the order parameter has not yet reached its low temperature value). The field-induced transition results from a competition between the interlayer coupling J_c and the Zeeman energy; the magnitude of J_c may be estimated from the following relation: $H_C(0)M_F(0) = S^2|J_c|$, where $H_C(0)$ and $M_F(0)$ are the critical field and ferromagnetic moment per Fe atom, respectively, at $T = 0$. Our results indicate the ferromagnetic interlayer coupling $J_c = -0.014(12)$ meV where the large error bar comes from the uncertainty in extrapolating H_C and M_F to $T = 0$. The value of -0.03(1) meV is obtained if we used the canting angle of $1.9(2)^\circ$ obtained from our spin-wave measurements as shown in Table. 3.1. We find that the magnitude of J_c is several hundred times smaller than the nearest-neighbor J, attesting to the two-dimensionality of the system.

High critical field in K jarosite prevented us from measuring the spin re-orientation transition down to base temperature. Below 50 K, the critical field is higher than the PPMS maximum field of 14 T. However, to calculate accurately the values of spin anisotropies, canting angle and inter-layer coupling, one needs the values of canted moments and critical field at zero temperature. Therefore, we studied similar compound called Ag jarosite, where potassium is replaced by silver. Low critical field in this compound allows for measurements down to base temperature. The magnetic properties due to Fe^{3+} ions in the kagomé plane, however, are basically the same due to the structurally homologous magnetic unit, the $Fe_3^{III}(\mu - OH)_3$. The lower critical field is a result of a smaller value of the inter-layer coupling.

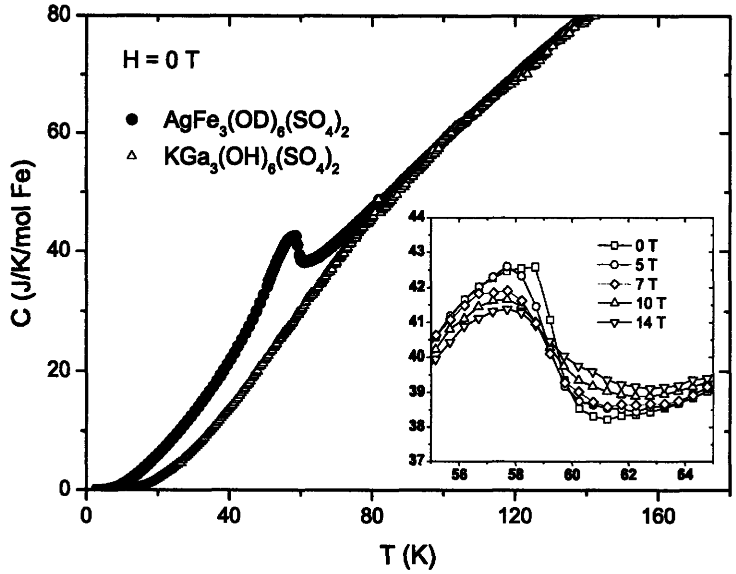

Figure 3-6: Specific heat of deuterated powder samples of $AgFe_3(OD)_6(SO_4)_2$ (red squares), and powder sample of non-magnetic isostructural compound $KGa_3(OH)_6(SO_4)_2$ (blue circles) measured at $H = 0$ T. The $KGa_3(OH)_6(SO_4)_2$ data are scaled to match the Ag jarosite data at high temperatures and are used to estimate the phonon contribution. The inset shows the specific heat of $AgFe_3(OD)_6(SO_4)_2$ at different magnetic fields.

$\mathbf{AgFe_3(OH)_6(SO_4)_2}$

We have performed similar measurements on powder samples of Ag jarosite $AgFe_3(OX)_6(SO_4)_2$ where X = H or D. Due to its low critical field, we are able to measure the field-induced transition down to base temperature, and determine the values of the canting angle and the spin Hamiltonian parameters with more accuracy. Details of the synthesis, X-ray crystal structure refinement, and SQUID magnetometry measurements of Ag jarosite have been previously reported in Ref. [94].

The specific heat C of deuterated power samples (mass of 22 mg) of $AgFe_3(OD)_6(SO_4)_2$ was measured using the PPMS magnetometer over a 5-150 K temperature range at field strengths varying from 0-14 T. The non-magnetic isostructural compound $KGa_3(OH)_6(SO_4)_2$ was used to estimate the phonon contribution as shown in Fig. 3-6. At zero field, a peak in the specific heat at T_N = 60 K indicates the transition to magnetic LRO. At higher fields, this peak becomes broader. Nevertheless, its position does not change very much with field, indicative of weak field-dependence of T_N. In contrast to the results from the single crystal sample of K jarosite, the second transition at lower temperature is not observed in the power sample of Ag jarosite. We believe that the absence of the second transition is a result of powder average. The entropy associated with the 3D magnetic order, which is obtained from integrating C/T over the temperature range from 5 K to 150 K, represents about 70% of the $R \ln 6$ (where R is the molar gas constant) total entropy expected from the spin-5/2 system compared with 50% for $KFe_3(OH)_6(SO_4)_2$ [110]. This suggests that short-range correlations have already formed at much higher temperature.

Magnetization measurements were performed using a commercial Magnetic Properties Measurement System (SQUID) by Quantum Design and PPMS over a 5-300 K temperature range at field strengths varying from 0-5 T for SQUID and 0-14 T for PPMS. Powder samples of non-deuterated Ag jarosite of mass 289.3 mg and deuterated Ag jarosite of mass 399.8 mg were packed inside a plastic capsule, and put inside a plastic straw. The straw is then secured to the tip of the measuring stick. Each data point is the average of 10 or 25 magnetometry scans in PPMS, or 3 scans in SQUID. All raw magnetization data were corrected for diamagnetism due to core electrons, and paramagnetic contributions due to free spins and/or impurities. To extract the paramagnetic contributions, the low-field region of the magnetization $M(H)$ for $H < 9.5$ T at $T = 5$ K was fit to

$$M(H,T) = P_1 B_J(H/T) + P_2 H + P_3, \tag{3.3}$$

where P_n are empirical prefactors, $B_J(x)$ is the Brillouin function with $J = 5/2$, H and T are a magnetic field and temperature, respectively. Fig. 3-7 shows the data before and after subtracting the Brillouin function.

The Brillouin prefactor gives a measure of the non-interacting, free Fe^{3+} spins in the ordered state. For a pure paramagnet, all spins are non-interacting, and the Brillouin function prefactor would be $P_1 = 5\ \mu_B$. The average value of P_1 for the measurements upon increasing and decreasing field at 5 K (shown in Fig. 3-10(a)) is

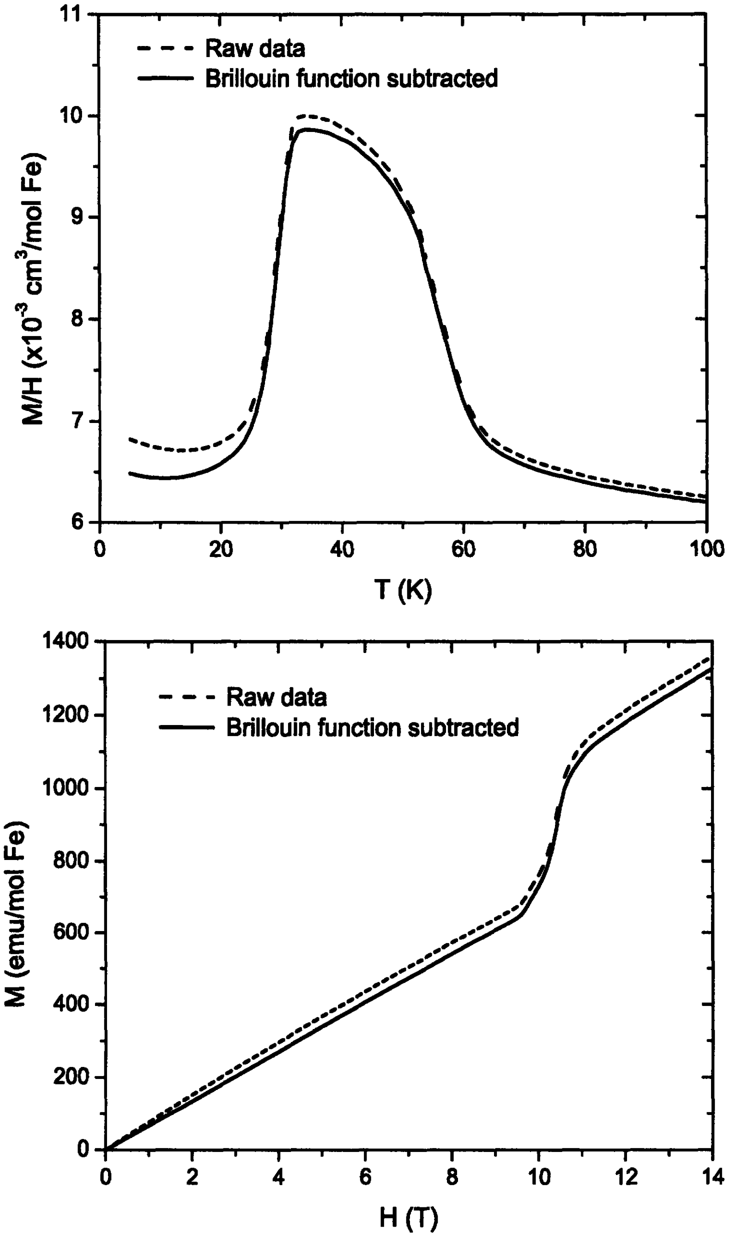

Figure 3-7: Magnetization data before and after subtracting the Brillouin function. The M versus H curve was measured at $T = 5$ K, and the M/H versus T curve was measured at $H = 9.5$ T.

about 0.005 μ_B, which indicates that about 0.1% of the Fe^{3+} spins are non-interacting. This result shows that virtually all magnetic sites are occupied, and Ag jarosite has virtually no non-interacting spin in the ordered state.

The SQUID magnetometry measurements on non-deuterated samples at low field of 100 Oe (not shown) show LRO below the Néel ordering temperature T_N of 59.6 K, which is indicated by a peak in the d.c. susceptibility ($\chi = M/H$) [94]. At high temperatures (T> 150 K), χ follows the Curie-Weiss law $\chi = C'/(T - \Theta'_{CW})$. A fit to this equation yields $\Theta'_{CW} = -800(50)$ K, and $C' = 5.4(5)$ cm^3 K/mol Fe. The ordering temperature T_N is greatly reduced from the mean field value $|\Theta'_{cw}|$ due to geometric frustration, suggested by a large empirical frustration parameter, $f = |\Theta'_{cw}|/T_N \approx 13$ [1]. Therefore, the mean field theory cannot be applied to determine the effective moment μ_{eff}, and the nearest neighbor exchange coupling J. As discussed in Chapter 1, Harris *et al.* [35] introduce the corrections to the mean field theory to account for frustration using the high-temperature series analysis for the kagomé lattice, which gives $\Theta'_{CW} = \frac{3}{2}\Theta_{CW}$ and $C' = \frac{9}{8}C$ where Θ_{CW} and C are the mean-field Curie-Weiss temperature and constant, respectively. Using these corrections, we obtain the effective moment $\mu_{eff} = 6.2(6)\ \mu_B$ and the nearest neighbor exchange coupling $J = 3.9(2)$ meV. For comparison, the values of the nearest neighbor coupling and the effective moment for K jarosite deduced from the Curie-Weiss fit using Harris' correction are $J = 3.9(2)$ meV and $\mu_{eff} = 6.3(2)\ \mu_B$ [110], respectively. We note the similarity of the values of J and μ_{eff} for K jarosite and Ag jarosite due to the structural homology of the fundamental interacting unit, the $Fe^{III}{}_3(\mu$-$OH)_3$ triangle. Goodenough-Kanamori rules governing the frontier orbitals of the hydroxide-bridged iron trimer predict this antiferromagnetic exchange [179, 180]. The singly occupied $d_{x^2-y^2}$ orbitals of high spin Fe^{3+} overlap with the filled sp^3 hybrid orbitals of the hydroxide, giving a superexchange pathway of σ-symmetry.

The PPMS magnetometer was used to measure the magnetic susceptibility of the non-deuterated and deuterated samples at fields between 3 T and 14 T as a function of temperature. Fig. 3-8(a) shows the d.c. susceptibility of the deuterated sample. At high fields, the sharp peak at $T \approx 60$ K is no longer observed. Instead, the

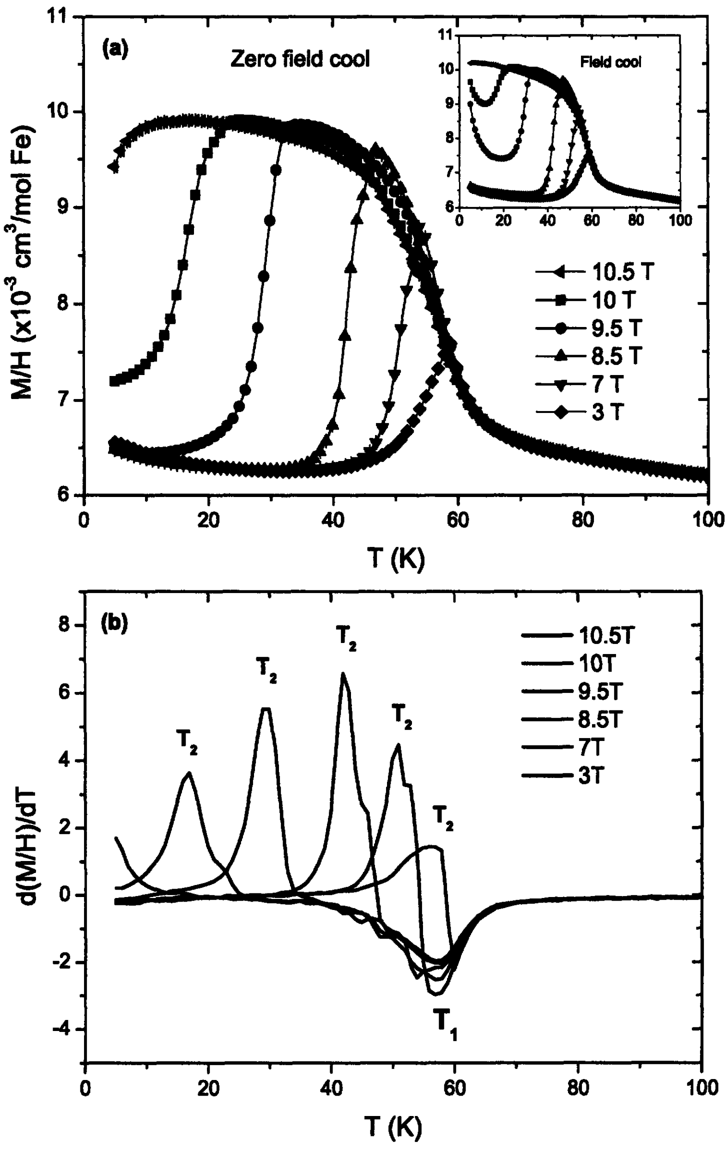

Figure 3-8: (a) Zero field-cooled and field-cooled (inset) d.c. susceptibility of deuterated Ag jarosite powder. (b) The derivatives of M/H with respect to temperature show dips at T_1 and peaks at T_2, indicative of transitions to the 3D ordered state and the ordered state with zero scalar chirality, respectively.

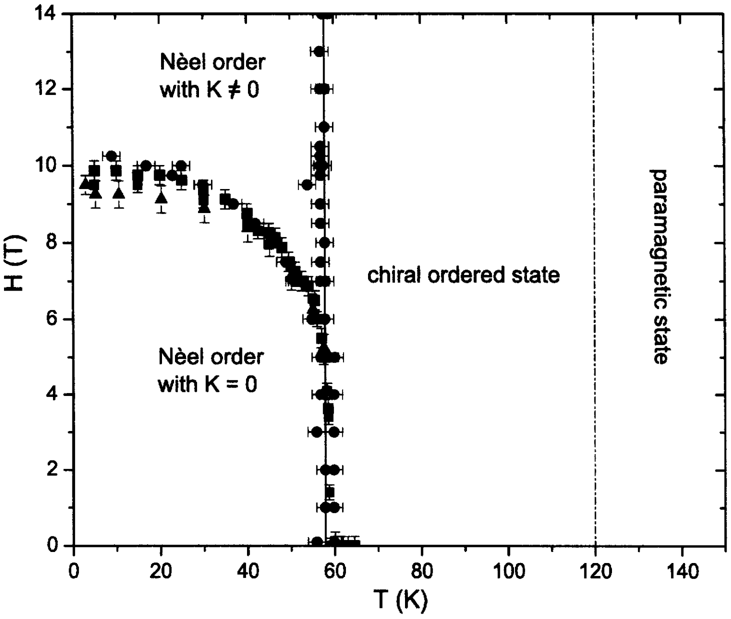

Figure 3-9: The phase diagram of Ag jarosite is deduced from magnetization and neutron scattering measurements. From the temperature scan measurements, T_1 and T_2 are shown in circles for both deuterated and non-deuterated samples. The average values of the critical fields are shown in squares. The average critical fields obtained from the neutron scattering measurements from both BENSC and NCNR experiments are shown in triangles. The dotted line at 120 K is deduced from a quasi-elastic neutron scattering experiment on a single crystal sample.

peak moves to lower temperature, and becomes a broad plateau for $H > 9.5$ T. The plateau is getting broader as the field increases, and extends to base temperature of 5 K for $H > 10.5$ T. The zero-field-cooling and field-cooling (shown in the inset of Fig. 3-8(a)) data resemble each other except at low temperatures where the field-cooling data show a rise in the susceptibility, which, we believe, is due to trapped ferromagnetic domains of the crystallite sample. The magnetic susceptibility of the non-deuterated sample (not shown) resembles that of the deuterated sample with the exception that the saturated value of the d.c. susceptibility of the non-deuterated sample at high field ($\chi_{max} \approx 9 \times 10^{-3}$ cm^3/mol Fe) is about 10% smaller than that of the deuterated sample, indicative of a smaller canting angle.

For these high field measurements, it is difficult to define the ordering temperature due to the lack of well-defined peaks. Fig. 3-8(a) shows the up-turn in the magnetic susceptibility at $T \approx 60$ K, which does not change with field, followed by the sharp decrease in the susceptibility at lower temperature. By taking the derivative of the magnetic susceptibility with respect to temperature, we can define T_1 and T_2 to be a dip and peak in the derivatives, respectively, as shown in Fig. 3-8(b). T_1 can be identified as the temperature at which the system goes into the 3D ordered state, and is field-independent. On the other hand, T_2 indicates the transition from the state with a net ferromagnetic moment to the state with no net moment, and is field-dependent. We note that the latter transition is not observed in specific heat measurements due to its small contribution.

The plot of T_1 and T_2 in Fig. 3-9 shows the phase diagram of Ag jarosite. The results of field scan measurements, which are discussed below, are also plotted, and they are in good agreement with the temperature scan measurements. The dotted line at 120 K is obtained from our quasi-elastic neutron scattering measurements on a single crystal sample of K jarosite at zero field, which will be discussed in Chapter 5. For $T < T_2(H)$, the system is in the 3D ordered state with no net ferromagnetic moment along the *c*-axis. In this state, the net scalar chirality is zero [110]. For $T_2(H) < T < T_1$, the system is still in the 3D ordered state but K is non-zero, and the net ferromagnetic moment along the *c*-axis is present. For $T_1 < T < 120$ K, the system no longer has 3D LRO but 2D short range correlations between spins still persist. The system is in the vector chiral ordered state with no spontaneously broken rotational symmetry [110]. Above $T = 120$ K, the system becomes a frustrated paramagnet where the susceptibility follows the modified Curie-Weiss law as discussed in Ref. [35].

Critical Field, H_c, and canted moment, ΔM

High field magnetization measurements were conducted using the PPMS magnetometer with a maximal field of 14 T to investigate the spin canting, which gives rise to the net ferromagnetic moment in the region between T_1 and $T_2(H)$ of the phase diagram. Fig. 3-10(a) shows the magnetization $M(H)$ at $T = 5$ K as a function of field after subtracting the paramagnetic contributions. M increases linearly with

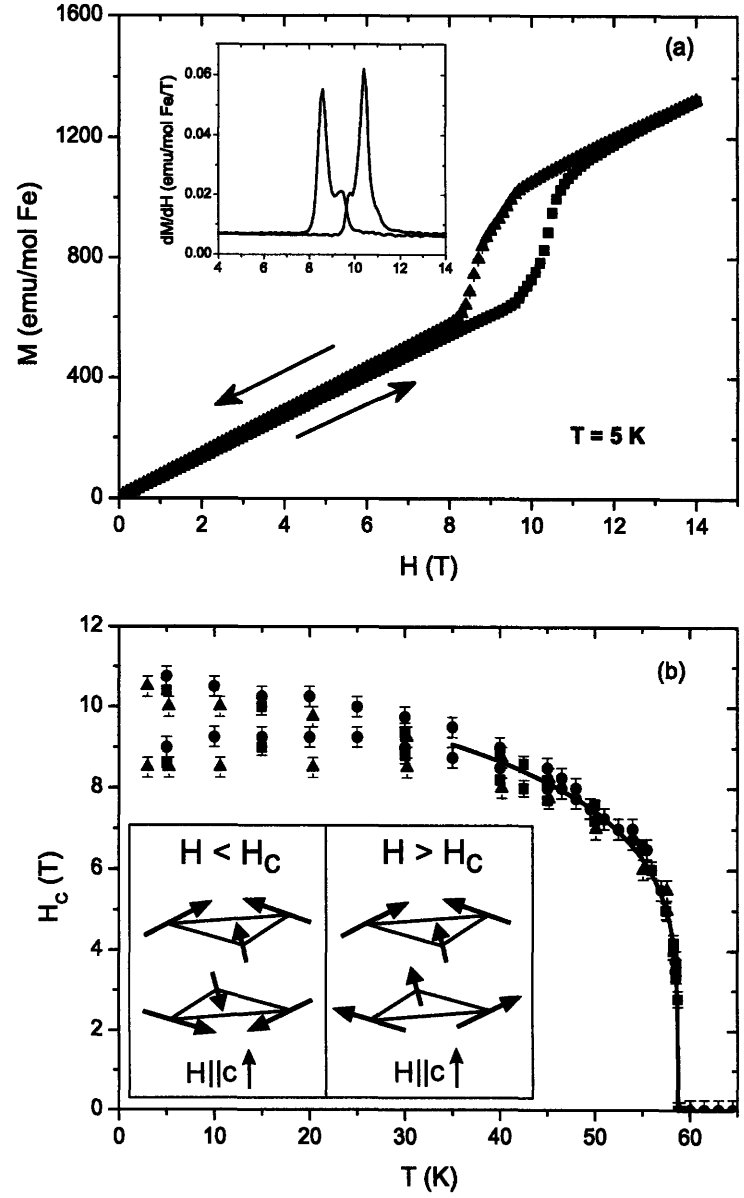

Figure 3-10: (a) The magnetization as a function of field at $T = 5$ K for deuterated Ag jarosite powder shows hysteretic behavior as the field is scanned up and down. The inset shows peaks of dM/dH, which are defined as critical fields. (b) Temperature-dependences of the critical field H_c between 5 K And 60 K are deduced from magnetization measurements on non-deuterated Ag jarosite (blue circles) and deuterated Ag jarosite (red squares), and neutron scattering measurements on deuterated Ag jarosite at BENSC (green triangles) and NCNR (green diamonds). The line corresponds to a power-law fit for H_c between $35 < T < 65$ K with the exponent $\beta = 0.2$ and $T_N = 58.8$ K. The inset shows the spin re-orientations of the first layer from the all-in arrangement for $H < H_c$ to the all-out arrangement for $H > H_c$.

increasing applied field upto 9.75 T, which is followed by a sharp increase between 9.75 – 11.5 T. The linear response is then recovered for $H > 11.5$ T with roughly the same slope. Continuing the measurement while decreasing the applied field, M decreases linearly to 10.5 T, then drops sharply between 8.75 – 10.5 T. The linear behavior then resumes for $H < 8.75$ T. The hysteresis in the bulk magnetization signifies ferromagnetic ordering, and is indicative of a first-order transition between the antiferromagnetic and ferromagnetic states. The anisotropic crystalline field of Fe^{3+} in a distorted octahedral geometry yields the hysteresis in the $M(H)$ curve with a coercive field of approximately 2 T as shown in Fig. 3-10(a). The critical field H_c, the field at which the sudden change in magnetization is observed, is defined as a maximum of $(dM/dH)|_T$, as shown in the inset of Fig. 3-10(a). Upon increasing (decreasing) field, $H_c = 10.75$ T (8.75 T) at $T = 5$ K. The same measurements were conducted at different temperatures to obtain $H_c(T)$ as a function of temperature. The results are shown in Fig. 3-10(b). The line corresponds to a fit to the power law $H_c(T) \propto |T - T_N|^\beta$ for temperatures between 35 K and 65 K giving the exponent $\beta = 0.2$ and $T_N = 58.8$ K compared with $\beta = 0.25$ and $T_N = 64.7$ K for K jarosite [110]. The average values of the critical fields are also plotted in Fig. 3-9, and to be compared with $T_2(H)$.

To extract a canted moment ΔM from the data, we fit the high field data ($H > H_c$) of the $M(H)$ curve to a linear function with a fixed slope and extrapolate that line to obtain a Y-intercept, which is defined as a canted moment ΔM as shown in Fig. 3-11(a). The slope was obtained from fitting low field data ($H < H_c$) fixing the Y-intercept to zero. ΔM's at different temperatures are plotted in Fig. 3-11(b). The hysteretic behavior persists up to $T \approx 50$ K, which is in agreement with the hysteretic behavior seen in the critical field (Fig. 3-10(b)). Fig. 3-11(b) also shows the difference of ΔM between deuterated and non-deuterated samples, which is not observed in the critical field data. This difference is due to a change in the in-plane component of the DM interaction (D_y) when hydrogen atoms are replaced by deuterium atoms. The increase of D_y in the deuterated sample results in the higher values of the canting angle and ΔM.

The presences of the critical field and the canted moment allow us to investigate the DM interaction and the interplane coupling directly. As discussed in the previous section, the sudden change in magnetization is a result of the difference in magnetic moment along the *c*-axis caused by 180° rotation of all spins on the alternating layers that were previously oppositely canted due to the ferromagnetic interplane coupling (shown in the diagram in Fig. 3-10(b)). At the critical field, the magnetic field energy overwhelms the ferromagnetic interplane coupling, and forces the spins on the alternating layers to rotate 180° causing the canted moment to align along the *c*-axis. The 180° spin rotation at $H = H_c$ results in the change from the all-in to all-out (vice versa) spin arrangements on the alternating kagomé planes as shown in Fig. 1-3. In the next section, the values of the canting moment and critical field will be used to calculate the spin Hamiltonian parameters and the canting angle.

Canting Angle, η, DM Parameters, D_y and D_z

Fig. 3-10(b) and Fig. 3-11(b) show the temperature-dependence of ΔM and H_c over the temperature range of 5-65 K, respectively. H_c saturates at low temperatures to an average value of $H_c(0) = 9.5(1.0)$ T. As temperature increases, H_c monotonically decreases and goes to zero as T approaches T_N. ΔM also appears to saturate for temperatures below 30 K, and goes to zero as T approaches T_N. We, therefore, fit the data below 30 K to a constant to obtain the average value of the canted moment at zero temperature $\Delta M(0)$. The dashed lines in Fig. 3-10(b) show that ΔM saturates at $\Delta M(0) = 300(30)$ emu/mol Fe $= 0.054(5)\ \mu_B$ ($390(30)$ emu/mol Fe $= 0.070(5)\ \mu_B$) for the non-deuterated (deuterated) sample. However, since the data was taken on powder samples, ΔM is multiplied to a factor of 3 to take into account the powder average. Given the expected moment $M = 5\ \mu_B$ for $S = 5/2$, the canting angle at zero temperature η is defined as $\eta = \sin^{-1}\left(\frac{\Delta M}{M}\right)$, which gives $\eta = 1.8(2)°$ ($\eta = 2.4(2)°$) for the non-deuterated (deuterated) sample, which is in good agreement with the canting angle of 1.9(2)° for K jarosite deduced from the spin-wave data [112]. The similar measurements of the spin canting in La_2CuO_4, a parent compound of high-T_c

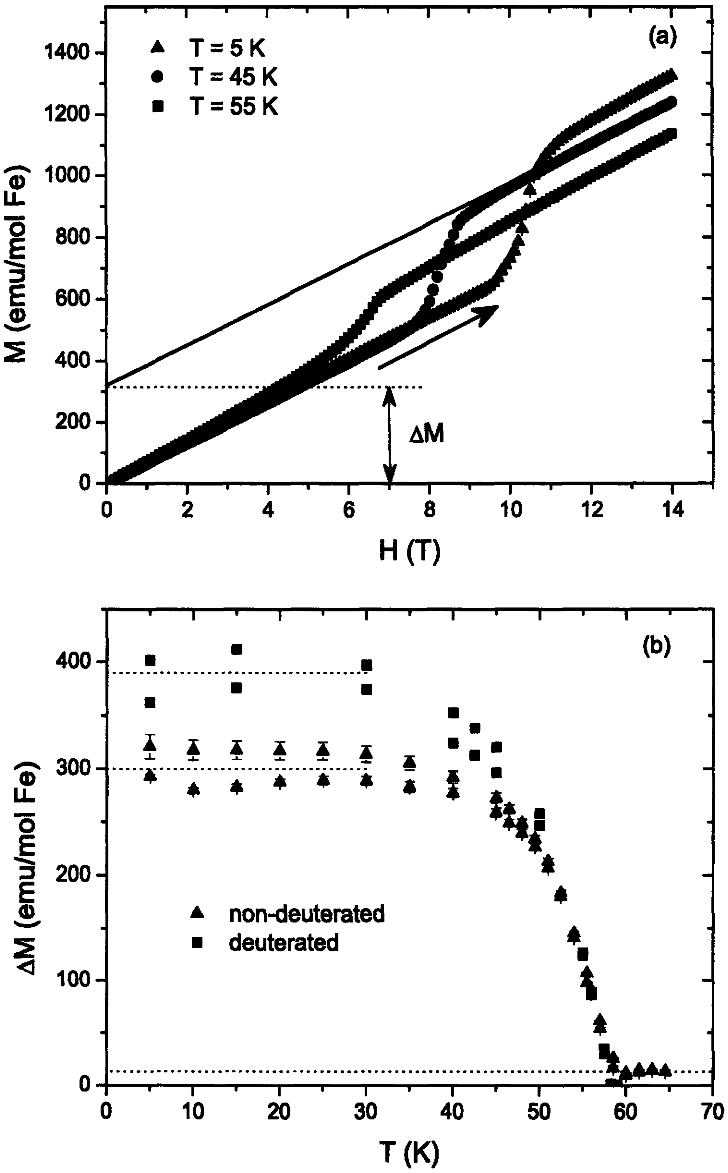

Figure 3-11: (a) The $H > H_c$ range is fit to a linear function with the same slope as that of the low field ($H < H_c$). Y-intersect is defined as the canted moment ΔM. (b) shows temperature-dependence of ΔM for for non-deuterated Ag jarosite (triangles) and deuterated Ag jarosite (squares). ΔM saturates at 300(30) emu/mol Fe (390(30) emu/mol Fe) for the non-deuterated (deuterated) sample.

Table 3.1: This table shows the critical fields, canted moments at zero temperature, canting angles, and the spin Hamiltonian parameters for K jarosite and Ag jarosite. The parameters for Ag jarosite were obtained from the magnetization measurements, while those for K jarosite were obtained from magnetization and inelastic neutron scattering measurements.

Compound	$AgFe_3(OH)_6(SO_4)_2$	$AgFe_3(OD)_6(SO_4)_2$	$KFe_3(OH)_6(SO_4)_2$
$H_C(0)$ (T)	9.5(1.0)	9.5(1.0)	18(5)
$\Delta M(0)$ (μ_B)	0.16(2)	0.21(2)	0.17(2)**
η (°)	1.8(2)	2.4(2)	1.9(2)†
$\lvert D_p \rvert$ (meV)	0.18(2)	0.24(2)	0.197(2)†
D_z (meV)	-0.17(3)	-0.17(3)	-0.196(4)†
J_c (meV)	-0.014(3)	-0.018(4)	-0.03(1)
T_N (K)	60(1)*	60(1)*	64.5(3)
$\hbar\omega_0$ (meV)	6.2(4)††	6.2(4)††	6.7(1)†

* T_N is defined to be the peak in the d.c. magnetic susceptibility. ** The value of the canted moment is calculated from the canting angle obtained from the spin-wave measurements [112]. † Ref. [112]. ‡ Ref. [110]. †† The value of the energy gap of the lifted zero energy mode is estimated using the results from the inelastic neutron scattering measurements on deuterated powder samples.

superconductors, by Thio *et al.* yields a much smaller value of the canting angle ($\eta = 0.17°$) [178].

Elhajal *et al.* have calculated the canting angle in terms of D_y and D_z, which is given by [39]:

$$\eta = \left| \frac{1}{2} \tan^{-1} \left[\frac{-2D_y}{\sqrt{3}J - D_z} \right] \right| . \tag{3.4}$$

We note that signs of D_y and D_z are reversed and different from Ref. [39] to be consistent with the DM vector defined in Ref. [117]. The absolute value indicates that the sign of the canting angle with respect to the in-plane order cannot be determined from the magnetization measurements. In addition, Yildirim and Harris have derived the canting angle induced by the DM interaction. The expression for the canting angle is given by [117]:

$$\eta = \left| \frac{1}{2} \sin^{-1} \left[\frac{-2D_y}{\sqrt{3}J - D_z} \right] \right| ., \tag{3.5}$$

where $J = J_1 + J_2$ if the next-nearest-neighbor interaction J_2 is non-zero. Both Eq. 3.4 and Eq. 3.5 approach the same limiting value for a small canting angle. In order to determine both in-plane D_y and out-of plane D_z components of the DM interaction, we also need the value of the energy gap of the lifted zero energy mode, and therefore rely on previous single crystal neutron scattering measurements on K jarosite. The spin wave calculations by Yildirim and Harris give the following expression for the two energy gaps at 7 meV [117, 112]:

$$\hbar\omega_0 = S\left(\sqrt{3D_p^2 + 18D_z^2 - 6\sqrt{3}JD_z} \pm \frac{2D_zD_y}{J}\right). \tag{3.6}$$

The energy splitting of these two gaps is about 0.1 meV, and the gap of the lifted zero energy mode has a lower value. This value of the gap is independent of the signs of D_y due to the ± sign in front of the last term. We note that the negative value of D_z yields the spin arrangement with positive vector chirality, which has been verified by Inami [37].

By assuming that the spin Hamiltonian parameters giving rise to the energy gap are the same for both Ag and K jarosites, the values of D_y and D_z can be calculated by solving Eq. 3.5 and 3.6. The inelastic neutron scattering measurements on Ag and K jarosite, which will be discussed later in this chapter, will provide evidence for the similarity in the spin Hamiltonian parameters. Given $\hbar\omega_0 = 6.7(1)$ meV [112] from the single-crystal neutron scattering measurements of K jarosite, and the lifted zero energies measured on powder samples of Ag and K jarosite as shown in Fig. 3-12, the energy gap for Ag jarosite can be estimated to be 6.2(4) meV. In addition, given J from the spin-wave measurements on single crystals of K jarosite ($J = 3.18(5)$ meV), and the canting angles from the magnetization measurements, we obtained $|D_y| = 0.18(3)$ meV (0.24(3) meV), and $D_z = -0.17(3)$ meV ($-0.17(3)$ meV) for non-deuterated (deuterated) sample. These values are in good agreement with the spin-wave results, which is presented in Chapter 4, measured on single crystals of K jarosite, where $|D_y| = 0.197(2)$ meV and $D_z = -0.196(4)$ meV [112]. It is interesting to note that the sign of D_y cannot be determined from the magnetization and spin wave measurements, which lack the information on the direction of the spin canting relative to the in-plane order. This information would be crucial for verifying microscopic calculations of the DM interaction.

In addition, the presence of the single-ion anisotropy can also induce the 'umbrella' structure. The canting angle due to the single-ion type anisotropy has been calculated by Nishiyama *et al.*, and is given by [38]:

$$\eta = \left| \frac{1}{2} \sin^{-1} \left(\frac{D+E}{6J} \sin 2\theta_0 \right) \right| . \tag{3.7}$$

where θ_0 is the tilting angle of the oxygen octahedron. The more general expression for the canting angle including both the DM interaction and single-ion type anisotropic (Eq. 1.14) by Yildirim and Harris [117] is given by:

$$\eta = \left| \frac{1}{2} \sin^{-1} \left(\frac{2}{3} \frac{J_{yz} - C_{yz} - \sqrt{3} D_y}{J - (4\sqrt{3}/3) D_z + \frac{1}{12}(\eta_J + \Delta_J)} \right) \right| , \tag{3.8}$$

where J_{yz} is zero if the exchange interaction is isotropic, C_{yz} is a matrix element of the generic single-ion matrix C defined in Chapter 4, $\eta_J = J_{xx} - J_{zz}$ and $\Delta_J = J_{xx} + J_{zz} - 2J_{yy}$ (η_J and Δ_J is zero if the exchange interaction is isotropic). Eq. 3.8 can be written as Eq. 3.7 (Eq. 3.5) if the exchange interaction is isotropic and the DM interaction (single-ion type anisotropy) vanished. However, as previously discussed, being second order in the spin-orbit coupling, the single-ion type anisotropy is very small compared with the DM interaction in jarosite.

Interplane coupling, J_c

In addition, knowing $\Delta M(0)$ and $H_c(0)$ from the magnetization measurements allows us to calculate the interplane coupling constant, J_c. The field-induced transition is a result of the competition between the ferromagnetic interplane coupling J_c and the

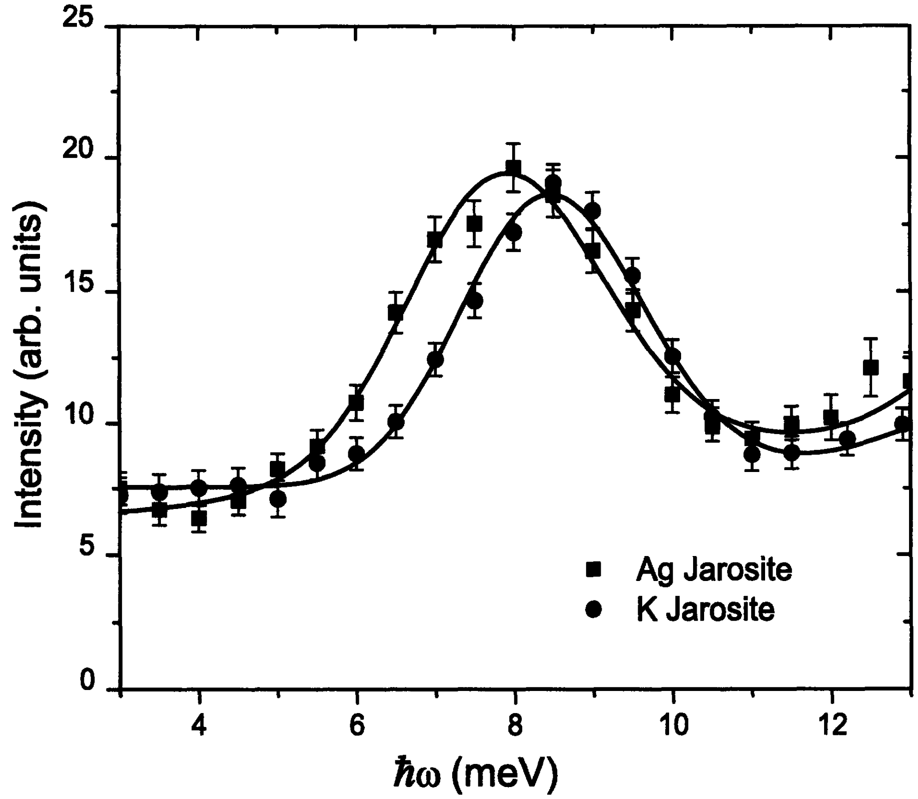

Figure 3-12: Inelastic neutron scattering measurements were performed using the triple-axis spectrometers at NCNR. The constant-Q scan at $|Q| = 1.7$ Å^{-1} on the Ag jarosite power sample (red squares) was measured at BT7, and the constant-Q scan at $|Q| = 1.5$ Å^{-1} on the K jarosite powder samples (blue circles) was measured at BT9. The energy scans show the lifted zero energy mode at energy transfer of 7.9(4) meV (8.5(3) meV) for Ag jarosite (K jarosite). The solid lines show the fits to the spin wave dispersion relation, convoluted with the instrumental resolution function.

Zeeman energy. Using the following equation [178, 110], $J_c = -\Delta M(0) \cdot H_c(0)/S^2$, we find that $J_c = -0.014(3)$ meV ($-0.018(4)$ meV) for the non-deuterated (deuterated) sample. The minus sign indicates that the interplane spin interaction is ferromagnetic. For K jarosite, using the canting angle of 1.9(2)° from the spin-wave measurements, which gives $\Delta M = 0.17(2)\mu_B$, we obtain $J_c = -0.03(1)$ meV as shown in Table 3.1. For both Ag and K jarosites, the magnitude of J_c is hundreds times small than the magnitude of J, which substantiates the two dimensionality of this spin system. On the other hand, the interplane coupling prompts three-dimensionality, and 3D LRO thus exists in this system due to the presence of both the interplane coupling and the DM interaction.

3.3 Neutron scattering measurements

We performed neutron scattering experiments on powder and single crystal samples of jarosite. The first set of experiments was done on the powder samples of two deuterated jarosites, $KFe_3(OD)_6(SO_4)_2$ and $AgFe_3(OD)_6(SO_4)_2$ to measure the spin-wave excitations at low temperature. The preliminary results of the lifted zero energy mode are discussed in this chapter. Detailed measurements of the spin-wave dispersion on single crystal sample are presented in the next chapter. The second set of experiments was performed in high magnetic field to investigate the spin-reorientation transition in a single crystal sample of $KFe_3(OH)_6(SO_4)_2$ and deuterated powder sample of $AgFe_3(OD)_6(SO_4)_2$. The neutron scattering experiments were performed at NCNR for the inelastic scattering, and at BENSC for the elastic scattering at high field.

The integrated intensity of the (1, 1, 3/2) magnetic Bragg peak shown in Fig. 3-5 and Fig. 4-11 was measured using the BT7 spectrometer. The incident neutron energy was fixed at 13.46 meV and the horizontal collimation sequence was open-open-sample-40′-open. Pyrolytic graphite (PG) crystals were used to monochromate and analyze the incident and scatterer neutron beams using the (002) reflection.

3.3.1 Inelastic neutron scattering on powder samples

The inelastic neutron scattering measurements in zero field were performed using the thermal triple-axis spectrometers BT7 and BT9 at NCNR to measure spin-wave excitations on the Ag jarosite and K jarosite powder samples, respectively. The incident neutron energy of 14.7 meV and the horizontal collimations of open$-50'-$S$-60'-120'$ were used at BT7, and the incident neutron energy of 14.7 meV and the horizontal collimations of $40' - 56'-$S$-52'-$open were used at BT9. Pyrolytic graphite (PG) crystals were used to monochromate and analyze the incident and scattered neutron beams using the (002) reflection. PG filters were placed in the scattered beam to reduce higher-order contamination. The deuterated powder samples of Ag and K jarosites were cooled to $T = 14$ K using a closed cycle ^{4}He cryostat and to $T = 5.3$ K using a ^{4}He cryostat, respectively.

The energy scans shown in Fig. 3-12 at $|Q| = 1.7$ Å^{-1} for Ag jarosite (squares) and $|Q| = 1.5$ Å^{-1} for K jarosite (circles) reveal the lifted zero energy mode at energy transfer of 7.9(4) meV and 8.5(3) meV, respectively. The K jarosite data were normalized so that they lie on top of the Ag jarosite data. For K jarosite, the peak is shifted to higher energy compared with the single crystal data [112] due to powder average. The solid lines show the fits to the spin wave dispersion relation described in Chapter 4, convoluted with the instrumental resolution function. The similarity between the spin-wave excitation energies of Ag and K jarosites gives evidence for the resemblance of the spin Hamiltonian parameters of both Ag and K jarosites. The slight difference in the value of the spin-wave excitations is due to the difference in the out-of plan component of the DM vector (D_z). From Table 3.1, the value of D_z for K jarosite is higher than that of Ag jarosite, hence the higher values of the lifted zero energy mode and of the ordering temperature T_N in K jarosite. This result is also in agreement with the calculations by Elhajal *et.al.* [39], who show that the ordering temperature is scaled with the DM parameters.

3.3.2 Spin re-orientation transition in high field

$AgFe_3(OD)_6(SO_4)_2$

To verify the 180° spin rotation at $H = H_c$, the elastic neutron scattering measurements in high magnetic field were performed using the triple-axis spectrometer E1 at BENSC, and BT7 at NCNR. The incident neutron wavelength of 2.425 Å ($\hbar\omega = 13.90$ meV) and the horizontal collimations of $40' - 80'$–sample–$40' - 40'$ were used at E1, and the incident neutron energy of 14.7 meV and the horizontal collimations of open–$50'$–S–$60' - 120'$ were used at BT7. Pyrolytic graphite (PG) crystals were used to monochromate and analyze the incident and scattered neutron beam using the (0 0 2) reflection. A PG filter was placed in the incident beam at E1, and two PG filters were places before and after the sample at BT7 to reduce higher-order contamination. At BENSC, the deuterated Ag jarosite powder sample of mass 5.5 g was placed inside the VM-1 magnet, whose highest field is 14.5 T, and at NCNR the

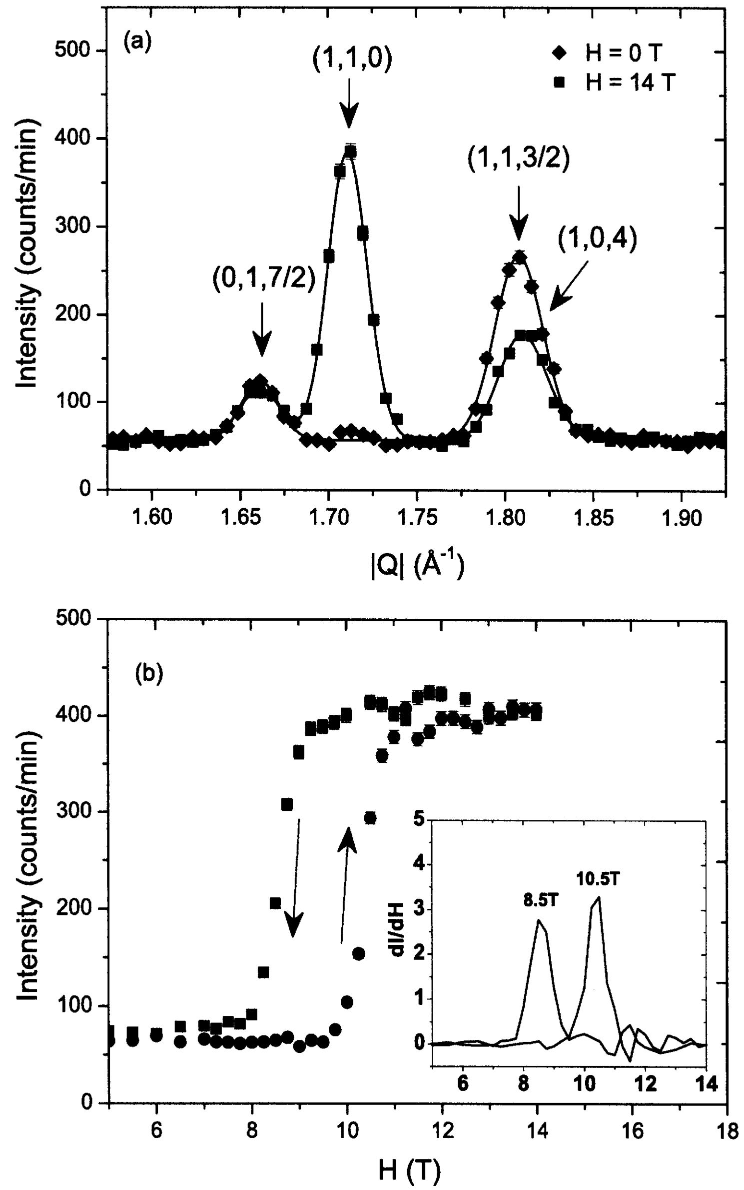

Figure 3-13: Elastic neutron scattering measurements were performed using the triple-axis spectrometer E1 at BENSC. (a) The 2θ scans at $T = 3$ K show two magnetic Bragg peaks in zero field (blue diamonds) at (1 1 3/2) and (0 1 7/2), and one magnetic peak in $H = 14$ T (red squares) at (1 1 0). The structural peak at (1 0 4) is also denoted by the green arrow. (b) The field dependence of the (1 1 0) peak intensity shows the transition to the spin-canting state at high field. The inset shows the derivative of the intensity.

sample of mass 5.4 g was placed inside the 11 T magnet. The sample was then cooled using a ^{4}He cryostat. The BENSC results are shown in Fig. 3-13.

At zero field and $T < T_N$, Ag jarosite is in the anti-aligned canting state, and the spins on successive kagomé plans are reversed as determined by Inami *et al.* [37]. Therefore, it takes six layers to form a magnetic unit cell instead of three layers that forms a structural unit cell as shown in Fig. 3-14. This causes a doubling of the unit cell along c-axis, indicated by magnetic Bragg peaks at a half integer value along L. For $H > H_c$, the system is in the aligned canting state, and the spins on alternating layers rotate 180° changing the spin arrangement from all-in to all-out and vice versa. Fig. 3-14 show such spin re-orientation on the second, forth and sixth kagomé planes. In this state, the magnetic unit cell contains only three kagomé planes, and is the same as the structural unit cell, indicated by the change of magnetic Bragg positions along L from a half integer value in the anti-aligned canting state ($H < H_c$) to a whole integer value in the aligned canting state ($H > H_c$). If the transition to the aligned canting state were caused by simply flipping the spins on the alternating layers, then the magnetic Bragg peaks would not change their positions.

In order to overcome the ferromagnetic interplane coupling and induce the 180° spin rotation, an applied field greater than the critical field is required along the crystallographic c-axis. Fig. 3-13(a) shows 2θ scans at zero and 14 T fields at $T = 3$ K. At zero field, there are two magnetic Bragg peaks at (0 1 7/2) and (1 1 3/2) in this range in $|Q|$. At $H = 14$ T ($H > H_c$), the peak at (1 1 3/2) disappears, while a new peak at (1 1 0) becomes apparent. The intensity at (0 1 7/2) does not change because the magnitude of the magnetic field component along the c-axis is less than the critical field at this temperature. At (1 1 0), the c-axis is along the vertical direction, hence along the direction of the applied field. On the other hand, at (1 1 3/2) and (0 1 7/2), the field is not along the c-axis. The angles between the field direction and the c-axis are 18° and 53° for (1 1 3/2) and (0 1 7/2), respectively. Therefore, the field component along the c-axis is reduced by about 5% at (1 1 3/2) and about 40% at (0 1 7/2). With the applied field of 14 T, the field strengths along the c-axis at (1 1 3/2) and (0 1 7/2) are 13.3 T and 8.4 T, respectively; the critical

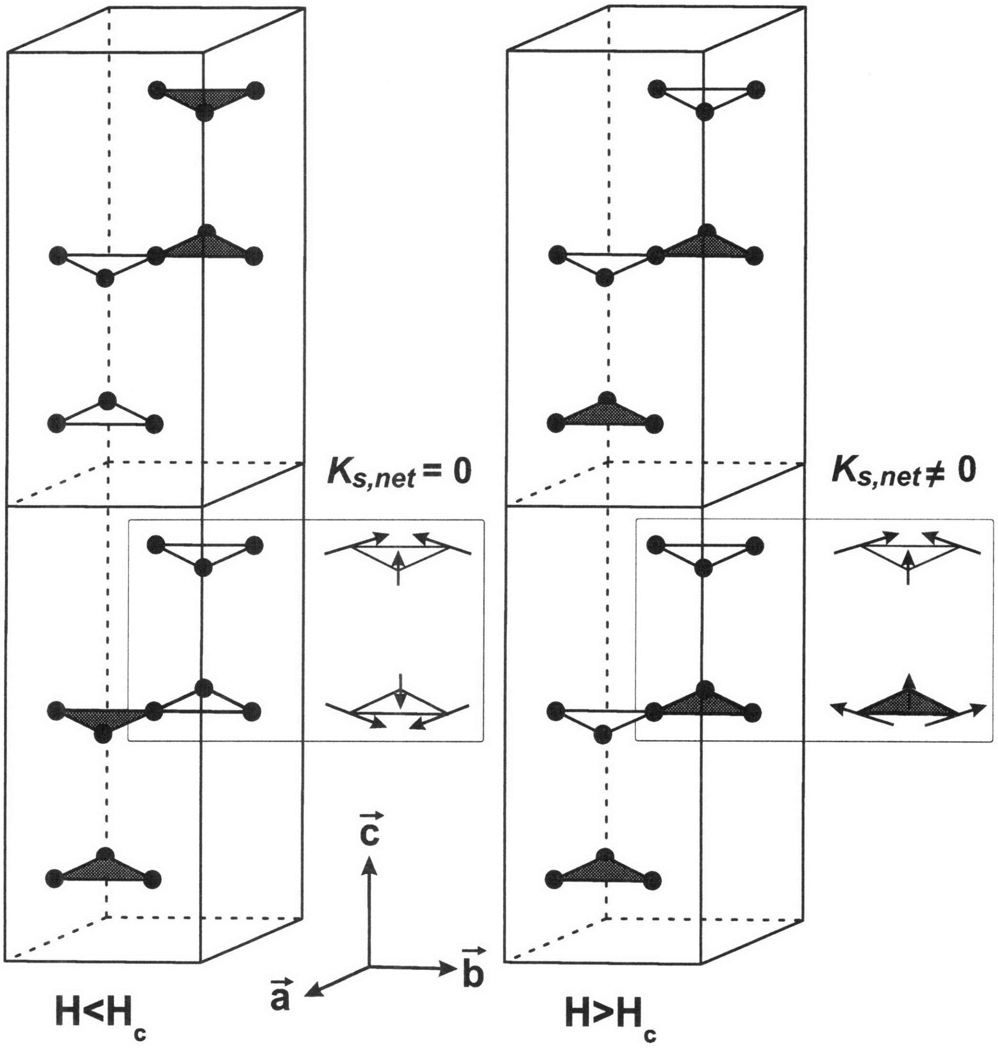

Figure 3-14: The diagram shows spin re-orientations on the second, forth and sixth layers (from the bottom) when $H > H_c$. The system makes the transition from the net $K_s = 0$ state to $K_s \neq 0$ state. White triangles indicate all-in arrangement, and blue triangles indicate all-out arrangement.

field at $T = 3$ K is about 10.5 T. Thus, Fig. 3-13(a) shows a decrease in intensity at (1 1 3/2), but no change in intensity at (0 1 7/2).

Therefore, the critical field measurements, which are indicated by the sudden change in the scattering intensity, were done at (1 1 0) where the applied field is perfectly along the crystallographic c-axis, and the change in the intensity is maximal. Fig. 3-13(b) shows the field dependence of the intensity I of the (1 1 0) peak at $T = 3$ K. The critical field is defined as the maximum of dI/dH as shown in the inset of Fig. 3-13(b). The critical field is 10.5 T (8.5 T) for the increasing (decreasing) field scan as shown by green triangles in Fig. 3-10(b); the results from the measurements at NCNR are shown by diamonds. The hysteresis shown in Fig. 3-13 is in agreement with the magnetization measurements. This result provides the first direct evidence of the 180° spin rotation at high field causing the canted moment to ferromagnetically align along c-axis in the kagomé lattice antiferromagnet.

$\mathbf{KFe_3(OH)_6(SO_4)_2}$

For K jarosite, since H_C is much larger than 14.5 T at base temperature, in order to see the transition to the canting state, we have done the measurement close to the ordering temperature ($T_N = 65$ K) between $50\text{ K} < T < 64$ K.

Elastic neutron scattering was used to study the transition of jarosite in an ordered state below $T_N = 65$ K in magnetic field. Similarly, one can induce the transition from the anti-aligned canting state to the aligned canting state by applying a magnetic field larger than a critical field, $H > H_C$, to overcome the inter-plane coupling [110]. For $H > H_C$, the canted spins rotates 180 degrees with respect to the low field state. This will cause a shift in position of magnetic Bragg peaks from (1,1,3/2) at low field to (1,1,0) at high field. In this experiment, we have verified this field-induced transition in K jarosite by measuring the intensity of the (1,1,0) peak in a single crystal sample as a function of magnetic field and temperature.

The elastic neutron scattering measurements were performed using the triple-axis spectrometer E1 at BENSC. The incident neutron wavelength is 2.425 Å ($\hbar\omega = 13.90$

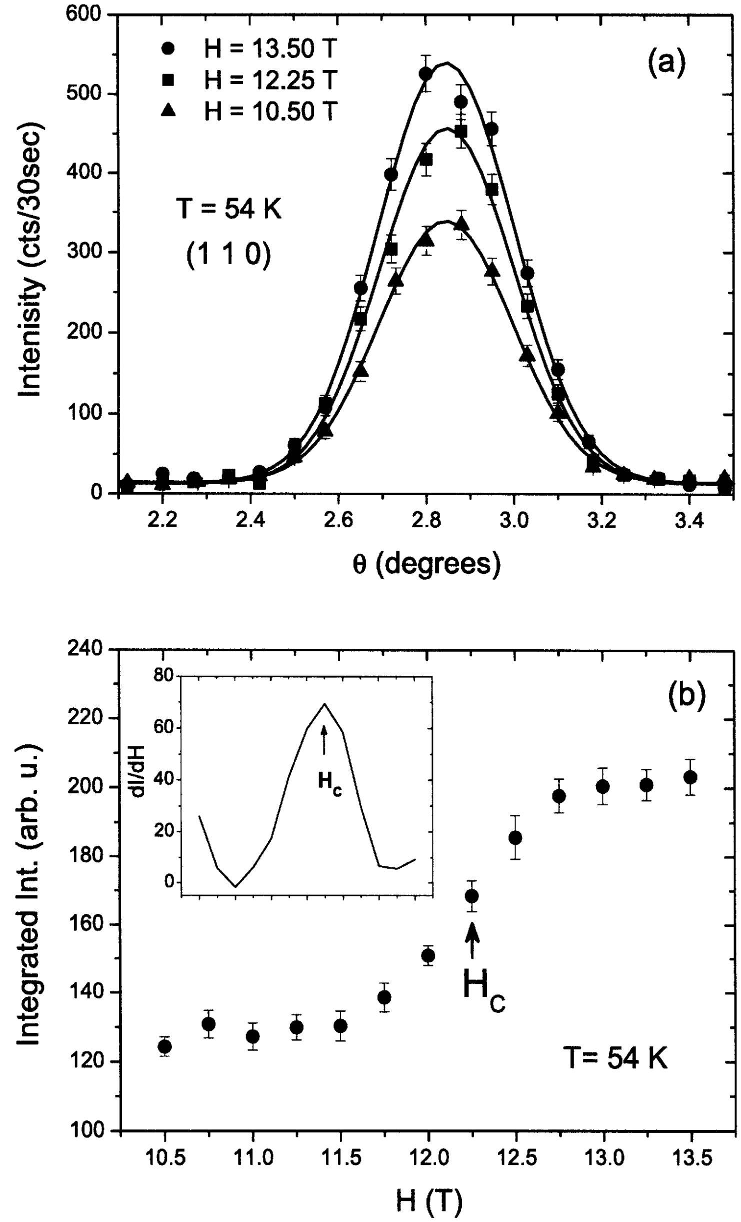

Figure 3-15: (a) Rocking scans around (110) at three different magnetic fields at $T = 54$ K. The magnetic field is applied along the c direction, perpendicular to the scattering plane. It shows the decrease in the integrated intensity of the (110) peak as the field crosses the critical field H_C. (b) The integrated intensity as a function of the magnetic fields measured at $T = 54$ K shows a sudden change in intensity at the critical field. The inset shows the derivative of the integrated intensity as a function of field. A peak of the derivative plot indicates the critical field.

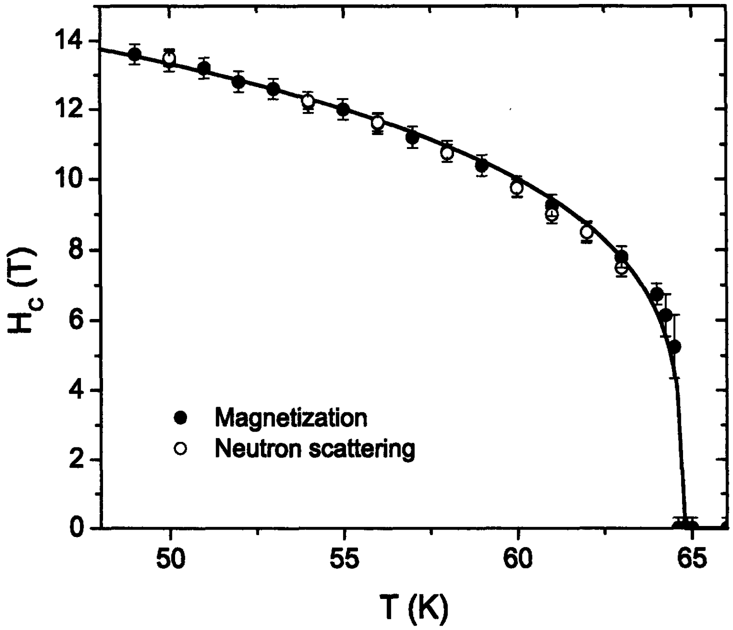

Figure 3-16: The critical fields are plotted as a function of temperature. The agreement between the magnetization results and the neutron scattering results are shown. The solid line is a power law fit with the exponent $\beta = 0.25$.

meV), and the horizontal collimations is $40' - 80' - 40' - 40'$. Pyrolytic graphite (PG) crystals were used to monochromate and analyze the incident and scattered neutron beam using (0 0 2) reflection. A PG filter was placed in the incident beam to reduce higher-order contamination. The single crystal sample (mass $\approx$ 20 mg) was put into the VM-1 magnet, whose highest field is 14.5 T. The sample was cooled using a ^{4}He cryostat. The sample is lined up in (HK0) zone. The intensity of (1 1 0) peak was measured as a function of field and temperature.

Fig. 3-15(a) shows θ scans at (1 1 0) peaks at three different fields at T = 54K. The data are fitted to Gaussians. Fig. 3-15(b) shows integrated intensity, which is extracted from the fit in Fig. 3-15(b), as a function of field at T = 54K. The inset shows the derivative of the intensity as a function of field. The maximum is defined to be the critical field. We have done the same measurements at several temperature. The results are shown in Fig. 3-16. The plot of the critical field as a function of temperature shows the agreement between the magnetization and neutron scattering measurements.

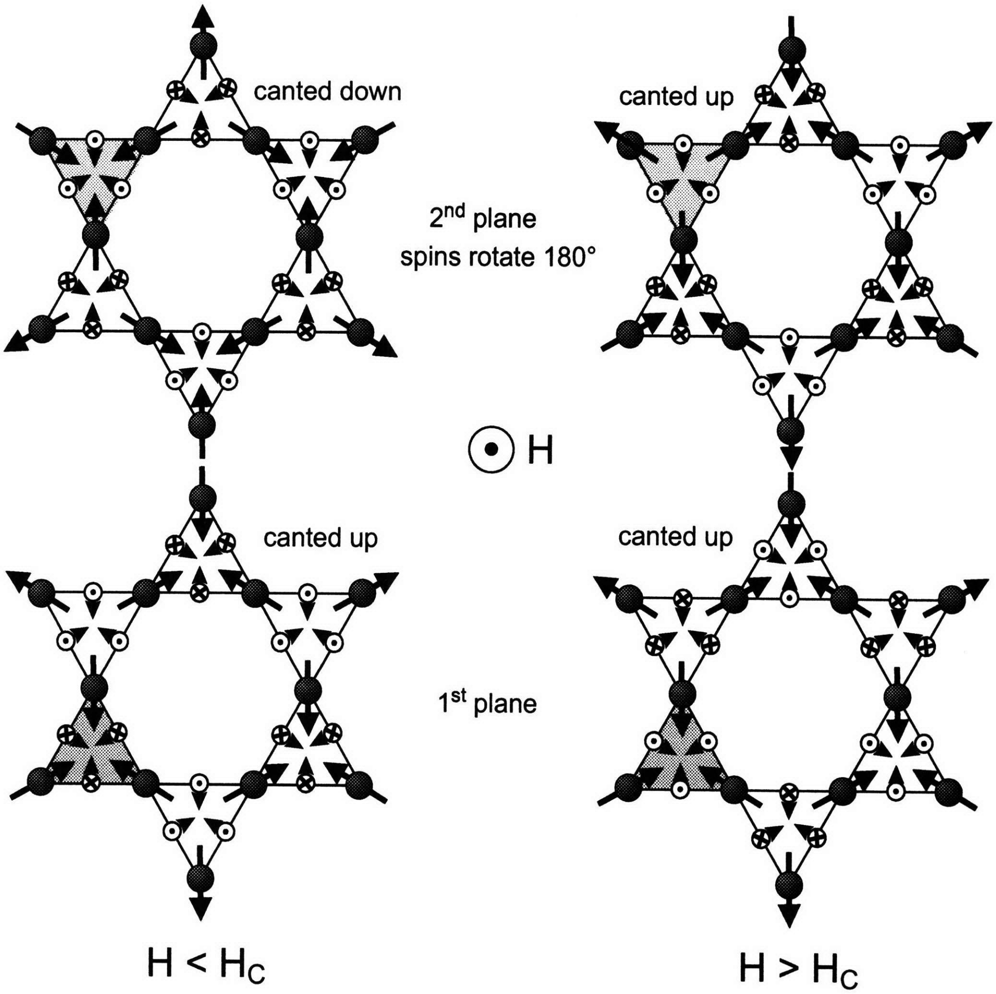

Figure 3-17: A diagram shows the DM vectors and the spin canting on two adjacent kagomé plane in the ground state assuming a ferromagnetic interplane coupling for $H < H_C$ (a) and $H > H_C$ (b), where H is along the $+z$ direction (out of the page). All spins on the second layer rotate 180° for $H > H_C$ causing the canted moment to change from down to up. Note that the second plane is shifted with respect to the first plane so that the two shaded triangles lie on top of each other.

3.4 $H - T$ phase diagram

The results of magnetization and neutron scattering measurements in high field are summarized in the phase diagram as a function of field and temperature shown in Fig. 3-18. At low temperature, both magnetization and neutron scattering measurements on Ag jarosite show hysteresis in magnetization and neutron scattering intensity measured at (1 1 0) as a function of field as shown in Fig. 3-10–3-11 and in Fig. 3-13, respectively. However, the hysteresis, which is indicative of first order transition, disappears at $T \approx 50$ K and $H \approx 8$ T. As discussed in the previous section, in the low-field phase, the canted moments on adjacent kagomé planes point in an opposite direction along the c-axis due to the weak ferromagnetic inter-layer coupling, resulting in a zero net magnetic moment along the c-direction. However, at the critical field H_C, the spins on every other kagomé planes rotates 180° due to the fact that the Zeeman energy overcomes the inter-layer coupling, resulting in the reversal of the canted moments along the c-direction, which can be observed by both magnetization and neutron scattering measurements. For magnetization measurements, the transition results in the abrupt increase of the magnetization at the critical field. For neutron scattering measurements, this transition causes the shift of the magnetic Bragg peak from half integer value to whole integer value in the L component. The scalar chirality of the ferromagnetic state is non-zero ($K_s \neq 0$), while that of the antiferromagnetic state vanishes ($K_s = 0$). These two states are depicted in Fig. 3-18.

One very important point is the fact that the transition between the $K_s = 0$ and $K_s \neq 0$ states (Fig. 3-9) appears to be first order at low temperature, and changes to second order for temperature above 50 K. This raises a question of whether the existence of a tricritical point in this system at the point indicated by the arrow in Fig. 3-18 is possible. In addition, this hysteresis was observed in Ag jarosite but not in K jarosite. We speculate that the hysteretic behavior also exists in the K jarosite samples. However, due to a very large critical field at low temperature, hysteresis cannot be detected using PPMS and the magnet at BENSC, both of which have the

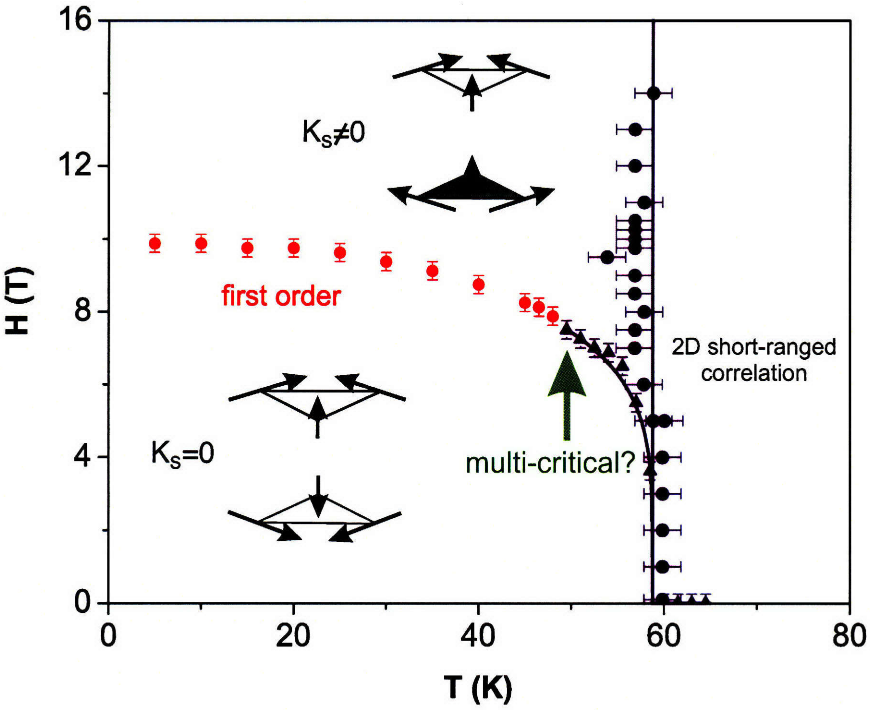

Figure 3-18: A phase diagram of Ag jarosite as functions of field and temperature. The arrow indicates the possibility of a multi-critical point.

maximal field of 14 T. Further investigation using a magnet with higher maximum field is needed to verify this speculation.

This phase diagram with the presence of the tricritical point at T_C **6** T_N is similar to that which has been observed in systems called metamagnets, such as $FeCl_2$ [181]. In these system, the coupling between spins within 2D layers is ferromagnetic, and that between the layers is antiferromagnetic, which is similar to jarosite, where the in-plane ferromagnetic canted moments prefer antiferromagnetic interlayer alignment in zero field. It is also similar to the phase diagram proposed for La_2CuO_4 [178, 182].

In contrast to the spin re-orientation transition, the 3D ordering transition at $T_N = 65$ K does not depend on magnetic field. This is verified by both magnetization and neutron scattering measurements at high field. Above the ordering temperature T_N, 2D short-range correlations are present, and persist up to $T \approx 120$ K. This region of the phase diagram was studied using quasi-elastic and inelastic neutron scattering techniques, whose data are presented in Chapter 5. Above $T = 120$ K, the spins are in a paramagnet state. However, strong influence from frustration increases the

Curie-Weiss temperature to a value higher than that predicted by Mean Field Theory. This effect of frustration has been captured by high-temperature expansion done by Harris *et al.* [35].

3.5 Summary

We have investigated the spin canting due to the DM interaction in jarosite using the magnetization and neutron scattering measurements. From the observed critical field and canted moment obtained from our magnetization measurements, we are able to calculate the canting angle η, the DM parameters $|D_y|$ and D_z, and the interplane coupling constant J_c. These values are consistent with the inelastic neutron scattering results, which will be discussed in the next chapter[1]. Our elastic neutron scattering measurements in high magnetic field provide the first direct evidence of the 180° spin rotation that gives rise to the magnetic transition at high field in the kagomé lattice antiferromagnet.

The in-plane component of the DM interaction forces the spins on a triangle to cant out of the kagomé planes to form an "umbrella" structure of ferromagnetically aligned moments within the layers. Fig. 3-17 shows the canting direction of the spins and the in-plane component of the DM vector on each kagomé plane. The direction of the canted moment is set by the direction of the in-plane component of the DM vector and the in-plane orientation of the spins as discussed previously. However, in zero field field, the weak ferromagnetic interplane coupling forces the spins on the adjacent plane to align in such an arrangement that the canted moments on any two adjacent layers cancel out each other. In high field, the Zeeman energy overcomes the ferromagnetic interplane coupling causing the spins on the alternating layers to rotate 180°. This 180° spin rotation flips the direction of the canted moment on the alternating layers causing the sudden increase in the magnetization at the critical field as shown in Fig. 3-10(a) and 3-11(a). This field-induced spin-canting transition

---

[1] J_c is very small; hence it cannot be measured given the resolution of our neutron scattering measurements.

corresponds to the non-trivial change in the spin-texture. In particular, the transition yields a net, non-zero value for the scalar chirality.

The 180° spin rotation also causes the change in the in-plane orientation of the spin from all-in to all-out arrangements and vice versa. This change in the in-plane spin order can be detected by neutron scattering. The observation of the change of magnetic Bragg positions from a half integer value in L for $H < H_c$ to a whole integer value for $H > H_C$ verifies the spin-re-orientation transition at the critical field. Furthermore, the temperature dependence of the critical field is in agreement with the results from the magnetization measurements. The phase diagram shows a possibility of a multi-critical point in this system. Further theoretical studies are needed to verify and explain this finding.

Chapter 4

Spin-wave excitations

As discussed in Chapter 1, one of the hallmarks of highly frustrated systems is the presence of "zero energy modes" that result from the highly degenerate, but connected, ground-state manifold [33, 40, 41]. For the kagomé lattice Heisenberg model, the only constraint for the ground state is that the spins on each triangle be oriented 120° relative to each other. A "zero energy mode" for the kagomé lattice is depicted in Fig. 1-6. The small loops at the tips of the spins illustrate rotations of two of the spin sublattices about the axis defined by the third spin sublattice. In the $q = 0$ structure, these spins, forming a chain, can collectively rotate around the loop paths with no change in energy (the 120° angles on each triangle are maintained). Furthermore, the spins on different parallel chains can be excited independently. Hence, this type of excitation costs no energy and is non-dispersive [35, 40, 41, 38]. This mode has not been directly observed previously, and, since it occurs at zero energy, it is difficult to measure with most experimental techniques. Here we report the first observation of such a mode in iron jarosite which is lifted to a finite energy due to the presence of spin anisotropy resulting from the antisymmetric DM interaction [112, 117].

In this chapter, we discuss the spin-wave excitations in the kagomé lattice. The spin wave spectrum of the $S = 5/2$ kagomé lattice antiferromagnet $KFe_3(OH)_6(SO_4)_2$ was measured using high-resolution inelastic neutron scattering. We directly observed a flat mode which corresponds to a lifted "zero energy mode," verifying a fundamental prediction for the kagomé lattice. A simple Heisenberg spin Hamiltonian provides an excellent fit to our spin wave data. The antisymmetric Dzyaloshinskii-Moriya interaction is the primary source of anisotropy and explains the low temperature magnetization and spin structure. This chapter is organized as follows. In Section 4.1, a model spin Hamiltonian and spin-wave spectrum in the kagomé lattice are reviewed. Section 4.2 describes experimental set-ups. In Section 4.3, the results of neutron scattering experiments are presented. Section 4.4 contains analysis of the spin wave results. We will end this chapter with the summary in Section 4.5.

4.1 Spin Hamiltonian and spin-wave spectrum

Detailed calculations of spin wave spectrum in the kagomé lattice antiferromagnet with the $q = 0$ spin structure can be found in Ref. [35, 38, 117]. The spin-wave calculations reproduced in this chapter are based on Ref. [117]. The readers should turn to the paper by Yildirim and Harris [117] for comprehensive and detailed discussions of the spin-wave spectrum in the kagomé lattice antiferromagnet. The more detailed calculations are also reproduced in Appendix A. In this section, we only represent their results that are used to fit our spin-wave data. As discussed in Chapter 1, to first approximation, the generic form of the spin Hamiltonian for the kagomé lattice antiferromagnet is given by:

$$\begin{aligned}\mathcal{H} &= \sum_{nn}\Big[J_1\,\mathbf{S}_i\cdot\mathbf{S}_j + \mathbf{D}_{ij}\cdot\mathbf{S}_i\times\mathbf{S}_j\Big] + \sum_{nnn} J_2\,\mathbf{S}_k\cdot\mathbf{S}_l \\ &\quad + D\sum_i (S_i^{y'})^2 - E\sum_i[(S_i^{z'})^2 - (S_i^{x'})^2] \end{aligned} \tag{4.1}$$

where Σ_{nn} (Σ_{nnn}) indicates summation over pairs of nearest neighbors (next nearest neighbors), $\mathbf{D}_{ij} = [0, D_y(i,j), D_z(i,j)]$ is the DM vector for bond $i - j$ as shown in Fig. 3-1, and the single-ion anisotropy terms (D and E) are those used by Nishiyama *et al.* [38] in their treatment of the spin wave spectrum in jarosites. Here the primed spin components refer to the local axis associated with the rotated oxygen octahedra (see Ref. [38] for details). We ignore the weak interplane coupling, which is several hundred times smaller than J_1 [110], as discussed in the previous chapter.

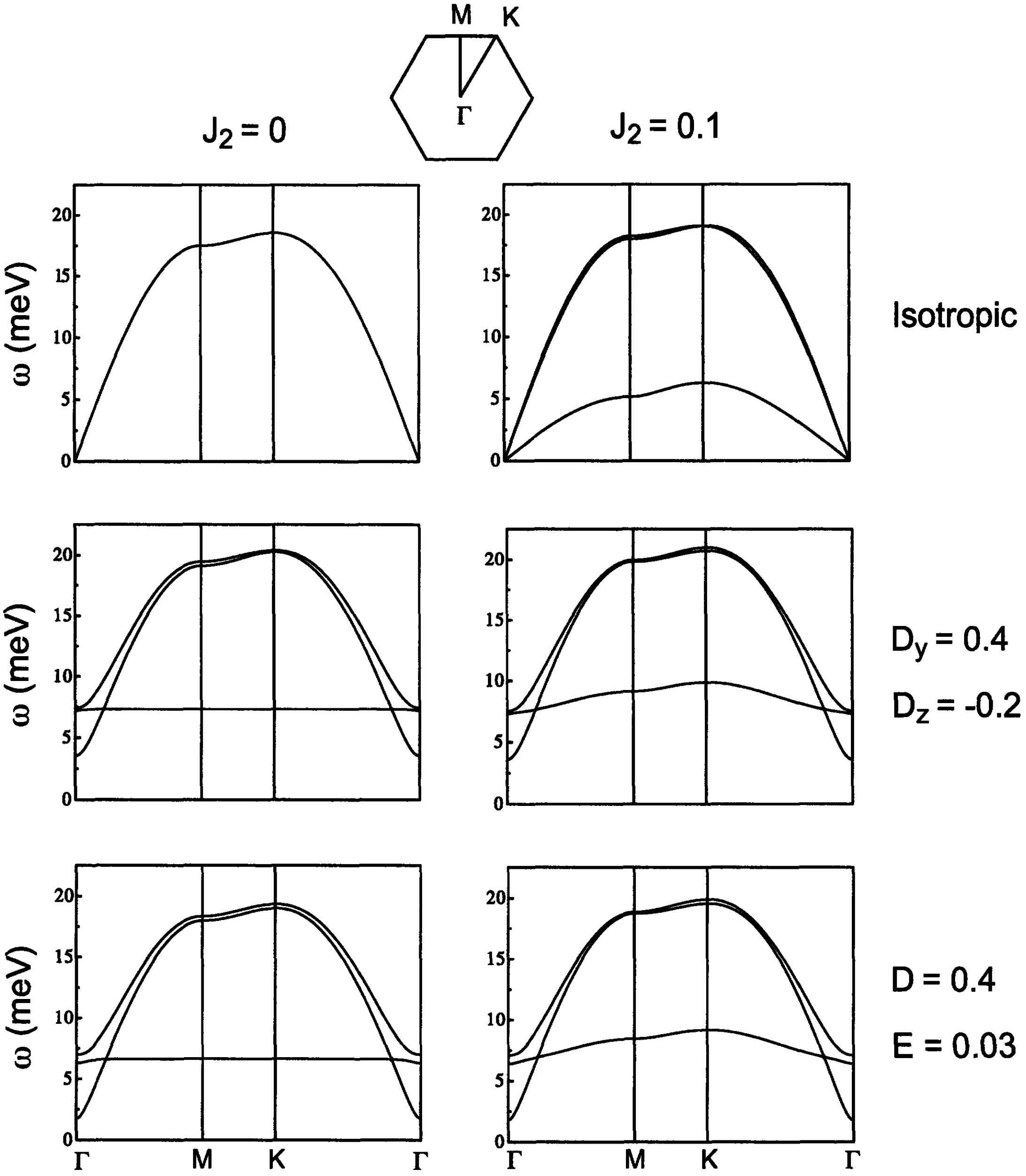

Figure 4-1: Spin-wave spectra for the kagomé lattice antiferromagnet. The first column shows the spectra with a zero value of the next-nearest neighbor interaction. The second column shows the spectra with a non-zero value of the next-nearest neighbor interaction. The first, second and third rows indicate no anisotropic term, the DM interaction, and the single-ion anisotropy, respectively. All spin Hamiltonian parameters are given in a unit of meV.

This spin Hamiltonian can be written in terms of boson operators, and the wavevector dependent spin-wave dynamic matrix $\mathbf{M(q)}$ is determined. The spin-wave energies are the eigenvalues of this matrix. $\mathbf{M(q)}$ can be written as:

$$\mathbf{M(q)} = \begin{bmatrix} \mathbf{A(q)} & -\mathbf{B(q)} \\ \mathbf{B(q)}^* & -\mathbf{A(q)}^* \end{bmatrix}, \tag{4.2}$$

where $\mathbf{A(q)}$ and $\mathbf{B(q)}$ are 3×3 matrices. For simplicity, we will assume that the next-nearest neighbor interaction J_2 is isotropic, and ignore all further neighbor interactions. Then, the matrix $\mathbf{A(q)}$ can be written as:

$$\mathbf{A(q)} = \begin{array}{|c|c|c|} \hline A_0 + 2J_2 & \begin{array}{c} [A_1 - i\alpha]\,\gamma_{12}^{(1)}(\mathbf{q}) \\ +\frac{1}{2}J_2\gamma_{12}^{(2)}(\mathbf{q}) \end{array} & \begin{array}{c} [A_1 + i\alpha]\,\gamma_{13}^{(1)}(\mathbf{q}) \\ +\frac{1}{2}J_2\gamma_{13}^{(2)}(\mathbf{q}) \end{array} \\ \hline \begin{array}{c} [A_1 + i\alpha]\,\gamma_{12}^{(1)}(\mathbf{q}) \\ +\frac{1}{2}J_2\gamma_{12}^{(2)}(\mathbf{q}) \end{array} & A_0 + 2J_2 & \begin{array}{c} [A_1 - i\alpha]\,\gamma_{23}^{(1)}(\mathbf{q}) \\ +\frac{1}{2}J_2\gamma_{23}^{(2)}(\mathbf{q}) \end{array} \\ \hline \begin{array}{c} [A_1 - i\alpha]\,\gamma_{13}^{(1)}(\mathbf{q}) \\ +\frac{1}{2}J_2\gamma_{13}^{(2)}(\mathbf{q}) \end{array} & \begin{array}{c} [A_1 + i\alpha]\,\gamma_{23}^{(1)}(\mathbf{q}) \\ +\frac{1}{2}J_2\gamma_{23}^{(2)}(\mathbf{q}) \end{array} & A_0 + 2J_2 \\ \hline \end{array}, \tag{4.3}$$

and the matrix $\mathbf{B(q)}$ can be written as:

$$\mathbf{B(q)} = \begin{array}{|c|c|c|} \hline B_0 & \begin{array}{c} B_1\gamma_{12}^{(1)}(\mathbf{q}) \\ -\frac{3}{2}J_2\gamma_{12}^{(2)}(\mathbf{q}) \end{array} & \begin{array}{c} B_1\gamma_{13}^{(1)}(\mathbf{q}) \\ -\frac{3}{2}J_2\gamma_{13}^{(2)}(\mathbf{q}) \end{array} \\ \hline \begin{array}{c} B_1\gamma_{12}^{(1)}(\mathbf{q}) \\ -\frac{3}{2}J_2\gamma_{12}^{(2)}(\mathbf{q}) \end{array} & A_0 + 2J_2 & \begin{array}{c} B_1\gamma_{23}^{(1)}(\mathbf{q}) \\ -\frac{3}{2}J_2\gamma_{23}^{(2)}(\mathbf{q}) \end{array} \\ \hline \begin{array}{c} B_1\gamma_{13}^{(1)}(\mathbf{q}) \\ -\frac{3}{2}J_2\gamma_{13}^{(2)}(\mathbf{q}) \end{array} & \begin{array}{c} B_1\gamma_{23}^{(1)}(\mathbf{q}) \\ -\frac{3}{2}J_2\gamma_{23}^{(2)}(\mathbf{q}) \end{array} & A_0 + 2J_2 \\ \hline \end{array}. \tag{4.4}$$

$\gamma_{ll'}^{(n)}(\mathbf{q})$ are the normalized form factors for the n^{th} shell of neighbors, where $n = 1$

and 2 for the nearest neighbors and next-nearest neighbors, respectively.

$$\begin{aligned}
\gamma_{12}^{(1)}(\mathbf{q}) &= \cos(aq_x/2), \\
\gamma_{13}^{(1)}(\mathbf{q}) &= \cos\left[(a(q_x+\sqrt{3}q_y)/4\right], \\
\gamma_{23}^{(1)}(\mathbf{q}) &= \cos\left[(a(q_x-\sqrt{3}q_y)/4\right], \\
\gamma_{12}^{(2)}(\mathbf{q}) &= \cos(aq_y\sqrt{3}/2), \\
\gamma_{13}^{(2)}(\mathbf{q}) &= \cos\left[(a(3q_x-\sqrt{3}q_y)/4\right], \\
\gamma_{23}^{(2)}(\mathbf{q}) &= \cos\left[(a(3q_x+\sqrt{3}q_y)/4\right],
\end{aligned} \tag{4.5}$$

where a is an in-plane lattice constant. The matrix elements are given by:

$$\begin{aligned}
A_0 &= 2J_1+\Delta-2\sqrt{3}D_z+\frac{2}{3J_1}\left[3D_y^2+2C_{yz}^2\right], \\
A_1 &= \frac{1}{2}J_1+\frac{\sqrt{3}}{2}D_z+\frac{1}{6J_1}\left[3D_y^2-C_{yz}^2\right], \\
B_0 &= C_{xx}-C_{yy}-\frac{2C_{yz}^2}{3J_1}, \\
B_1 &= -\frac{3}{2}J_1+\frac{\sqrt{3}}{2}D_z+\frac{C_{yz}^2-3D_y^2}{6J_1}, \\
\alpha &= \frac{1}{\sqrt{3}}C_{yz}+\frac{5\sqrt{3}D_yD_z}{3J_1},
\end{aligned} \tag{4.6}$$

where $\Delta = C_{xx}+C_{yy}-2C_{zz}$. The single-ion anisotropy constant D and E is related to the generic single-ion matrix $\mathbf{C}$, whose matrix elements are defined in the local frame by (see Appendix A):

$$\begin{aligned}
C_{xx} &= E, \\
C_{xy} &= C_{xz}=C_{yx}=C_{zx}=0, \\
C_{yy} &= C(\cos\theta_0)^2-E(\sin\theta_0)^2, \\
C_{yz} &= C_{zy}=(D+E)\sin\theta_0\cos\theta_0, \\
C_{zz} &= D(\sin\theta_0)^2-E(\cos\theta_0)^2,
\end{aligned} \tag{4.7}$$

where θ_0 is the canting angle of the FeO_6 octahedral environment ($\theta_0 = 20°$ [37]). The eigenvalues of the matrix $\mathbf{M(q)}$ come in pairs with opposite signs. The spin-wave energies are taken to be those with the positive sign. The eigenvalues are calculated using a computer program written in IDL. The spin-wave energies are then fit to the results from the neutron scattering measurements to extract the spin Hamiltonian parameters.

Fig. 4-1 shows examples of spin-wave spectra in the kagomé antiferromagnet. We begin by considering the first column, where the next-nearest-neighbor interaction is zero. In the first row, the anisotropic interactions are absent. The zero energy mode is truly flat and vanishes for all wavevectors. Furthermore, the two dispersed modes are degenerate. In the second row, the DM interaction is present but the single-ion anisotropy is turned off. The zero energy mode is lifted to a finite energy, but is still flat. In addition, the two higher energy modes are no longer degenerate. In the third row, the DM interaction is turned off but the single-ion anisotropy is turned on. Similarly, the zero energy mode is flat, and lifted to a finite energy, and the two dispersive modes become non-degenerate. The presence of the anisotropic terms also result in the presence of three spin gaps at $q = 0$. The second column shows the spin-wave spectra when the next-nearest-neighbor interaction is non-zero. For all three cases, the next-nearest-neighbor interaction causes the zero energy mode to become dispersive. From this spin-wave analysis, one can see that the ground state degeneracy, namely the zero energy mode, can be lifted by the next-nearest-neighbor interaction, DM interaction, and single-ion anisotropy, which lead to the magnetically ordered state.

There are three types of low energy excitations of the spins on a triangular plaquette [183, 184], which correspond to the rotational fluctuations around three axes as shown in Fig. 4-2 [38]. The first axis is along one of the spins. The second axis is parallel to one side of the triangle, and bisects the triangle. The third axis is perpendicular to the plane. The fluctuations labeled as ω_1 correspond to the non-dispersive zero energy mode. The energy gap of this mode is a result of both easy-plane and Ising-type anisotropic interactions. Therefore, the gap energy $\hbar\omega_1$ depends on both D_y and D_z for the DM interaction, and on D and E for the single-ion anisotropy.

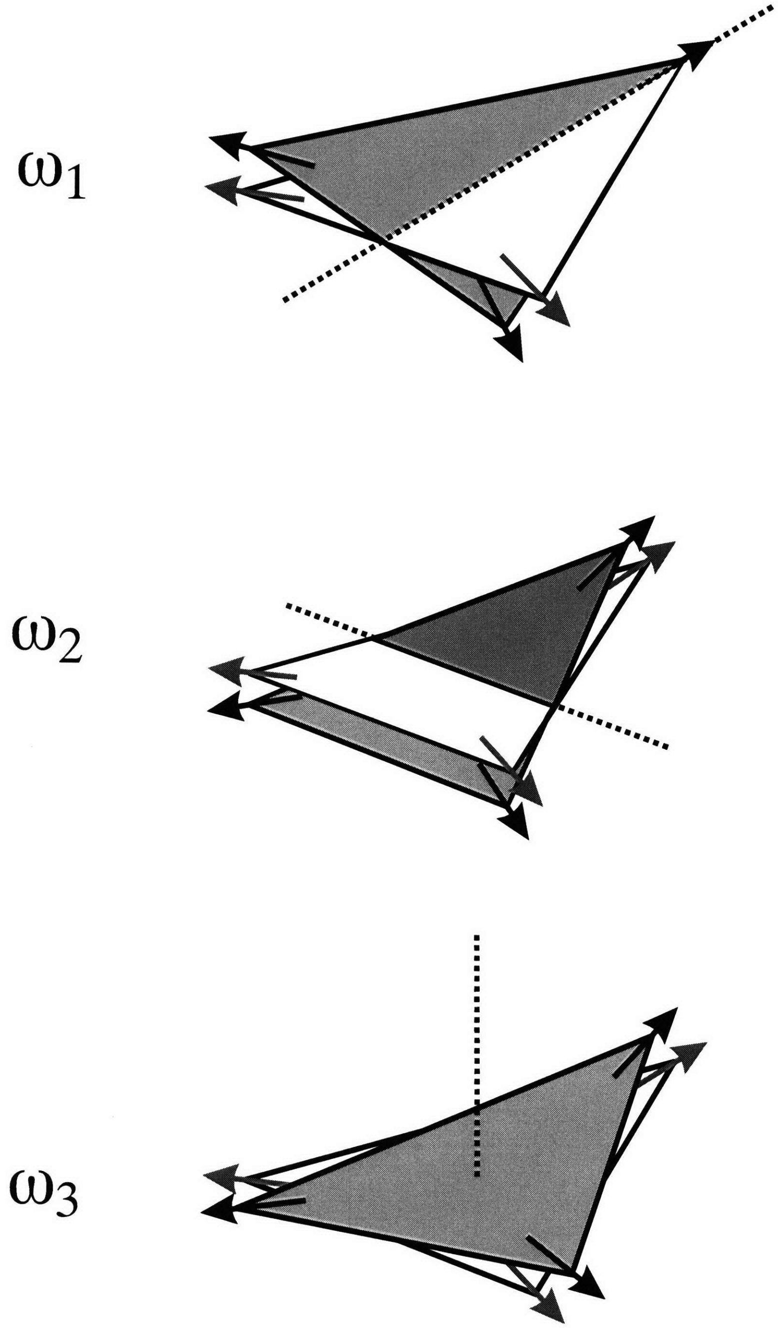

Figure 4-2: Low energy excitations of the spins on a triangular plaquette. The dotted lines are the axes of the rotational fluctuations of each mode.

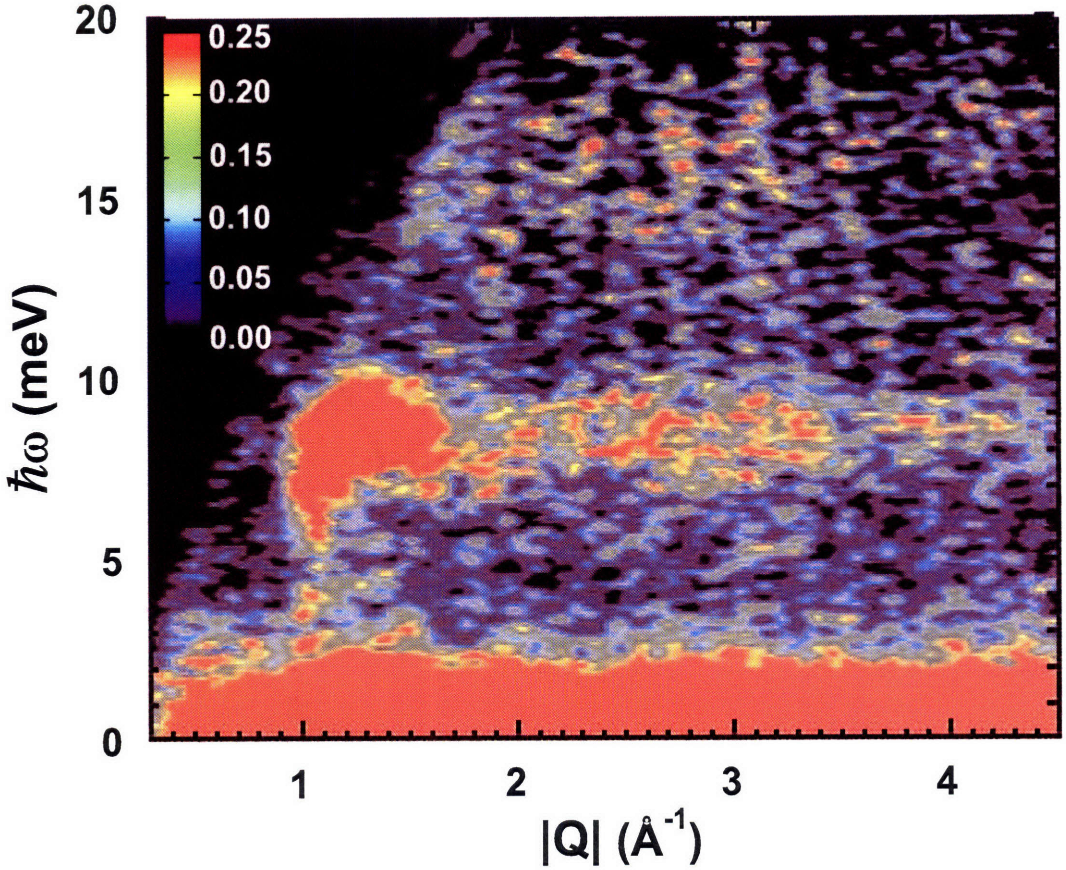

Figure 4-3: Intensity contour map of the inelastic scattering spectrum at $T = 4$ K of a powder sample measured using the time-of-flight DCS spectrometer with an incident neutron wavelength of 1.8 Å.

The flow energy excitations labeled as ω_2 is also a result of both easy-plane and Ising-type anisotropic interactions; hence $\hbar\omega_2$ depends on both D_y and D_z, or on D and E. On the other hand, $\hbar\omega_3$ only depends on in-plane Ising-type anisotropy (D_y or E) since the fluctuations are confined only within the plane. In the absence of spin anisotropies, ω_2 and ω_3 are degenerate.

4.2 Spin-wave measurements using unpolarized beam

We first studied the magnetic excitations using a deuterated powder sample (mass = 4.92 g) on the Disk Chopper Spectrometer (DCS) and Filter-Analyzer Spectrometer (FANS) at the NIST Center for Neutron Research, as shown in Fig. 4-3 and 4-4. The time-of-flight DCS spectrometer with an incident neutron wavelength of 1.8 Åwas used to measure an intensity contour map of the inelastic scattering at $T = 4$ K of a powder sample. Inelastic neutron scattering was measured on a powder sample using the FANS spectrometer with collimations $40' - 20'$. The data show the difference between the intensities above ($T = 70$ K) and below ($T = 13$ K) the Néel temperature $T_N = 65$ K and represent a measure of the spin wave density of states. For this sample, elemental analysis of the chemical composition and neutron powder refinement indicated that the K site occupancy was 100(1)%, the Fe site occupancy was > 96%, and the level of deuteration was 100(1)%.

The spin wave dispersions were obtained from inelastic neutron scattering measurements on a non-deuterated single crystal sample (composed of four co-aligned crystals of total mass 101 mg) grown using a hydrothermal method by Grohol *et al.* [89, 110]. High-resolution measurements were performed using the triple-axis spectrometer HB1 at the High Flux Isotope Reactor at Oak Ridge National Laboratory with the sample aligned in the (HK0) and (HHL) zones, and with the final energy fixed at either 13.6 meV or 14.7 meV. Vertically focused pyrolytic graphite (PG) crystals were used to monochromate and analyze the incident and scattered neutron beams using the (0 0 2) reflection. Horizontal collimations of $48' - 60' - \text{sample} - 40' - 120'$ were employed. However, due to the small sample, the effective horizontal collimations of $48' - 18' - \text{sample} - 25' - 120'$ were used to calculate the resolution function, which gave better agreement with the data. PG filters were placed in the scattered beam to reduce higher-order contamination. The energy and momentum resolutions of 1 meV and 0.2 Å^{-1} are achieved, respectively. The sample was cooled to $T = 10$ K using a closed cycle ^{4}He cryostat.

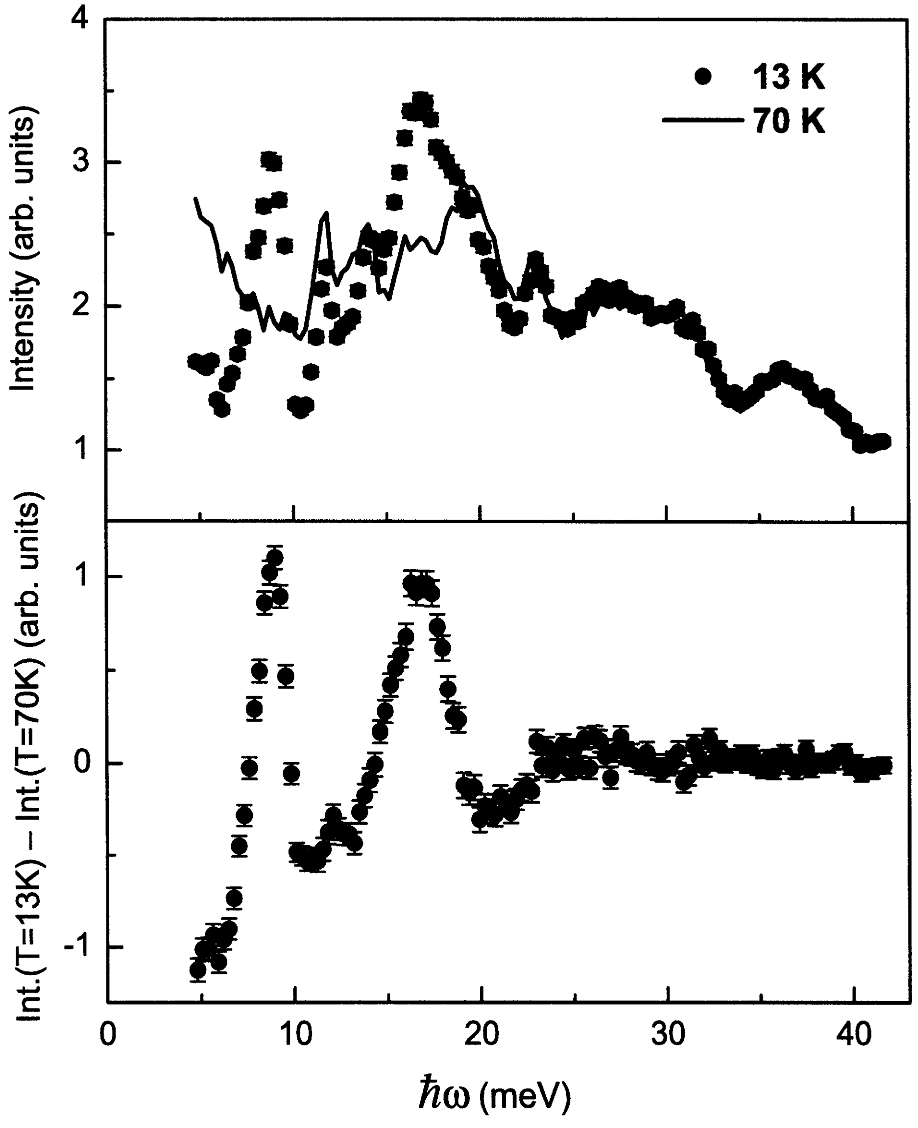

Figure 4-4: Inelastic neutron scattering measured on a powder sample using the FANS (BT4) spectrometer with collimations $40' - 20'$. The data show the difference between the intensities above ($T = 70$ K) and below ($T = 13$ K) the Néel temperature $T_N = 65$ K and are a measure of the spin wave density of states.

4.2.1 Results and discussion

Fig. 4-4 shows a difference plot of the intensity as a function of neutron energy loss measured above ($T = 70$ K) and below ($T = 13$ K) the Néel temperature. The measurements were carried out using the FANS spectrometer. This difference plot removes most of the phonon contributions to the spectrum, yielding the spin wave density of states. Despite the powder average, the spectrum shows one sharp feature at $\hbar\omega_0 \sim 8$ meV and a second broad peak at about $2\omega_0$. Both features appear as excitation bands over a wide range of $|\mathbf{Q}|$, as shown in Fig. 4-3, which shows the intensity contour map of the inelastic scattering spectrum at $T = 4$ K of a powder sample measured using the time-of-flight DCS spectrometer. This behavior is quite similar to that observed in strongly frustrated spinel systems where the excitation at ω_0 has been described as a local resonance [185]. At first sight, it is tempting to identify the features observed in the excitation spectrum as one- and two-magnon scattering since strong multi-magnon scattering might be expected due to the strong frustration and cubic terms in the spin-Hamiltonian resulting from the non-collinear spin structure. However, as shown in the following text, our single crystal measurements provide much greater detail and demonstrate that these are regular spin wave modes, albeit with unusual dispersive behavior.

The results from our high-resolution neutron scattering measurements on the single crystals give a complete picture of the magnetic excitations. A series of energy scans (at constant $\mathbf{Q}$) and $\mathbf{Q}$-scans (at constant energy) were performed, and a few representative scans are shown in Fig. 4-5, 4-6, and 4-7. The observed peaks were initially fit with narrow Gaussians convoluted with the experimental resolution function. Subsequent fits were performed taking into account the empirical dispersion of the excitations. Fig. 4-8 shows the empirical dispersion used in our fitting routine, where J_2 is ignored, resulting in a non-dispersive zero energy mode. For comparison, the best fit to our spin wave data is shown in the bottom panel. The peaks are resolution-limited, and the line-shapes are simply governed by the convolution with the instrumental resolution. A summary of all of the peak positions and intensities is

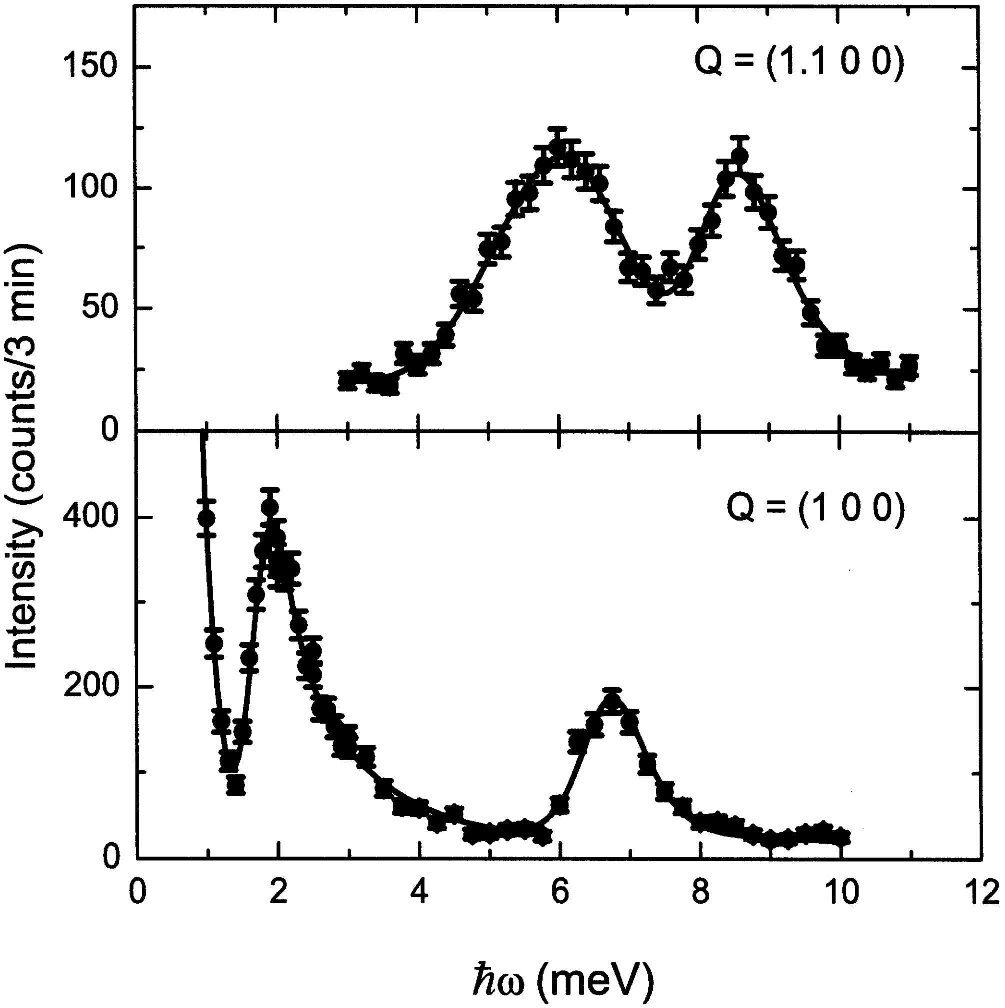

Figure 4-5: Energy scans at $\mathbf{Q}$ = (1 0 0) and (1.1 0 0) at T = 10 K. The solid lines show the fits to the spin wave dispersion relation described in the text, convoluted with the instrumental resolution function.

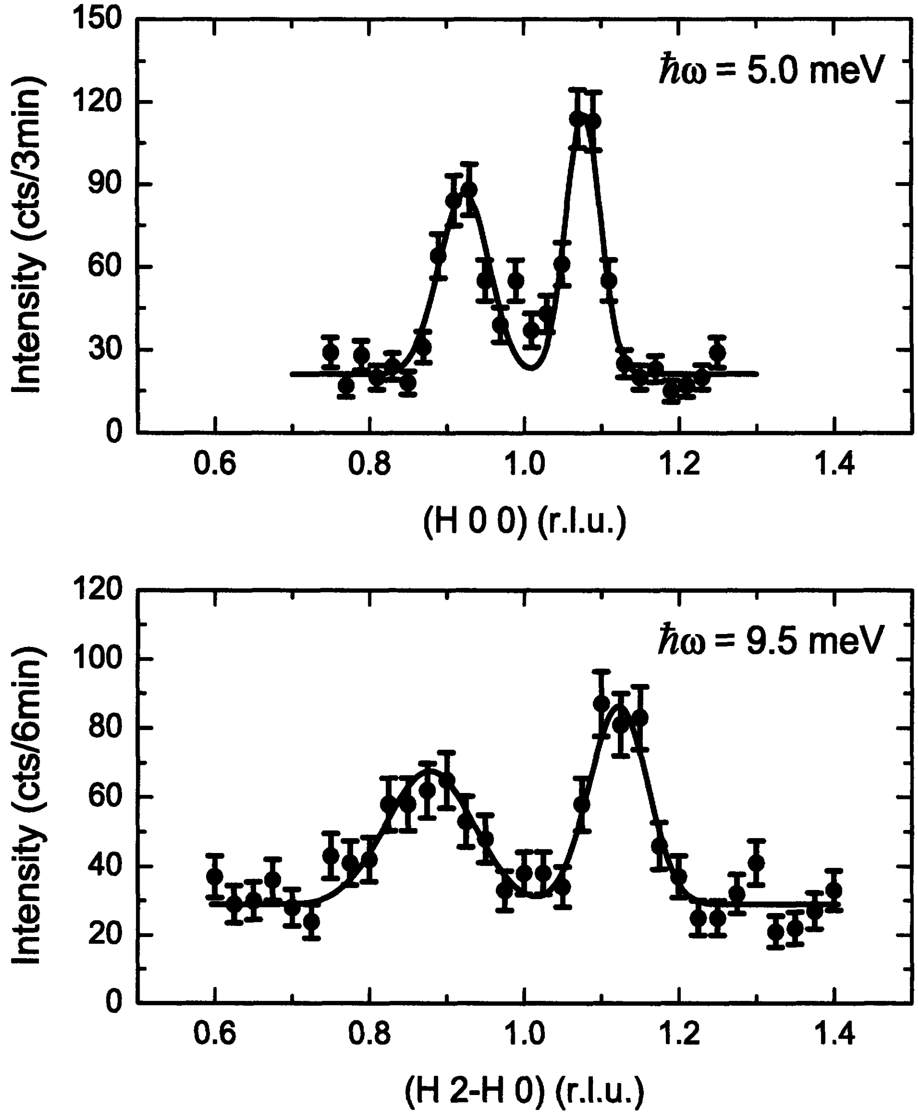

Figure 4-6: Longitudinal and transverse Q-scans at $\hbar\omega = 5$ meV and 9.5 meV, respectively. The solid lines show the fits to the spin wave dispersion relation described in the text, convoluted with the instrumental resolution function.

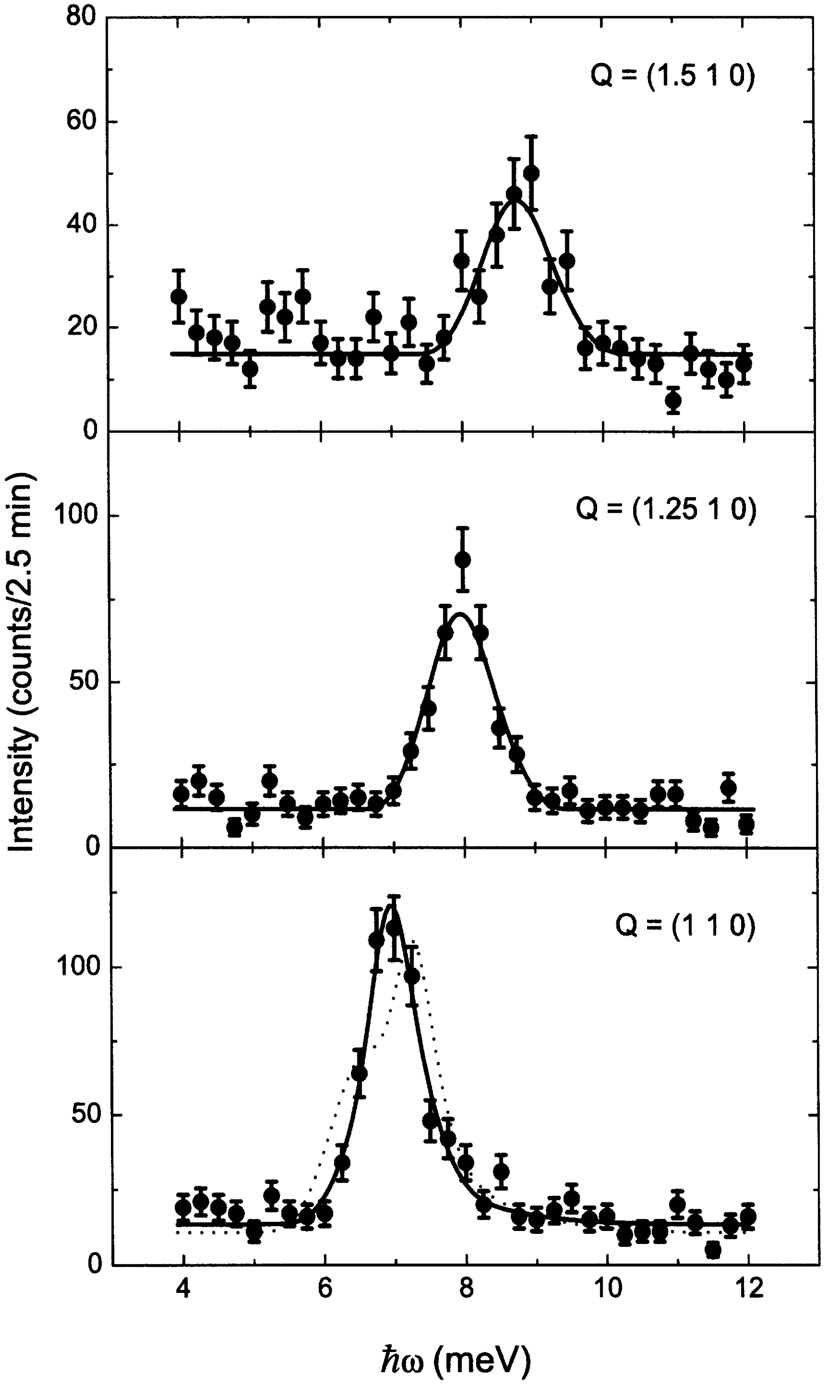

Figure 4-7: Energy scans around the zero energy mode at $\mathbf{Q} = (1\ 1\ 0)$, $(1.25\ 1\ 0)$, and $(1.5\ 1\ 0)$. The solid lines show the fits to the spin wave dispersion relation described in the text, convoluted with the instrumental resolution function. In the lower panel, the CF prediction is shown by the dotted line and the DM prediction by the solid line.

shown in Fig. 4-9. The error bars plotted in Figs. 4-9 correspond to three times the statistical error or one-tenth of the instrumental resolution, whichever is larger. The most striking feature of the data is the relatively flat mode near 7 meV which barely disperses, even out to the zone boundary.

The energy scans in Fig. 4-5 at the magnetic Brillouin zone centered at (1 0 0) reveal two spin gaps, one at 1.8(1) meV (which is non-degenerate), and the other at 6.7(1) meV (which is two-fold degenerate within the experimental resolution). At $\mathbf{Q} = (1.1\ 0\ 0)$, the lower-energy mode disperses to higher energy and merges with the flat mode located around 7 meV. The other upper-energy mode disperses strongly, moving to a high zone boundary energy of about 19 meV. Fig. 4-7 shows constant-Q scans of the flat mode within a Brillouin zone centered at (1 1 0). This excitation barely disperses, starting from about 7 meV at the zone center and reaching about 9 meV at the zone boundary. We identify this flat mode as the "zero energy mode" of the kagomé lattice which is lifted in energy for reasons discussed below.

4.2.2 Analysis of the spin-wave modes

We fit the observed spin wave dispersions using the generic Hamiltonian in Eq. 4.1. We may describe the spin wave data in terms of two simple spin models. In the first of these, which we call the DM model, we neglect the single ion anisotropy, so that the only nonzero parameters are J_1, J_2, D_y, and D_z. In the second model, which we call the CF (crystal field) model, all the anisotropy is attributed to the single-ion crystal field, so that the only nonzero parameters are J_1, J_2, D, and E. In both cases, J_1 is the dominant interaction. The numerical results obtained from these two models are plotted as the lines in Fig. 4-9, and the approximate analytic expressions for the spin gaps at the Γ point are given in Table 4.2.

To account for the observed umbrella spin structure, we considered the effect of spin-canting on the spin wave energies. We find that the splitting of the mode energies at the high symmetry points is particularly sensitive to the magnitude of the spin canting angle out of the kagomé plane. The best χ^2-fit to the DM model is depicted by the lines in Fig. 4-9 and describes the data very well. We reproduce

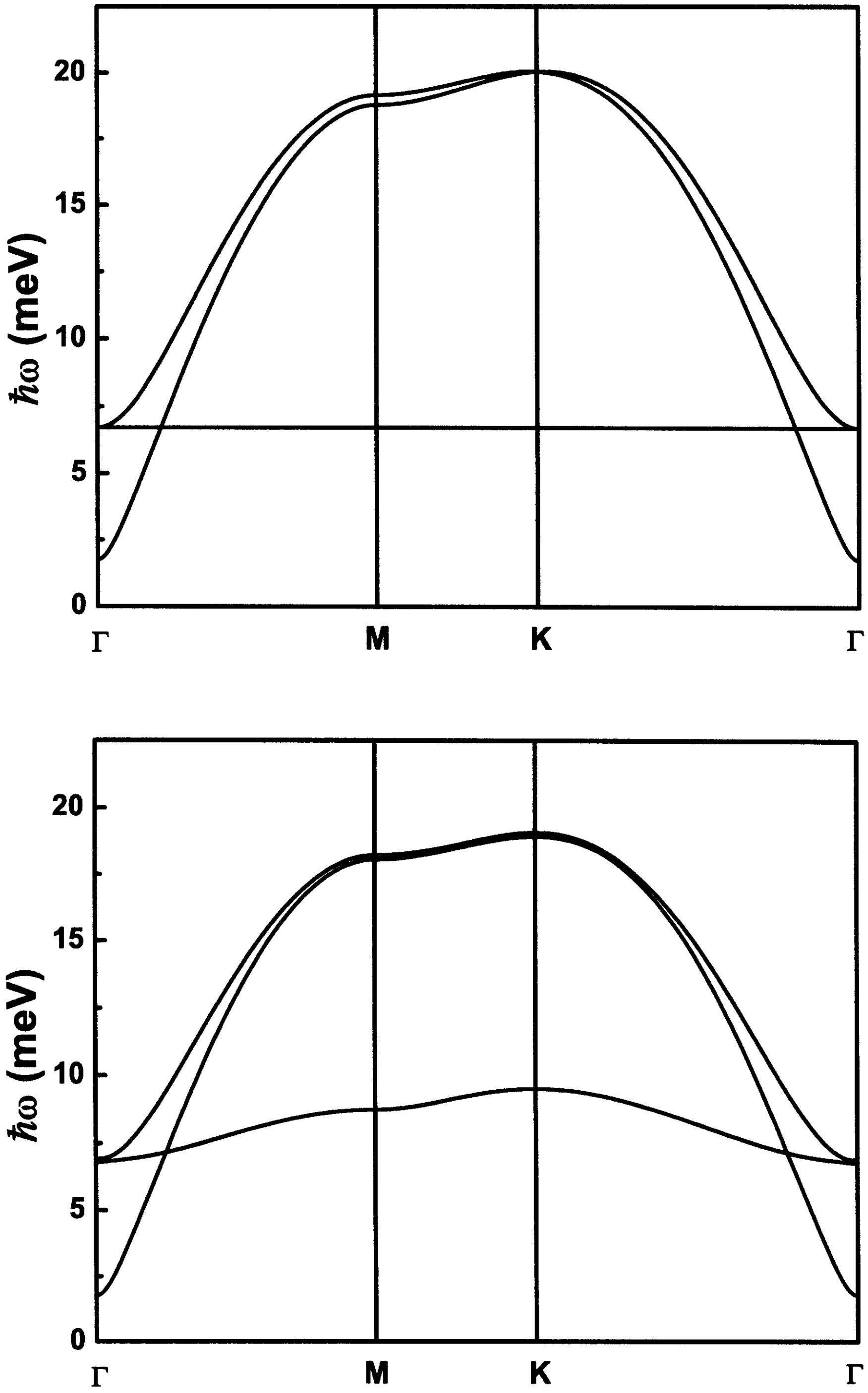

Figure 4-8: The top panel shows the empirical dispersion used to fit the momentum and energy scans of the spin wave excitations. The bottom panel shows the best fit to our spin wave results.

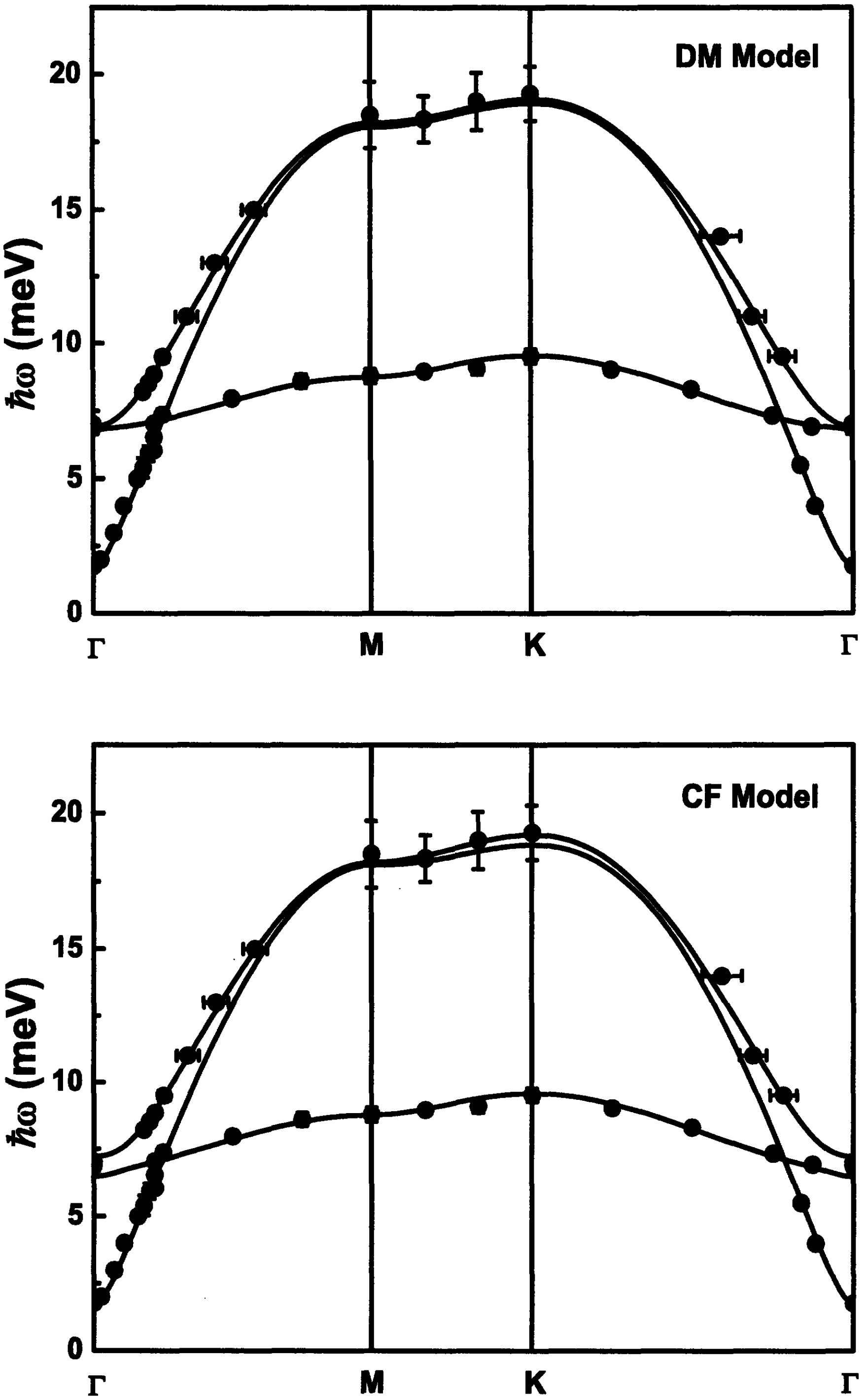

Figure 4-9: Spin wave dispersion along the high symmetry directions in the 2D Brillouin zone at $T = 10$ K. As discussed in the text, the lines in the top panel denote a fit to the DM model, with fit parameters $J_1 = 3.18(5)$, $J_2 = 0.11(1)$, $|D_y| = 0.197(2)$, and $D_z = -0.196(4)$ meV. The lines in the bottom panel denote a fit to the CF model, with fit parameters $J_1 = 3.34(9)$, $J_2 = 0.12(2)$, $D = 0.428(5)$, and $E = 0.0316(3)$ meV.

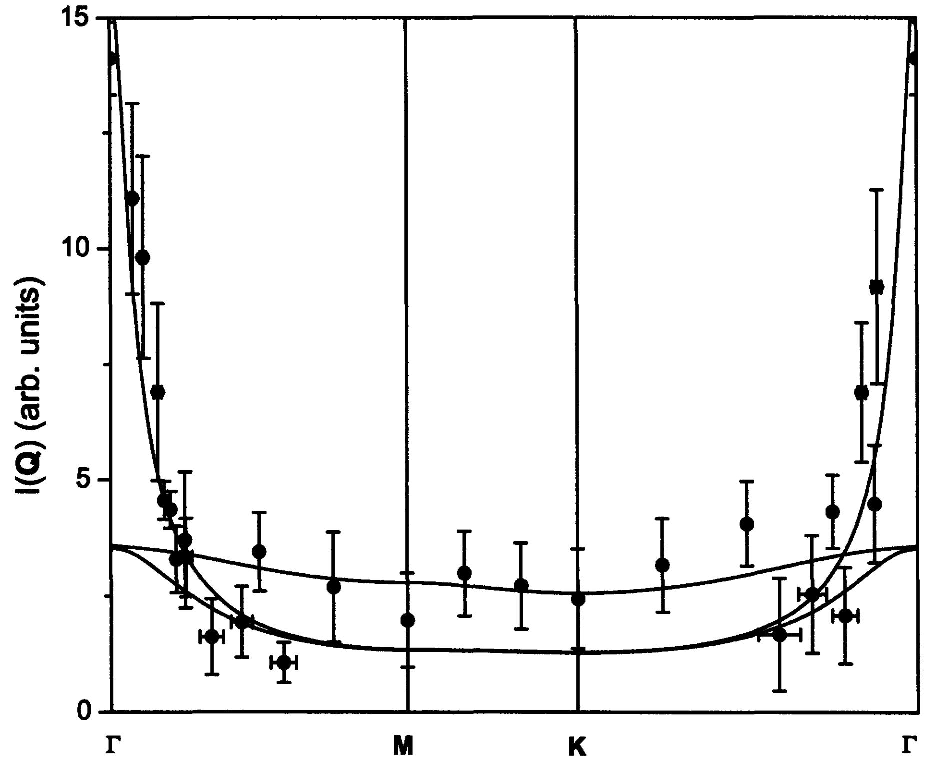

Figure 4-10: Wave vector dependence of the spin wave intensities. The solid lines correspond to $(n(\omega) + 1)/\omega(\mathbf{Q})$ with an overall scale factor as a fit parameter, where $n(\omega)$ is the Bose occupation factor and $\omega(\mathbf{Q})$ is obtained from the DM model. The data take into account the deconvolution with the instrumental resolution and the Fe^{3+} magnetic form factor.

not only the gaps at the zone center, but also the small dispersion of the flat-mode. This small dispersion is a result of a weak next-nearest-neighbor interaction J_2. We note that J_2 is positive (antiferromagnetic), which favors the experimentally observed ground state. The D_z component of the DM vector also reinforces selection of this ground state. The "zero energy mode" is lifted by an energy equal to the out-of-plane spin wave gap, consistent with the spin rotations depicted in Fig. 1-6. The gaps at the Γ point obtained numerically are in good agreement with the analytic results given in Table 4.2. The DM model yields a spin-canting angle of 1.9(2)°. This low-temperature value is larger than the experimentally deduced canting angle of 0.65(6)° at T = 50 K [110], which is expected since the sublattice magnetization has not yet saturated at T = 50 K.

The lines in Fig. 4-9 show the best fit to the CF model, which also is in reasonable agreement with the data, and yields a spin-canting angle of 0.8(2)°. However, the reduced-χ^2 value of 2.9 for the CF model fit is significantly higher than the reduced-χ^2 value of 0.63 for the DM model fit. The difference is most apparent in the numerical results for the mode splitting at the zone center. The CF model yields a relatively large splitting of about 0.71 meV for the 7 meV mode at the Γ point, whereas the data indicate that this splitting is smaller than 0.4 meV. The dotted line in Fig. 4-7 shows the CF prediction for the energy scan at the zone center, and we see that this does not describe the line-shape very well. The DM model, depicted by the solid line, describes the data better. Moreover, as pointed out in Ref. [39], the single ion anisotropy of the Fe^{3+} ion is expected to be small since it appears at second order in the spin-orbit coupling, whereas the DM term appears at first order.

Table 4.1: Hamiltonian parameters in meV obtained from the fits to the spin-wave data.

DM Model			CF Model		
J_1	**3.18**	**±0.05**	J_1	3.34	±0.09
J_2	**0.11**	**±0.01**	J_2	0.12	±0.03
$\lvert D_y \rvert$	**0.197**	**±0.002**	D	0.428	±0.003
D_z	**-0.196**	**±0.004**	E	0.0316	±0.0003
$\eta(°)$	**1.9**	**±0.2**	$\eta(°)$	0.8	± 0.2

Therefore, we believe that the observed spin wave spectrum is most naturally explained by a simple model which has only nearest and next-nearest isotropic interactions plus the DM interaction. The obtained fit parameters (in meV) are $J_1 = 3.18(5)$, $J_2 = 0.11(1)$, $|D_y| = 0.197(2)$, and $D_z = -0.196(4)$, where the error bars denote three times the statistical error. From a previous study [110], a value for J_1 of 3.9(2) meV was obtained from a fit of the susceptibility to a high-temperature series expansion result [35]. The values of J_1 are in reasonable agreement, and the agreement would be even closer if the effects of J_2 and the DM term were taken into account in the susceptibility fit. As a further comparison, the susceptibility in Ref. [110] indicated a value of $\Delta g/g \sim 0.06$, where g is the free electron Landé factor and Δg is its shift in the crystalline environment. The magnitude of the DM vector can be estimated

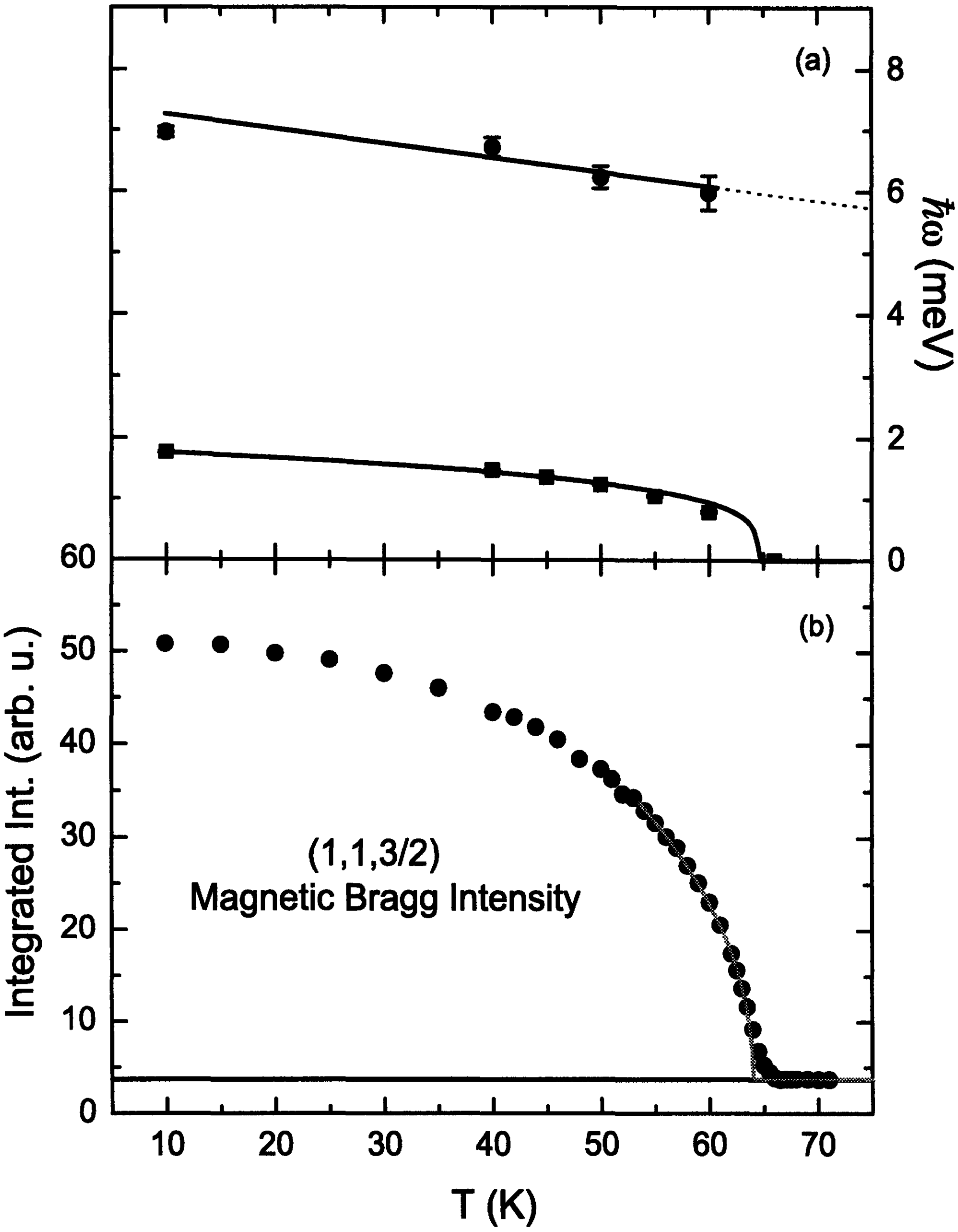

Figure 4-11: (a) Temperature dependence of the two spin gaps at 2 meV and 7 meV. The lines are drawn as guides to the eye. (b) Temperature dependence of the order parameter. The solid grey line is a fit to power law with the exponent $2\beta = 0.58(2)$ and $T_N = 64.5$ K for 58 K $< T <$ 64 K.

Table 4.2: Spin wave energies at the zone center for the DM and CF models. Here, $\tilde{\omega} \equiv \omega/S$, $J \equiv J_1 + J_2$, $C_1 \equiv E - D\sin^2\theta_o + E\cos^2\theta_o$, $C_2 \equiv (D+E)\cos(2\theta_o)$, $C_3 \equiv (D+E)\sin(2\theta_o)/2$, and $\theta_o \approx 20^\circ$ is the oxygen octahedra tilting angle.

	DM Model	CF Model
$\tilde{\omega}_0$	$\sqrt{12}\lvert D_y\rvert$	$[12JC_1 + 4C_1C_2 + 4C_3^2]^{1/2}$
$\tilde{\omega}_\pm$	$\left[3D_y^2 + 18D_z^2 - 6\sqrt{3}JD_z\right]^{1/2}$ $\pm 2D_yD_z/J$	$[6JC_2 + 4C_1C_2 + 7C_3^2]^{1/2}$ $\pm C_3$

from Moriya's calculation as $|\mathbf{D}|/J_1 \sim \Delta g/g$ [115]. From the current study, we have $D_y/J_1 \sim |D_z|/J_1 \sim 0.06 \sim \Delta g/g$, showing very good agreement between measurements of the spin dynamics and the bulk thermodynamics. The best fit to the CF model gives $J_1 = 3.34(9)$, $J_2 = 0.12(3)$, $D = 0.428(3)$, and $E = 0.0316(3)$.

Finally, from the analytic expressions for the spin gaps given in Table 4.2, we note that the in-plane gap is proportional to $|D_y|$ while the out-of-plane gaps are proportional to $\sqrt{J_1D_z}$. Since J_1 is large compared to other interactions, the out-of-plane gap is significantly larger than the in-plane gap, despite the similar magnitude of D_y and D_z. This results also suggests that at high temperatures (even above T_N), the spins would feel an easy-plane anisotropy and therefore display XY-like spin dynamics. This easy-plane anisotropy gives rise to the spin gap at 7 meV. Fig. 4-12 and Fig. 4-13 show energy scans of the spin gaps at 2 meV and 7 meV, respectively. The 2 meV spin gap decreases in energy more rapidly than the 7 meV spin gap, and almost disappear at 66 K, while the 7 meV gap still exists at 6 meV at 66 K. Fig. 4-11 shows temperature dependences of the two spin gap at 2 meV and 7 meV. The 2 meV spin gap disappears at T_N, while the 7 meV gap seems to persist above T_N. This picture is also consistent with the neutron scattering measurements of the critical fluctuations showing the presence of XY symmetry above T_N [110], which will be discussed in the next chapter. That study also shows that uniform vector chiral order is apparent above T_N, consistent with the presence of the DM term and the positive sign of J_2. Another interesting aspect of the analytic results is that the spin wave spectrum does not depend on the sign of D_y, which determines the direction of the

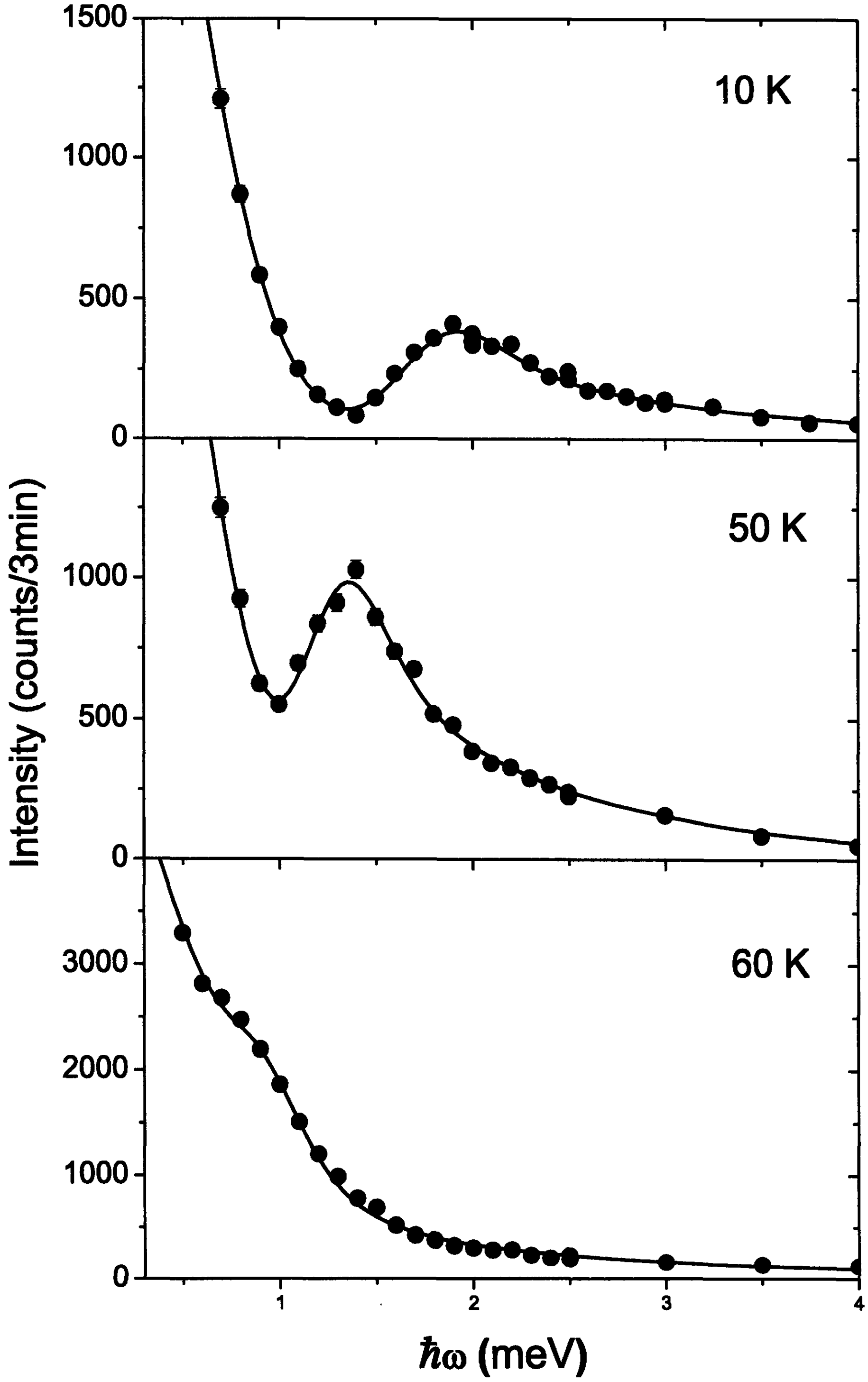

Figure 4-12: Energy scans of the 2 meV spin gap at Q = (100) at 10 K, 50 K and 60 K.

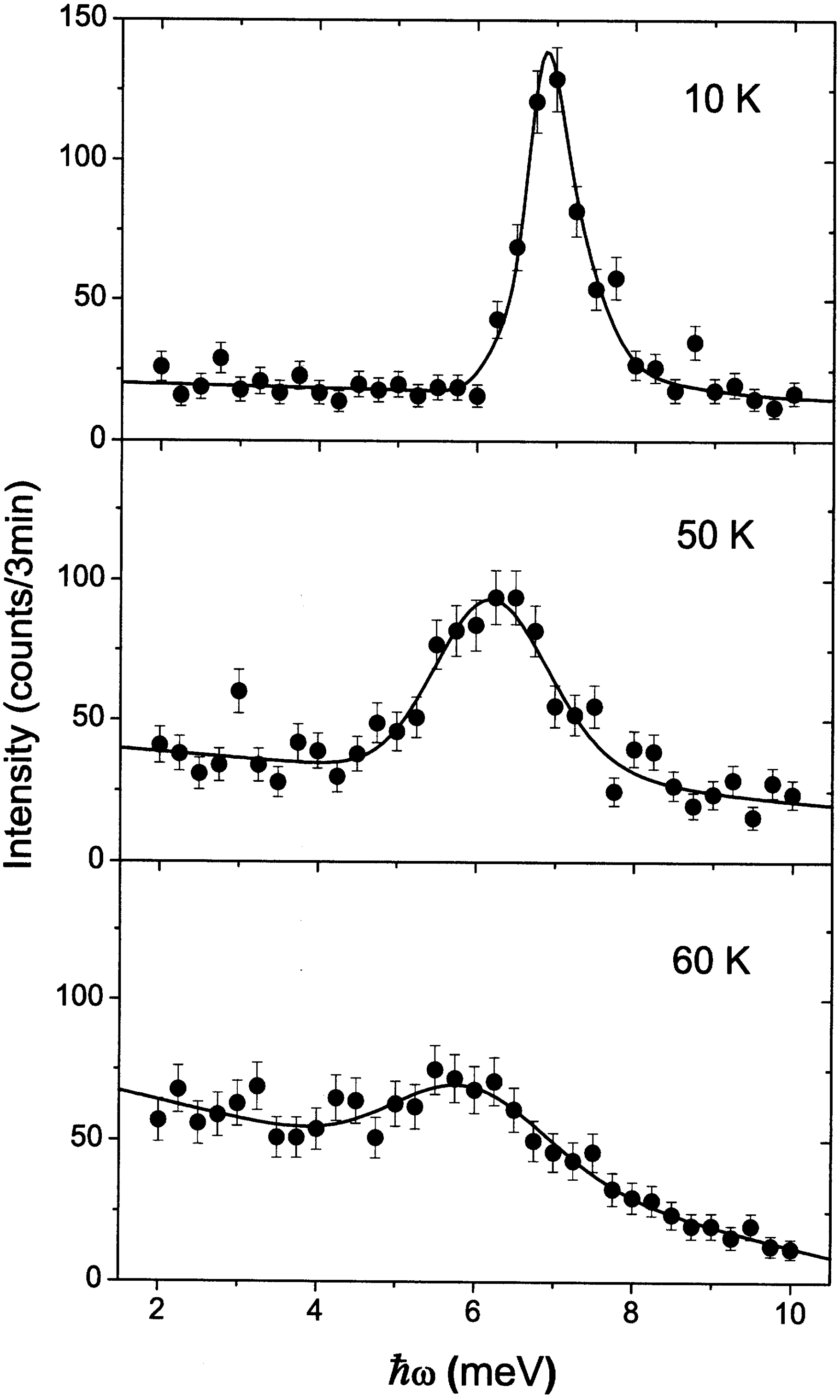

Figure 4-13: Energy scans of the 7 meV spin gap at $\mathbf{Q} = (110)$ at 10 K, 50 K and 60 K.

spin-canting relative to the in-plane order. This information on the canting cannot be determined from the currently available data obtained from both magnetization and neuron scattering measurements, and would be important for testing microscopic calculations of the DM interactions.

After our spin-wave paper was published, we learned that Coomer *et al.* [186] performed similar measurements on a natural-grown single crystal, and their results are in agreement with our results. However, due to their lack of good-quality single crystal, they were unable to map out all spin-wave modes throughout the Brillouin zone.

4.3 Polarization of the spin-wave modes

The polarization studies of the spin-waves in jarosite were carried out using inelastic polarized neutron scattering. The measurements were performed on TAS-1 spectrometer at JAEA. This state-of-the-art instrument utilized double-focusing Heussler crystals to monochromate and analyze the incident and scattered neutron beam to increase the flux. The beam polarization was about 90%, corresponding to a flipping ratio of 20. A single crystal of K jarosite (mass of 48 mg) was oriented in the (HK0) zone, where the (001) axis was perpendicular to the scattering plane. The alignment in this zone enabled us to measure the spin-wave excitations throughout an in-plane Brillouin zone (BZ). The sample was cooled by a ^{4}He close-cycle displex to 10 K. Horizontal collimations of open$-80'-$sample$-$open$-$open were employed. However, due to the small sample, effective horizontal collimations of $48' - 18' -$ sample $- 25' - 240'$ were used to calculate the resolution function. PG filters were placed in the scattered beam to reduce higher-order contaminations. The energy resolutions of about 1.2 meV was achieved, as well as the background of about one count per minute. The low background is very important in inelastic polarized neutron measurements due to low scattering intensity.

Fig. 4-14 shows the polarization of the three spin-wave modes for the kagomé lattice antiferromagnet. As previously discussed, ω_1, which is a non-dispersive, zero-energy mode, is an out-of-plane excitation, and ω_2 and ω_3, which are dispersive, are out-of-plane and in-plane excitations, respectively. To experimentally measure their polarization, we have performed inelastic polarized neutron scattering measurements. As discussed in Chapter 2, polarized neutron scattering can detect and distinguish between in-plane and out-of-plane spin wave excitations. If **P** and **Q** are parallel, both in-plane and out-of plane excitations will give rise to scattering intensity in the spin-flip channel. On the other hand, if **P** is perpendicular to **Q**, then the magnetic scattering in the spin-flip channel is due to the excitations that are perpendicular to both **Q** and **P**, and the magnetic scattering in the non-spin-flip channel is due to the spin excitations parallel to **P**.

Fig. 4-14 shows constant-**Q** scans at (1,0,0), the center of a BZ ($\Gamma-$point), at 10 K. The observed peaks were fit with narrow Gaussian convoluted with the experimental resolution function assuming the empirical dispersion as shown in Fig. 4-7. All fitting parameters except peak intensities were the same as the unpolarized neutron data (Fig. 4-5). The peak intensities at 2 meV and 7 meV were optimized to fit all data sets equally well. The rise at high energy was due to the contamination from the main beam at $2\theta = 0$. For a guide field along **Q** or horizontal field (HF) scattering, both spin-wave excitations at 2 meV and 7 meV were observed in the spin-flip channel, consistent with Fig. 4-5, while there is no magnetic scattering in the non-spin-flip channel. For the guide field perpendicular to **Q**, and perpendicular to the scattering plane (VF), the peak at 2 meV was observed in the spin-flip channel, and the peak at 7 meV was observed in the non-spin-flip channel. On the other hand, if the guide field was perpendicular to **Q**, but lay within the scattering plane ($\mathrm{HF_y}$), then the peak at 2 meV was observed in the non-spin-channel and the peak at 7 meV was observed in the spin-flip channel. These results are consistent with the fact that the 2 meV gap is an in-plane excitation, and the 7 meV gap is an out-of-plane excitation. The equivalent intensities of the VF spin-flip channel and HF spin-flip channel and the absence of intensity in the VF non-spin-flip channel at 2 meV indicate that the 2 meV excitation is an in-plane excitation. Similarly, the equivalent intensities of the VF non-spin channel and HF spin channel and the absence of intensity in the

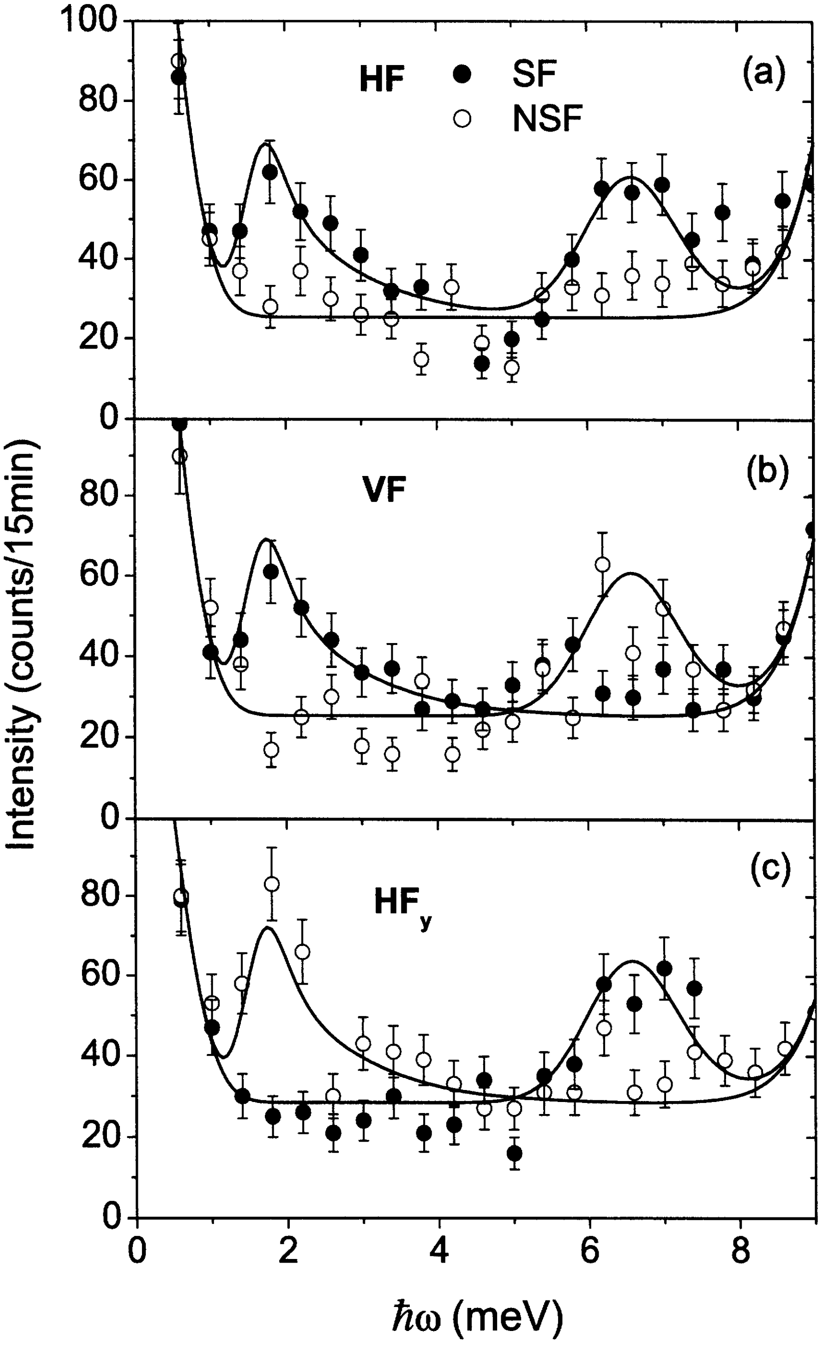

Figure 4-14: Inelastic polarized neutron scattering measurements of spin-wave excitations at the zone center, $\mathbf{Q} = (100)$. The guide field is (a) parallel to $\mathbf{Q}$, (b) perpendicular to $\mathbf{Q}$ and scattering plane, and (c) perpendicular to $\mathbf{Q}$ but lies the scattering plane.

VF spin-flip channel at 7 meV indicate that the 7 meV excitation is an out-of-plane excitation at 7 meV.

4.4 Summary

The spin wave spectrum of a kagomé lattice antiferromagnet has been measured using inelastic neutron scattering. We observe a flat, lifted "zero energy mode" at ~7 meV, whose presence reflects the extensive ground-state degeneracy of the ideal kagomé Heisenberg antiferromagnet. We have also determined the relevant spin Hamiltonian parameters by fitting our data to a Heisenberg model with the antisymmetric DM interaction. The data were also fit to the CF model with single-ion anisotropy. However, the model fails to reproduce precisely the energy gap at zone center, and gives a value of the canting angle, which is smaller than that suggested by the magnetization measurements. This result suggests that the DM interaction dominates the single-ion anisotropy in this kagomé lattice antiferromagnet. It is still possible that both DM interaction and single-ion anisotropy coexist in the system, and contribute to the exchange interaction between the spins on the lattice. In addition, the DM interaction can explain a chiral ordered state of spin fluctuations above T_N, whose results are presented in the next chapter. In contrast, the presence of the single-ion anisotropy does not *a priori* lead to the chiral ordered state at high temperature. An addition of next-nearest-neighbor interaction (J_2) is needed to stabilize the chiral order state. However, with J_2 of 0.11 meV, the energy scale of the next-nearest-neighbor interaction is much smaller than the thermal energy at 70 K ($\approx$ 6 meV).

This realization of the kagomé antiferromagnet is perhaps the best characterized geometrically frustrated spin system, and, as such, would be useful for precise tests of theoretical predictions. In addition, using polarized neutron scattering, we have verified the polarization of each spin-wave mode predicted by theorists. These results also highlight the importance of single crystal measurements for accurate interpretation of data acquired with powder samples of frustrated magnets.

Chapter 5

Spin chirality and critical behavior

In the previous two chapters, we learned that the antisymmetric DM interaction describes the spin structure and spin-wave excitations below the ordering temperature T_N in jarosite. In this chapter, we will investigate the spin chirality and spin fluctuations above T_N, and argue that the presence of the DM interaction is consistent with the phenomena observed above the ordering temperature. Furthermore, the critical behavior is discussed, and the measurements of the critical exponents α, β, γ, and ν are presented. The discussion also includes the Berezinskii-Kosterlitz-Thouless theory, $SO(2)$, and Z_2 symmetries.

The presence of spin chirality in condensed matter systems may play a role in important phenomena ranging from high-temperature (high-T_C) superconductivity [187] to the anomalous Hall effect [26, 27, 188]. Currently, there are relatively few experimental studies of spin chirality in frustrated magnets. One example is the study of spin chirality in the triangular lattice antiferromagnet $CsMnBr_3$ [150], where the chiral critical exponents, β_c, γ_c, and ν_c of the average chirality (chiral order parameter), the chiral susceptibility, and the chiral correlation length for the triangular lattice were determined using polarized neutron scattering. Unfortunately, similar measurements cannot be done in jarosite due to the vanishing chiral term in the polarized neutron cross section as discussed in Chapter 2. However, an indirect observation of the chiral ordered state above T_N is possible in jarosite. In this chapter, we report the study of the non-trivial spin-textures related to chirality in a jarosite material

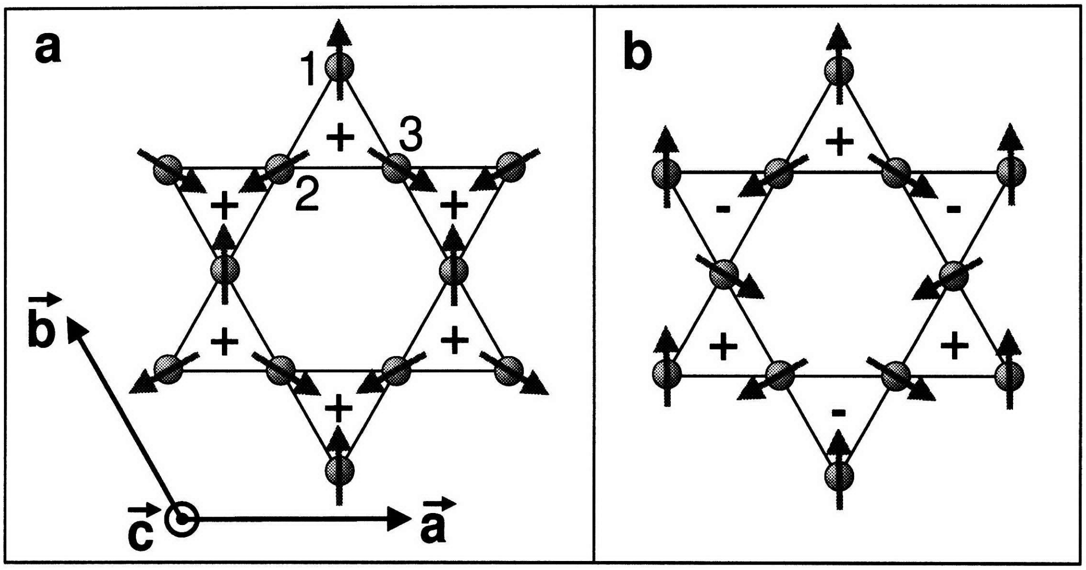

Figure 5-1: As discussed in Chapter 1, spins on the kagomé lattice can be arranged in two different configurations. (a) The $q = 0$ structure with positive vector chirality, which is the ground state configuration for Fe jarosite. The spin arrangement has uniform, positive (negative) vector chirality, indicated by the + (−) within each triangular plaquette. (b) An alternate spin arrangement with staggered vector chirality, called "$\sqrt{3} \times \sqrt{3}$" structure.

in the spin-disordered states ($T_N < T < 120$ K). Our magnetic neutron scattering measurements on pure single crystals show the presence of a chiral order above the ordering temperature.

The iron jarosite $KFe_3(OH)_6(SO_4)_2$ possesses robust chiral correlations related to the arrangement of spins around triangular plaquettes [37, 87]. As discussed in the first chapter, even though the kagomé lattice antiferromagnet should not order at any non-zero temperature, powder neutron diffraction measurements on $KFe_3(OH)_6(SO_4)_2$ indicate that the spins order in a coplanar $q = 0$ arrangement below $T_N \sim 65$ K [37, 87]. In the $q = 0$ structure, the spins on each triangle are oriented at 120° to each other, and the 2D magnetic unit cell is identical to the 2D structure unit cell, as shown in Fig. 1a. The ordered spins can be decomposed into three sublattices, with the spins on each triangle labeled as $\mathbf{S}_1$, $\mathbf{S}_2$, and $\mathbf{S}_3$. The *vector* *chirality* for each triangle may be defined as:

$$\mathbf{K}_V = \frac{2}{3\sqrt{3}}(\hat{S}_1 \times \hat{S}_2 \ + \ \hat{S}_2 \times \hat{S}_3 \ + \ \hat{S}_3 \times \hat{S}_1). \tag{5.1}$$

For the coplanar arrangement, this vector is parallel to the c-axis with amplitude +1 or -1 [37]. The neutron powder results [37, 87] indicate that each triangle has positive chirality (+1) in the ordered state, such that the spins point directly toward or away from the center of each triangle. Similarly, the scalar chirality for each triangle can be defined as:

$$K_S = \mathbf{S}_1 \cdot (\mathbf{S}_2 \times \mathbf{S}_3). \tag{5.2}$$

K_S is zero for perfect coplanar spins, and positive (negative) if the canted moment is along the positive (negative) c direction. The ordered state as well as the spin-reorientation transition between zero and non-zero total scalar chirality at high field has been discussed in Chapter 4.

For this jarosite compound, like most other frustrated magnetic materials, the interaction Hamiltonian of the spins contains terms beyond isotropic Heisenberg exchange. These additional terms cause the system to order at a non-zero T_N and determine the ground-state spin arrangement. From our magnetization and neutron scattering measurements discussed in Chapter 3 and 4, we found that the transition to long-range order is driven by weak ferromagnetic interplane coupling and the antisymmetric DM interaction. This ordered phase on a kagomé lattice can be characterized by two order parameters (the sublattice magnetization and the vector chirality) which have different symmetries. Below T_N, both of these symmetries are broken. An intriguing possibility is that these symmetries are broken at different temperatures. Possibly, the chiral symmetry is broken at a chiral-ordering temperature $T_C > T_N$, in which case the system is in the chiral ordered state without broken rotational symmetry of the spins. This has been proposed as a result of numerical work on XY or planar triangular lattice systems [189, 190]. However, it has not been conclusively observed by experiments [191, 192]. For kagomé lattice systems, relatively little is known about the nature of the phase transitions that occur. In this chapter, we will explore the possibility of having two magnetic transitions in jarosite, and study their nature using neutron scattering measurements.

5.1 Chiral ordered state

To probe the microscopic behavior of the magnetism in the temperature regime above T_N, we performed inelastic neutron scattering measurements of the spin fluctuations at $T = 70$ K within the $L = 0$ plane of reciprocal space. For the temperature range $T_N < T < 120$ K, the susceptibilities for $H \parallel c$ and $H \parallel ab$ deviate from each other, indicative of the growing influence of a spin-anisotropy as shown in Fig. 1-11. For the 3D ordered spin structure below T_N, the stacking arrangement of the planes doubles the magnetic unit cell with respect to the structural unit cell such that the magnetic Bragg peaks occur at half-odd-integer values of L ($L \neq 0$). However, for temperatures above T_N, the correlations between layers are destroyed, and the 2D spin fluctuations yield "rods" of scattering in reciprocal space along the L direction.

Fig. 5-5 show a scan along the L direction through (1 1 0) at $T = 66$ K above T_N of 64.5 K revealing the 2D nature of the critical scattering. Small oscillation is due to 3D short-range correlations that start to appear at the temperature close the the ordering temperature. The measurements were done in the 2-axis mode on a single crystal of K jarosite at HFIR. The sample was aligned in (HHL) zone with collimations $48' - 40' -$ *sample* $- 40' -$ *open*. Two PG filters, before and after the sample, were used to reduce contaminations. The solid line in Fig. 5-5 is a guild to the eye assuming Lorentzian line-shape convoluted with the resolution function. Peak positions were fixed at $L = -4.5$, -1.5, 1.5, and 4.5, and the intensity of each peak is proportional to the magnetic form factor squared of Fe^{3+}.

Fig. 5-4a shows a reciprocal contour map measured on a single crystal of K jarosite at 70 K. The experimental set-up for this measurement will be discussed in the next section. We have verified that all of the signal in Fig. 5-4a disappears upon cooling below T_N, as expected for the transfer of the intensity of the 2D critical scattering into 3D Bragg points lying out of the scattering plane. Therefore, the scans in Fig. 5-4a pass through these 2D rods of scattering and directly measure the dynamic structure factor of the spin correlations of the single kagomé planes in iron jarosite. The instantaneous spin correlation length, measured separately in an energy-integrating configuration, is $\xi = 20(2)$ Å at this temperature.

Experiment

The neutron scattering data were taken at the NIST Center for Neutron Research. The measurements were done on single crystal sample of K jarosite, whose mass is 48 mg, the largest single crystal. For the two-axis (energy-integrating) measurement of the instantaneous spin correlation length at T=70 K, we used the BT9 spectrometer with the sample aligned in the (HK0) scattering zone. The incident neutron energy was 35 meV, with a collimation sequence of 40′-24′-sample-20′. From these measurements, the instantaneous in-plane spin correlation length of 20(2) Å of roughly three lattice constants is determined. A PG filter was placed in the incident beam to remove higher order neutrons. The inelastic neutron scattering data shown in Fig. 5-4 were taken using the SPINS NG5 triple-axis spectrometer, which utilizes cold neutrons for higher energy resolution. The final neutron energy was fixed at 5 meV and the horizontal collimation sequence was $guide - 80' - S - 40'(radial) - open$. A liquid-nitrogen-cooled beryllium filter was placed in the scattered beam to remove higher order neutrons. The sample was cooled using a ^{4}He closed-cycle displex.

Results and discussion

A reciprocal space map of the intensity of the spin fluctuations is shown in Fig. 5-4a. Outlined in red are the boundaries of the structural Brillioun zones (BZ). The strongest scattering occurs at the centers of certain BZ's. The neutron scattering intensity can be calculated by

$$I \propto f(\mathbf{Q})^2 \sum_{\alpha,\beta} (\delta_{\alpha\beta} - \hat{Q}_\alpha \hat{Q}_\beta)\, S^{\alpha\beta}(\mathbf{Q},\omega), \tag{5.3}$$

where α, β refer to x, y, z vector components, $f(\mathbf{Q})$ is the magnetic form factor, and $S(\mathbf{Q}, \omega)$ is the space- and time- Fourier transform of the spin-spin correlation function. The intensity variation reveals a wealth of information about the short-range ordered state in the critical regime just above T_N.

First, the fact that the intensities are centered within the structural Brillioun zones indicates that the fluctuations have the $q = 0$ arrangement. The absence of scattering at the (2 0 0) position is consistent with this spin arrangement. The $\sqrt{3} \times \sqrt{3}$ would give a different scattering pattern as shown in Fig. 5-4b. In addition, the absence of scattering at (2 0 0) also indicates that the spin fluctuations are mostly in-plane. Therefore, from the scattering pattern, we conclude that the spin fluctuations have the uniform chirality or $q = 0$ arrangement, and the fluctuations are confined within the kagomé plane.

Second, the nearly equivalent intensities at the (1 0 0) and (1 1 0) positions reveal that the spin direction on each sublattice is not fixed. Rather, the two orthogonal spin directions within the kagomé plane are equally likely. Fig. 5-2 shows the scattering intensity of two spin arrangements with uniformly positive chirality calculated using Eq. 5.3. The spin directions of these two arrangements are orthogonal to each other. As shown in the figure, the scattering pattern of the individual spin arrangement does not agree with the data; however, their superposition matches quite well with the data. The same calculations can be done for the spin arrangement with uniformly negative chirality as shown in Fig. 5-3. Similarly, the scattering pattern from the individual spin arrangement does not agree with the data, but their superposition matched well with data. Hence, the spin fluctuations have XY symmetry at this temperature (the spin-rotational symmetry within the kagomé plane is not broken). The spins are free to rotate within the plane as long as the vector chirality remains uniform. In contrast, at low temperature in the 3D ordered state, a preferred spin direction is chosen, and the intensities at (1 0 L) and (1 1 L) differ considerably [37, 38].

The observation of short-range $q = 0$ correlations in the 2D fluctuations implies a particular arrangement of the *vector* chirality. In each region of correlated spins, the vector chirality must be uniform (all positive or all negative for each plaquette). Using

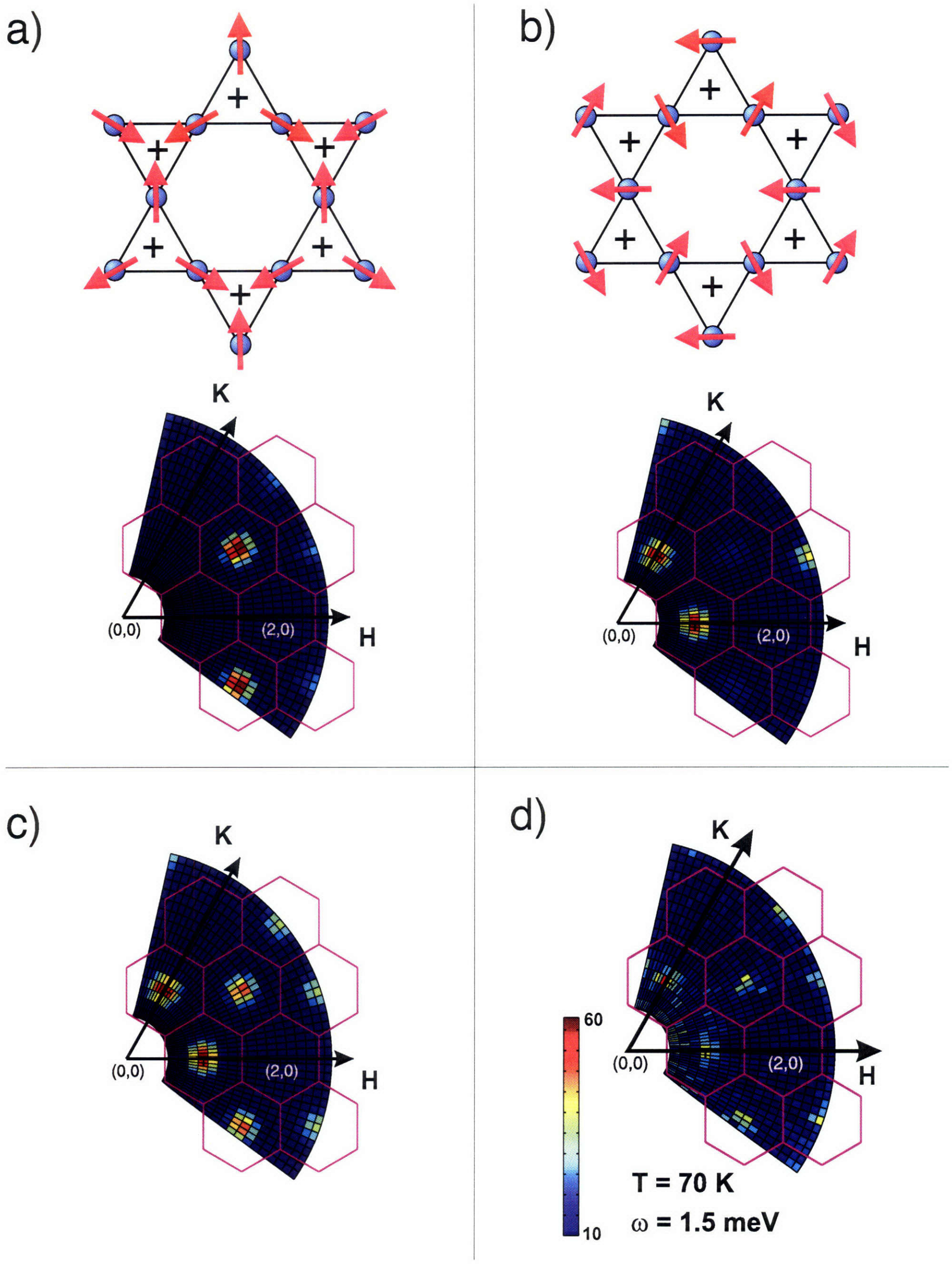

Figure 5-2: This diagram shows the $q = 0$ spin arrangement with positive chirality. (a) All-in-all-out spin arrangement and its corresponding scattering pattern are shown. (b) Spin arrangement that is orthogonal to (a) is shown with its corresponding scattering pattern. (c) Superposition of two scattering patterns shown in (a) and (b). (d) The result from inelastic neutron scattering measurements at $\hbar\omega = 1.5$ meV and $T = 70$ K.

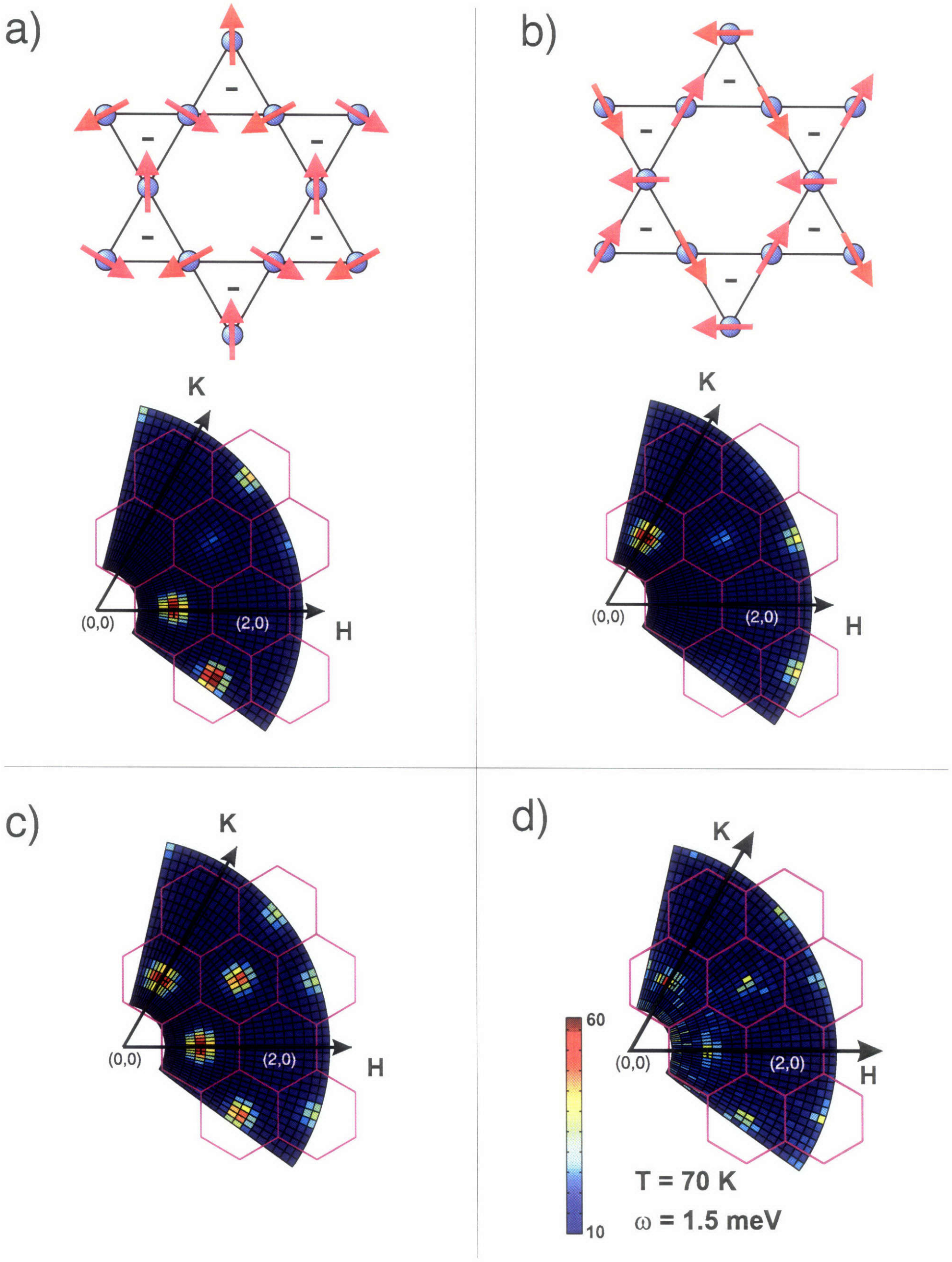

Figure 5-3: This diagram shows the $q = 0$ spin arrangement with negative chirality. (a)-(b) Two spin arrangements with orthogonal spin directions are shown with their corresponding scattering patterns. (c) Superposition of two scattering patterns shown in (a) and (b). (d) The result from inelastic neutron scattering measurements at $\hbar\omega = 1.5$ meV and $T = 70$ K.

Eq. 5.3, we calculated the neutron scattering intensity arising from $q = 0$ correlations between coplanar spins assuming only positive chirality. Our model calculations are based on 7-unit cell clusters of spins, and we have averaged over all spin directions within the kagomé plane. The results are shown in Fig. 5-4 and the agreement with the data is excellent. Also shown in Fig. 5-4 is a calculation for the intensity if the chirality were staggered as in the $\sqrt{3} \times \sqrt{3}$ arrangement. If such correlated regions exist, the error bars on our data indicate that the fraction must be less than 5%.

Our results shed light on several basic questions regarding the magnetic phase transition in iron jarosite. First, we find that the instantaneous spin correlations above T_N are two-dimensional in nature, and the $q = 0$ arrangement is preferred. Therefore, the selection of $q = 0$ order (as opposed to $\sqrt{3} \times \sqrt{3}$ order which is predicted to be the preferred ground state for the pure Heisenberg model [33, 135]) is caused by interactions within a single kagomé layer and is not controlled by the interplane interaction [88]. Second, our neutron measurements reveal critical spin fluctuations above T_N that have XY symmetry; hence, the magnetic ordering is not driven by 2D Ising physics [37]. Most interestingly, we find that the spin-rotational symmetry and the vector chiral symmetry are not broken simultaneously at T_N.

The presence of vector chiral order above T_N may be naturally explained in light of the DM interaction. One possibility is that the DM interaction is the dominant source of spin anisotropy in iron jarosite. In this case, the vector chiral order appears concomitantly with the growing spin correlations and does not represent a spontaneously broken symmetry. Another possibility is that the XY anisotropy has an origin (such as symmetric exchange anisotropy [193]) distinct from the DM interaction. Once the spin correlations become coplanar within the kagomé plane, the vector chirality of a triangular plaquette becomes a discrete symmetry (the chirality vector is either up or down with respect to the c-axis). Hence, long-range chiral order is not precluded by the Mermin-Wagner theorem [194]. However, chiral order is easily disrupted on a kagomé lattice by the proliferation of domain walls (thermally induced defects) which can form with little cost in energy [31, 41, 195]. Then the presence of a small DM interaction (in particular, the non-zero out-of-plane component

D_z) selects a particular chirality for each triangle, and thereby inhibits domain wall formation. It remains possible that the vector chirality represents a spontaneously broken symmetry; however, clarification of this point requires further neutron scattering measurements at higher temperatures. Sato predicted the coexistence of vector chiral order with unbroken spin-rotational symmetry and Tomonaga-Luttinger liquid phase in the frustrated three-leg spin tube in magnetic field [196] by means of Abelian bosonization techniques. Recently, staggered chiral spin fluctuations has been reported in $Y_{0.5}Ca_{0.5}BaCo_4O_7$, which contains kagomé layers of Co ions with $S = 3/2$. The system does not order down to base temperature, but diffuse neutron scattering measurements with polarization analysis reveal short-range spin correlation with staggered chirality [197].

5.2 Spin fluctuations and critical scattering

Magnetic neutron scattering measurements were utilized to investigate spin fluctuations above T_N in the kagomé lattice antiferromagnet $KFe_3(OH)_6(SO_4)_2$. For example of the magnetic neutron scattering study of other systems, the readers are encouraged to turn to Ref. [198, 199], where magnetic neutron scattering was used to study magnetic excitations in La_2CuO_4. One similarity between La_2CuO_4 and jarosite is a 2D structure of the CuO_2 planes and kagomé plane, which give rise to a scattering rod along the direction perpendicular to the plane in the critical regime above the ordering temperature. We will start this section by reviewing the cross section for the magnetic neutron scattering as discussed in Chapter 2. The magnetic cross section measured using neutron scattering is related to the spin-pair correlation function, which can be written as (Eq. 2.9),

$$\frac{d^2\sigma}{d\Omega\, dE'} \sim \frac{\mathbf{k}'}{\mathbf{k}} f(\mathbf{Q})^2 \sum_{\alpha,\beta} \left(\delta_{\alpha\beta} - \hat{Q}_\alpha \hat{Q}_\beta\right) S^{\alpha\beta}\left(\mathbf{Q}, \omega\right). \tag{5.4}$$

$S^{\alpha\beta}\left(\mathbf{Q}, \omega\right)$ is the dynamic magnetic structure factor. It is the space and time Fourier transform of the spin-pair correlation function $\left\langle S^\alpha(0,0) S^\beta(\mathbf{r},t)\right\rangle$, which is given by

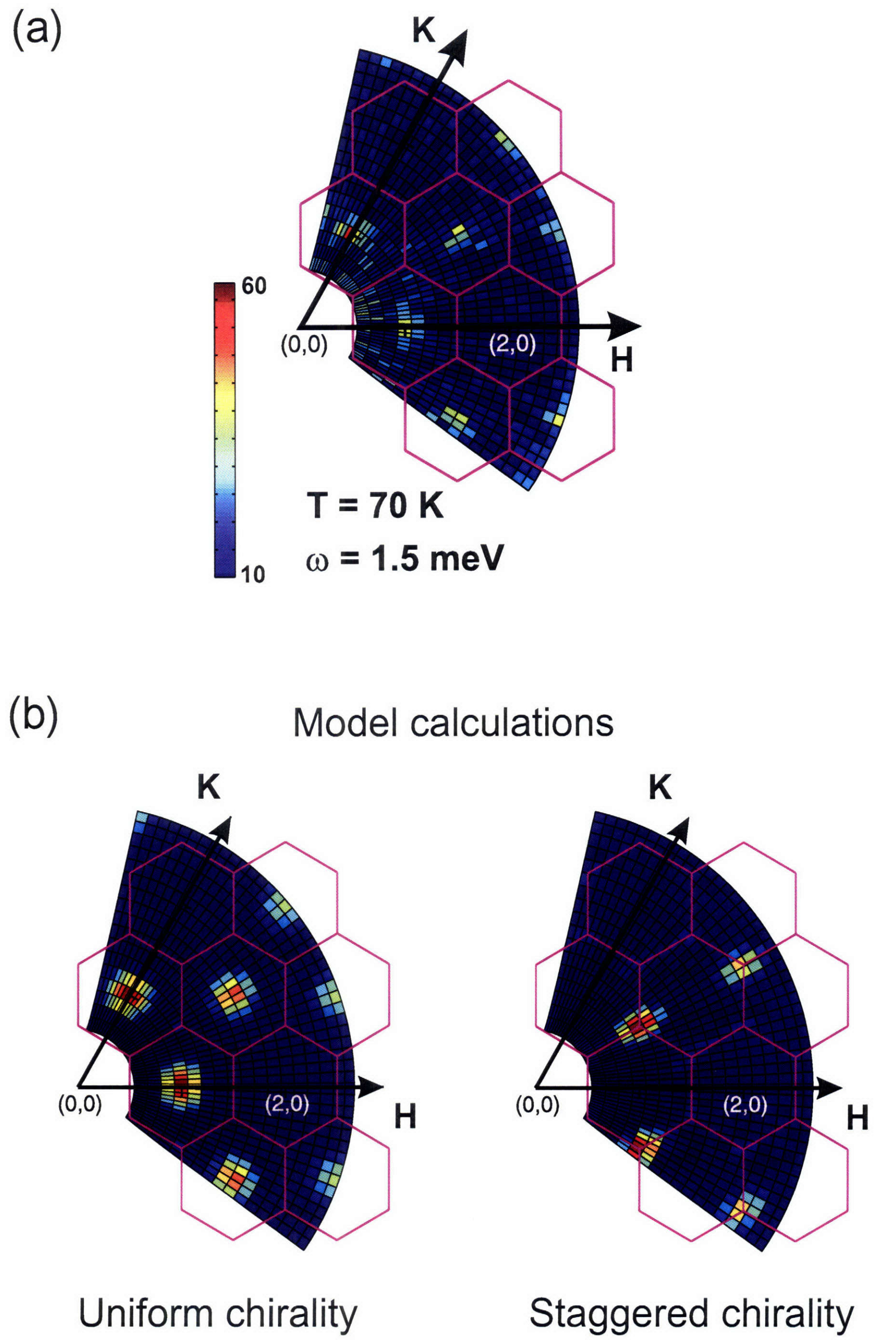

Figure 5-4: Inelastic neutron scattering data for $KFe_3(OH)_6(SO_4)_2$ measured above T_N, along with structure factor calculations. (a) Intensity contour plot of data from inelastic neutron scattering measurements of a single crystal sample (mass= 48 mg). The bright regions are the loci of scattering intensity for the low energy ($\hbar\omega = 1.5$ meV) spin fluctuations at $T = 70$ K above T_N. (b) Model calculations of the intensity as described in the text. The left plot corresponds to short-range $q = 0$ correlations with uniform vector chirality, whereas the plot on the right depicts $\sqrt{3} \times \sqrt{3}$ correlations. Both calculations are for the case in which there is no preferred spin direction within the kagomé plane.

(Eq. 2.10):

$$S^{\alpha\beta}(\mathbf{Q},\omega) = \frac{1}{2\pi\hbar}\sum_{\mathbf{r}}\int_{-\infty}^{\infty} dt\; e^{i(\mathbf{Q}\cdot\mathbf{r}-\omega t)} \left\langle S^{\alpha}(0,0)S^{\beta}(\mathbf{r},t)\right\rangle \tag{5.5}$$

The dynamic magnetic structure for two-dimensionally correlated spin systems, such as $KFe_3(OH)_6(SO_4)_2$ and La_2CuO_4, is independent of the momentum transfer along the L direction, which is perpendicular to the kagomé and CuO_2 layers, respectively. Therefore, the scattering intensity forms a rod extending in the L direction as shown in Fig. 2-1. As briefly mentioned in Chapter 1, one can take advantage of this rod of magnetic scattering in the studies of magnetic correlation length and spin fluctuations using quasi-elastic approximation pioneered by Birgeneau, Skalyo and Shirane [162]. The instantaneous correlation function is, then, measured in an 2-axis mode, where the analyzer is removed from a triple-axis spectrometer, and a sample is oriented such that the scattering wave vector is parallel to the 2D scattering rod. Alternatively, one can measure the instantaneous correlation function in the 2D systems by aligning the 2D scattering rod along the direction perpendicular to the scattering plane. In this configuration, a wide range momentum transfer along the L direction can be reached due to a large momentum resolution along the vertical direction. We have utilized both methods to investigate spin correlations in $KFe_3(OH)_6(SO_4)_2$, and found that in our case the latter provided better measurements of the spin correlation function with less contamination from spurious scattering.

We conducted quasi-elastic neutron scattering measurements in the 2-axis mode on a highly geometrically frustrated system $KFe_3(OH)_6(SO_4)_2$ at HFIR, Oak Ridge National Laboratory. The high quality single crystal of mass 48 mg was aligned in (HK0) zone with collimations $48' - 40'$–sample–$40'$–open. The scattering rod in the L direction was aligned perpendicular to the scattering plane. To lower the background, masks of dimension (3/4" × 3/4") and (3/4" × 3/4") were placed before and after the sample, respectively. An additional mask of dimension (2" × 4") was placed in front of the detector. Two PG filters, before and after the sample, were used to reduce the contamination at (1 0 0) that is due to $\lambda/3$ neutrons. We check and eliminate the possibility that the contamination is due to the vertical tail of (1 0 1) peak. All quasi-elastic scattering scans are longitudinal scans centered at (1 0 0). The measurements were made at temperatures between 66 K and 100 K with neutron initial energies of 13.5 meV and 30.5 meV. For temperatures above 100 K, the intensity at (1 0 0) is too weak to measure the critical scattering.

The collimations in this measurement were the same as those in the spin-wave measurements. Therefore, to fit the data we used the same values of effective collimations of $48' - 18'$–sample–$25'$–open, which is smaller than the experimental values due to the small size of the sample. We found that this set of effective collimations fit a $\lambda/3$ Bragg peak at (1 0 0) very well (not shown). We then fit the quasi-elastic scans with a Lorentzian function convoluted with the instrumental resolution ellipsoid. Background was fit to a linear function of Q, whose slope is independent of temperature and fixed for all scans, but whose constant term is temperature-dependent. As expected, we found that critical scattering becomes weaker, and correlation length becomes shorter as temperature increases above the ordering temperature, $T_N = 64.5$ K (this value of the ordering temperature is obtained from our specific heat measurements and the order parameter measurements using neutron scattering).

Fig. 5-2 shows three representative scans measured at 66 K, 75 K and 100 K. The dashed lines show the resolution of the instrument. The intrinsic widths were extracted by fitting the data to Lorentzian given in Eq. 5.6 convoluted with the experimental resolution function.

$$S(q) = \frac{S(0)}{1 + q^2\xi^2}, \tag{5.6}$$

where ξ is the correlation length. For all scans above the ordering temperature $T_N = 64.5$ K, the intrinsic width is larger than the instrumental resolution, indicative of short-range spin correlation. This short-range correlation persists up to 100 K. Background weakly depends on temperature, and the linear relation of the background as a function of temperature was assumed in the fit. As temperature increases, the quasi-elastic scattering at (1 0 0) becomes weaker, and the width of the peak be-

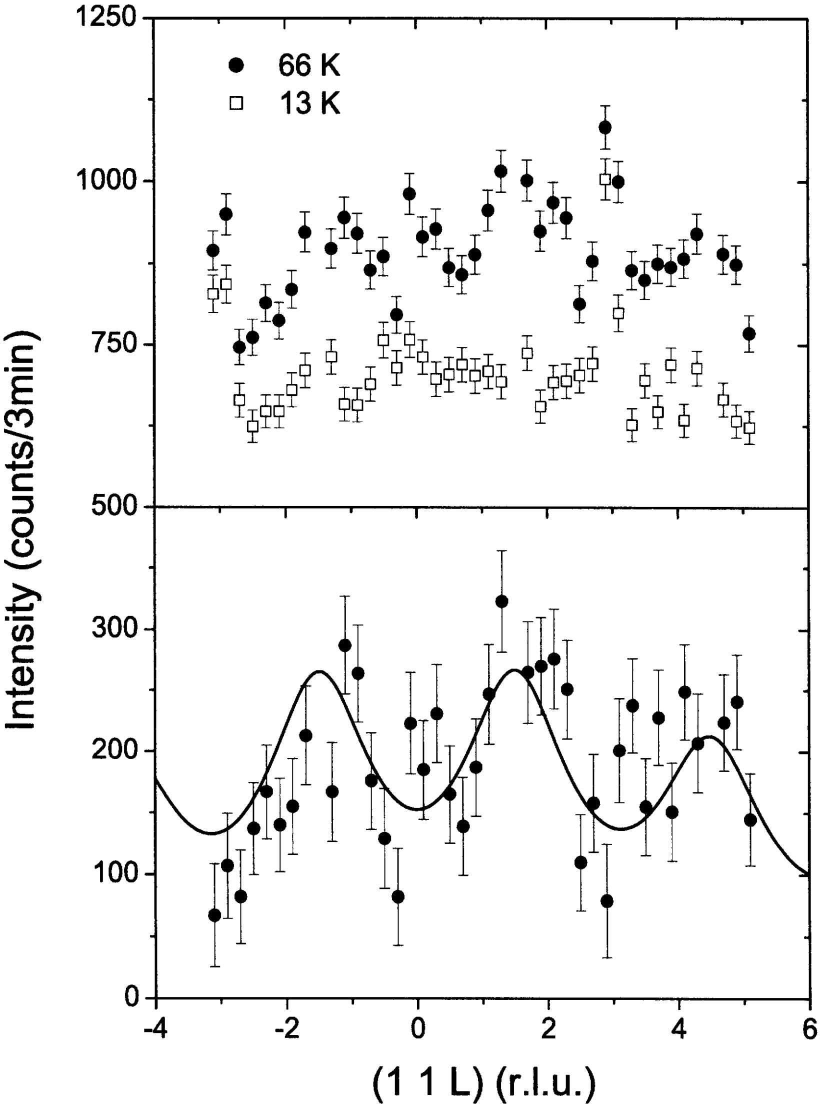

Figure 5-5: (a) This plot shows the 2D scattering rod along the L-direction measured at 66 K. Below T_N, magnetic Bragg peaks are located at $L = -1.5$, 1.5, and 4.5, whose intensities are higher than the maximum plot range in (a). (b) This plot shows the difference between the intensities at 66 K and 13 K. The solid is a guild to the eye.

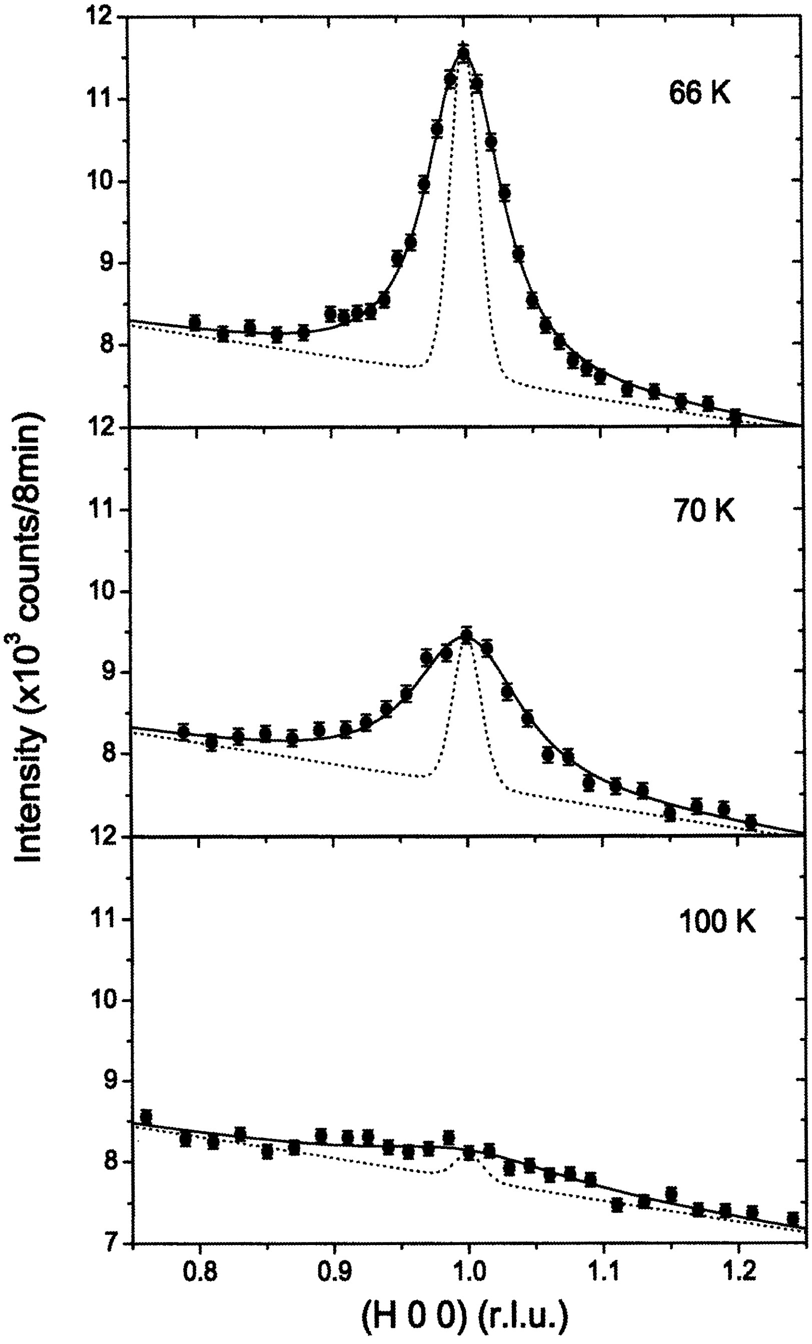

Figure 5-6: Representative scans of the quasi-elastic scattering at (1 0 0) at $T = 66$, 70 K, and 100 K. The solid lines are fits to Lorentzian convoluted with the resolution function. The dotted lines show the resolution of the instrument.

comes smaller. Above 100 K, the peak around (1 0 0) becomes too small and broad to measure. The log-log plots of $S(0)$ and ξ as a function of reduced temperature for the incident neutron energies of 13.5 meV (circles) and 30.5 meV (squares) are shown in Fig. 5-12 and 5-13. Detailed discussion of critical behavior will be presented in Section 5.4.

5.3 Polarized neutron scattering of spin fluctuations

As discussed in Chapter 2, using polarized neutron scattering technique, one can measure polarization of the spin fluctuations. In Chapter 3, polarized neutrons were used to study the polarization of the spin-wave excitations. In this chapter, they will be used to study polarization of the critical scattering above the ordering temperature. Polarized neutron scattering can distinguish between in-plane and out-of-plane spin fluctuations. As discussed in Chapter 2 and 4, if **P** and **Q** are parallel, both in-plane and out-of plane fluctuations will give rise to scattering intensity in the spin-flip channel. On the other hand, if **P** is perpendicular to **Q**, then the magnetic scattering in the spin-flip channel is due to the fluctuations that is perpendicular to both **Q** and **P**, and the magnetic scattering in the non-spin-flip channel is due to the spin component parallel to **P**.

The polarization of the spin fluctuations in jarosite were studied using inelastic polarized neutron scattering. The measurements were performed on TAS-1 spectrometer at JAEA. The detail of the instrument was discussed in Section 4.3. A single crystal of K jarosite of mass 48 mg was oriented in the (HK0) zone, where the (001) axis is perpendicular to the scattering plane. Double-focusing Heussler crystals were used to monochromate and analyze the incident and scattered neutron beam to obtain the beam polarization of about 90%, corresponding to a flipping ratio of 20. Horizontal collimations of open−80−open−open were employed. PG filters were placed in the scattered beam to reduce higher-order contaminations. The sample was cooled

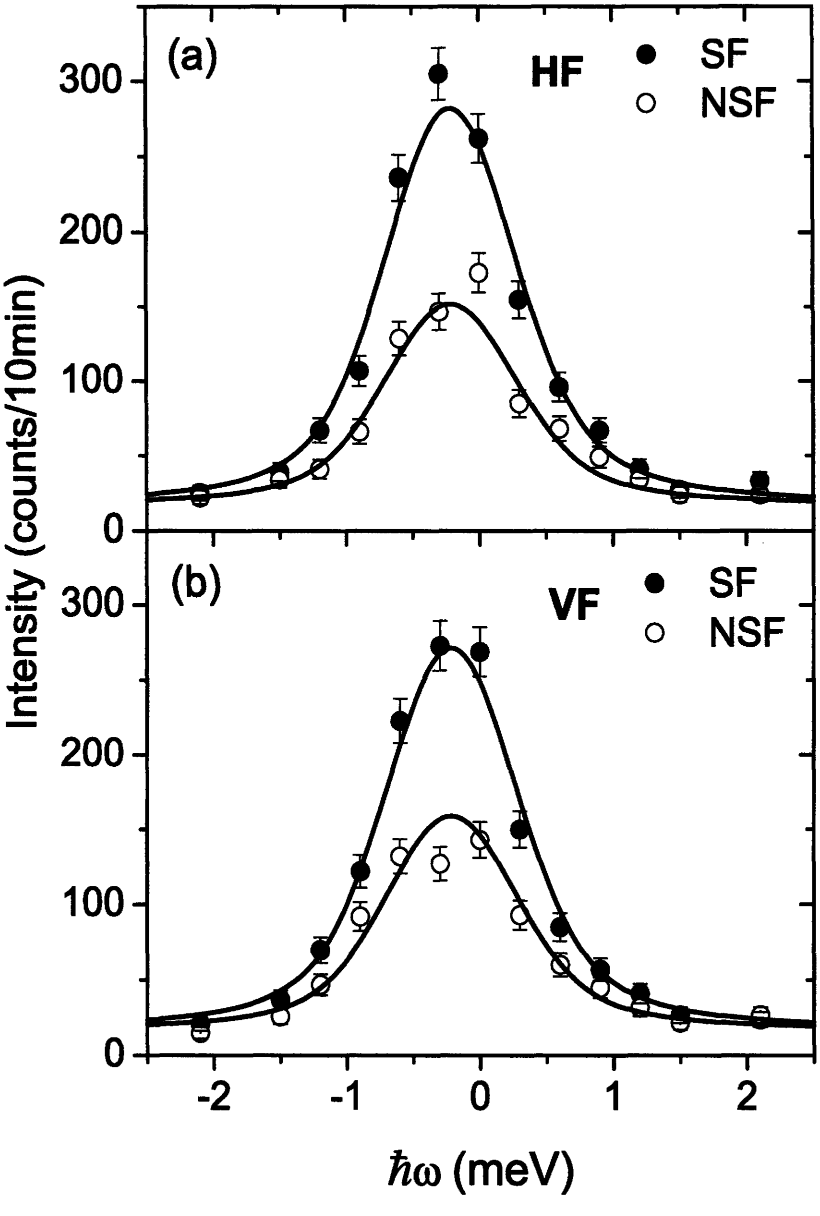

Figure 5-7: These plots show quasi-elastic scattering centered at (1 0 0) measured by polarized neutrons at 67 K, when the guide field is parallel to **Q** (a), and perpendicular to **Q** and the scattering plane (b).

by a ^{4}He close-cycle displex to 67 K.

Fig. 5-7 shows constant-**Q** scan at (1 0 0) through a quasi-elastic peak at $T = 67$ K. The observed quasi-elastic peak at zero energy was fit to Lorentzian convoluted with the experimental resolution function. Backgrounds and peak widths were kept constant for all four data sets. As previously discussed, for a guide field along **Q** (HF), all magnetic, quasi-elastic scattering is observed in the spin-flip channel, while for a guide field perpendicular to **Q** and the scattering plane (VF), the in-plane component of magnetic scattering is observed in the spin-flip channel (SF) and the out-of-plane component is observed in the non-spin-flip channel (NSF). Fig. 5-7 shows equivalent intensities in SF and NSF for both HF and VF, indicative of the predominantly in-plane spin fluctuations. This result gives direct evidence for the presence of XY symmetry discussed in the previous section.

5.4 Critical exponents α, β, γ, and ν

The critical behavior near second-order phase transitions can be characterized by a set of a few universal parameters called *critical exponents.* These exponents are independent of the detailed description of the interactions, and are dictated only by the symmetries of the systems, such as spatial dimension d, dimensionality of the order parameter n, and extent of the interaction. They illustrate the non-analytical behaviors of various thermodynamic properties indicated by the divergence at the phase transition. The most common thermodynamic quantities used to characterize the critical behaviors are the specific heat C, the staggered magnetization M, the staggered susceptibility χ, and the correlation length ξ, whose critical behavior near the phase transitions at zero field can be defined in the following forms:

$$
\begin{aligned}
C^{\pm}(T, h=0) &= A^{\pm}|t|^{-\alpha} && (5.7)\\
M(T, h=0) &= M_0|t|^{\beta} && (5.8)\\
\chi^{\pm}(T, h=0) &= \chi_0^{\pm}|t|^{-\gamma} && (5.9)\\
\xi^{\pm}(T, h=0) &= \xi_0^{\pm}|t|^{-\nu}, && (5.10)
\end{aligned}
$$

where $t = \frac{T-T_N}{T_N}$ is reduced temperature (T_N is the Néel temperature), and plus and minus signs indicate above and below T_N, respectively. Theoretical values of the critical exponents have been obtained for $n-$component spins in $d-$dimensional space, e.g., Ising ($n = 1$), XY ($n = 2$), and Heisenberg ($n = 3$). Table 5.1 shows experimental values of the critical exponents for different types of spins in 3-dimensional space [200]. These values should be compared with the theoretical values listed in Table 5.2 [200]. The agreement between the experimental values and theoretical values listed in Table 5.1 and 5.2 is indicative of the success of the renormalization-group (RG) in the studies of the critical exponents, whose properties are determined by the so-called "Wilson-Fisher $O(n)$" fixed point.

Table 5.1: Experimental values of critical exponents for different types of $n-$component spins in 3-dimensional space.

Transition type	Material	α	β	γ	ν
Ferromagnets ($n = 3$)	Fe, Ni	-0.1	0.4	1.3	-
Superfluid ($n = 2$)	^{4}He	0	0.3	1.3	0.7
Liquid-Gas ($n = 1$)	CO_2, Xe	0.1	0.3	1.2	0.7

However, frustrated antiferromagnets with non-collinear spin order exhibit unconventional critical behavior, which cannot be described by the Wilson-Fisher $O(n)$ universality class, leading to a possibility of a new universality class [201]. A symmetry analysis and Monte Carlo simulations by Kawamura show that the phase transitions of the stacked-triangular lattice antiferromagnets for both XY and Heisenberg spins in 3D are unconventional due to the presence of the chiral degree of freedom, possibly belonging to a novel universality class called the *chiral universality class* [202, 203, 204, 205]. For the $n = 2$ XY spins, the order-parameter space for frustrated non-collinear systems is $SO(2) \times Z_2$, where Z_2 represents the two-fold chiral degeneracy, and $SO(2)$ represents the rotational symmetry of the standard XY

Table 5.2: Theoretical values of critical exponents for different types of $n-$component spins in 3-dimensional space.

Transition type	α	β	γ	ν
$n=3$	-0.11	0.36	1.39	0.70
$n=2$	-0.01	0.35	1.32	0.67
$n=1$	0.11	0.32	1.24	0.63
Mean-field tricriticality	0.5	0.25	1	0.5

model [201]. Therefore, the critical exponents for this chiral universality class are different from the standard Wilson-Fisher $O(n)$ universality class listed in Table 5.2. Using Monte Carlo simulations, Kawamura was able to determine the values of the critical exponents [206], whose values are listed in Table 5.3.

Table 5.3: Critical exponents for the stacked-triangular lattice antiferromagnets in 3-dimensional space determined by Monte Carlo simulations.

Transition type	α	β	γ	ν
XY ($n=2$) or $SO(2) \times Z_2$	0.34(6)	0.253(10)	1.13(5)	0.54(2)
Heisenberg ($n=3$)	0.24(8)	0.30(2)	1.17(7)	0.59(2)

To test the theoretical prediction of this universality class, several experimental measurements on the stacked-triangular XY antiferromagnet $CsMnBr_3$ were carried out. Neutron scattering measurements were preformed independently by Ajiro and Kadowaki *et al.* [207, 208] in Japan, and Mason *et al.* [209] at McMaster University to measure the critical exponents β, γ, and ν. In addition, high-precision specific-heat measurements were conducted to extract the critical exponent α by Wang *et al.* [210] at the University of California at Santa Cruz and Deutschmann *et. al* [211] in Germany. Their results are summarized in Table 5.4. These critical exponent values should be compared with those obtained from the Monte Carlo simulations for XY spins listed in Table 5.3. The agreement give strong evidence for the presence of the novel chiral universality class. However, more recent work by the McMaster group [212] using elastic neutron scattering to determine the magnetic phase diagram of $CsMnBr_3$ shows that the application of a field splits the antiferromagnetic transition, and results in an intermediate phase. This phase terminates near $H = 0$ and $T = 8.32$ K, which is believed to be a tetracritical point. Therefore, they argue that the anomalous critical properties may not suggest a new universality class, but may be due to the tetracriticality.

Table 5.4: Experimental values of the critical exponents for the stacked-triangular lattice antiferromagnet $CsMnBr_3$ in 3-dimensional space.

Reference	α	β	γ	ν
Aijiro *et al.* [207]	–	0.25(1)	–	–
Kadowaki *et al.* [208]	–	–	1.10(5)	0.57(3)
Mason *et al.* [209]	–	0.21(2)	1.01(8)	0.54(3)
Wang *et al.* [210]	0.39(9)	–	–	–
Deutschmann *et. al* [211]	0.40(5)	–	–	–

Similar to the stacked-triangular lattice antiferromagnet $CsMnBr_3$, the presence of the chiral degree of freedom in the kagomé lattice antiferromagnet may lead to the observation of the same set of critical exponents indicative of the chiral universality class in jarosite. In the following section, the experimental values of the critical exponents α, β, γ, and ν obtained by means of the thermodynamic and neutron scattering measurements on jarosite are presented.

The details of the specific heat measurements on powder samples of K and Ag jarosites were discussed in Section 3.2. The specific heat measurements of a single crystal sample of K jarosite were carried out using a PPMS. To extract spin-only contributions to the specific heat, the specific heat of a non-magnetic $KGa_3(OH)_6(SO_4)_2$ (Ga jarosite), which was then re-scaled to match the specific heat of K jarosite at high temperature, was used to subtract out the lattice-contribution background (BG) from the data. Fig. 5-8 show the spin-only specific heat C_s of K jarosite after subtracting the lattice contributions with an over-all scaling factor of 1.245.

This spin-only specific heat was then fit to Eq. 5.7 for $67.5 < T < 80$ K. The open symbols in Fig. 5-8 show the fitting range. The critical exponent α is dependent of the BG scaling factor. The inset of Fig. 5-10 shows the value of the reduced-χ^2 as a function of the scaling factor. The open symbol indicates the fit to Eq. 5.7 at the scaling factor of 1.245. Fig. 5-10 shows the dependence of the critical exponent on the scaling factor. The value of the critical exponent increases monotonically as a function of the scaling factor, and falls within a range between 0.4 and 0.6. The open symbol indicates the critical exponent with the scaling factor of 1.245. The scaling factor of 1.245 was chosen because it matches well with the high temperature data of K jarosite. The data cannot be fit to a single power law for $67.5 < T < 80$ K. The best fit to the spin-only specific heat for $65.7 < T < 70.2$ K shown in Fig. 5-9 corresponds to $\alpha = 0.53(7)$ with $T_N = 64.5$ K. This value is much larger than that predicted by Kawamura [206] and that measured on $CsMnBr_3$ by Wang *et al.* [210] and Deutschmann *et. al* [211], but close to mean-field tricriticality. The dependence of α on T_N will be discussed in detail in the following section.

The order parameter measurements on a single crystal sample of K jarosite were previously discussed in Section 3.3, and the details of the critical scattering measurements above T_N were presented in Section 5.2. In the following section, the critical exponents β, γ, and ν are extracted using those results.

The magnetic Bragg peak intensity I is proportional to the square of the sublattice magnetization M, i.e. $I \propto M^2$. Therefore, according to Eq. 5.8, in the proximity of T_N, the intensity I as a function of reduced temperature should vary as a power law

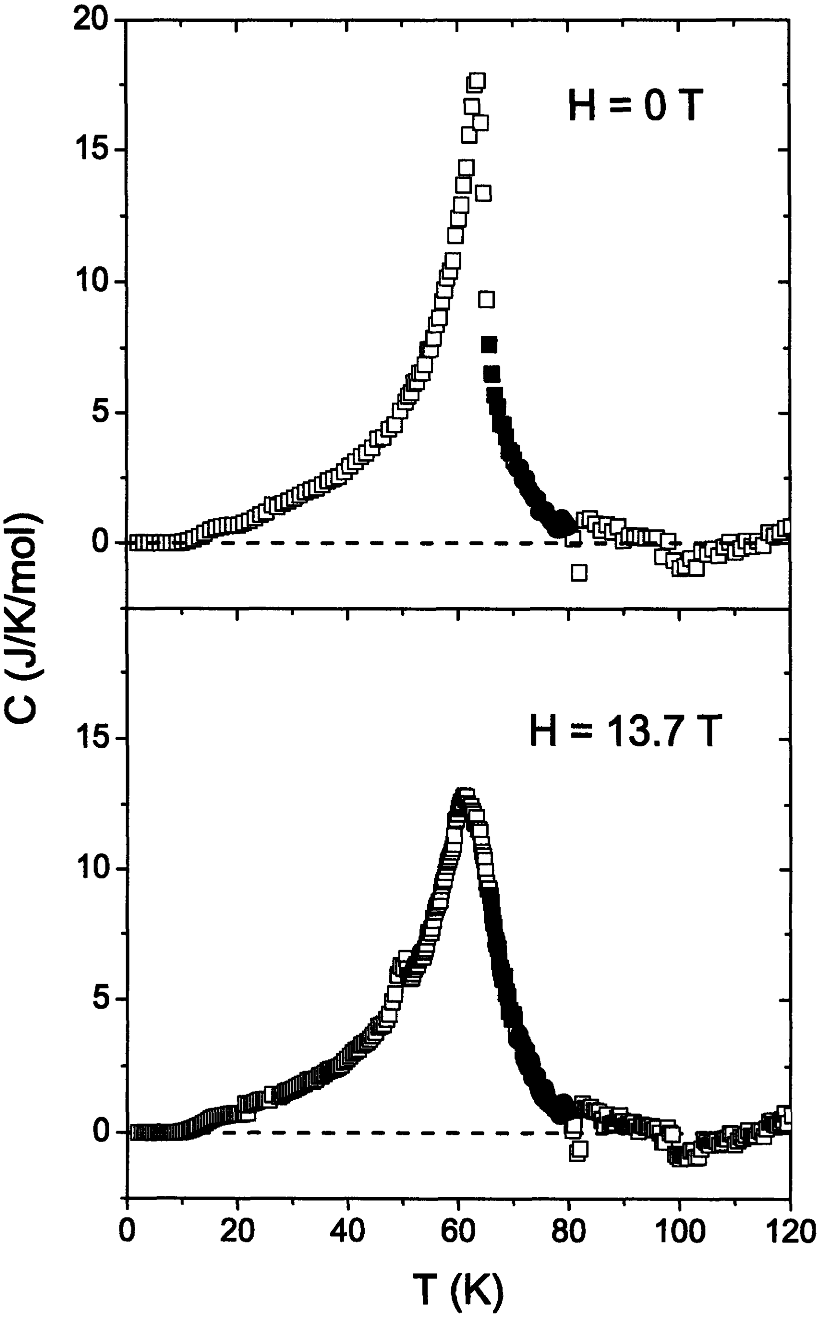

Figure 5-8: The spin-only specific heat measured on a single crystal sample of K jarosite at 0 and 13.7 T after subtracting the lattice contributions with a scaling factor of 1.245. Closed symbols show the fitting range of the data.

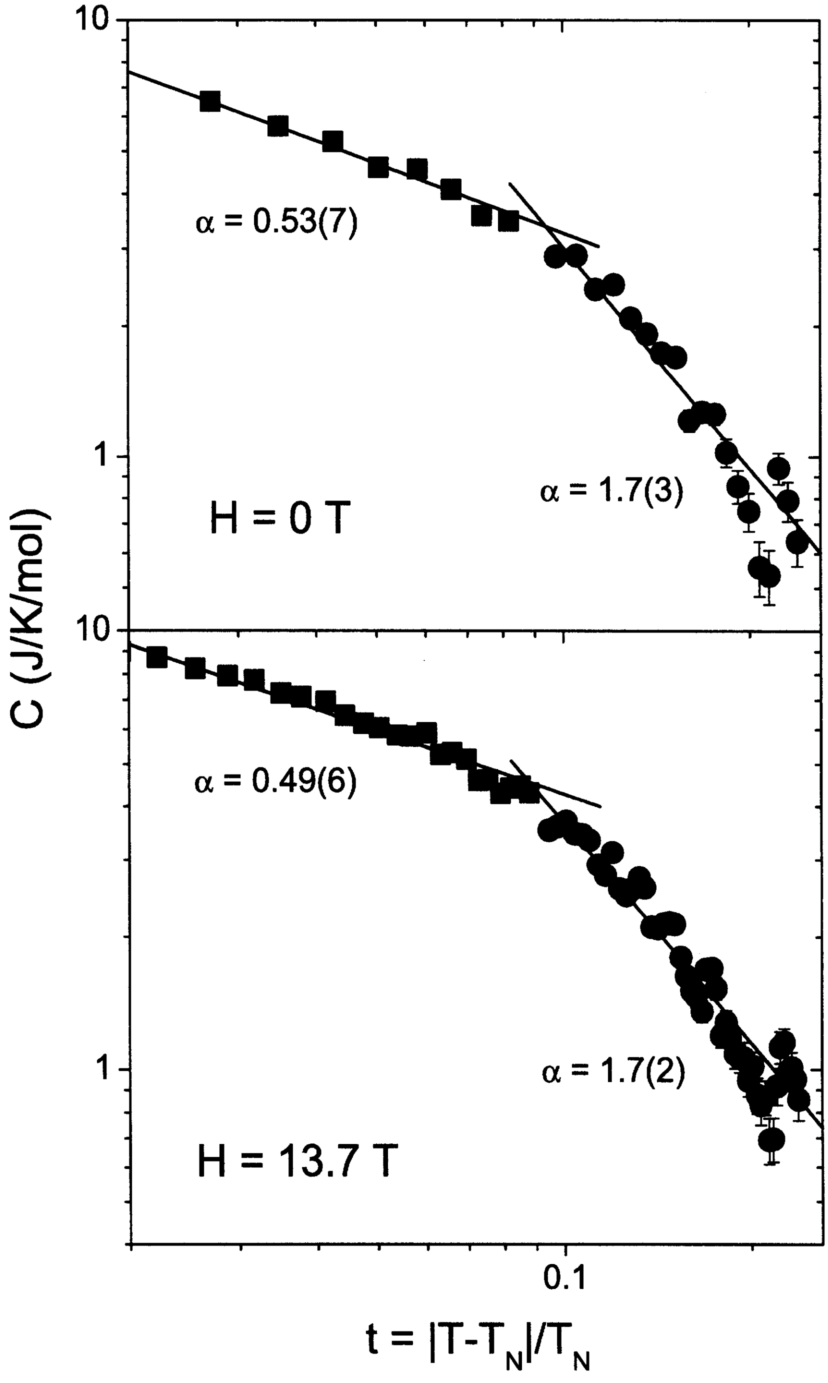

Figure 5-9: The spin-only specific heat with the BG scaling factor of 1.245 is fit to Eq. 5.7 with $T_N = 64.5$ K. The specific heat cannot be fit to one exponent for 65 K $< T <$ 80 K.

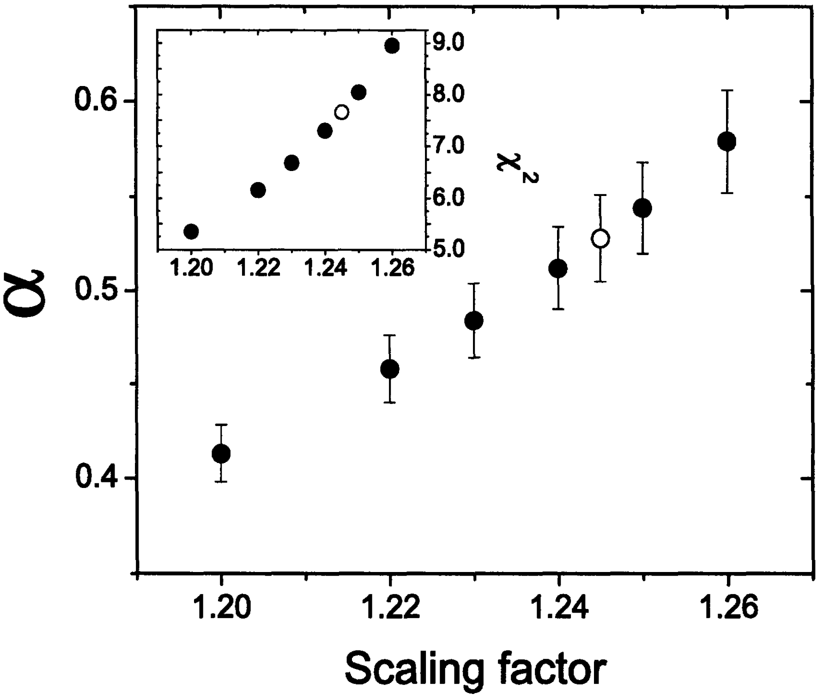

Figure 5-10: The exponent α is plotted as a function of the BG scaling factor with $T_N = 64.5$ K.

with the critical exponent equal to 2β:

$$M^2(T) \propto I(T) = I_0|t|^{2\beta}. \tag{5.11}$$

To determine β for the kagomé lattice antiferromagnet, the magnetic Bragg peak integrated intensities at $Q = (1\ 1\ \frac{3}{2})$ were measured on a single crystal sample of K jarosite as a function of temperature. Fig. 4-11(b) shows the temperature dependence of the order parameter down to base temperature. The measurements above T_N were used to determine the background, which is temperature-independent.

The energy-integrated intensities of the quasi-elastic neutron scattering above T_N were measured at $Q = (1\ 0\ 0)$. Fig. 5-6 shows three representative scans at $T = 66$, 70, and 100 K with the neutron incident energy of 13.5 meV. The data were fit to Lorentzian shown in Eq. 5.6 convoluted with the resolution function to extract $S(0)$ and ξ. From Eq. 5.6, $S(0)$ is proportional to the sublattice susceptibility χ, and ξ is

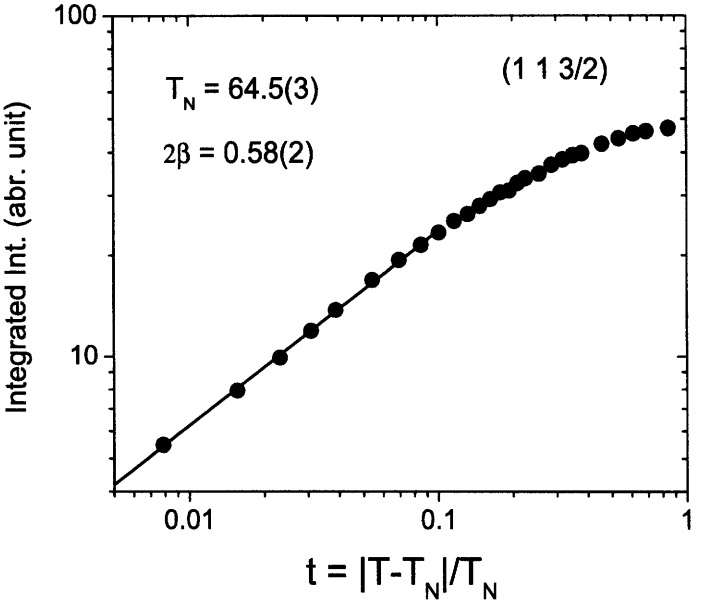

Figure 5-11: The log-log plot of the magnetic Bragg peak integrated intensity as a function of reduced temperature for $Q = (1\ 1\ \frac{3}{2})$. The line is the result of a fit to power law with the critical exponent $2\beta = 0.58(2)$ and $T_N = 64.5(3)$ K.

the correlation length.

The magnetic Bragg peak integrated intensity I, the sublattice susceptibility χ ($\propto S(0)$), and the correlation length ξ were then fit to power laws as a function of reduced temperature using Eq. 5.11, 5.9, and 5.10, respectively. The log-log plots of I, $S(0)$, and ξ as a function of reduced temperature are shown in Fig. 5-11, 5-12, and 5-13, respectively. The solid lines are the best fits to those equations.

The values of the critical exponent varies with T_N. Fig. 5-14 shows the variation of the fit critical exponent with T_N for 63.1 K $\leq T_N \leq$ 65.9 K. As T_N increases, the values of the critical exponents α, γ, and ν increase monotonically, while the value of the critical exponent β decreases almost linearly. The inset shows a reduced$-\chi^2$ as a function of T_N for the same range of T_N. While, the values of the reduced$-\chi^2$ of α and γ decrease monotonically as T_N decreases, that of ν remains roughly constant throughout the whole range of T_N, indicative of much smaller dependence of the reduced$-\chi^2$ on T_N. β shows strong dependence on T_N with the lowest reduced$-\chi^2$ at $T_N = 64.5$ K. Using $T_N = 64.5$ K, deduced from the specific heat measurements and

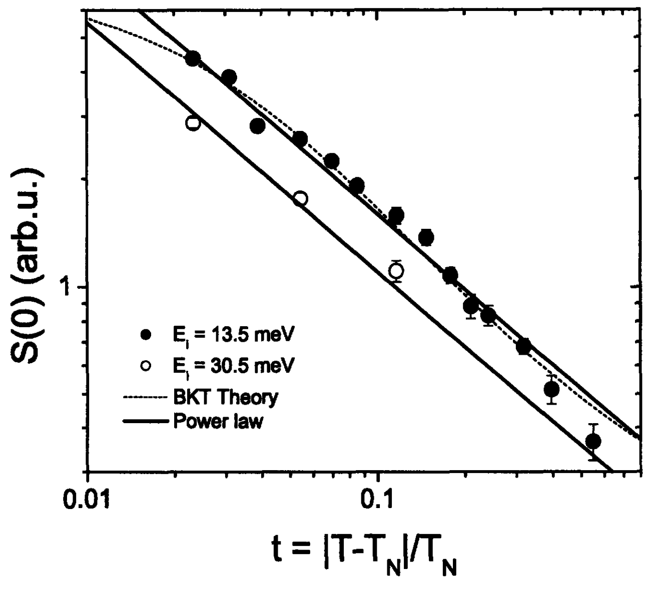

Figure 5-12: The log-log plot of $S(0)$ as a function of reduced temperature for the incident neutron energies of 13.5 meV (circles) and 30.5 meV (squares). The solid lines are the result of a fit to power law with the critical exponent $\gamma = 0.70(7)$ and $T_N = 64.5$ K. The dashed line is a fit to the Berezinskii-Kosterlitz-Thouless theory for the 2D XY model described in the text with $\nu = 0.5$ and $T_{BKT} = 60.0$ K.

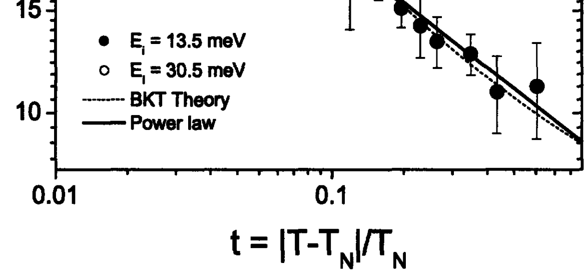

Figure 5-13: The log-log plot of the correlation length ξ as a function of reduced temperature for the incident neutron energies of 13.5 meV (circles) and 30.5 meV (squares). The solid line is the result of a fit to power law with the critical exponent $\nu = 0.37(7)$ and $T_N = 64.5$ K. The dashed line is a fit to the Berezinskii-Kosterlitz-Thouless theory for the 2D XY model described in the text with $\nu = 0.5$ and $T_{BKT} = 60.0$ K.

neutron scattering measurements of the order parameter at zero field, we obtained $\alpha = 0.53(7)$, $\beta = 0.29(1)$, $\gamma = 0.70(7)$, and $\nu = 0.37(7)$, where the errors correspond to three times the statistical error obtained from the fit. The best fits for $S(0)$ and ξ are shown by the solid lines in Fig. 5-12 and 5-13.

The measured critical exponents for the kagomé lattice antiferromagnet $KFe_3(OH)_6(SO_4)_2$ are summarized in Table 5.5 along with the theoretical predictions for the $SO(2) \times Z_2$ universality class in 3D [206], standard XY model in 3D, mean-field tricritical point, and Ising model in 2D. The experimental values are not consistent with any of these theoretical models, leading to a possibility that the kagomé lattice antiferromagnet belongs to a new universality class[1]. In particular, they are very different from the standard XY model in 3D. However, the critical exponents are suggestively close to the mean-field tricritical predictions, although this is probably coincidental. The value of the exponent β for the order parameter is also suggestively close to a 2D XY model. Using the modified renormalization group, Bramwell and Holdsworth [213] predicted $\beta = \frac{3\pi^2}{128} = 0.231$ for the 2D XY model, which is reasonably close to 0.29(1) obtained in jarosite. The agreement becomes better for $T_N = 64.0$ K, which gives $\beta = 0.23(1)$. The discussion of the 2D XY model in terms of the Berezinskii-Kosterlitz-Thouless theory will be presented in the next section.

There are a couple of exponent identities representing the relation among the critical exponents α, β, γ, and ν. The first identity is called *Rushbrooke's Identity* relating α, β, and γ by the following relation:

$$\alpha + 2\beta + \gamma = 2. \tag{5.12}$$

The second identity is called *Joshephson's Identity* relating α and ν to the dimensionality of the system d, which is given by:

$$d = \frac{2 - \alpha}{\nu}. \tag{5.13}$$

---

[1] The specific heat data can be fit to the Onsager solution for the 2D Ising model. This point will be explored in the next section.

Table 5.5: Experimental values of the critical exponents for the kagomé lattice antiferromagnet $KFe_3(OH)_6(SO_4)_2$ with $T_N = 64.5$ K

Exponents	α	β	γ	ν
Experimental	**0.53(7)**	**0.29(1)**	**0.70(7)**	**0.37(7)**
$SO(2) \times Z_2$ in 3D [206]	0.34(6)	0.253(10)	1.13(5)	0.54(2)
XY model in 3D	-0.01	0.35	1.32	0.67
Mean-field tricritical	0.5	0.25	1	0.5
Ising model in 2D	$0^\dagger$	0.125	1.75	1

† Logarithmic divergence.

These two exponent identities, which are also known as *hyperscaling relations*, are obtained from the generalized homogeneity assumption in the d dimension. For the stacked-triangular lattice antiferromagnet $CsMnBr_3$, using the critical exponents in Table 5.1 ($\alpha = 0.40, \beta = 0.21, \gamma = 1.01$, and $\nu = 0.54$), one obtains $\alpha + 2\beta + \gamma \approx 1.83$, and $d \approx 2.96$, which is reasonably consistent with the hyperscaling relations with $d = 3$.

Fig. 5-15 shows the hyperscaling relations as a function of T_N for K jarosite. Rushbrooke's Identity deviates from 2 to a smaller value as T_N increases. On the other hand, d becomes larger as T_N increases. Rushbrooke's Identity obtains a value of 1.8 at $T_N = 64.5$ K, which is close to the hyperscaling relation (Eq. 5.12). However, Joshephson's Identity gives $d = 4.0$, which is not consistent with $d = 2$ or 3, the dimensionality of the system. One would expect that $d = 2$ for jarosite due to the well-separated kagomé planes. However, it should be pointed out that at a lower value of T_N, the agreement with the hyperscaling relations improves. For example, at $T_N = 64$ K, Rushbrooke's Identity obtains a value of 1.9 and Joshephson's Identity gives $d = 3.2$. The facts that the hyperscaling relations are not satisfied, and that these critical exponents do not fall into any known universality classes, give rise to three interesting possibilities. First, the kagomé lattice antiferromagnet may belong

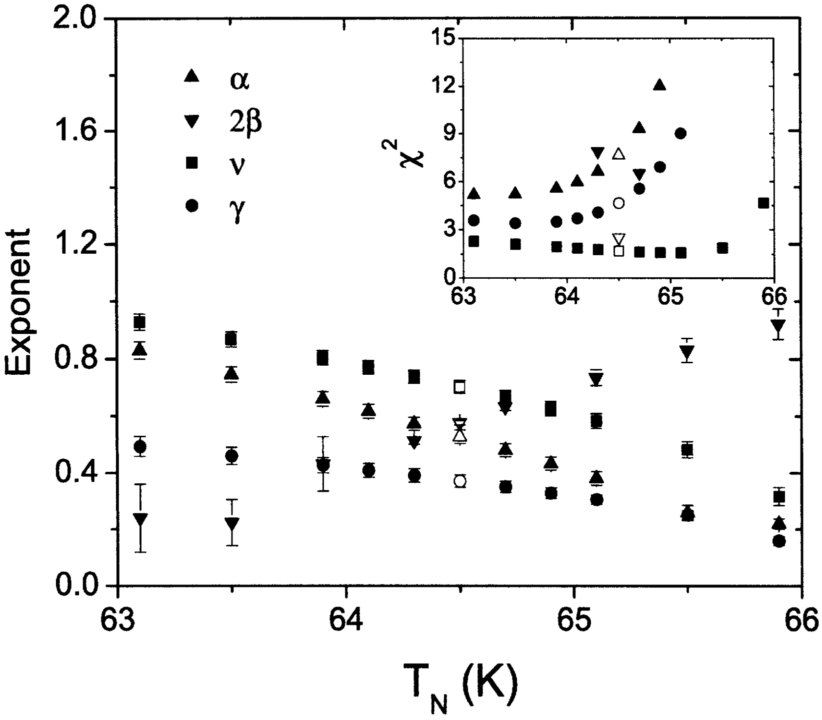

Figure 5-14: Variation of the critical exponents with the critical temperature T_N for 63.1 K $\leq T_N \leq$ 65.9 K. The inset shows the reduced$-\chi^2$ as a function of T_N for the same range of T_N.

to a novel class of material with a distinct set of critical exponents. Second, suggested by the similarity between the critical exponents of jarosite and those of the tricriticality, another possible explanation of the unusual critical exponents in jarosite is the existence of the tricritical point at $T_C \leq T_N$ as discussed in Chapter 3. As in the case of $CsMnBr_3$, Gaulin *et al.* argued that the presence of the tetracritical point at T_N and $H = 0$ is probably sufficient to explain the unusual critical exponents without the necessity of a new universality class [212]. Third, the similarity is coincidental, and the kagomé lattice antiferromagnet really belongs to a 2D XY model with discrete Z_2 symmetry due to the presence of spin chirality. We will focus on the third possibility, and argue that jarosite belongs to the $SO(2)$ and Z_2 universality classes.

The 2D XY model is governed by the Berezinskii-Kosterlitz-Thouless (BKT) theory, while the Z_2 symmetry in 2D belongs to the same universality class as a 2D Ising model. In this case, the critical behavior in the specific heat is indicative of

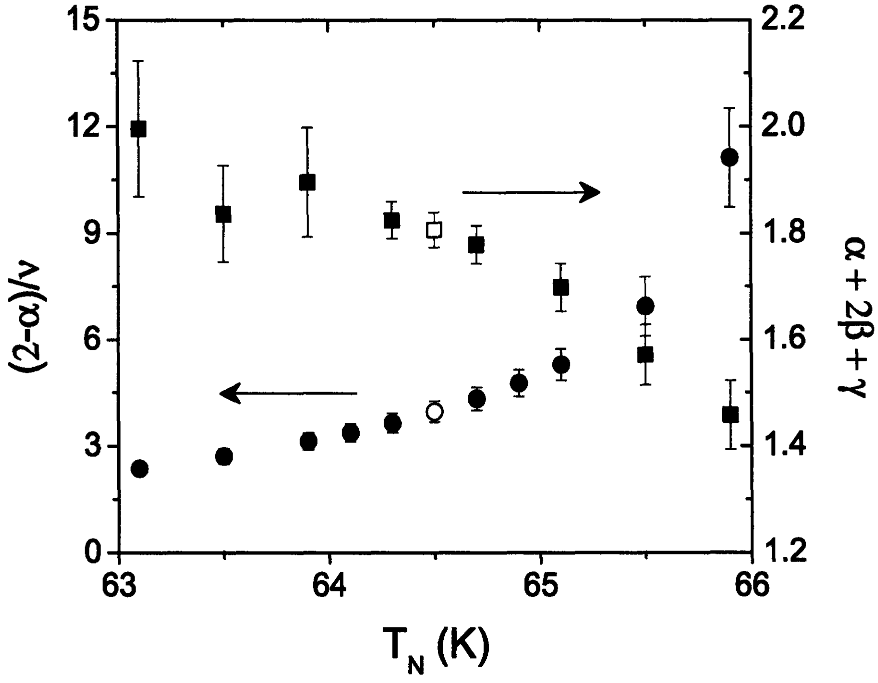

Figure 5-15: Variation of the hyperscaling relations with the critical temperature T_N for 63.1 K < T_N < 65.9 K. The open symbols correspond to the best-fit values of the critical exponents with $T_N = 64.5$ K.

the spontaneous breaking of the discrete Z_2 symmetry at T_N, while the critical behavior observed in S(0) and correlation length can be described by the continuous $SO(2)$ symmetry due to planar spins, giving rise to the BKT transition of vortex unbinding at $T_{BKT} \leq T_N$. It has been shown by Monte-Carlo simulations that the Z_2 transition occurs at higher temperature than the BKT transition in a triangular lattice [214, 215, 216, 217] and in a fully frustrated XY model in a square lattice [218]. Similarly, it is expected that the 2D antiferromagnetic XY model with the DM interaction in a kagomé lattice has the discrete Z_2 symmetry due to spin chirality and the $SO(2)$ spin-rotational symmetry. Furthermore, the exponent β of 0.29(1) can be understood as a result of a finite-site 2D XY model [213, 219]. The presence of $SO(2)$ and Z_2 symmetries in jarosite will be further discussed in detail in the following section.

5.5 $SO(2)$ and Z_2 symmetries in 2D

As discussed in the previous section, the critical exponents α, β, γ, and ν for jarosite do not belong to any known universality classes. However, due to a combination of the DM interaction, weak interplane coupling, and frustration, this realization of an antiferromagnetic kagomé lattice is expected to show a similar critical behavior to the frustrated XY model in 2D. One characteristic of such a system is the presence of two order parameters. In an antiferromagnetic triangular lattice, these two order parameters are the in-plane magnetization with a continuous rotational $SO(2)$ symmetry, and the vector chirality defined in Eq. 5.1 with a discrete Z_2 symmetry. Monte Carlo simulations on the classical XY antiferromagnet, and the classical and quantum Heisenberg antiferromagnet with easy-plane anisotropy or the XXZ model on a triangular lattice (TAXY) show the feature of the BKT transition, corresponding to vortex-antivortex unbinding, and of an Ising-like transition, associated with chiral order, which occurs at a slightly higher temperature than the BKT transition [215, 216, 217, 220, 221]. Two sets of critical behaviors for TAXY belong to the 2D XY and 2D Ising models, separately. Monte Carlo simulations on the fully frustrated XY model (FFXY) on a square lattice show the BKT transition followed by the Ising-like transition at a slightly higher temperature [218, 222, 223]. However, in contrast to TAXY, Monte Carlo simulations by Ramirez-Santiago *et al.* shows that FFXY appears to be in a novel universality class, whose critical exponents are different from separate 2D XY and 2D Ising models [224, 225].

For TAXY, it was shown by Lee *et al.* [220] that besides spin-wave excitation and vortex-antivortex unbinding, there is an addition type of elementary excitation due to domain-wall formation (solitons) between regions with opposite staggered chirality, similar to domain walls formed in the 2D Ising model. While the spin-wave and vortex excitations cause the loss of orientational and topological order, respectively, the solitons destroy the chiral order in the 2D frustrated XY model. Table 5.7 shows transition temperatures T_C and T_{BKT} for the XXZ model on the triangular lattice and the fully frustrated XY model on the square lattice.

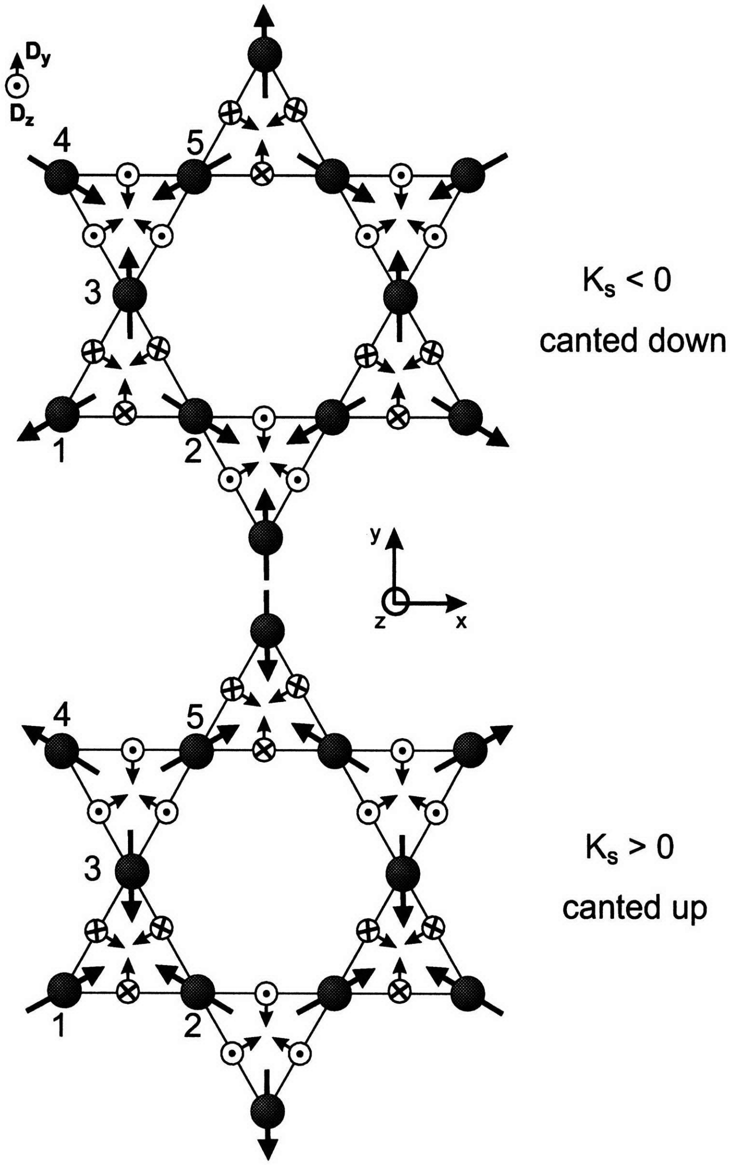

Figure 5-16: Spin structures for positive and negative scalar chirality, which represent two degenerate spin states for the antiferromagnetic kagomé lattice with the DM interaction.

For the antiferromagnetic kagomé lattice in the absence of spin anisotropy, the phase transition occurring above the BKT transition is not of the Ising type as pointed out by Korshunov [226, 227] due to the appearance of domain walls associated with the mixing of many states with different topology rather than two states in the case of the triangular lattice. However, for jarosite, the presence of the DM interaction lifts some of those degeneracies, giving rise to two degenerate ground states. In this case, the scalar chirality defined in Eq. 5.2, rather than the vector chirality in the case of the triangular lattice or FFXY [215, 216, 217, 218, 222, 223], can be taken as the order parameter. The scalar chirality, which is a psudoscalar quantity, is non-zero due to spin canting in the direction perpendicular to the kagomé plane, giving rise to a non-coplanar spin structure. Fig. 5-16 shows the two degenerate ground states, associated with positive and negative scalar chirality on a single kagomé plane, and Fig. 5-23 shows examples of domain walls between these two states.

The underlying symmetry of the spin Hamiltonian with the DM interaction (Eq. 5.14) is a time-reversal symmetry, which is equivalent to a Z_2 symmetry. The spin Hamiltonian for jarosite is:

$$\mathcal{H} = \sum_{nn} \left[J\,\mathbf{S}_i \cdot \mathbf{S}_j \,+\, \mathbf{D}_{ij}\,(\cdot\mathbf{S}_i \times \mathbf{S}_j) \right], \tag{5.14}$$

where Σ_{nn} indicates summation over pairs of nearest neighbors, $\mathbf{D}_{ij} = [0, D_y(i,j), D_z(i,j)]$ is the DM vector. The time-reversal operator, which acts on $\mathbf{S}$ and changes it to $-\mathbf{S}$, transforms one ground state into the other and vice versa, when globally acting on all spins. It should be pointed out that $SO(2)$ is not an underlying symmetry of the Hamiltonian due to the DM term. Since the time reversal or Z_2 symmetry is discrete, long-range order associated with the simultaneously breaking of this symmetry is not precluded by the Mermin-Wagner theorem [228]. Therefore, it is possible that the time-reversal symmetry is broken at finite temperature, giving rise to the critical behavior belonging to the 2D Ising universality class.

For jarosite, we propose a scenario where both $SO(2)$ and Z_2 are present. The system shows the presence of two symmetries associated with continuous planar rotation of spins and discrete Ising-like behavior, depending on which kind of measurements are performed. Neutron scattering measurements show a signature of the BKT transition belonging to the $SO(2)$ universality class, which can be observed in the critical behavior of the correlation length and sublattice susceptibility or S(0). Specific heat measurements show a feature of the 2D Ising transition due to the spontaneously breaking of the Z_2 symmetry. Since the Z_2 and $SO(2)$ symmetries are coupled to each other in jarosite, once the Z_2 symmetry is broken, the $SO(2)$ symmetry is also broken. Therefore, we cannot probe the critical behavior near the BKT transition, which would occur at 60.0 K, slightly lower than the Ising transition, which occurs at 64.5 K. It is interesting to note that neutron scattering gives the same scattering cross section for both degenerate ground states shown in Fig. 5-16. The energy barrier separating the two ground states is much smaller than the energy resolution of the neutron beam, making neutron scattering insensitive to the existence of the two degenerate ground states. Furthermore, the in-plane energy gap at 2 meV, which exists below T_N, also appears to go to zero at T_N as shown in Fig. 4-11. This implies that above T_N neutrons would see the full $SO(2)$ symmetry and be insensitive to the Z_2 symmetry. Therefore, it is not possible to measure the Ising order parameter or Ising critical behavior due to the Z_2 symmetry using neutron scattering. On the other hand, the divergence of the specific heat at the 2D Ising ordering temperature conceals the behavior of the specific heat at the BKT transition, which shows a broad maximum at temperature slightly above T_{BKT} [229, 230], making it undetectable. In addition, specific heat is a macroscopic and extensive quantity, which is sensitive to the underlying symmetry of the spin Hamiltonian, which is the time-reversal or Z_2 symmetry for jarosite.

5.5.1 Berezinskii-Kosterlitz-Thouless theory for 2D XY model

In 1966, Mermin and Wagner showed that in the thermodynamic limit, the 2D XY model cannot sustain long-range order at $T > 0$ [228]. However, other physicists argued that the existence of a phase transition at $T > 0$ is possible, indicated by a divergence of the susceptibility and correlation length [231, 232, 233, 234]. To resolve this seemingly contradiction, Berezinskii [235], Kosterlitz and Thouless [236] introduced a theory to explain a phase transition to the so-called topological order in two dimensions for the two-dimension solid, neutral superfluid, and $XY-$spin model, which is hereafter collectively called a 2D XY model. Berezinskii, Kosterlitz and Thouless showed that although there is no spontaneous symmetry breaking and long-range order, the 2D XY model shows a phase transition to a state with infinite correlation length at low temperature. This phase transition is characterized by a sudden change in the response to an external perturbation, such as a magnetic field [237]. In the high-temperature phase ($T > T_{BKT}$), the antivortex-vortex pairs unbind and isolated vortices are formed. In the low-temperature phase ($T < T_{BKT}$), the energy of an isolated vortex is so large that it is unfavorable to form isolated vortices, and the antivortex and vortex are bound together. The transition temperature T_{BKT}, where the antivortex-vortex binding occurs, can be calculated by comparing the energy of a single vortex or antivortex to the entropic free energy. For the XY spin in 2D, the transition temperature is approximately equal to [237]:

$$k_B T_{BKT} \approx \pi J, \tag{5.15}$$

where J is the next-nearest neighbor interaction. The BKT theory predicts an exponential singularity at T_{BKT}, where the correlation length ξ and the sublattice magnetic susceptibility χ diverge exponentially for $T^+ \rightarrow T_{BKT}$ as described by the following equations [237, 236]:

$$\begin{aligned} \xi(t) &= a_\xi e^{b_\xi t^{-\nu}} && (5.16) \\ \chi(t) &= a_\chi e^{b_\chi t^{-\nu}}, && (5.17) \end{aligned}$$

where $t = \frac{|T-T_{BKT}|}{T_{BKT}}$, $\nu = 0.5$, and b_ξ and b_χ are non-universal parameters.

The BKT theory successfully explains phase transitions in dilute ^{4}He$-^3$He superfluid mixtures [238], thin superconducting aluminum films [239], and planar Josephson junction arrays [240]. However, the theory fails to explain a phase transition in a realization of the XY spins in 2D. The difficulty is due to the lack of a perfect planar spin system, which does not exist in nature. The closest realization of the planar spins is the Heisenberg model with easy-plane anisotropy, where it is more preferable for spins to lie within the plane, but the out-of-plane fluctuations are still allowed. Monte-Carlo-Molecular dynamics simulations by Mertens *et al.* [241, 242] show that to minimize the exchange energy at the vortex core, the spins near the center cant out of the plane. Furthermore, in a study of a XXZ model on a square lattice by means of Monte-Carlo simulations, Cuccoli *et al.* showed that an arbitrary small easy-plane anisotropy can induce a BKT transition at $T_{BKT} \neq 0$ [229]. The realizations of the 2D XY model found in literatures includes $BaNi_2(PO_4)_2$ [243, 244], $BaNi_2(VO_4)_2$ [245, 246], stage-2 $CoCl_2$-graphite intercalation compounds (GIC) [247], and Rb_2CrCl_2 [248]. Most of these materials are not perfect planar systems, but rather Heisenberg spin systems with easy plane anisotropy. They all appear to have two critical temperatures associated with the BKT transition and 3D long-range order, which occurs at higher temperature than the BKT transition. Table 5.6 shows the theoretical and experimental values of ordering temperatures for the 2D XY systems.

For jarosite, the weakly-coupled kagomé planes and strong easy-plane anisotropy in jarosite result in the spatial two dimensions and XY spins, which should be best described by the BKT theory. The out-of-plane component of the DM vector causes a reasonably large easy-plane anisotropy, which survives at high-temperature probably up to 100 K, indicated by anisotropic magnetic susceptibility and neutron scattering measurements of spin fluctuations above T_N. However, compared with other similar Heisenberg spin systems with easy-plane anisotropy, such as $BaNi_2(PO_4)_2$, $BaNi_2(VO_4)_2$, stage-2 $CoCl_2$-GIC, and Rb_2CrCl_4, jarosite has a relatively large interlayer coupling J_c. While the ratio of J/J_c for most compounds with suggestive evidence of the BKT transition is as large as 10^3, it is about 10^2 in jarosite. This relative small J/J_c indicates that 3D nature is more significant in jarosite near the ordering temperature than in those compounds. Nevertheless, neutron scattering measurements of spin fluctuations at 66 K show that the correlation length along

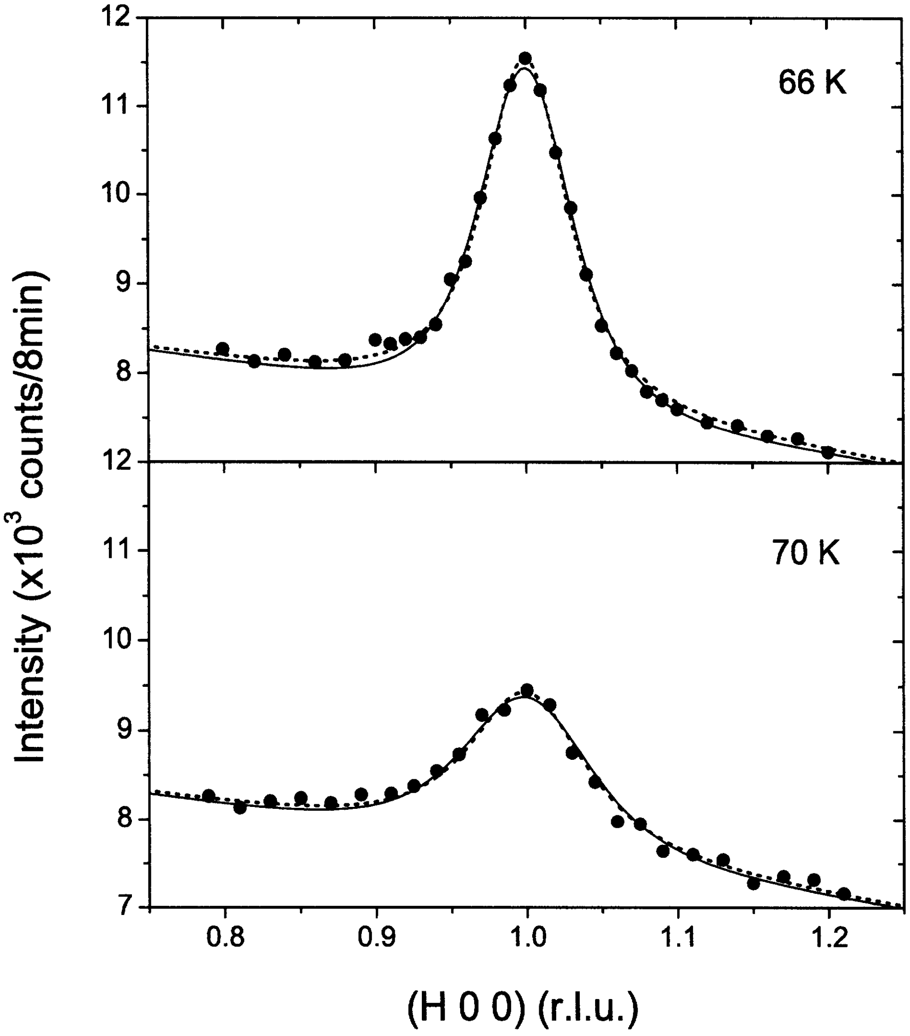

Figure 5-17: The quasi-elastic scattering intensities measured at 66 K and 70 K are fit to Lorentzian to the $3/2^{th}$ power (solid line), and to Lorentzian (dotted line).

the $c-$direction is a few angstroms, which translates to half of the interlayer separation. Therefore, close to T_N, one would expect that 3D correlations in jarosite are very short-ranged, and 2D critical behavior still dominates, which might be a result of geometric frustration. Furthermore, T_N appears to be too large to be exclusively caused by the interlayer coupling. Instead, the DM interaction within the planes is more likely to explain the long-range order in this layered antiferromagnetic system [39].

Bramwell *et al.* proposed a phenomenological finding that only when connected clusters grow to sizes greater than $N_{eff} = J/J_c$ spins, does the interlayer coupling become relevant [213, 219, 249]. They argued that at the critical point, the renormalization of the length scale from l to l' does not change the exchange coupling J, but will rescale any relevant perturbations to the spin Hamiltonian such as J_c to a larger value, i.e. $J_c(l') = l^{\mu} J_c$, where $\mu \leq d$ is the scaling dimension. When $J_c(l')$ is approximately equal to J, the system becomes three-dimensional, giving a characteristic length scale $L_{eff} = (J/J_c)^{1/\mu}$. For classical scaling containing only Gaussian fluctuations, μ is equal to $d = 2$, giving $L_{eff} = \sqrt{J/J_c}$. A plot of the correlation length ξ, measured on a single crystal sample of K jarosite at NCNR and HFIR, as a function of temperature (Fig. 5-18) shows that ξ is small than L_{eff} for the whole temperature range of the measurements. Therefore, the crossover to the 3D critical regime was not observed in jarosite.

The critical behavior of the order parameter can be understood as a result of a finite-size-induced magnetization. The BKT theory for the *infinite* 2D XY model predicts that the magnetization below the critical temperature is zero. However, Berezinskii and Blank argued that a finite 2D XY system can have a measurable finite-size-induced magnetization [250]. Bramwell *et al.* studied a universal behavior of this magnetization, and identified the critical exponent $\beta = 0.23$ [249]. For the classical 2D XY model, the magnetization can be calculated exactly for a system

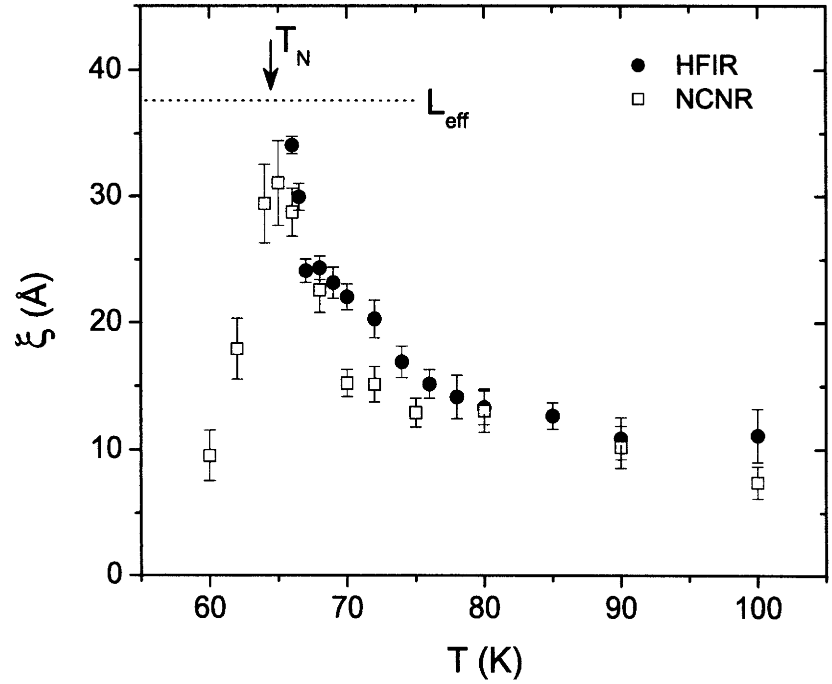

Figure 5-18: A correlation length as a function of temperature measured on a single crystal sample of K jarosite at NCNR and HFIR. A dotted line shows $\xi = L_{eff}$.

with N spin assuming that only a quadratic term is retained in the expansion [249]:

$$M(N,T) = \left\langle \left| \frac{1}{N} \sum_{i=1,N} \mathbf{S}_i \right| \right\rangle = \left[\frac{1}{2N} \right]^{1/8\pi K}, \tag{5.18}$$

where $K = \frac{J}{k_B T}$ is the spin-wave stiffness and the angular bracket represents a thermal average. In the thermodynamic limit, where $N \rightarrow \infty$, the magnetization goes to zero. As pointed out by Bramwell *et al.*, in the renormalization group of the infinite system, $K = K_{eff}$ jumps discontinuously from 0 at high temperature to a universal value of $2/\pi$ at T_{BKT}. Therefore, for the infinite system, the magnetization vanishes below T_{BKT} as $N \rightarrow \infty$. However, for a finite-size system ($N < \infty$), K_{eff} continuously drops to zero, giving a non-zero magnetization, which smoothly varies with temperature with a universal value of the exponent $\beta = 0.231$.

For jarosite, in approaching T_N from high temperature, ξ follows the exponential form characteristic of the BKT transition. At T_N, the system enters a long-range

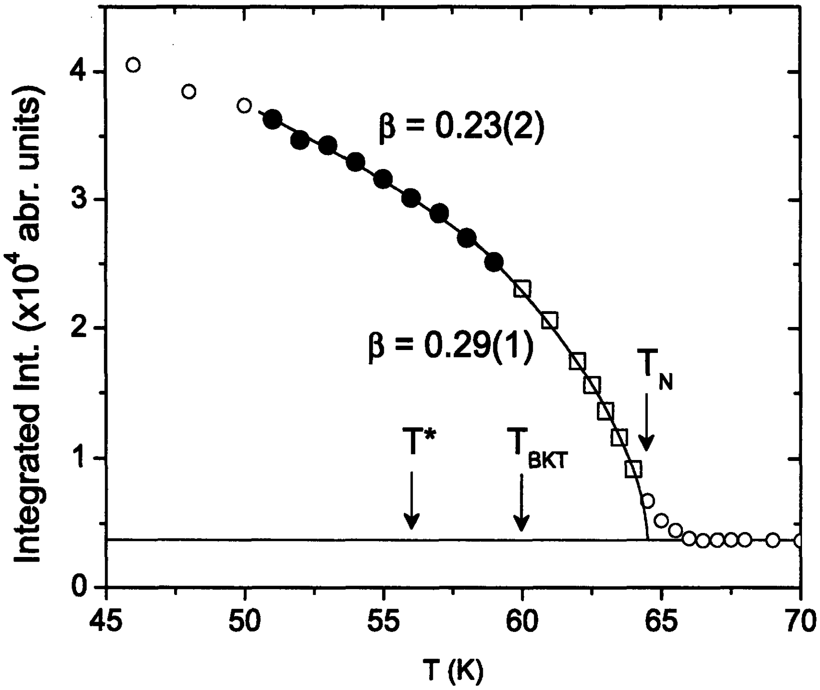

Figure 5-19: Integrated intensity of the magnetic Bragg peak measured at (1, 1, 1.5) as a function of temperature is fit to power law showing the crossover to the 2D finite-size-induced magnetization. The arrows indicate T^*, T_{BKT} and T_N with $T^* < T_{BKT} < T_N$.

ordered state due to the simultaneously breaking of the time-reversal (Z_2) symmetry. At a temperature $T^* \sim T_{BKT} < T_N$, where the correlation length is much larger than the system size, the spin-waves with a finite K_{eff} coexists with a low density of bound vortices. T^* is defined to be the temperature at which $K_{eff} = 2/\pi$. In this regime, the unbound vortices becomes irrelevant since they exists at a length scale much larger than the system size. A finite K_{eff} gives a measurable finite-size-induced magnetization according to Eq. 5.18. Fig. 5-19 shows power law fits to the integrated intensity of the magnetic Bragg peak, which is proportional to the magnetization squared, for 58 K $< T <$ 64 K, yielding $\beta = 0.29(1)$, and for 50 K $< T <$ 59 K, yielding $\beta = 0.23(2)$, which is consistent with $\beta = 0.231$ predicted by Bramwell *et al.* [249]. At T^*, Bramwell *et al.* estimated the magnetization $M(T^*)/M(0) = 0.55(2)$. For jarosite, this value is obtained at 56 K falling within the above temperature range, where $\beta = 0.23(2)$.

Table 5.6: Theoretical and experimental values of the BKT parameters.

Reference	b_ξ	b_χ	ν	T_{BKT}	$T_N^{\dagger\dagger}$
Kosterlitz and Thouless [237, 236]	~ 1.9	~ 3.3	0.25	$1.35^\dagger$	-
Monte Carlo [230, 251]	1.73	2.82	0.37	$0.89^\dagger$	-
Rb_2CrCl_4 [248]	2.12(57)	4.36(8)	~ 0	43.4 K	52 K
$BaNi_2(VO_4)_2$ [245]	$\frac{\pi}{2}$ (fixed)	–	–	43.3 K	50 K
$BaNi_2(PO_4)_2$ [243]	0.95	–	–	22.4 K	23.6 K
Jarosite	**0.61(13)**	**1.15(12)**	**$\sim$0**	**60.0 K**	**64.5 K**

† Calculations were done for $J = 1$ and $|\mathbf{S}| = 1$. †† Associated with 3D long-range order.

Assuming an ideal gas of free vortices in the high-temperature phase for the 2D XY model, Mertens *et al.* predicted that the correlations between unbounded vortices above T_{BKT} give rise to a quasi-elastic scattering with a line-shape given by Lorentzian to the $3/2^{th}$ power [241, 242]. In contrast, the correlation function in most systems is Lorentzian, the Ornstein-Zernike result. Fig. 5-17 shows the quasi-elastic scattering intensity measured at 66 K and 70 K fit to Lorentzian to the $3/2^{th}$ power (solid line) compared with a fit to Lorentzian (dotted line). Both functional forms seems to fit the data equally well with a slightly better reduced-χ^2 for the Lorentzian fit. Therefore, this does not rule out the possibility of the presence of free vortices above T_{BKT}. The data shown in Fig. 5-20 and Fig. 5-21 are the results of the Ornstein-Zernike fit using the Lorentzian equation.

The correlation length ξ and sublattice susceptibility χ as a function of reduced temperature are fit to the BKT theory for the 2D XY model using Eq. 5.16 and 5.17. Fig. 5-20 and Fig. 5-21, as well as the dotted lines in Fig. 5-12 and 5-13, show the results of the fit. The fit to the BKT theory is as good as the fit to the standard second-order critical behavior (shown by the solid line in Fig. 5-12 and 5-13), indicated by relatively the same values of the reduced-χ^2. With the fixed T_{BKT}

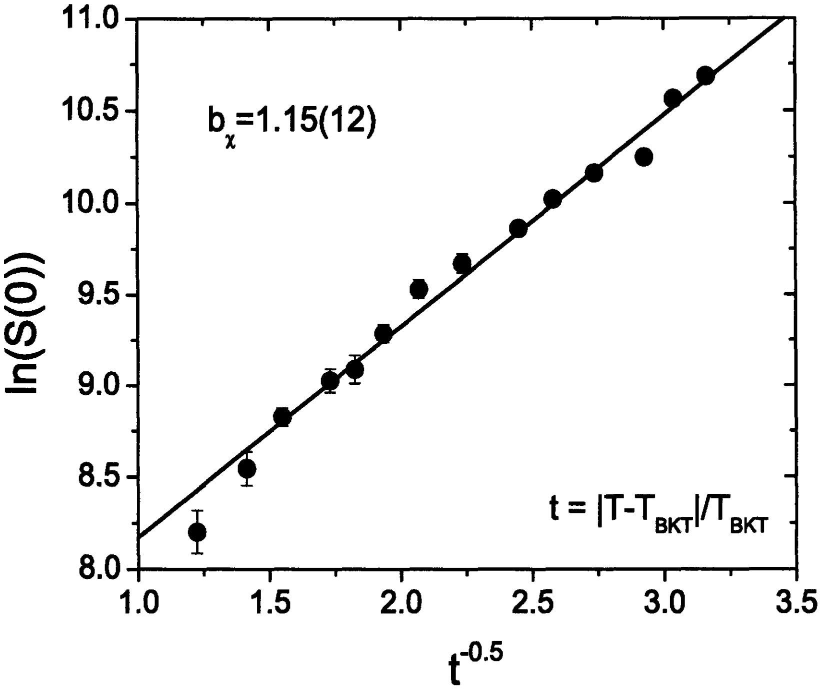

Figure 5-20: The log of $S(0)$ is plotted as a function of $t^{-0.5}$, where $t = \frac{T-T_{BKT}}{T_{BKT}}$ with $T_{BKT} = 60.0$ K. The solid line shows a fit to the BKT theory with $b_\chi = 1.15(12)$.

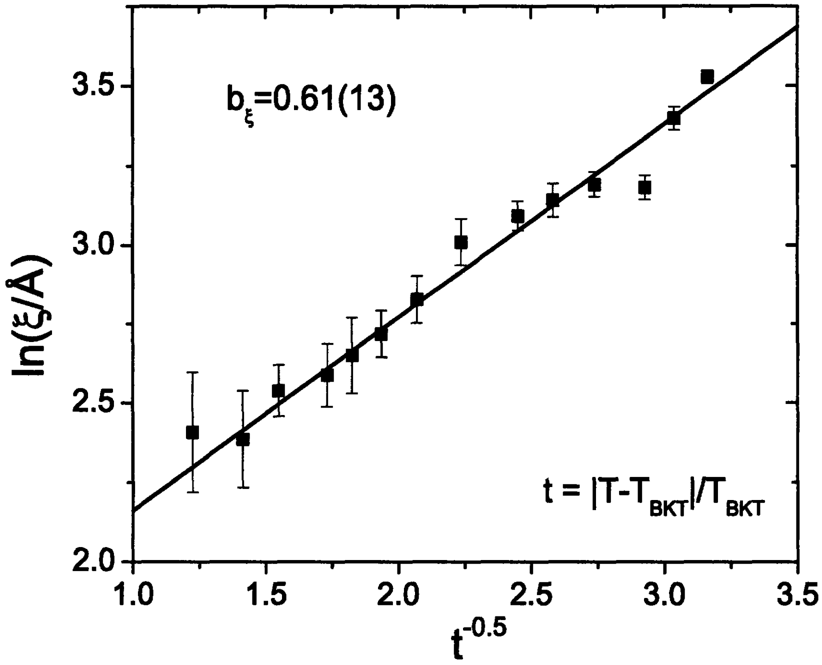

Figure 5-21: The log of correlation length is plotted as a function of $t^{-0.5}$, where $t = \frac{T-T_{BKT}}{T_{BKT}}$ with $T_{BKT} = 60.0$ K. The solid line shows a fit to the BKT theory with $b_\xi = 0.61(13)$.

of 60.0 K, the obtained fit parameters are $b_\chi = 1.15(12)$ and $b_\xi = 0.61(13)$. The exponent η characterizing the spin correlation length, i.e. $\langle \mathbf{S}_0 \cdot \mathbf{S}_r \rangle \sim r^{-\eta}$, can be extracted from b_χ and b_ξ using the following relation,

$$\eta = 2 - \frac{b_\chi}{b_\xi}. \tag{5.19}$$

Within this temperature range (66 K $< T <$ 100 K), η is approximately equal to zero. For the 2D XY model, η is predicted to approach 0.25 as $T \rightarrow T_{BKT} =$ 60.0 K. Since the temperature range, in which the measurements were done (66 K $< T <$ 100K), is far away from T_{BKT}, the variation from the universal value of η is expected [248]. The value of T_{BKT} is roughly consistent with that predicted by Elhajal. By means of numerical calculations on the kagomé antiferromagnet using the DM parameter obtained from our spin-wave measurements, Elhajal predicted the 2D long-range ordering temperature of $\sim$ 52 K [252]. The agreement would be better if J_2, which will serve to increase the ordering temperature, is included in the calculations.

In addition, studying the XY model on a square lattice by means by Monte-Carlo simulations and drawing a comparison with $Sr_2CuO_2Cl_2$, Cuccoli *et al.* observed a crossover from an isotropic behavior at high temperature to a 2D XY behavior followed by 3D ordering at T_N, which is slightly higher than T_{BKT} due to the interlayer coupling in the real system [253, 254]. For jarosite, the crossover from 2D XY to 3D XY is not observed. However, the crossover from the Heisenberg to XY behavior in 2D might occur around 100 K, above which magnetic susceptibility becomes isotropic, and in-plane short-range correlation vanishes.

The Ising critical behavior due to the spontaneous breaking of the Z_2 symmetry cannot be detected using neutron scattering since the neutron scattering technique cannot distinguish between the two degenerate ground states. Furthermore, the in-plane spin gap vanishes above T_N as shown in Fig. 4-11. Therefore, ξ and χ measured using neutron scattering do not show the critical behavior belonging to the 2D Ising model. On the other hand, we have observed a sharp transition in specific heat, which cannot be explained by the BKT theory, but which gives an indication of the Ising phase transition at T_N as shown by a logarithmic divergence in Fig. 5-22. The origin of this Ising degree of freedom in jarosite, which gives rise to the Z_2 symmetry will also be discussed in detail in the next section.

5.5.2 2D Ising

The 2D Ising model was solved exactly by Onsager in 1944. A solution, the so-called Onsager solution, provides analytical forms for the spontaneous magnetization, and specific heat as a function of temperature, which diverges logarithmically as temperature approaches a critical temperature [255, 256]. The expression for the specific heat C for the 2D XY model is given by [255]

$$\frac{C}{k} = \frac{2}{\pi}\left(\frac{2\epsilon}{kT_N}\right)^2\left[-\log\left|\frac{T-T_N}{T_N}\right| + \log\left(\frac{kT_N}{2\epsilon}\right) - \left(1+\frac{\pi}{4}\right)\right], \tag{5.20}$$

where ϵ is a coupling constant between two nearest-neighbor Ising spins, and T_N is the ordering temperature. Examples of the realizations of the 2D Ising model are C_2F_6 monolayer on graphite, whose specific heat shows the logarithmic divergence at the critical temperature [257], K_2CoF_4 [258], and Rb_2CoF_4 [259]. For the frustrated spin systems, Monte Carlo simulations on TAXY and FFXY models show the Ising transition due to the presence of spin chirality [215, 216, 217, 218].

For the triangular lattice, the classical and quantum XXZ models with easy-plane anisotropy were studied using Monte Carlo simulations by Capriotti *et al.* [215, 216, 217]. The system shows a BKT transition, which is associated with vortex-antivortex unbinding, and an Ising-like transition due to the vector chirality. This Ising-like transition occurs at a slightly higher temperature than the BKT transition as shown in Table 5.7. In this system, the staggered vector chirality κ is taken as the order parameter, which vanishes for $T > T_N$. Below T_N, the finite-size scaling analysis shows that the critical behavior of κ is consistent with 2D Ising with $\nu = 1$ and $\beta = 1/8$. Specific heat data also show a divergence at T_N associated with the spontaneous breaking of the Z_2 symmetry. This divergence conceals the behavior of the specific

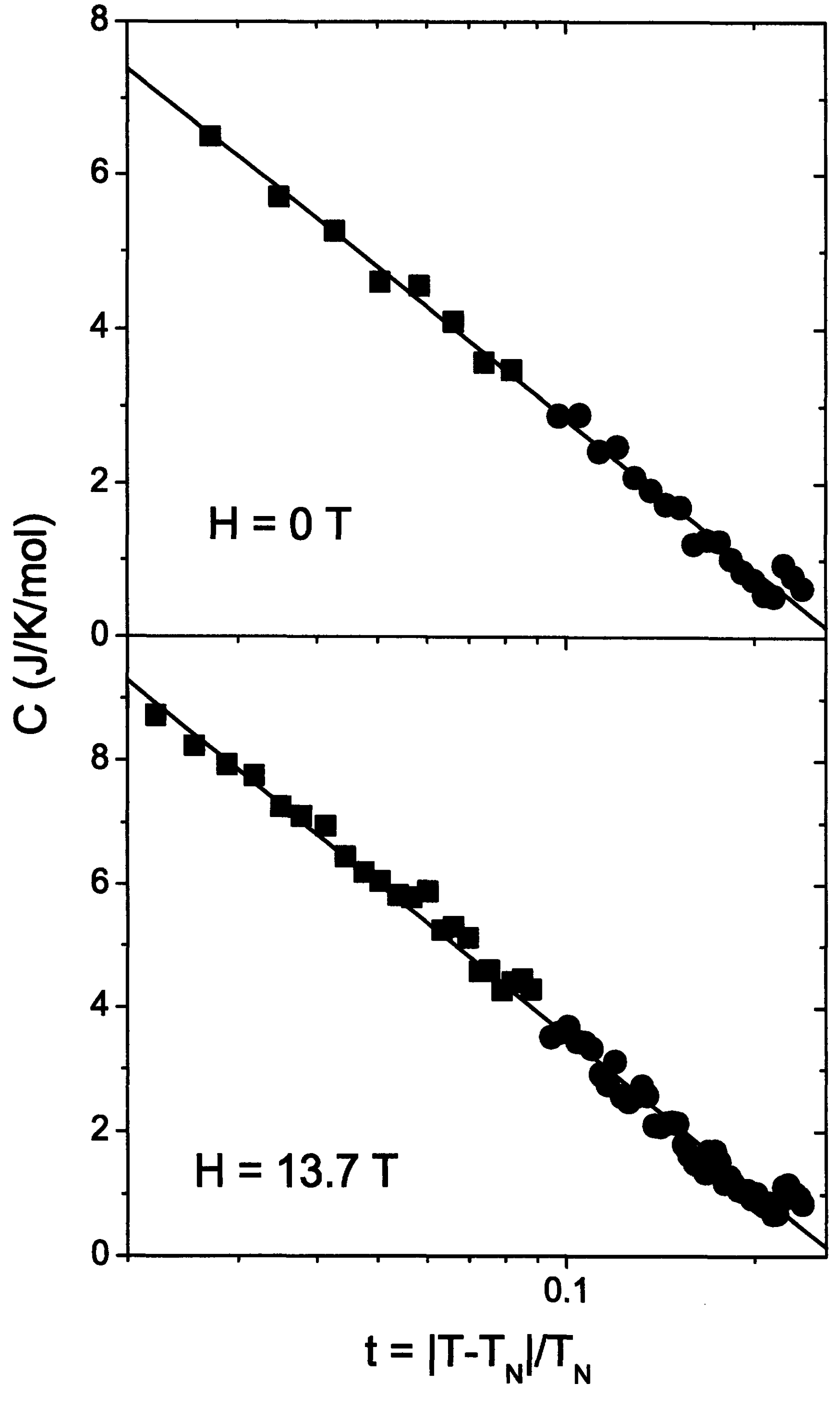

Figure 5-22: The spin-only specific heat with the BG scaling factor of 1.245 is fit to a logarithmic function with $T_N = 64.5$ K, indicative of the Ising transition in 2D. In contrast to the power law fit in Fig. 5-9, the specific heat can be fit to one functional form for 65 K $< T <$ 80 K. The fit to Eq. 5.20 yields $\epsilon = 2.03(5)$ meV.

heat at the BKT transition, which shows a broad maximum at temperature slightly above T_{BKT} in unfrustrated planar systems [229, 230].

A case of the antiferromagnetic kagomé lattice is quite different from the triangular lattice. While the staggered vector chirality has two degenerate states in the triangular lattice, the arrangement of vector chirality results in many different degenerate states in the kagomé lattice. However, for jarosite, the DM interaction lifts some of these degenerate states. In particular, the out-of-plane component of the DM interaction favors those states with positive vector chirality. From quasi-elastic neutron scattering measurements discussed in the previous section, the vector chirality orders at much higher temperature than T_N, possibly around $T \sim 100$. For $T_N < T < 100$ K, a $SO(2)$ symmetry is not broken and spins are free to rotate within the plane as long as the vector chirality remains uniformly positive or negative. In addition to the $SO(2)$ symmetry, the system also has a Z_2 symmetry associated with scalar chirality. The scalar chirality in this system is not zero because the spin structure is not perfectly planar. The in-plane component of the DM interaction favors spin-canting out of the plane. This small spin canting results in a non-zero value of the scalar chirality, which can be taken as the order parameter. Therefore, the combination of the in-plane and out-of-plane components of the DM interaction reduces the number of the degenerate states to two, which correspond to positive (canted-up) or negative (canted-down) scalar chirality as shown in Fig. 5-16.

The spin structures of these two states give the same neutron scattering cross section. Therefore, the Ising critical behavior due to the scalar chirality cannot be detected using neutron scattering. However, the signature of the Ising transition can be observed in the specific heat data, which shows the logarithmic divergence as shown in Fig. 5-22. In contrast to the power law fit in Fig. 5-9, where the specific heat data cannot be fit to a single exponent, the data can be fit to one logarithmic form for 65 K $< T <$ 80 K. It is interesting to note that for the 2D Ising model in a finite field, since the field breaks the Ising symmetry, there can no longer be a phase transition, but rather a crossover, which is indicated by the broadening of the peak as shown in Fig. 5-8b for K jarosite and Fig. 3-6 for Ag jarosite.

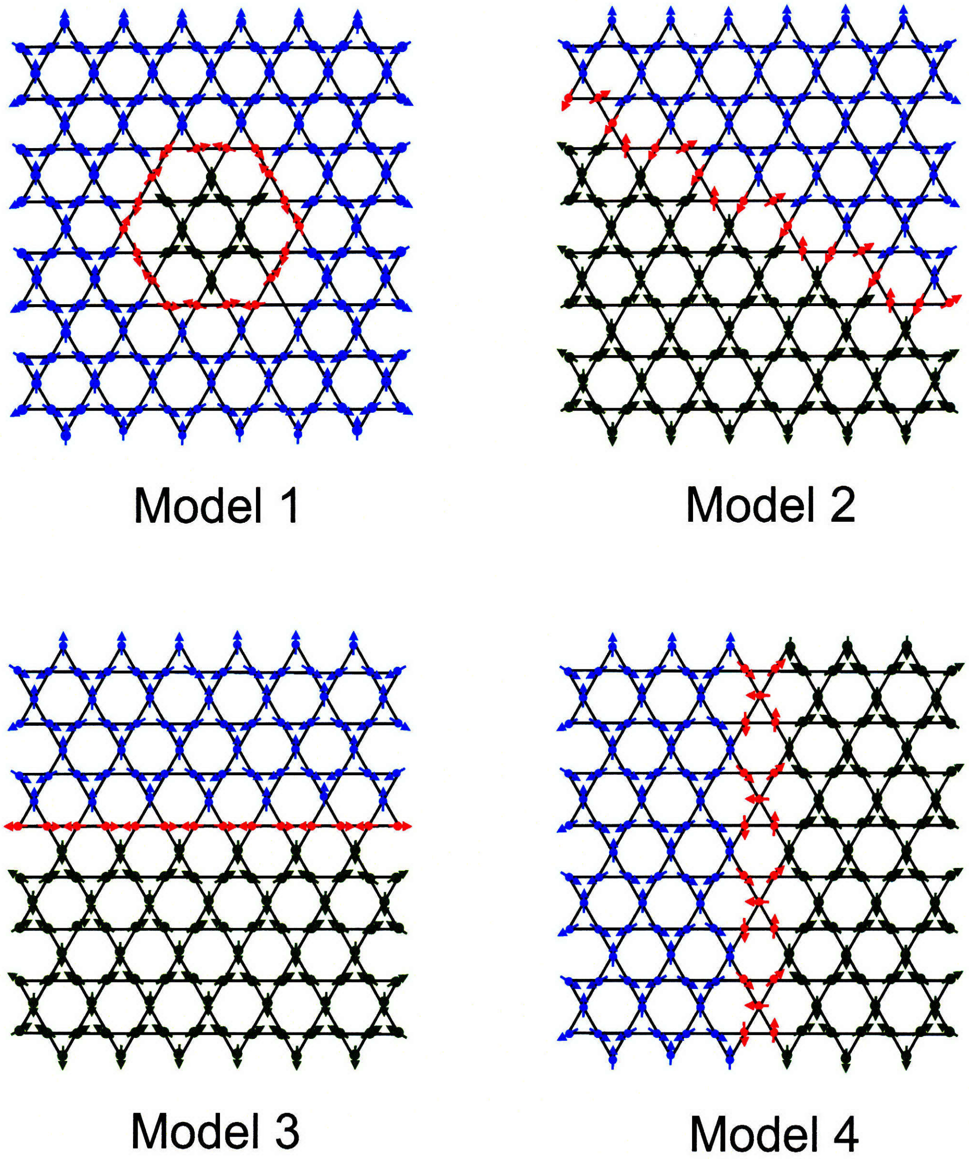

Model 1

Model 2

Model 3

Model 4

Figure 5-23: Structure of domain walls separating two degenerate ground states with positive and negative scalar chirality.

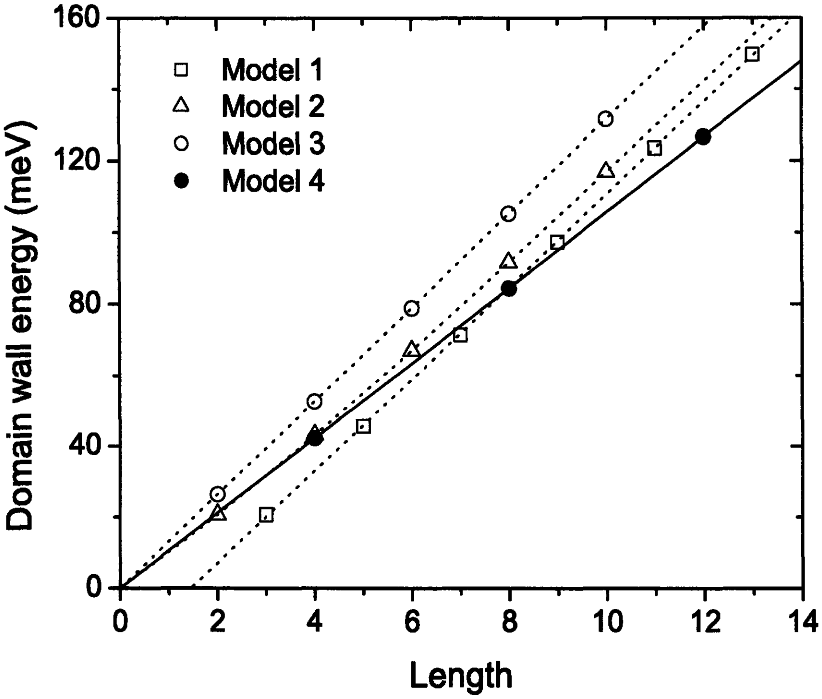

Figure 5-24: Domain wall energy as a function of length for four types of domain walls shown in Fig. 5-23.

Fig. 5-22a shows the specific heat data measured at zero field on a single crystal sample of K jarosite. The result is fit to Eq. 5.20 plus a small constant background due to a residual lattice contribution. The obtained coupling constant ϵ is 2.03(5) meV with a fixed $T_N = 64.5$ K. The effective coupling normalized to $S = 5/2$ is equal to 0.325(8) meV, which is of the order of the DM interaction **D**, indicating that **D**, as well as the in-plane exchange coupling J, plays a significant role. The ferromagnetic interlayer coupling plays a role in propagating the planer ordered state along the c–direction, giving rise to the observed 3D arrangement shown in Fig. 1-8.

Unfortunately, there is no Monte Carlo simulation on a kagomé lattice antiferromagnet with the DM interaction available, with which we can compare our results. Therefore, to obtain an estimate of the ordering temperature for the 2D Ising in jarosite, we calculated the energy of domain walls separating the two states with positive and negative values of the scalar chirality using the Hamiltonian parameters obtained from the spin wave measurements on K jarosite. Then, we compared the

Table 5.7: Transition temperatures T_N and T_{BKT} in a unit of JS^2 for the XXZ model on the triangular lattice (TAXY) and the fully frustrated XY model on the square lattice (FFXY) using Monte Carlo simulations. The experimental values for K jarosite are shown on the last row.

Model	$T_N^\dagger$	T_{BKT}
FFXY [218]	0.4576(14)	0.440
TAXY classical spins [215]	0.412(5)	0.403(1)
TAXY $S = \frac{5}{2}$ [216]	0.364(4)	0.352(1)
Jarosite	**0.280(1)**	**0.260(2)**

† denotes the 2D Ising transition temperature.

domain energy with the XXZ model on the triangular lattice, which was studied by means of Monte Carlo simulations [215, 216, 217, 260].

Fig. 5-23 shows four types of the domain walls. Spin configurations along the domain walls were obtained by minimizing the total energy. We found that the energy of the domain walls is linearly proportional to the length L for large L , which is typical for the 2D Ising model. For small L, the domain wall energy for Model 2 follows an exponential decay in addition to the linear form, and that for Model 1 shows a much weaker exponential decay. In addition, the domain wall energy per unit length is very robust, and virtually independent of the spin configuration along the domain walls. The plot of the domain wall energy as a function of length for all four models are shown in Fig. 5-24. All of them have approximately the same energy per unit length ranging from 10.56 to 13.15 meV per unit length (one unit length is equal to a distance between the nearest neighbors) with Model 4 yielding the lowest value of 10.56 meV or $0.53 \cdot JS^2$ per unit length, where $J = 3.18$ meV and $S = 5/2$. This value is close to the domain wall energy per unit length $E_{dw} = 0.50 \cdot J$ for classical spins with $|S| = 1$ in the triangular lattice antiferromagnet [227]. Therefore, one would expect that the ordering temperature in jarosite and in the triangular lattice antiferromagnet should be of the same order.

In order to measure the order parameter of the 2D Ising model in jarosite, one needs to measure the magnetization of the canting moment of a single kagomé plane at zero field. However, a magnetometer measure a bulk property, and the total magnetization along the $c-$direction is zero for jarosite due to the interlayer coupling. Therefore, it is not possible to measure the order parameter using a magnetometer, such as PPMS or SQUID. Similarly, neutron scattering is not sensitive enough to measure the small canted moments of the spins, whose canting angle is about a few degrees. An ideal probe would be a local probe, which can measure a local field along the $c-$direction due to small canting. In fact, the NMR measurements of the local field at a hydrogen site (shown by orange circles in Fig. 1-7) by Nishiyama *et al.* show the critical exponent $\beta = 0.194$ [38], which is much smaller, and closer to the 2D Ising model ($\beta = 0.125$) than the value obtained from our neutron scattering measurements. This emphasizes the fact that the critical behavior in jarosite belongs to either the 2D Ising and finite-size 2D XY models, depending on which order parameter is measured. In this case, the two order parameters are probably total and out-of-plane sublattice magnetizations. Neutron scattering is more sensitive to the total sublattice magnetization, while NMR is sensitive to both total and out-of-plane magnetizations. Therefore, the critical exponent β measured by NMR lies between the predicted values of these two models.

Using Monte Carlo simulations to study the XXZ model on the triangular lattice, Capriotti *et al.* found (in a unit of JS^2) $T_N = 0.412(5)$ for classical spins and 0.364 for $S = 5/2$ spins, which is close to the experimental value of T_N in jarosite; with the ordering temperature of 64.5(3) K, T_N is equal to 0.280(1) for K jarosite (Table 5.7). A better agreement can be obtained if one considers the domain wall energy per spin. A lattice constant of the kagomé lattice is twice as large as that of the triangular lattice, while its unit cell contains three times as many spins as the triangular lattice unit cell. The domain wall energy per spin in the kagomé lattice is 7.04 meV or $0.35 \cdot JS^2$ per spin. Since T_N is proportional to the domain wall energy, one would expect that T_N for the kagomé lattice is reduced by a factor of 0.71 from T_N for the triangular lattice. This gives $T_N = 0.26$ for the kagomé lattice, which is very close to the experimental value of 0.280(1). Nevertheless, a Monte Carlo simulation on the kagomé lattice antiferromagnet with the DM interaction is needed to fully explain our experimental results of the critical behavior in jarosite.

5.6 Summary

In this chapter, spin fluctuations and quasi-elastic scattering above the ordering temperature were studied using unpolarized and polarized neutron scattering measurements. Inelastic unpolarized neutron scattering shows the presence of chiral ordered state in the absence of broken spin-rotational symmetry. The in-plane fluctuation has been confirmed by polarized neutron scattering measurements. Furthermore, the study of the critical behavior raises a possibility of jarosite belonging to both 2D XY and 2D Ising universality classes.

Our measurements of this ideal kagomé compound reveal new magnetic behavior related to two types of spin chirality, vector and scalar. The DM interaction is a significant perturbation to the Heisenberg Hamiltonian and strongly influences the low temperature physics. For $T > T_N$, the vector spin chirality is ordered even in the absence of broken spin-rotational symmetry. In the ordered state below T_N, we have discovered a field-induced transition to a state with non-zero scalar chirality, which was discussed in Chapter 3. Thus, materials based on jarosites may be promising candidates for studies of the coupling between non-trivial spin textures and the transport of electrons in frustrated systems. For example, carrier-doped compounds would probably show an anomalous Hall effect of topological origin, [26] and this might have useful applications in spin-based electronics.

The critical exponents of the kagomé lattice antiferromagnet cannot be categorized by any known universality classes. The measurements of the sublattice susceptibility and correlation length as a function of reduced temperature give the critical exponents $\gamma = 0.70(7)$ and $\nu = 0.37(7)$ close to the mean-field tricritical values of 1 and 0.5, respectively. The critical exponent β describing the critical behavior of the order parameter is equal to 0.29(1), and the critical exponent α for specific heat is equal to 0.53(7), which is again close to the mean-field tricritical values of 0.25 and 0.5, respectively. However, one would expect this system to be in the same universality class as frustrated XY spins in two dimensions ($n = 2$ and $d = 2$), which can be described by the Berezinskii-Kosterlitz-Thouless theory, or as Ising spins in two dimensions ($n = 1$ and $d = 2$).

We propose a scenario where both 2D XY and 2D Ising behaviors are present. Depending on which measurements are performed, the critical behavior can show the characteristic that belongs to either 2D XY or 2D Ising universality classes with two distinct critical temperatures; one is associated with the spontaneous breaking of the Z_2 symmetry, and the other corresponds to a topological order (BKT transition) due to vortex-antivortex binding. The former occurs at 64.5 K, slightly at higher temperature than the BKT transition, which would occur at 60.0 K. Neutron scattering measurements show a signature of the BKT transition. Above T_N, the in-plane spin gap vanishes, and the system retains the $SO(2)$ symmetry when measured with neutron scattering. On the other hand, specific heat measurements show a feature of the 2D Ising transition, since the underlying symmetry of the spin Hamiltonian is the time-reversal or Z_2 symmetry.

Appendix A

Spin-wave spectrum in the kagomé lattice antiferromagnet

The derivations given in this section are taken from Ref. [117]. The readers are encouraged to turn to the paper by Yildirim and Harris for in-depth discussions. From Eq. 4.1, we will neglect the interplane interactions. Therefore, the following derivations of the spin-wave spectrum are for a single kagomé plane. One can divide Eq. 4.1 into three parts:

$$\mathcal{H} = \mathcal{H}^{(1)} + \mathcal{H}^{(2)} + \mathcal{H}^{(3)}, \tag{A.1}$$

where $\mathcal{H}^{(1)}$ and $\mathcal{H}^{(2)}$ are the spin Hamiltonian between the nearest neighbors (nn) (e.g. between the spin labeled 1 and 2 in Fig. 3-1) and next-nearest neighbors (nnn) (e.g. between the spin labeled 2 and 5 in Fig. 3-1), respectively, and $\mathcal{H}^{(3)}$ represents the single-ion anisotropy (e.g. of the spin labeled 3 in Fig. 3-1). One can write $\mathcal{H}^{(n)}$ in matrix forms as the following:

$$\begin{aligned}
\mathcal{H}^{(1)} &= \sum_{\alpha\beta} \mathrm{M}_{1,2}^{\alpha,\beta} S_1^{\alpha} S_2^{\beta}, \\
\mathcal{H}^{(2)} &= \sum_{\alpha\beta} \mathrm{M}_{2,5}^{\alpha,\beta} S_2^{\alpha} S_5^{\beta}, \\
\mathcal{H}^{(3)} &= \frac{1}{2} \sum_{\alpha\beta} [\mathrm{C}']_3^{\alpha\beta} \left[S_3^{\alpha} S_3^{\beta} + S_3^{\beta} S_3^{\alpha} \right],
\end{aligned} \tag{A.2}$$

where $\mathbf{M}_{1,2}$, $\mathbf{M}_{2,5}$ and $\mathbf{C}_3$ are matrices, which are given by:

$$\begin{aligned}
\mathbf{M}_{1,2} \equiv \mathbf{M}^{(1)} &= \begin{bmatrix} J^{(1)}_{xx} & D^{(1)}_z & -D^{(1)}_y \\ -D^{(1)}_z & J^{(1)}_{yy} & J^{(1)}_{yz} \\ D^{(1)}_y & J^{(1)}_y z & J^{(1)}_{zz} \end{bmatrix}, \\
\mathbf{M}_{2,5} \equiv \mathbf{M}^{(2)} &= \begin{bmatrix} J^{(2)}_{xx} & D^{(2)}_z & -D^{(2)}_y \\ -D^{(2)}_z & J^{(2)}_{yy} & J^{(2)}_{yz} \\ D^{(2)}_y & J^{(2)}_{yz} & J^{(2)}_{zz} \end{bmatrix}, \\
\mathbf{C}'_3 \equiv \mathbf{C}' &= \begin{bmatrix} C'_{xx} & 0 & 0 \\ 0 & C'_{yy} & C'_{yz} \\ 0 & C'_{yz} & C'_{zz} \end{bmatrix}.
\end{aligned} \tag{A.3}$$

Now, the nn and nnn interactions will be expressed in terms of local axes, which are defined in such a way that the local $z-$axis is along the projection of the local spin onto the kagomé plane, the local $y-$axis is perpendicular to the plane, and the local $x-$axis is defined by the right-hand rule. The rotational matrix to transform these local axes from site to site are

$$\begin{aligned}
\mathcal{R}(\tau_1) &= \begin{bmatrix} \frac{1}{2} & 0 & -\frac{\sqrt{3}}{2} \\ -\frac{\sqrt{3}}{2} & 0 & -\frac{1}{2} \\ 0 & 1 & 0 \end{bmatrix}, \\
\mathcal{R}(\tau_2) &= \begin{bmatrix} \frac{1}{2} & 0 & \frac{\sqrt{3}}{2} \\ \frac{\sqrt{3}}{2} & 0 & -\frac{1}{2} \\ 0 & 1 & 0 \end{bmatrix}, \\
\mathcal{R}(\tau_3) &= \begin{bmatrix} -1 & 0 & 0 \\ 0 & 0 & 1 \\ 0 & 1 & 0 \end{bmatrix}.
\end{aligned} \tag{A.4}$$

One big advantage of writing the interaction matrices in term of the local axes is that the single-ion anisotropies and nn interactions for all sites are identical. The transformed interaction matrices of the interactions in Eq. A.3, denoted by $\mathcal{I}$, in the local axes can be written as

$$
\begin{aligned}
\mathcal{I}^{(1)} &\equiv \mathcal{I}_{1,2} = \tilde{\mathcal{R}}(\tau_1)\mathbf{M}_{1,2}\mathcal{R}(\tau_2), \\
\mathcal{I}^{(2)} &\equiv \mathcal{I}_{2,5} = \tilde{\mathcal{R}}(\tau_1)\mathbf{M}_{5,2}\mathcal{R}(\tau_2),
\end{aligned}
\tag{A.5}
$$

where

$$
\mathcal{I}^{(n)} = \begin{bmatrix} -E_x^{(n)} & d_z^{(n)} & -d_y^{(n)} \\ -d_z^{(n)} & -E_y^{(n)} & E_{yz}^{(n)} \\ d_y^{(n)} & E_{yz}^{(n)} & -E_z^{(n)} \end{bmatrix}.
\tag{A.6}
$$

The matrix elements can be written in terms of the spin Hamiltonian parameters as

$$
\begin{aligned}
E_x^{(n)} &= \frac{3}{4}J_{yy}^{(n)} - \frac{1}{4}J_{xx}^{(n)} - \frac{\sqrt{3}}{2}D_z^{(n)}, \\
E_y^{(n)} &= -J_{zz}^{(n)}, \\
E_z^{(n)} &= \frac{3}{4}J_{xx}^{(n)} - \frac{1}{4}J_{yy}^{(n)} - \frac{\sqrt{3}}{2}D_z^{(n)}, \\
E_{yz}^{(n)} &= \frac{\sqrt{3}}{2}D^{(n)} - \frac{1}{2}J_{yz}^{(n)}, \\
d_z^{(n)} &= -\frac{1}{2}D_y^{(n)} - \frac{\sqrt{3}}{2}J_{yz}^{(n)}, \\
d_y^{(n)} &= -\frac{\sqrt{3}}{4}\left(J_{xx}^{(n)} + J_{yy}^{(n)}\right) - \frac{1}{2}D_z^{(n)}.
\end{aligned}
\tag{A.7}
$$

The single-ion anisotropy in the local axes can be written as

$$
\mathbf{C} = \begin{bmatrix} C_{xx} & 0 & 0 \\ 0 & C_{yy} & C_{yz} \\ 0 & C_{yz} & C_{zz} \end{bmatrix},
\tag{A.8}
$$

where the matrix elements are given in Eq. 4.7. Using the three-fold axis and inversion symmetry, one can transform the interaction matrices given above to other bonds.

Both DM interaction and single-ion anisotropy can lead to a canted spin structure resulting in weak ferromagnetism as we discussed in Chapter 3. However, so far we have taken the local axes to lie in the kagomé plane. Next, we will take into account the fact the spins are canted out of the plane by defining canted local axes (prime axes), where the canted $z-$axis is along the canted spin. The initial local axes can be expressed in terms of the canted local axes as the following

$$\begin{aligned} S_x &= S'_x \\ S_y &= S'_z \sin\theta + S'_y \cos\theta, \\ S_z &= S'_z \cos\theta - S'_y \sin\theta, \end{aligned} \tag{A.9}$$

where θ is the canting angle, which can be calculated using Eq. 3.8 if the spin Hamiltonian parameters are known. In the canted local axes, the transformed interaction matrices become

$$\mathcal{I}^{(n)} = \begin{bmatrix} -E_x^{(n)} & \bar{d}_z^{(n)} & -\bar{d}_y^{(n)} \\ -\bar{d}_z^{(n)} & -\bar{E}_y^{(n)} & \bar{E}_{yz}^{(n)} \\ \bar{d}_y^{(n)} & \bar{E}_{yz}^{(n)} & -\bar{E}_z^{(n)} \end{bmatrix}. \tag{A.10}$$

The matrix elements can be written in terms of the spin Hamiltonian parameters as

$$\begin{aligned} \bar{E}_y^{(n)} &= s^2 E_z^{(n)} + c^2 E_y^{(n)} + 2cs E_{yz}^{(n)}, \\ \bar{E}_z^{(n)} &= c^2 E_z^{(n)} + s^2 E_y^{(n)} - 2cs E_{yz}^{(n)}, \\ \bar{E}_{yz}^{(n)} &= E_{yz}^{(n)} \cos\, 2\theta + \frac{1}{2}\left[E_z^{(n)} - E_y^{(n)}\right] \sin\, 2\theta, \\ \bar{d}_z^{(n)} &= c d_z^{(n)} + s d_y^{(n)}, \\ \bar{d}_y^{(n)} &= c d_y^{(n)} - s d_z^{(n)}, \end{aligned} \tag{A.11}$$

where $c \equiv \cos\theta$ and $s \equiv \sin\theta$. The local single-ion anisotropy in the canted local axes can be written as

$$\bar{\mathbf{C}} = \begin{bmatrix} C_{xx} & 0 & 0 \\ 0 & \bar{C}_{yy} & \bar{C}_{yz} \\ 0 & \bar{C}_{yz} & \bar{C}_{zz} \end{bmatrix}, \tag{A.12}$$

where

$$\begin{aligned}
\bar{C}_z z &= c^2 C_{zz} + s^2 C_{yy} + 2cs C_{yz}, \\
\bar{C}_y y &= s^2 C_{zz} + c^2 C_{yy} - 2cs C_{yz}, \\
\bar{C}_y z &= C_{yz} \cos\ 2\theta + \frac{1}{2}\left[C_{yy} - C_{zz}\right] \sin\ 2\theta.
\end{aligned} \tag{A.13}$$

To construct the boson Hamiltonian, we will use spherical components, where $+ = x - iy$ and $- = x - iy$. Then, the transformed interaction matrices for interactions between site τ in unit cell i located at $\mathbf{R}_i$ and site τ' in unit cell j located at $\mathbf{R}_j$ can be written as the following

$$\begin{aligned}
\bar{\mathcal{I}}^{zz}_{\tau\tau'}(i,j) &= \bar{\mathcal{I}}^{(n)}_{zz}, \\
\bar{\mathcal{I}}^{\pm\pm}_{\tau\tau'}(i,j) &= \frac{1}{4}\left[\bar{\mathcal{I}}^{(n)}_{xx} - i\bar{\mathcal{I}}^{(n)}_{xy} - i\bar{\mathcal{I}}^{(n)}_{yx} - \bar{\mathcal{I}}^{(n)}_{xx}\right], \\
\bar{\mathcal{I}}^{\pm\mp}_{\tau\tau'}(i,j) &= \frac{1}{4}\left[\bar{\mathcal{I}}^{(n)}_{xx} \pm i\bar{\mathcal{I}}^{(n)}_{xy} \mp i\bar{\mathcal{I}}^{(n)}_{yx} + \bar{\mathcal{I}}^{(n)}_{xx}\right],
\end{aligned} \tag{A.14}$$

and similarly for the single-ion anisotropy matrix $\bar{\mathbf{C}}$. Using the Holstein-Primakoff transformation, one can express the spin operators in terms of the annihilation and creation operators as the following

$$\begin{aligned}
S^z_{i,\tau} &= S - a^\dagger_{i\tau} a_{i\tau}, \\
S^+_{i,\tau} &= \sqrt{2S} a_{i\tau}, \\
S^-_{i,\tau} &= \sqrt{2S} a^\dagger_{i\tau}.
\end{aligned} \tag{A.15}$$

Ignoring a constant term, one can write the spin Hamiltonian in terms of the Bose operators in the following form:

$$\begin{aligned}
\mathcal{H} &= 2S\sum_{i\tau}\Big[-\bar{C}_{\tau}^{zz}a_{i\tau}^{\dagger}a_{i\tau}+\bar{C}_{\tau}^{++}a_{i\tau}a_{i\tau}+\bar{C}_{\tau}^{--}a_{i\tau}^{\dagger}a_{i\tau}^{\dagger}+\bar{C}_{\tau}^{+-}a_{i\tau}^{\dagger}a_{i\tau}+\bar{C}_{\tau}^{-+}a_{i\tau}^{\dagger}a_{i\tau}\Big] \\
&\quad +S\sum_{<i\tau,j\tau'>}\Bigg[-\frac{1}{2}\bar{\mathcal{I}}_{\tau\tau'}^{zz}(i,j)\left(a_{i\tau}^{\dagger}a_{i\tau}+a_{j\tau'}^{\dagger}a_{j\tau'}\right) \qquad \text{(A.16)} \\
&\quad +\bar{\mathcal{I}}_{\tau\tau'}^{++}(i,j)a_{i\tau}a_{j\tau'}+\bar{\mathcal{I}}_{\tau\tau'}^{--}(i,j)a_{i\tau}^{\dagger}a_{j\tau'}^{\dagger}+\bar{\mathcal{I}}_{\tau\tau'}^{+-}(i,j)a_{i\tau}a_{j\tau'}^{\dagger}+\bar{\mathcal{I}}_{\tau\tau'}^{-+}(i,j)a_{i\tau}^{\dagger}a_{j\tau'}\Bigg],
\end{aligned}$$

where $\sum_{<i\tau,j\tau'>}$ indicates that the summation does not include terms with $(i,\tau) = (j,\tau')$. The Bose operators are transformed as

$$\begin{aligned}
a_{i\tau} &= \frac{1}{\sqrt{N}}\sum_{\mathbf{q}} e^{i\mathbf{q}\cdot(\mathbf{R}_i+\tau)}a_{\tau}(\mathbf{q}), \\
a_{i\tau}^{\dagger} &= \frac{1}{\sqrt{N}}\sum_{\mathbf{q}} e^{-i\mathbf{q}\cdot(\mathbf{R}_i+\tau)}a_{\tau}^{\dagger}(\mathbf{q}). \qquad \text{(A.17)}
\end{aligned}$$

The Hamiltonian in Eq. A.17 becomes

$$\mathcal{H} = E_0 + \sum_{\mathbf{q}}\mathcal{H}(\mathbf{q}), \qquad \text{(A.18)}$$

where E_0 is the ground state energy and

$$\begin{aligned}
\mathcal{H}(\mathbf{q}) &= S\sum_{\mu\nu}A_{\mu\nu}(\mathbf{q})a_{\mu}^{\dagger}(\mathbf{q})a_{\nu}(\mathbf{q}) \\
&\quad +\frac{1}{2}\sum_{\alpha\beta}B_{\alpha\beta}(\mathbf{q})a_{\alpha}^{\dagger}(\mathbf{q})a_{\beta}^{\dagger}(-\mathbf{q}) \\
&\quad +\frac{1}{2}\sum_{\alpha\beta}B_{\alpha\beta}^{*}(\mathbf{q})a_{\alpha}(\mathbf{q})a_{\beta}(-\mathbf{q}), \qquad \text{(A.19)}
\end{aligned}$$

where

$$\begin{aligned}
A_{\tau\tau'}(\mathbf{q}) &= \Big[2\bar{C}_{\tau}^{+-} + 2\bar{C}_{\tau}^{-+} - 2\bar{C}_{\tau}^{zz} - \sum_{\tau''} \bar{\mathcal{I}}_{\tau\tau''}^{zz}(q=0)\Big]\delta_{\tau\tau'} + \bar{\mathcal{I}}_{\tau'\tau}^{+-}(\mathbf{q}) + \bar{\mathcal{I}}_{\tau\tau'}^{-+}(-\mathbf{q}) \\
&= \Big[C_{xx} + \bar{C}_{yy} - 2\bar{C}_{zz} - \sum_{\tau''} \bar{\mathcal{I}}_{\tau\tau''}^{zz}(q=0)\Big]\delta_{\tau\tau'} + \bar{\mathcal{I}}_{\tau'\tau}^{+-}(\mathbf{q}) + \bar{\mathcal{I}}_{\tau\tau'}^{-+}(-\mathbf{q}), \\
B_{\tau\tau'}(\mathbf{q}) &= 4\bar{C}_{\tau}^{--}\delta_{\tau\tau'} + 2\bar{\mathcal{I}}_{\tau\tau'}^{--}(-\mathbf{q}) \\
&= \Big[C_{xx} - \bar{C}_{yy}\Big]\delta_{\tau\tau'} + +2\bar{\mathcal{I}}_{\tau\tau'}^{--}(-\mathbf{q}),
\end{aligned} \tag{A.20}$$

where

$$\bar{\mathcal{I}}_{\tau\tau'}^{\alpha\beta}(\mathbf{q}) = \sum_{i} \bar{\mathcal{I}}_{\tau\tau'}^{\alpha\beta}(i,j)e^{i\mathbf{q}\cdot(\tau+\mathbf{R}_{ij}-\tau')} \tag{A.21}$$

We introduce the normal mode operators, which are defined as

$$X_{\mu}^{\dagger}(\mathbf{q}) = \sum_{\alpha}\Big[c_{\alpha}^{\mu}(\mathbf{q})a_{\alpha}^{\dagger}(\mathbf{q}) + d_{\alpha}^{\mu}(\mathbf{q})a_{\alpha}(-\mathbf{q})\Big], \tag{A.22}$$

which are determined by

$$\Big[\mathcal{H}, X_{\mu}^{\dagger}(\mathbf{q})\Big] = \omega^{(\mu)}(\mathbf{q})X_{\mu}^{\dagger}(\mathbf{q}). \tag{A.23}$$

This gives

$$\begin{aligned}
&\omega^{(\mu)}(\mathbf{q})\sum_{\alpha}\Big[c_{\alpha}^{\mu}(\mathbf{q})a_{\alpha}^{\dagger}(\mathbf{q}) + d_{\alpha}^{\mu}(\mathbf{q})a_{\alpha}(-\mathbf{q})\Big] \\
&= S\sum_{\alpha\beta}\Bigg[c_{\alpha}^{\mu}(\mathbf{q})A_{\beta\alpha}(\mathbf{q})a_{\beta}^{\dagger}(\mathbf{q}) + c_{\alpha}^{\mu}(\mathbf{q})B_{\alpha\beta}^{*}(\mathbf{q})a_{\beta}(-\mathbf{q})\Bigg] \\
&- \sum_{\alpha\beta}\Bigg[d_{\alpha}^{\mu}(\mathbf{q})A_{\alpha\beta}(-\mathbf{q})a_{\beta}(-\mathbf{q}) + d_{\alpha}^{\mu}(\mathbf{q})B_{\alpha\beta}(-\mathbf{q})a_{\beta}(\mathbf{q})\Bigg].
\end{aligned} \tag{A.24}$$

By taking into account of the inversion symmetry, we will now have to solve the following eigenvalues problem.

$$\mathbf{M}(\mathbf{q})\begin{bmatrix} \mathbf{c}^{\mu}(\mathbf{q}) \\ \mathbf{d}^{\mu}(\mathbf{q}) \end{bmatrix} \equiv \begin{bmatrix} \mathbf{A}(\mathbf{q}) & -\mathbf{B}(\mathbf{q}) \\ \mathbf{B}(\mathbf{q})^{*} & -\mathbf{A}(\mathbf{q})^{*} \end{bmatrix}\begin{bmatrix} \mathbf{c}^{\mu}(\mathbf{q}) \\ \mathbf{d}^{\mu}(\mathbf{q}) \end{bmatrix} = \tilde{\omega}^{(\mu)}(\mathbf{q})\begin{bmatrix} \mathbf{c}^{\mu}(\mathbf{q}) \\ \mathbf{d}^{\mu}(\mathbf{q}) \end{bmatrix}, \tag{A.25}$$

where $\tilde{\omega} = \omega/S$. The matrix elements for $\mathbf{M}(\mathbf{q})$ are given in Chapter 4. For kagomé lattice, there are three spins in the unit cell. Therefore, there are six spin-waves modes. However, the eigenvalues of the matrix $\mathbf{M}$ can be divided into two groups with opposite signs. Eq. A.25 can be written as

$$\begin{bmatrix} \mathbf{A}(\mathbf{q}) & -\mathbf{B}(\mathbf{q}) \\ \mathbf{B}(\mathbf{q})^* & -\mathbf{A}(\mathbf{q})^* \end{bmatrix} \begin{bmatrix} \mathbf{c}(\mathbf{q}) & \mathbf{d}(\mathbf{q})^* \\ \mathbf{d}(\mathbf{q}) & \mathbf{c}(\mathbf{q})^* \end{bmatrix} = \begin{bmatrix} \mathbf{c}(\mathbf{q}) & \mathbf{d}(\mathbf{q})^* \\ \mathbf{d}(\mathbf{q}) & \mathbf{c}(\mathbf{q})^* \end{bmatrix} \begin{bmatrix} \tilde{\omega}(\mathbf{q}) & 0 \\ 0 & -\tilde{\omega}(\mathbf{q}) \end{bmatrix},$$

where $\mathbf{c}(\mathbf{q})$ and $\mathbf{d}(\mathbf{q})$ are 3×3 matrices composed of the vectors $\mathbf{c}^{\mu}(\mathbf{q})$ and $\mathbf{d}^{\mu}(\mathbf{q})$, respectively, and $\tilde{\omega}(\mathbf{q})$ is a 3×3 diagonal matrix, whose diagonal elements are the eigenvalues $\tilde{\omega}^{\mu}(\mathbf{q})$.

Bibliography

[1] A. P. RAMIREZ, *Annu. Rev. Mater. Sci.* **24**, 453 (1994).

[2] H. T. DIEP, editor, *Frustrated Spin Systems*, World Scientific Publishing Co. Pte. Ltd., 2004.

[3] A. P. RAMIREZ, A. HAYASHI, R. J. CAVA, R. SIDDHARTHAN, and B. S. SHASTRY, *Nature* **399**, 333 (1999).

[4] R. MOESSNER and S. L. SONDHI, *Phys. Rev. B* **68**, 064411 (2003).

[5] A. S. WILLS, R. BALLOU, and C. LACROIX, *Phys. Rev. B* **66**, 144407 (2002).

[6] Y. TABATA, H. KADOWAKI, K. MATSUHIRA, Z. HIROI, N. ASO, E. RESSOUCHE, and B. FK, *Phys. Rev. Lett.* **97**, 257205 (2006).

[7] K. DAMLE and T. SENTHIL, *Phys. Rev. Lett.* **97**, 067202 (2006).

[8] P. SINDZINGRE, G. MISGUICH, C. LHUILLIER, B. BERNU, L. PIERRE, C. WALDTMANN, and H.-U. EVERTS, *Phys. Rev. Lett.* **84**, 2953 (2000).

[9] F. MILA, *Phys. Rev. Lett.* **81**, 2356 (1998).

[10] C. LHUILLIER, B. BERNU, and G. MISGUICH, *International Journal of Modern Physics B* **13**, 687 (1999).

[11] M. J. P. GINGRAS, C. V. STAGER, N. P. RAJU, B. D. GAULIN, and J. E. GREEDAN, *Phys. Rev. Lett.* **78**, 947 (1997).

[12] M. FERRERO, F. BECCA, and F. MILA, *Phys. Rev. B* **68**, 214431 (2003).

[13] J. S. GARDNER, B. D. GAULIN, S.-H. LEE, C. BROHOLM, N. P. RAJU, and J. E. GREEDAN, *Phys. Rev. Lett.* **83**, 211 (1999).

[14] M. A. GÎRTU, C. M. WYNN, W. FUJITA, K. AWAGA, and A. J. EPSTEIN, *Phys. Rev. B* **57**, R11058 (1998).

[15] V. DUPUIS, E. VINCENT, and J. HAMMANN, *The European Physical Journal B* **29**, 19 (2002).

[16] M. B. HASTINGS, *Phys. Rev. B* **63**, 014413 (2001).

[17] P. W. ANDERSON, *Science* **235**, 1196 (1987).

[18] R. J. BIRGENEAU, *American Journal of Physics* **58**, 28 (1990).

[19] M. A. KASTNER, R. J. BIRGENEAU, G. SHIRANE, and Y. ENDOH, *Rev. Mod. Phys.* **70**, 897 (1998).

[20] S. T. BRAMWELL and M. J. P. GINGRAS, *Science* **294**, 1495 (2001).

[21] C. ZENG and V. ELSER, *Phys. Rev. B* **42**, 8436 (1990).

[22] J. B. MARSTON and C. ZENG, *Journal of Applied Physics* **69**, 5962 (1991).

[23] R. R. P. SINGH and D. A. HUSE, *Phys. Rev. Lett.* **68**, 1766 (1992).

[24] C. WALDTMANN, H.-U. EVERTS, B. BERNU, C. LHUILLIER, P. SINDZINGRE, P. LECHEMINANT, and L. PIERRE, *Eur. Phys. J. B* **2**, 501 (1998).

[25] J. VILLAIN, *Journal of Physics C: Solid State Physics* **10**, 4793 (1977).

[26] K. OHGUSHI, S. MURAKAMI, and N. NAGAOSA, *Phys. Rev. B* **62**, R6065 (2000).

[27] Y. TAGUCHI, Y. OOHARA, H. YOSHIZAWA, N. NAGAOSA, and Y. TOKURA, *Science* **291**, 2573 (2001).

[28] D. A. HUSE and A. D. RUTENBERG, *Phys. Rev. B* **45**, 7536 (1992).

[29] J. N. REIMERS and A. J. BERLINSKY, *Phys. Rev. B* **48**, 9539 (1993).

[30] A. CHUBUKOV, *Journal of Applied Physics* **73**, 5639 (1993).

[31] J. T. CHALKER, P. C. W. HOLDSWORTH, and E. F. SHENDER, *Phys. Rev. Lett.* **68**, 855 (1992).

[32] A. CHUBUKOV, *Phys. Rev. Lett.* **69**, 832 (1992).

[33] S. SACHDEV, *Phys. Rev. B* **45**, 12377 (1992).

[34] J.-C. DOMENGE, P. SINDZINGRE, C. LHUILLIER, and L. PIERRE, *Phys. Rev. B* **72**, 024433 (2005).

[35] A. B. HARRIS, C. KALLIN, and A. J. BERLINSKY, *Phys. Rev. B* **45**, 2899 (1992).

[36] R. S. GEKHT and I. N. BONDARENKO, *Journal of Experimental and Theoretical Physics* **86**, 1209 (1998).

[37] T. INAMI, M. NISHIYAMA, S. MAEGAWA, and Y. OKA, *Phys. Rev. B* **61**, 12181 (2000).

[38] M. NISHIYAMA, S. MAEGAWA, T. INAMI, and Y. OKA, *Phys. Rev. B* **67**, 224435:1 (2003).

[39] M. ELHAJAL, B. CANALS, and C. LACROIX, *Phys. Rev. B* **66**, 014422:1 (2002).

[40] I. RITCHEY, P. CHANDRA, and P. COLEMAN, *Phys. Rev. B* **47**, 15342 (1993).

[41] J. N. REIMERS and A. J. BERLINSKY, *Phys. Rev. B* **48**, 9539 (1993).

[42] A. P. RAMIREZ, G. P. ESPINOSA, and A. S. COOPER, *Phys. Rev. Lett.* **64**, 2070 (1990).

[43] C. BROHOLM, G. AEPPLI, G. P. ESPINOSA, and A. S. COOPER, *Phys. Rev. Lett.* **65**, 3173 (1990).

[44] G. AEPPLI, S. LEE, C. BROHOLM, T. G. PERRING, M. ADAMS, C. CARLILE, A. D. TAYLOR, A. P. RAMIREZ, and B. HESSEN, *Physica B: Condensed Matter* **213-214**, 142 (1995).

[45] P. MENDELS, A. KEREN, L. LIMOT, M. MEKATA, G. COLLIN, and M. HORVATIĆ, *Phys. Rev. Lett.* **85**, 3496 (2000).

[46] A. KEREN, Y. J. UEMURA, G. LUKE, P. MENDELS, M. MEKATA, and T. ASANO, *Phys. Rev. Lett.* **84**, 3450 (2000).

[47] A. P. RAMIREZ, B. HESSEN, and M. WINKLEMANN, *Phys. Rev. Lett.* **84**, 2957 (2000).

[48] P. SCHIFFER, A. P. RAMIREZ, K. N. FRANKLIN, and S.-W. CHEONG, *Phys. Rev. Lett.* **77**, 2085 (1996).

[49] Y. J. UEMURA, A. KEREN, K. KOJIMA, L. P. LE, G. M. LUKE, W. D. WU, Y. AJIRO, T. ASANO, Y. KURIYAMA, M. MEKATA, H. KIKUCHI, and K. KAKURAI, *Phys. Rev. Lett.* **73**, 3306 (1994).

[50] X. OBRADORS, A. LABARTA, A. ISALGUE, J. TEJADA, J. RODRIGUEZ, and M. PERNET, *Solid State Communications* **65**, 189 (1988).

[51] H. MUTKA, G. EHLERS, C. PAYEN, D. BONO, J. R. STEWART, P. FOUQUET, P. MENDELS, J. Y. MEVELLEC, N. BLANCHARD, and G. COLLIN, *Phys. Rev. Lett.* **97**, 047203 (2006).

[52] D. BONO, P. MENDELS, G. COLLIN, and N. BLANCHARD, *Phys. Rev. Lett.* **92**, 217202 (2004).

[53] I. S. HAGEMANN, Q. HUANG, X. P. A. GAO, A. P. RAMIREZ, and R. J. CAVA, *Phys. Rev. Lett.* **86**, 894 (2001).

[54] D. BONO, L. LIMOT, P. MENDELS, G. COLLIN, and N. BLANCHARD, *Low Temperature Physics* **31**, 704 (2005).

[55] D. Bono, P. Mendels, G. Collin, N. Blanchard, F. Bert, A. Amato, C. Baines, and A. D. Hillier, *Physica B: Condensed Matter* **374-375**, 138 (2006).

[56] G. Lawes, M. Kenzelmann, N. Rogado, K. H. Kim, G. A. Jorge, R. J. Cava, A. Aharony, O. Entin-Wohlman, A. B. Harris, T. Yildirim, Q. Z. Huang, S. Park, C. Broholm, and A. P. Ramirez, *Phys. Rev. Lett.* **93**, 247201 (2004).

[57] N. Rogado, G. Lawes, D. A. Huse, A. P. Ramirez, and R. J. Cava, *Solid State Communications* **124**, 229 (2002).

[58] N. Rogado, M. K. Haas, G. Lawes, D. A. Huse, A. P. Ramirez, and R. J. Cava, *Journal of Physics: Condensed Matter* **15**, 907 (2003).

[59] G. Balakrishnan, O. A. Petrenko, M. R. Lees, and D. M. Paul, *Journal of Physics: Condensed Matter* **16**, L347 (2004).

[60] R. Szymczak, M. Baran, R. Diduszko, J. Fink-Finowicki, M. Gutowska, A. Szewczyk, and H. Szymczak, *Phys. Rev. B* **73**, 094425 (2006).

[61] Y. Chen, J. W. Lynn, Q. Huang, F. M. Woodward, T. Yildirim, G. Lawes, A. P. Ramirez, N. Rogado, R. J. Cava, A. Aharony, O. Entin-Wohlman, and A. B. Harris, *Phys. Rev. B* **74**, 014430 (2006).

[62] M. Kenzelmann, A. B. Harris, A. Aharony, O. Entin-Wohlman, T. Yildirim, Q. Huang, S. Park, G. Lawes, C. Broholm, N. Rogado, R. J. Cava, K. H. Kim, G. Jorge, and A. P. Ramirez, *Phys. Rev. B* **74**, 014429 (2006).

[63] N. Qureshi, H. Fuess, H. Ehrenberg, T. C. Hansen, C. Ritter, K. Prokes, A. Podlesnyak, and D. Schwabe, *Phys. Rev. B* **74**, 212407 (2006).

[64] T. Lancaster, S. J. Blundell, P. J. Baker, D. Prabhakaran, W. Hayes, and F. L. Pratt, *Phys. Rev. B* **75**, 064427 (2007).

[65] M. A. Lafontaine, A. Le Bail, and G. Ferey, *Journal of Solid State Chemistry* **85**, 220 (1990).

[66] Z. Hiroi, M. Hanawa, N. Kobayashi, M. Nohara, H. Takagi, Y. Kato, and M. Takigawa, *J. Phys. Soc. Jap.* **70**, 3377 (2001).

[67] F. Bert, D. Bono, P. Mendels, J.-C. Trombe, P. Millet, A. Amato, C. Baines, and A. Hillier, *Journal of Physics: Condensed Matter* **16**, S829 (2004).

[68] M. Shores, E. Nytko, B. Bartlett, and D. Nocera, *Journal of the American Chemical Society* **127**, 13462 (2005).

[69] M. Shores, B. Bartlett, and D. Nocera, *Journal of the American Chemical Society* **127**, 17986 (2005).

[70] J. S. Helton, K. Matan, M. P. Shores, E. A. Nytko, B. M. Bartlett, Y. Yoshida, Y. Takano, A. Suslov, Y. Qiu, J.-H. Chung, D. G. Nocera, and Y. S. Lee, *Phys. Rev. Lett.* **98**, 107204 (2007).

[71] O. Ofer, A. Keren, E. A. Nytko, M. P. Shores, B. M. Bartlett, D. G. Nocera, C. Baines, and A. Amato, *cond-mat/0610540* .

[72] P. Mendels, F. Bert, M. A. de Vries, A. Olariu, A. Harrison, F. Duc, J. C. Trombe, J. S. Lord, A. Amato, and C. Baines, *Phys. Rev. Lett.* **98**, 077204 (2007).

[73] M. Rigol and R. R. P. Singh, *Physical Review Letters* **98**, 207204 (2007).

[74] S. H. Lee, H. Kikuchi, Y. Qiu, B. Lake, Q. Huang, K. Habicht, and K. Kiefer, *Nat Mater* **advanced online publication**, (2007).

[75] R. Wang, W. F. Bradley, and H. Steinfink, *Acta Crystallographica* **18**, 249 (1965).

[76] J. L. JAMBOR, *The Canadian Mineralogist* **37**, 1323 (1999).

[77] J. L. JAMBOR, *The Canadian Mineralogist* **38**, 1298 (2000).

[78] K. M. SCOTT, *The Canadian Mineralogist* **38**, 1295 (2000).

[79] S. W. SQUYRES, J. P. GROTZINGER, R. E. ARVIDSON, I. BELL, J. F., W. CALVIN, P. R. CHRISTENSEN, B. C. CLARK, J. A. CRISP, W. H. FARRAND, K. E. HERKENHOFF, J. R. JOHNSON, G. KLINGELHOFER, A. H. KNOLL, S. M. MCLENNAN, J. MCSWEEN, H. Y., R. V. MORRIS, J. RICE, J. W., R. RIEDER, and L. A. SODERBLOM, *Science* **306**, 1709 (2004).

[80] P. R. CHRISTENSEN, M. B. WYATT, T. D. GLOTCH, A. D. ROGERS, S. ANWAR, R. E. ARVIDSON, J. L. BANDFIELD, D. L. BLANEY, C. BUDNEY, W. M. CALVIN, A. FALLACARO, R. L. FERGASON, N. GORELICK, T. G. GRAFF, V. E. HAMILTON, A. G. HAYES, J. R. JOHNSON, A. T. KNUDSON, J. MCSWEEN, H. Y., G. L. MEHALL, L. K. MEHALL, J. E. MOERSCH, R. V. MORRIS, M. D. SMITH, S. W. SQUYRES, S. W. RUFF, and M. J. WOLFF, *Science* **306**, 1733 (2004).

[81] G. KLINGELHOFER, R. V. MORRIS, B. BERNHARDT, C. SCHRODER, D. S. RODIONOV, J. DE SOUZA, P. A., A. YEN, R. GELLERT, E. N. EVLANOV, B. ZUBKOV, J. FOH, U. BONNES, E. KANKELEIT, P. GUTLICH, D. W. MING, F. RENZ, T. WDOWIAK, S. W. SQUYRES, and R. E. ARVIDSON, *Science* **306**, 1740 (2004).

[82] T. INAMI, S. MAEGAWA, and M. TAKANO, *Journal of Magnetism and Magnetic Materials* **177-181**, 752 (1998).

[83] T. INAMI, T. MORIMOTO, M. NISHIYAMA, S. MAEGAWA, Y. OKA, and H. OKUMURA, *Phys. Rev. B* **64**, 054421 (2001).

[84] M. NISHIYAMA and S. MAEGAWA, *Physica B: Condensed Matter* **329-333**, 1065 (2003).

[85] S. Maegawa, R. Kaji, S. Kanou, A. Oyamada, and M. Nishiyama, *Journal of Physics: Condensed Matter* **19**, 145250 (9pp) (2007).

[86] T. Morimoto, N. M., S. Maegawa, and Y. Oka, *Journal of the Physical Society of Japan* **72**, 2085 (2003).

[87] A. S. Wills, *Phys. Rev. B* **63**, 064430 (2001).

[88] S.-H. Lee, C. Broholm, M. F. Collins, L. Heller, A. P. Ramirez, C. Kloc, E. Bucher, R. W. Erwin, and N. Lacevic, *Phys. Rev. B* **56**, 8091 (1997).

[89] D. Grohol, D. G. Nocera, and D. Papoutsakis, *Phys. Rev. B* **67**, 064401:1 (2003).

[90] D. Grohol and D. Nocera, *Journal of the American Chemical Society* **124**, 2640 (2002).

[91] D. Grohol and D. G. Nocera, *J. AM. CHEM. SOC.* **124**, 2640 (2002).

[92] D. Papoutsakis, D. Grohol, and D. G. Nocera, *J. AM. CHEM. SOC.* **124**, 2647 (2002).

[93] D. G. Nocera, B. M. Bartlett, D. Grohol, D. Papoutsakis, and M. P. Shores, *Chem. Eur. J.* **10**, 3850 (2004).

[94] B. Bartlett and D. Nocera, *Journal of the American Chemical Society* **127**, 8985 (2005).

[95] J. Frunzke, T. Hansen, A. Harrison, J. S. Lord, G. S. Oakley, D. Visser, and A. S. Wills, *Journal of Materials Chemistry* **11**, 179 (2001).

[96] M. Takano, T. Shijo, M. Kiyama, and T. Takada, *Journal of the Physical Society of Japan* **25**, 902 (1968).

[97] M. Takano, T. Shijo, , and T. Takada, *Journal of the Physical Society of Japan* **30**, 1049 (1971).

[98] M. G. TOWNSEND, G. LONGWORTH, and E. ROUDAUT, *Phys. Rev. B* **33**, 4919 (1986).

[99] A. S. WILLS, G. S. OAKLEY, D. VISSER, J. FRUNZKE, A. HARRISON, and K. H. ANDERSEN, *Phys. Rev. B* **64**, 094436 (2001).

[100] V. DUPUIS, E. VINCENT, J. HAMMANN, J. E. GREEDAN, and A. S. WILLS, *Journal of Applied Physics* **91**, 8384 (2002).

[101] S. A. EARLE, A. P. RAMIREZ, and R. J. CAVA, *Physica B* **262**, 199 (1999).

[102] J. MAJZLAN, R. STEVENS, J. BOERIO-GOATES, B. F. WOODFIELD, A. NAVROTSKY, P. C. BURNS, M. K. CRAWFORD, and T. G. AMOS, *Physics and Chemistry of Minerals* **31**, 518 (2004).

[103] S. MAEGAWA, M. NISHIYAMA, N. TANAKA, A. OYAMADA, and M. TAKANO, *Journal of the Physical Society of Japan* **65**, 2776 (1996).

[104] A. S. WILLS, A. HARRISON, C. RITTER, and R. I. SMITH, *Phys. Rev. B* **61**, 6156 (2000).

[105] D. GROHOL and D. NOCERA, *Chemistry of Materials* **19**, 3061 (2007).

[106] C. DROUET and A. NAVROTSKY, *Geochimica et Cosmochimica Acta* **67**, 2063 (2003).

[107] C. DROUET, D. BARON, and A. NAVROTSKY, *American Mineralogist* **88**, 1949 (2003).

[108] K. SASAKI and H. KONNO, *The Canadian Mineralogist* **38**, 45 (2000).

[109] D. GROHOL, D. PAPOUTSAKIS, and D. G. NOCERA, *Angewandte Chemie International Edition* **40**, 1519 (2001).

[110] D. GROHOL, K. MATAN, J. H. CHO, S. H. LEE, J. W. LYNN, D. G. NOCERA, and Y. S. LEE, *Nature Mater.* **4**, 323 (2005).

[111] L. A. Groat, J. L. Jambor, and B. C. Pemberton, *The Canadian Mineralogist* **41**, 921 (2003).

[112] K. Matan, D. Grohol, D. G. Nocera, T. Yildirim, A. B. Harris, S. H. Lee, S. E. Nagler, and Y. S. Lee, *Phys. Rev. Lett.* **96**, 247201 (2006).

[113] B. M. Bartlett, *Synthesis, Structure and Magnetic Properties of Extended 2-D Triangular Lattice*, PhD thesis, Massachusetts Institute of Technology, 2005.

[114] I. Dzyaloshinskii, *Journal of Physics and Chemistry of Solids* **4**, 241 (1958).

[115] T. Moriya, *Phys. Rev.* **120**, 91 (1960).

[116] T. Moriya, *Phys. Rev. Lett.* **4**, 228 (1960).

[117] T. Yildirim and A. B. Harris, *Phys. Rev. B* **73**, 214446 (2006).

[118] D. Coffey, T. M. Rice, and F. C. Zhang, *Phys. Rev. B* **44**, 10112 (1991).

[119] L. Shekhtman, O. Entin-Wohlman, and A. Aharony, *Phys. Rev. Lett.* **69**, 836 (1992).

[120] A. Aharony, O. Entin-Wohlman, and A. B. Harris, *NATO ASI Series, Series E: Applied Science* **349**, 281 (1998).

[121] O. Cépas, K. Kakurai, L. P. Regnault, T. Ziman, J. P. Boucher, N. Aso, M. Nishi, H. Kageyama, and Y. Ueda, *Phys. Rev. Lett.* **87**, 167205 (2001).

[122] O. Cépas, T. Sakai, and T. Ziman, *Progress of Theoretical Physics Supplement* **145**, 43 (2002).

[123] L. B. Steren, M. Tovar, and S. B. Oseroff, *Phys. Rev. B* **46**, 2874 (1992).

[124] M. Hucker, V. Kataev, J. Pommer, U. Ammerahl, A. Revcolevschi, J. M. Tranquada, and B. Buchner, *Phys. Rev. B* **70**, 214515 (2004).

[125] R. K. Li, R. Kremer, and J. Maier, *Journal of Solid State Chemistry* **146**, 488 (1999).

[126] M. Elhajal, B. Canals, and C. Lacroix, *Journal of Physics: Condensed Matter* **16**, S917 (2004).

[127] M. Elhajal, B. Canals, R. Sunyer, and C. Lacroix, *Phys. Rev. B* **71**, 094420 (2005).

[128] M. A. Gîrţu, C. M. Wynn, W. Fujita, K. Awaga, and A. J. Epstein, *Phys. Rev. B* **61**, 4117 (2000).

[129] R. Blinc, K. Pokhodnia, P. Cevc, D. Arčon, A. Omerzu, D. Mihailović, P. Venturini, L. Golič, Z. Trontelj, J. Lužnik, Z. Jegličič, and J. Pirnat, *Phys. Rev. Lett.* **76**, 523 (1996).

[130] Z. Wang, B. Zhang, T. Otsuka, K. Inoue, H. Kobayashi, and M. Kurmoo, *J. Chem. Soc., Dalton Trans.* , 2209 (2004).

[131] J. M. Rawson, A. Alberola, H. El-Mkami, and G. M. Smith, *Journal of Physics and Chemistry of Solids* **65**, 727 (2004).

[132] P. A. Joy and S. Vasudevan, *The Journal of Chemical Physics* **99**, 4411 (1993).

[133] D. N. Aristov and S. V. Maleyev, *Physica B: Condensed Matter* **297**, 78 (2001).

[134] H. Asakawa and M. Suzuki, *Physica A: Statistical and Theoretical Physics* **205**, 687 (1994).

[135] A. Chubukov, *Phys. Rev. Lett.* **69**, 832 (1992).

[136] M. Tamine, *Surface Science* **369**, 403 (1996).

[137] M. Tamine, *Physica B: Condensed Matter* **315**, 38 (2002).

[138] C. G. SHULL, *Reviews of Modern Physics* **67**, 753 (1995).

[139] G. SHIRANE, *Reviews of Modern Physics* **46**, 437 (1974).

[140] G. SHIRANE, S. M. SHAPIRO, and J. M. TRANQUADA, *Neutron Scattering with a Triple-Axis Spectrometer*, Cambrdige University Press, 2002.

[141] S. W. LOVESEY, *Theory of Neutron Scattering from Condensed Matter*, volume 2, Oxford Science Publications, 1987.

[142] Y. S. LEE, *Neutron Scattering Study of the Magnetism and Structural Phases of Superconducting* La_2CuO_{4+y}, PhD thesis, Massachusetts Institute of Technology, 2000.

[143] T. HAHN, editor, *International tables for crystallography. Brief teaching edition of volume A, Space-group symmetry*, Published for the International Union of Crystallography by Kluwer Academic Publishers, 4th, rev. and enl. ed. edition, 1996.

[144] S. W. LOVESEY, *Theory of Neutron Scattering from Condensed Matter*, volume 1, Oxford Science Publications, 1987.

[145] G. L. SQUIRES, *Introduction to the Theory of Thermal Neutron Scattering*, Dover Publication, Inc. Mineola, New York, 1996.

[146] R. M. MOON, T. RISTE, and W. C. KOEHLER, *Phys. Rev.* **181**, 920 (1969).

[147] V. P. PLAKHTY, S. V. MALEYEV, J. KULDA, E. D. VISSER, J. WOSNITZA, E. V. MOSKVIN, T. BRUCKEL, and R. K. KREMER, *Physica B: Condensed Matter* **297**, 60 (2001).

[148] S. V. MALEYEV, *Physica B: Condensed Matter* **350**, 26 (2004).

[149] S. V. MALEYEV, *Journal of Physics: Condensed Matter* **16**, S899 (2004).

[150] V. P. PLAKHTY, J. KULDA, D. VISSER, E. V. MOSKVIN, and J. WOSNITZA, *Phys. Rev. Lett.* **85**, 3942 (2000).

[151] L. P. Regnault, H. M. Ronnow, C. Boullier, J. E. Lorenzo, and C. Marin, *Physica B: Condensed Matter* **345**, 111 (2004).

[152] V. P. Plakhty, S. V. Maleyev, J. Kulda, J. Wosnitza, D. Visser, and E. Moskvin, *Europhys. Lett.* **48**, 215 (1999).

[153] S. V. Maleyev, V. P. Plakhty, O. P. Smirnov, J. Wosnitza, D. Visser, R. K. Kremer, and J. Kulda, *Journal of Physics: Condensed Matter* **10**, 951 (1998).

[154] F. Tasset, E. Lelievre-Berna, T. W. Roberts, E. Bourgeat-Lami, S. Pujol, and M. Thomas, *Physica B: Condensed Matter* **241-243**, 177 (1997).

[155] L. P. Regnault, H. M. Ronnow, J. E. Lorenzo, R. Bellissent, and F. Tasset, *Physica B: Condensed Matter* **335**, 19 (2003).

[156] L. P. Regnault, B. Geffray, P. Fouilloux, B. Longuet, F. Mantegezza, F. Tasset, E. Lelievre-Berna, E. Bourgeat-Lami, M. Thomas, and Y. Gibert, *Physica B: Condensed Matter* **335**, 255 (2003).

[157] M. J. Cooper and R. Nathans, *Acta Crystallographica* **23**, 357 (1967).

[158] M. J. Cooper and R. Nathans, *Acta Crystallographica Section A* **24**, 481 (1968).

[159] M. J. Cooper and R. Nathans, *Acta Crystallographica Section A* **24**, 619 (1968).

[160] M. J. Cooper, *Acta Crystallographica Section A* **24**, 624 (1968).

[161] N. J. Chesser and J. D. Axe, *Acta Crystallographica Section A* **29**, 160 (1973).

[162] R. J. Birgeneau, J. J. Skalyo, and G. Shirane, *Physical Review B (Solid State)* **3**, 1736 (1971).

[163] R. J. BIRGENEAU, H. J. GUGGENHEIM, and G. SHIRANE, *Physical Review B (Solid State)* **1**, 2211 (1970).

[164] R. J. BIRGENEAU, J. J. SKALYO, and G. SHIRANE, *Journal of Applied Physics* **41**, 1303 (1970).

[165] M. ELHAJAL, B. CANALS, and C. LACROIX, *Physica B: Condensed Matter* **312-313**, 716 (2002).

[166] R. BALLOU, B. CANALS, M. ELHAJAL, C. LACROIX, and A. S. WILLS, *Journal of Magnetism and Magnetic Materials* **262**, 465 (2003).

[167] J. RICHTER, *Phys. Rev. B* **47**, 5794 (1993).

[168] T. MOMOI, K. KUBO, and K. NIKI, *Phys. Rev. Lett.* **79**, 2081 (1997).

[169] T. MOMOI, T. HIKIHARA, M. NAKAMURA, and X. HU, *Phys. Rev. B* **67**, 174410 (2003).

[170] K. KUBO, H. SAKAMOTO, T. MOMOI, and K. NIKI, *Journal of Low Temperature Physics* **111**, 583 (1998).

[171] K. KUBO and T. MOMOI, *Zeitschrift für Physik B Condensed Matter* **103**, 485 (1997).

[172] M. TAILLEFUMIER, B. CANALS, C. LACROIX, V. K. DUGAEV, and P. BRUNO, *Phys. Rev. B* **74**, 085105 (2006).

[173] Y.-Y. LI, *Phys. Rev.* **101**, 1450 (1956), and references therein.

[174] P. W. ANDERSON, *Physical Review* **115**, 2 (1959).

[175] M. ELHAJAL, *Propriétés de basse énergie et anisotropies d'interactions de systémes magnétigues géométriquement frustré*, PhD thesis, l'Université Joseph Fourier, 2002.

[176] Y. YAMABE, T. ONO, T. SUTO, and H. TANAKA, *cond-mat/0607440* .

[177] B. O. WELLS, R. J. BIRGENEAU, F. C. CHOU, Y. ENDOH, D. C. JOHNSTON, M. A. KASTNER, Y. S. LEE, G. SHIRANE, J. M. TRANQUADA, and K. YAMADA, *Z. Phys. B* **100**, 535 (1996).

[178] T. THIO, T. R. THURSTON, N. W. PREYER, P. J. PICONE, M. A. KASTNER, H. P. JENSSEN, D. R. GABBE, C. Y. CHEN, R. J. BIRGENEAU, and A. AHARONY, *Phys. Rev. B* **38**, 905 (1988).

[179] J. B. GOODENOUGH, *Journal of Physics and Chemistry of Solids* **6**, 287 (1958).

[180] J. KANAMORI, *Journal of Physics and Chemistry of Solids* **10**, 87 (1959).

[181] R. J. BIRGENEAU, G. SHIRANE, M. BLUME, and W. C. KOEHLER, *Phys. Rev. Lett.* **33**, 1098 (1974).

[182] T. THIO and A. AHARONY, *Phys. Rev. Lett.* **73**, 894 (1994).

[183] T. SUZUKI and Y. NATSUME, *Journal of the Physical Society of Japan* **56**, 1577 (1987).

[184] H. TANAKA, S. TERAOKA, E. KAKEHASHI, K. IIO, and K. NAGATA, *Journal of the Physical Society of Japan* **57**, 3979 (1988).

[185] S.-H. LEE, C. BROHOLM, G. AEPPLI, T. G. PERRING, B. HESSEN, and A. TAYLOR, *Phys. Rev. Lett.* **76**, 4424 (1996).

[186] F. C. COOMER, A. HARRISON, G. S. OAKLEY, J. KULDA, J. R. STEWART, J. A. STRIDE, B. FÅK, J. W. TAYLOR, and D. VISSER, *Journal of Physics: Condensed Matter* **18**, 8847 (2006).

[187] X. G. WEN, F. WILCZEK, and A. ZEE, *Phys. Rev. B* **39**, 11413 (1989).

[188] S. IGUCHI, N. HANASAKI, and Y. TOKURA, *Phys. Rev. Lett.* **99**, 077202 (2007).

[189] H. KAWAMURA, in *Proceeding of the workshop on "Low-Dimensional Quantum Antiferromagnets"* (Fukuoka, Nov. 2001), and reference therein.

[190] P. Calabrese and P. Parruccini, *Phys. Rev. B* **64**, 184408:1 (2001), and references therein.

[191] T. E. Mason, B. D. Gaulin, and M. F. Collins, *Phys. Rev. B* **39**, 586 (1989).

[192] V. P. Plakhty, W. Schweika, T. Bruckel, J. Kulda, S. V. Gavrilov, L.-P. Regnault, and D. Visser, *Phys. Rev. B* **64**, 100402:1 (2001).

[193] T. Yildirim, A. B. Harris, A. Aharony, and O. Entin-Wohlman, *Phys. Rev. B* **52**, 10239 (1995).

[194] N. Mermin and H. Wagner, *Phys. Rev. Lett.* **22**, 1133 (1966).

[195] J. von Delft and C. L. Henley, *Phys. Rev. B* **48**, 965 (1993).

[196] M. Sato, *Phys. Rev. B* **75**, 174407 (2007).

[197] W. Schweika, M. Valldor, and P. Lemmens, *Phys. Rev. Lett.* **98**, 067201 (2007).

[198] B. Keimer, N. Belk, R. J. Birgeneau, A. Cassanho, C. Y. Chen, M. Greven, M. A. Kastner, A. Aharony, Y. Endoh, R. W. Erwin, and G. Shirane, *Phys. Rev. B* **46**, 14034 (1992).

[199] B. Keimer, *Neutron Scattering Study of Magnetism in Pure and Lightly Doped* La_2CuO_4, PhD thesis, Massachusetts Institute of Technology, 1991.

[200] M. Kardar, *Lecture Notes of Statistical Mechanics 2*, 2006, based on lectures given at MIT.

[201] H. Kawamura, *Journal of Physics: Condensed Matter* **10**, 4707 (1998), and references therein.

[202] H. Kawamura, *Journal of the Physical Society of Japan* **54**, 3220 (1985).

[203] H. Kawamura, *Journal of the Physical Society of Japan* **56**, 474 (1987).

[204] H. KAWAMURA, *Journal of the Physical Society of Japan* **55**, 2095 (1986).

[205] H. KAWAMURA, *Journal of the Physical Society of Japan* **58**, 584 (1989).

[206] H. KAWAMURA, *Journal of the Physical Society of Japan* **61**, 1299 (1992).

[207] Y. AJIRO, T. NAKASHIMA, Y. UNNO, H. KADOWAKI, M. MEKATA, and N. ACHIWA, *Journal of the Physical Society of Japan* **57**, 2648 (1988).

[208] H. KADOWAKI, S. M. SHAPIRO, T. INAMI, and Y. AJIRO, *Journal of the Physical Society of Japan* **57**, 2640 (1988).

[209] T. E. MASON, B. D. GAULIN, and M. F. COLLINS, *Phys. Rev. B* **39**, 586 (1989).

[210] J. WANG, D. P. BELANGER, and B. D. GAULIN, *Phys. Rev. Lett.* **66**, 3195 (1991).

[211] R. DEUTSCHMANN, v. LÖHNEYSEN, J. WOSNITZA, R. K. KREMER, and D. VISSER, *Europhys. Lett.* **17**, 637 (1992).

[212] B. D. GAULIN, T. E. MASON, M. F. COLLINS, and J. Z. LARESE, *Phys. Rev. Lett.* **62**, 1380 (1989).

[213] S. T. BRAMWELL and P. C. W. HOLDSWORTH, *Journal of Physics: Condensed Matter* **5**, L53 (1993).

[214] H.-J. XU and B. W. SOUTHERN, *Journal of Physics A: Mathematical and General* **29**, L133 (1996).

[215] L. CAPRIOTTI, R. VAIA, A. CUCCOLI, and V. TOGNETTI, *Phys. Rev. B* **58**, 273 (1998).

[216] L. CAPRIOTTI, A. CUCCOLI, V. TOGNETTI, P. VERRUCCHI, and R. VAIA, *Phys. Rev. B* **60**, 7299 (1999).

[217] L. CAPRIOTTI, A. CUCCOLI, V. TOGNETTI, P. VERRUCCHI, and R. VAIA, *Journal of Applied Physics* **87**, 7037 (2000).

[218] P. Olsson, *Phys. Rev. Lett.* **75**, 2758 (1995).

[219] S. T. Bramwell, P. C. W. Holdsworth, and H. T. Hutchings, *Journal of the Physical Society of Japan* **64**, 3066 (1995).

[220] D. H. Lee, J. D. Joannopoulos, J. W. Negele, and D. P. Landau, *Phys. Rev. B* **33**, 450 (1986).

[221] K. Nho and D. P. Landau, *Phys. Rev. B* **66**, 174403 (2002).

[222] P. Olsson, *Phys. Rev. Lett.* **77**, 4850 (1996).

[223] P. Olsson, *Phys. Rev. B* **55**, 3585 (1997).

[224] G. Ramirez-Santiago and J. V. José, *Phys. Rev. Lett.* **68**, 1224 (1992).

[225] G. Ramirez-Santiago and J. V. José, *Phys. Rev. B* **49**, 9567 (1994).

[226] S. E. Korshunov, *Phys. Rev. B* **65**, 054416 (2002).

[227] S. E. Korshunov, *PHYS-USP* **49**, 225 (2006).

[228] N. D. Mermin and H. Wagner, *Phys. Rev. Lett.* **17**, 1133 (1966).

[229] A. Cuccoli, V. Tognetti, and R. Vaia, *Phys. Rev. B* **52**, 10221 (1995).

[230] R. Gupta and C. F. Baillie, *Phys. Rev. B* **45**, 2883 (1992).

[231] H. E. Stanley and T. A. Kaplan, *Phys. Rev. Lett.* **17**, 913 (1966).

[232] B. Jancovici, *Phys. Rev. Lett.* **19**, 20 (1967).

[233] M. A. Moore, *Phys. Rev. Lett.* **23**, 861 (1969).

[234] F. Wegner, *Z. Phys.* **206**, 465 (1967).

[235] B. L. Berezinskii, *Sov. Phys.-JETP* **32**, 493 (1971).

[236] J. M. Kosterlitz and D. J. Thouless, *Journal of Physics C: Solid State Physics* **6**, 1181 (1973).

[237] J. M. KOSTERLITZ, *Journal of Physics C: Solid State Physics* **7**, 1046 (1974).

[238] D. MCQUEENEY, G. AGNOLET, and J. D. REPPY, *Phys. Rev. Lett.* **52**, 1325 (1984).

[239] A. F. HEBARD and A. T. FIORY, *Phys. Rev. Lett.* **44**, 291 (1980).

[240] D. J. RESNICK, J. C. GARLAND, J. T. BOYD, S. SHOEMAKER, and R. S. NEWROCK, *Phys. Rev. Lett.* **47**, 1542 (1981).

[241] F. G. MERTENS, A. R. BISHOP, G. M. WYSIN, and C. KAWABATA, *Phys. Rev. Lett.* **59**, 117 (1987).

[242] F. G. MERTENS, A. R. BISHOP, G. M. WYSIN, and C. KAWABATA, *Phys. Rev. B* **39**, 591 (1989).

[243] P. GAVEAU, J. P. BOUCHER, L. P. REGNAULT, and Y. HENRY, *35th Annual Conference on Magnetism and Magnetic Materials* **69**, 6228 (1991).

[244] L. P. REGNAULT, J. ROSSAT-MIGNOD, J. Y. HENRY, and L. J. DE JONGH, *Journal of Magnetism and Magnetic Materials* **31-34**, 1205 (1983).

[245] M. HEINRICH, H.-A. KRUG VON NIDDA, A. LOIDL, N. ROGADO, and R. J. CAVA, *Phys. Rev. Lett.* **91**, 137601 (2003).

[246] W. KNAFO, C. MEINGAST, K. GRUBE, S. DROBNIK, P. POPOVICH, P. SCHWEISS, P. ADELMANN, T. WOLF, and H. V. LÖHNEYSEN, *Phys. Rev. Lett.* **99**, 137206 (2007).

[247] D. G. WIESLER, H. ZABEL, and S. M. SHAPIRO, *Zeitschrift für Physik B Condensed Matter* **93**, 277 (1994).

[248] J. ALS-NIELSEN, S. T. BRAMWELL, M. T. HUTCHINGS, G. J. MCINTYRE, and D. VISSER, *Journal of Physics: Condensed Matter* **5**, 7871 (1993).

[249] S. T. BRAMWELL and P. C. W. HOLDSWORTH, *Phys. Rev. B* **49**, 8811 (1994).

[250] B. L. BEREZINSKII and A. Y. BLANK, *Sov. Phys.-JETP* **37**, 369 (1973).

[251] R. GUPTA, J. DELAPP, G. G. BATROUNI, G. C. FOX, C. F. BAILLIE, and J. APOSTOLAKIS, *Phys. Rev. Lett.* **61**, 1996 (1988).

[252] M. Elhajal (private communication).

[253] A. CUCCOLI, T. ROSCILDE, R. VAIA, and P. VERRUCCHI, *Phys. Rev. Lett.* **90**, 167205 (2003).

[254] A. CUCCOLI, T. ROSCILDE, V. TOGNETTI, R. VAIA, and P. VERRUCCHI, *Phys. Rev. B* **67**, 104414 (2003).

[255] K. HUANG, *Statistical Mechanics*, John Wiley & Sons, 2nd edition, 1987.

[256] C. N. YANG, *Phys. Rev.* **85**, 808 (1952).

[257] D. ARNDT, S. FASSBENDER, M. ENDERLE, and K. KNORR, *Phys. Rev. Lett.* **80**, 1686 (1998).

[258] H. IKEDA and K. HIRAKAWA, *Solid State Communications* **14**, 529 (1974).

[259] E. J. SAMUELSEN, *Phys. Rev. Lett.* **31**, 936 (1973).

[260] C. BIAGINI, A. CUCCOLI, V. TOGNETTI, R. VAIA, and P. VERRUCCHI, *Journal of Applied Physics* **79**, 4638 (1996).